UNIVERSITY OF CALIFORNIA
RIVERSIDE

Vascular Biotransport Considerations in Signaling Cascades

A Dissertation submitted in partial satisfaction
of the requirements for the degree of

Doctor of Philosophy

in

Bioengineering

by

Prashanthi Vandrangi

December 2012

Dissertation Committee:
Dr. Victor G J Rodgers, Chairperson
Dr. John J Y Shyy
Dr. Jiayu Y Liao

The Dissertation of Prashanthi Vandrangi is approved:

_____

_____

_____

Committee Chairperson

University of California, Riverside

Acknowledgment Page

First and foremost, I express my deepest admiration and gratitude to my advisor, Dr. Victor G J Rodgers. Dr. Rodgers' deep insight to solve biological problems from an engineering perspective provided me the foundation to rationally design solutions. His patience, guidance, and invaluable mentorship, from the start to the end of my PhD program fostered my success as I juggled research, work, and community service. Dr. Rodgers' intellectual immensity is matched only by his genuinely welcoming personality and humbleness. I extend my gratitude to his twin brother Dr. Vincent Rodgers for his encouraging notes and words throughout the process. Knowing the hardships and challenges that you both went through while you obtained your PhDs not only shaped me into being a better individual but also made me grateful to my enriched education.

I sincerely want to thank my dissertation committee of Dr. John Shyy and Dr. Jaiyu Liao. Collaborations with Dr. John Shyy, the vascular biology guru and Dr. Masaru Rao, the expert in nanotechnology device design have opened doors to captivating problems. I thank my research group (the B2K group) for all their constructive criticism/suggestions in lab meetings and in Bourns Hall A135. Thank you Devin and Noriko for always being there for me. I thank all the undergraduate scholars that worked with me the past few years (Heran, Ryan, Nicole, Martha, Sruthi, Pamela, and Nidhi). It has been fun mentoring you and I was enriched through the process.

I take this moment to appreciate some of the courses that I took in my PhD. Dr. Rodgers' classes on biotransport phenomena, reaction engineering, mass transfer, advanced engineering mathematics, and multi-scale modelling provided me a breadth of

engineering topics that could be applied directly to my research. Dr. Liao's class on cellular and molecular engineering and Dr. Jolinda Traugh's class on signal transduction not only built my foundation in biotechnology but fascinated me in exploring the working of signaling pathways with an engineering and computational vigor.

Over the past five years I have received support and encouragement from a great number of individuals in the Department of Bioengineering. Ms. Denise Sanders has been a friend throughout my journey and I share a special bond with her. Ms. Hong Xu has been there to provide me any technical assistance at any time. I also thank Ms. Jennifer Morgan and Ms. Crissy Reissing for working with me so efficiently. Further, I acknowledge Dr. Dimitri Morikis and Dr. Bahman Anvari for their support. In a similar vein, I recognize Dr. Hyle Park for his friendly demeanor and supporting smile. During my stay at UCR, I had a unique opportunity to work at the Graduate Division. I thank Dean Joseph Childers, Dean Ken Baerenklau, and Dean Haimo for all their smiles and support while working as a mentor teaching assistant or while heading the GradPREP team. I am extremely thankful for the friendly suggestions and support provided by Assistant Dean Lai and Ms. Maria Franco Aguilar for their listening ears, wise suggestions, and helpful hands.

You always come across some wonderful beings whose mere presence inspires you. At this time, I would like to acknowledge the first National Academy recipient I ever met - Dr. Jerome Schultz and his beautiful wife, Dr. Jane Schultz for inspiring me in many ways. I would like to also thank one of the first woman chemical engineering

doctorates who I met – Dr. Lilia Abron for her grace and modesty and for leaving an ever-lasting impression on young female researchers like myself.

During these strides, I thank all my faithful and loyal friends who supported me personally and professionally. I would not have been here if it was not for the mentorship provided to me from my childhood. I acknowledge some of my teachers- Mrs. Baladino, Mrs. Sergant, Brother Roque, Brother TV Joseph, Brother KM Joseph, late Mrs. Jyosthna and my late grandfather Gopal Rao. Finally, I would be remiss if I didn't acknowledge the innumerable sacrifices made by my family. I know that it took a great deal of strength to encourage me while pursuing my PhD and I just want to thank you all.

I dedicate this dissertation to my family -

to Kuppili grandma for her prayers and blessings,

to late grandpas and grandmas (Vandrangi, Kuppili, and Konakalla)

for being the reason for my existence,

to mom, dad, and anniya

for their love and

for always instilling in me the importance of hard work and sincerity

to anniya and vadina for understanding me and

to Annanya for her laughter and smiles

that eased my stress during the last leap.

ABSTRACT OF THE DISSERTATION

Vascular Biotransport Considerations in Signaling Cascades
Filing Their Dissertations

by

Prashanthi Vandrangi

Doctor of Philosophy, Graduate Program in Bioengineering
University of California, Riverside, December 2012
Dr. Victor G J Rodgers Chairperson

The vasculature of our body sensitively responds to varied biomolecules. These biomolecules are critical in triggering downstream protein synthesis, mRNA transcription, and DNA synthesis, and hence vascular homeostasis. We take these studies as an opportunity to understand the orchestra of (1) charge properties, (2) mechanical topography, (3) fluid dynamics, and (4) molecular cues to obtain a systemic and integrative understanding of the vasculature. In this work, we introduce a novel *in-situ* streaming potential device to quantify the electrostatic contribution of morphological changes in confluent endothelial cells (ECs). We further study the effect of mechanical topographies of nan-patterned titanium on ECs. Both species mass transfer and mechanotransduction have been suggested as the underlying mechanisms for activating ECs. However, in recent years, the dominance of mechanotransduction at the endothelium has been qualitatively demonstrated through *in-vitro* experiments attempting to emulate the vasculature. Thus, it remains plausible that biomolecular mass transfer may be significant in vascular signaling pathways. This work shows that a more cautious

analysis that delineates endothelial mechanotransduction from mass transfer remains warranted. Having said that, we propose a novel, *in-vitro* experimental methodology using membrane separations technology. The methodology is flexible and robust, in that it can be used with mass transfer-limited and reaction-limited processes and can address a number of controllable scenarios. Finally, we characterize the endothelial behavior in healthy and diseased ECs by characterizing the sub-endothelium and the underlying endothelial signaling pathways. The work presented here demonstrates the vast number of biotransport factors to be captured while studying the fascinating vascular endothelium. Understanding these mechanistic factors of ECs and the triggered signaling pathways is crucial to our search for novel therapeutics.

Keywords – vasculature, charge, mechanical, mass transfer, mechanotransduction, signaling

TABLE OF CONTENTS

LIST OF TABLES

LIST OF FIGURES

CHAPTER 1

INTRODUCTION

The vasculature of our body is fascinatingly sensitive as it continually responds to varied biomolecules and mitogens. These biomolecules are critical in triggering downstream protein synthesis, mRNA transcription, and DNA synthesis. Understanding the mechanistic behavior of these signaling pathways is crucial to our search for new therapeutic drugs for vascular diseases. We take these studies as an opportunity to understand the interplay of fluid dynamics, mechanical signals, molecular cues, and charge properties to obtain a systemic integrative approach to our understanding of signaling pathways (a) while we characterize charge properties and microvilli growth in mucosal cells and endothelial cells, (b) in cells seeded on different biomaterials with nano-structured and micro-structured grooves, (c) to understand their causal underlying mechanisms in endothelial cells under dynamic flow, and (d) in endothelial cells grown on extracellular matrix compositions related to atherosclerosis.

Section 1 introduces a novel in-situ streaming potential device to quantify the electrostatic contribution of morphological changes in cells. Capturing the electrostatic properties of cells plays an important role in designing novel bio-compatible pharmaceuticals. Streaming potential, measured as the potential along/across a cellular monolayer for a given pressure drop, is a commonly utilized method to study ion conductivity and para-cellular uptake. In this study, we employ a streaming potential device that measures the electric potential across the apico-basal surfaces of the cellular monolayer.

In Section 2, we study the effect of nano-scale features on vascular metallic surfaces which mimic the natural structure of the healthy vessel wall. In this study, we

investigate endothelial cell adhesion, alignment, proliferation, and spreading on surfaces with rationally designed patterns on Ti surfaces composed of nanometer-wide grooves compared with both micrometer wide grooves and no grooves at all. The results show that the nanometer grooves on the Ti surfaces enhance the cell proliferation rate.

Collectively, these results demonstrate the superior performance of nano-patterned Ti substrates for possible stent deployment. The results also demonstrate the utilization of Ti substrates in areas that need neo-vascularization. The underlying reason of the behavior of these cellular systems on the substrates is still largely unknown even after studying the signaling pathways in these cellular systems. Both species mass transfer and mechanotransduction have been suggested as the underlying mechanisms for activating endothelial signaling pathways. However, in recent years, the dominance of mechanotransduction at the endothelium has been qualitatively demonstrated through in-vitro experiments attempting to emulate the vasculature.

As evident from our results, shown in Section 3, the use of viscosity variation relative to shear rate and shear stress are not enough to eliminate mass transfer in determining the signaling mechanism in endothelium processes. Thus, it remains plausible that biomolecular mass transfer may be significant in vascular signaling pathways. This work shows that a more cautious analysis that delineates endothelial mechanotransduction from mass transfer remains warranted. Here, we propose a novel, *in-vitro* experimental methodology using membrane separations technology. The proposed technique can decouple mechanotransduction effects from mass transfer in

flow-induced studies. The methodology is flexible and robust, in can be used with mass transfer-limited and reaction-limited processes and can address a number of controllable scenarios.

In Section 4, we study the biomolecular aspect of a model signaling cascade during atherosclerosis. Initiation and progression of atherosclerosis is characterized by varied expression of extracellular proteins and molecules, and altered composition of extracellular matrix (ECM). Appropriate ECM composition establishes the functioning of endothelial cells of the vascular intima. Altered ECM is an important biomarker for determining vessel stiffening in atherosclerosis and also in aging vessels. The resulting vascular shear stress is conversed by ECM into internal cell signaling pathways. We determine the effect of altered composition and organization of the extracellular milieu, as a response to laminar flow patterns on the AMPK-eNOS signalling cascade.

SECTION 1

CHARACTERIZING CELL-CHARGE INTERACTIONS

PRELUDE

Optimal intestinal absorption is required for an efficient pharmaceutical administration by the per-oral route. Several molecular mechanisms are involved in intestinal absorption and can profoundly influence the extent of uptake including (1) permeation of the mucosa by passive diffusion, (2) transport across the intestinal wall by carrier mediated processes, (3) chemical and enzymatic alteration of the molecule in the intestinal lumen and/or in the enterocyte, and (4) dissolution of the drug and interaction with food ingredients or co-administered drugs at the suspension and transport level. These cellular efflux mechanisms typically act simultaneously and depend on the drug molecule and epithelium related- chemical and biological factors whose effect is not definitely established. This makes intestinal absorption a rather complex process, which, despite recent advances, is fundamentally still poorly understood.

Capturing the electrostatic properties cells plays an important role in designing novel bio-compatible pharmaceuticals. Streaming potential, measured as the potential along/across a cellular monolayer for a pressure drop, is a commonly utilized method to study ion conductivity and para-cellular uptake. In this study, we employ a streaming potential device that measures the electric potential across the apico-basal surfaces of the cellular monolayer.

The objective of the present work is to design a streaming potential device and establish a methodology for determining the contribution of cellular features on passive diffusion, carrier-mediated transport, enzymatic degradation and non-specific

binding/adsorption to drug absorption. The *in-situ* normal streaming potential device quantitatively measures the electrostatic and transport properties in confluent and intact cells. The device will facilitate the simultaneous measurement of the (1) Hydraulic permeability (L_P); (2) Trans-electrical resistance (TER); and (3) Zeta potential (ζ).

In Chapter 2, the design of this novel device and the successful measurement of zeta potential was measured across membrane properties (material and pore size) and electrolyte conductivity (both composition and ionic strength) of the medium flowing across the membranes.

In Chapter 3, the implementation of this novel device was tested for capturing the streaming potential of human kidney cells (HEK), Chinese hamster ovary cells (CHO), colon carcinogenic cells (Caco2), and human endothelial cells (EA926). The zeta potential was deconolved mathematically to obtain the zeta potential of a confluent cell layer from a cell seeded - membrane configuration. The results were further validated using a commercial Zetasizer®.

In Chapter 4, the novel *in-situ* streaming potential device was employed to delineate the contribution of morphological processes and tight junctions in the popularly used *in-vitro* intestinal model, Caco2 cells. In this particular study, EA926 cells were used as a control as they exhibit similar tight junction ion-selectivity but lack the characteristic brush borders, hence speculating the change in zeta potential to be directly correlated to the microvilli growing on the Caco-2 cell surface.

In conclusion, the designed device and methodology provides a quantitative insight into the characteristic cellular features that effects the process of drug absorption. These studies can be used to better understand the widely employed Caco2 model to study drug permeability studies. The experiments can also potentially be used as a means to support the prediction of *in-vivo* absorption based on cell culture data and to elucidate the effects of the involved mechanisms.

CHAPTER 2

DESIGN OF NOVEL *IN-SITU*

STREAMING POTENTIAL DEVICE

2.1 ABSTRACT

In this Chapter, we introduce a novel streaming potential measurement device to characterize the normal electrostatic properties of varied electrolyte and membrane configurations. The streaming potential device encompasses a 24 mm cell-seeded Transwell® with two AgCl electrodes on either side of the cell-seeded Transwell®. PBS, NaCl, or KCl is pressurized transversal to the Transwell® and the resultant pressure gradient induces a potential difference. cellulosic, collagen coated PTFE, and polycarbonate membranes of varied pore sizes (0.4 μm, 3 μm, and 8 μm) were used to study their effects on the measured streaming potentials. The corresponding zeta potential of the membrane-electrolyte configuration is calculated using the Helmholtz Smochulski equation. The streaming potential of polycarbonate membranes was -23.41 mV, cellulosic was -0.67 mV, and collagen coated PTFE was -1.23 mV when soaked in water. When soaked in DMEM, we observed a decrease in the streaming potential to 0-13.4 mV and an increase in streaming potential to -2.97 mV for polycarbonate and cellulosic membranes respectively. Collagen coated PTFE membranes exhibited minimal change with change in soaking conditions. In summary, polycarbonate membranes with pore size of 3.0 um have exhibited the most favorable streaming potential variations. This sensitivity of the membrane with PBS (1.8 mS/cm) makes them the ideal combination for studying streaming potential while employing our methodology to study cellular systems and drug permeability.

Keywords – streaming potential, membrane, electrolyte

2.2 INTRODUCTION

2.2.1 Formation of interfacial double layers

When a charged species is submerged in an aqueous ionic media, an electric double layer (EDL) is developed around its surface. EDL consists of two layers: the Stern layer and the diffuse layer. The layer which contains the adsorbed ions is the Stern layer (outer Helmholtz plane) and it defines the surface charge of the charged species. The second layer, the diffuse layer consists of ions freely moving in the solution and loosely attached to the surface of the species through Coulomb's Law. Despite its small magnitude, the first layer, the Stern layer can have significant effects on double layer properties [1]. Its thickness is given by δ, where δ os in the order of a hydrated ion. The variation of potential from the stern layer is given by:

$$\psi = \psi_s e^{-kx} \tag{1}$$

where ψ is the potential, x is the distance away from the membrane and k is the Debye-Huckel parameter. The Debye length directly characterizes the length of the diffuse layer and is inversely proportional to the square of the ionic strength of the solution and is defined as:

$$k^2 = \frac{1000F^2}{\varepsilon RT}\sum\left(c_i z_i^2\right) \tag{2}$$

where F is Faraday's constant, c_i is the concentration of all significant ions in solution and z_i is the charge valence.

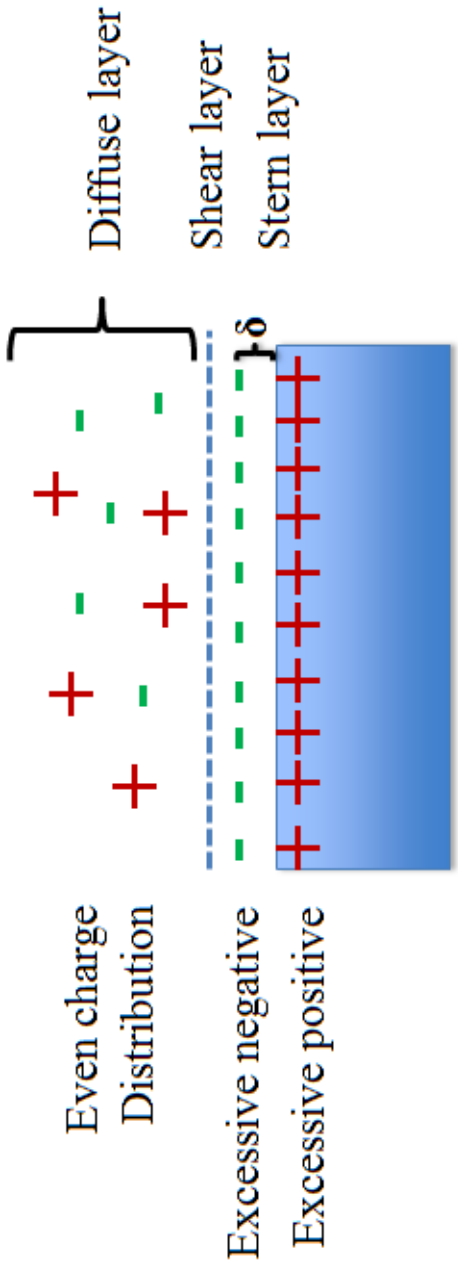

Figure 2.1| EDL formation for a positively charged surface in an electrolyte. The thickness of the Stern layer is given as δ.

2.2.2 Helmoltz - Smoluchowski theory

When a tangential shear force is applied along the diffuse layer, at least a part of the diffuse layer is moved under its influence. The electric potential measured at this plane is represented as the zeta potential [2]. Hence zeta potential arises from the electrokinetic interactions between the surface charge and dissolved ions in solution [3].

Further, when pressure is applied along/across the diffuse layer, the streaming potential that arises is directly related to the corresponding zeta potential by the Helmholtz – Smoluuchowski equation. In a given colloidal system, for a definite pressure drop, the zeta potential can be calculated based on the variations of streaming potential across the charged species using Helmholtz-Smoluchowski equation:

$$\frac{\Delta\Psi}{\Delta P} = \frac{\varepsilon_0 \varepsilon_r \zeta}{\mu \Lambda_0} \tag{3}$$

where $\Delta\Psi$ is the streaming potential (V), ΔP is the pressure drop (Pa), ε_0 is the permittivity of free space, ε_r is the relative dielectric constant of the solvent, μ is the viscosity of the solution and Λ_0 is the conductivity of the electrolyte solution [4-5].

In this chapter, we introduce a novel *in-situ* streaming potential device to measure the charge properties of a test bed. The test bed implements commercial Transwells® with membrane configurations. We study the effect of membranes, electrodes, electrolyte solution, composition, and conductivity on measured streaming potential and calculated zeta potential.

In the subsequent paragraphs, we account for various device specifications while designing the streaming potential device. The ultimate purpose of the device is to detect a

difference in potential between the charged surface and electrolyte solution [6]. In addition to the experimental artifacts that can be introduced due to the choice of the electrodes and membranes, the choice of the electrolyte solution highly affects the accuracy of streaming potential measurements.

2.2.3 Choosing membranes

When employing membranes in streaming potential measurements, care must be taken to pre-soak membranes so that they are completely and uniformly hydrated. It is important to note that its molecular weight cutoff (MWCO) does not affect the measurements at high pressure ranges; also there is a possible overlap of both Stern and diffuse layers when the pore width is relatively smaller than EDL [7-8]. In this study, we consider the treatment effects through the evaluation of zeta potential across three types of Transwell® membranes (collagen coated PTFE, polycarbonate, and cellulosic) for three different pore sizes (0.4µm, 3µm and 8µm).

2.2.4 Choosing electrodes

Measuring electrodes are the most crucial aspect to be considered while setting up streaming potential device [9]. The intercept of the linear fit of potential variations with respect to the measured pressure demonstrates the accuracy of voltage measured between electrodes. Enumerous studies have been performed by employing many metals such as platinum, nickle, gold, and silver. In our study, we employ Ag/AgCl electrodes since AgCl is stable regardless of flow direction and introduces minimal offset in measured

potential. The Ag electrodes were often recoated when the noise in the measured values became noticable. The electrodes were recoated by inserting them in solution with surplus Cl^- ions (See Appendix). Symetrically aligning the electrodes was also important.

2.2.5 Electrolyte solution and conductivity

The ionic strength of the electrolyte solution and its chemical composition plays a critical role in the accuracy of the measurements [10-12]. In fact, the valence of ions in electrolyte highly affects the measurements. An increase in anions valence leads to high reduction in zeta potential whereas an increase in cation valence leads to an increase in zeta potential.

While changes in monovalent salts as NaCl, KCl and LiCl do not affect ion binding interactions, the ionic concentration of the electrolyte solution needs to remain significantly low. In this study, phosphate buffered saline (PBS) solutions were used as an electrolyte in order to maintain favorable physiological conditions. Although streaming potential measurements across the cells were mainly undertaken at low ionic strength, the effect of different PBS concentrations was also taken into account.

2.3 METHODS

2.3.1 Membranes

In the test cell, we employed the use of three membrane types (A) collogen-coated PTFE, (B) polycarbonate, and (C) cellulosic. Collagen-coated PTFE membranes (Corning®, Lot no 3491), polycarbonate membranes (Corning®, Lot no 3422), and cellulosic membranes (Millipore®, HAWP03700) having diameters of 24 mm and pore sizes of 0.4 μm, 3 μm, and 8 μm were implemented. The cellulosic membranes were glued to the Transwell®s and had an molecular weight cut off (MWCO) of 30 kDa.

2.3.2 Electrolyte

PBS solution is used as an electrolyte in order to maintain favorable physiological conditions. Since the valence of ions in electrolyte solution and its concentration highly affects the accuracy of streaming potential measurements, the PBS solution is kept at low ionic strength in this study to prevent masking of the streaming potential of the cellular monolayer. The solution was maintained at 7.4 pH. The composition of the PBS was 8 g of NaCl, 0.2 g of KCl, 1.44 g of Na_2HPO_4, 0.24 g of KH_2PO_4 with a final concentration of 137 mM NaCl, 10 mM Phosphate, 2.7 mM KCl at a pH of 7.4. The electrolyte solution of PBS was diluted approximately 10 times to obtain a conductivity of 1.8 mS/cm. In some cases, 0.15 M NaCl or10 mM KCl were used as electrolytes.

2.3.3 Soaking conditions

The membranes were either soaked in DI water, DMEM, NaCl, KCl, or 200 g/L BSA and the effect of varied soaking solutions was studied.

2.3.4 Electrode configuration

Ag/AgCl electrodes (Sigma Aldrich) were utilized for these experiments. With 1.0 mm diameter and 99.9 % trace metal basis with resistivity of 1.59 μΩ-cm 20 ^{O}C and density 10.49 g/cm^{3}.

2.4 RESULTS

2.4.1 Design of streaming potential device

We design a streaming potential device that allows the measurement of streaming potential variations membranes. The device was designed using industrial grade clear polycarbonate to enable easy monitoring and inspection of void space and air bubbles allowing for uniform passage of electrolyte solution. The device has a test bed that allows the usage of standard Transwell® inserts (24 mm diameter).

Flow of the electrolyte solution is restricted by 1 mm diameter porous structure in proximity of the Transwell surface. Under pressure application, changes in streaming potential are detected by a voltmeter connected to electrodes inserted in proximity of both sides of the Transwell's membrane. Data was collected representing the change of streaming potential $\Delta\Psi$ in volts with respect to pressure drop ΔP. After performing a linear regression on the data points, the slope of the line is determined graphically and used to compute ζ using the Helmholtz-Smoluchowski equation.

In order to further eliminate any experimental errors introduced due to flow directions, pressure application was varied in crescendo and decrescendo phases. Data are expected to be collected after steady state is reached. All streaming potential measurements were repeated at least three times for each studied Transwell.

A

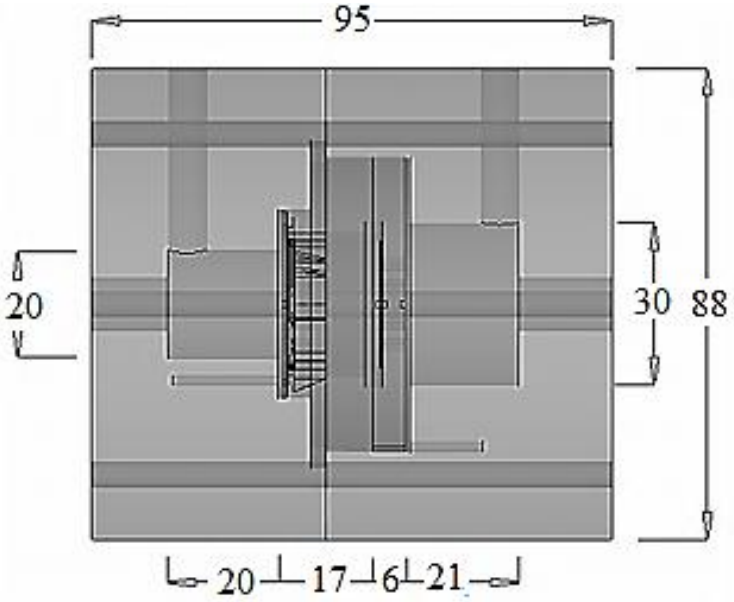

B

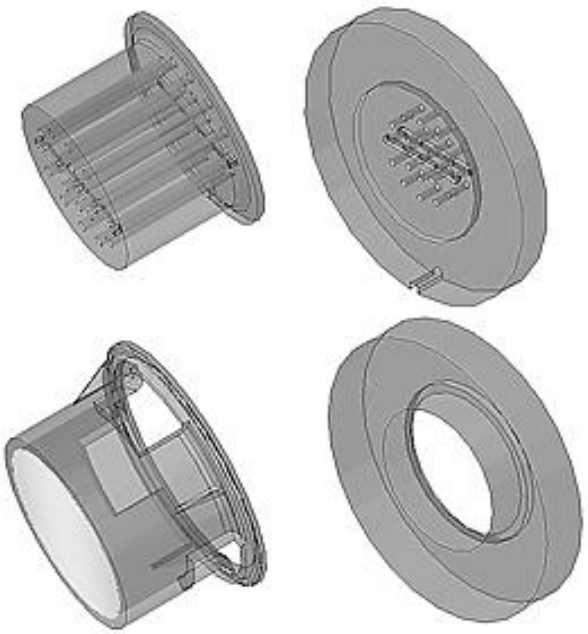

Figure 2.2| CAD images of the prototype of the streaming potential device: A. Side View, B. Inner components of the device. All units are in mm.

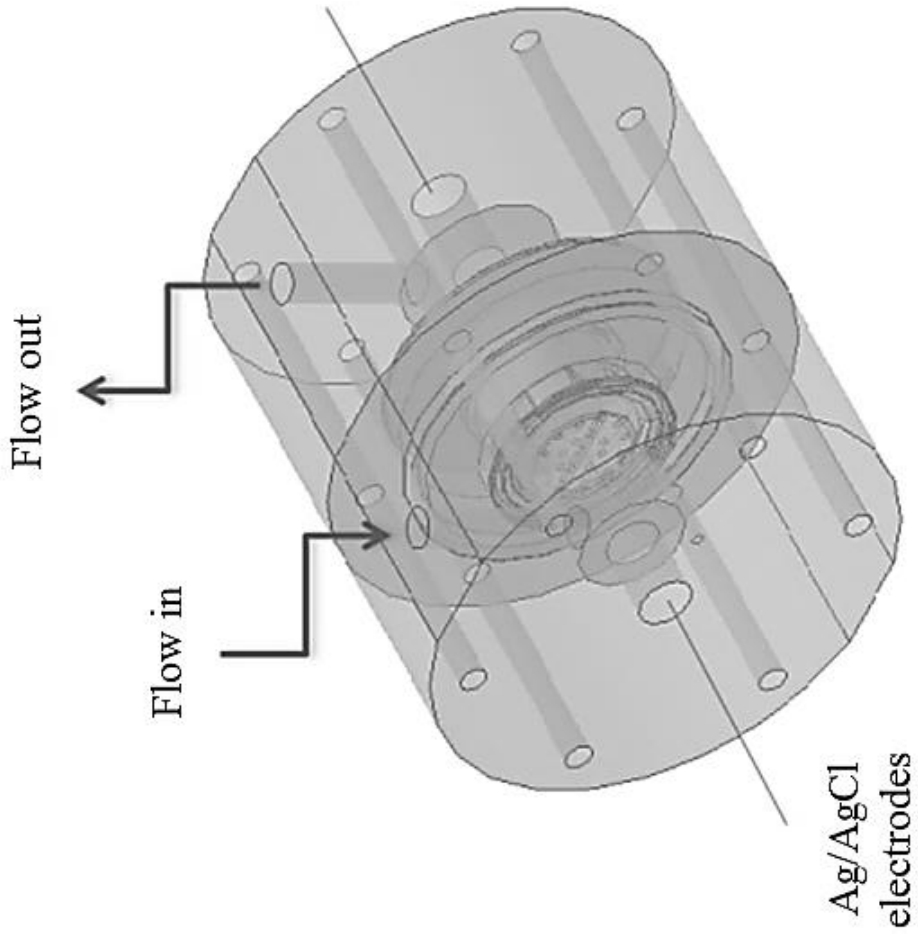

Figure 2.3| Isotropic view of the prototype of the streaming potential device

Figure 2.4| Designed streaming potential device: images of the final product

2.4.2 Normal zeta potential measurements using streaming potential device

Streaming potential experiments are performed using an *in-situ* streaming potential device shown in Figure 2.2. The device measures the potential across the cells cultured on the hosted 24 *mm* Transwells® (Corning, Corning, NY). Electrolytic solution of phosphate buffered saline (PBS) (1.87 mS/cm^2) flows through the feed side of the device, normal to the Transwell® (with a known pressure drop), and exits out through the permeate side of the device. The developed normal streaming potential across the membrane is measured by the Ag/AgCl electrodes on the feed and permeate sides of the Transwell®. Zeta potential (ζ) is calculated using the Helmholtz-Smoluchowski equation [29-30].

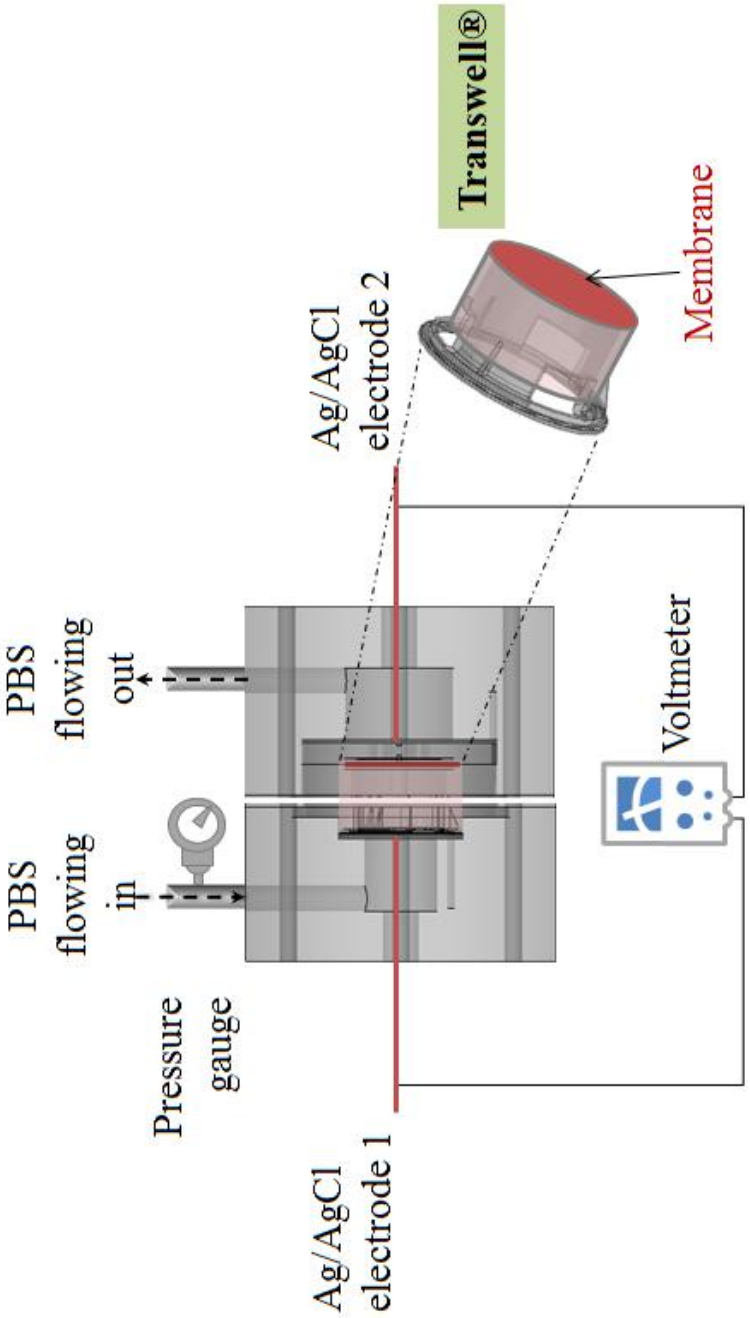

Figure 2.5. Schematic of the normal streaming potential device. Ag/AgCl electrodes are used to measure the streaming potential with a voltmeter (110 True RMS Multimeter, Fluke Inc.). PBS (1.87 mS/cm) was used as the electrolyte solution and the pressure at the inlet was monitored using a pressure gauge. Polycarbonate Transwell® seeded with confluent EA926 cells or HEK cells or with no cells are hosted in the chamber.

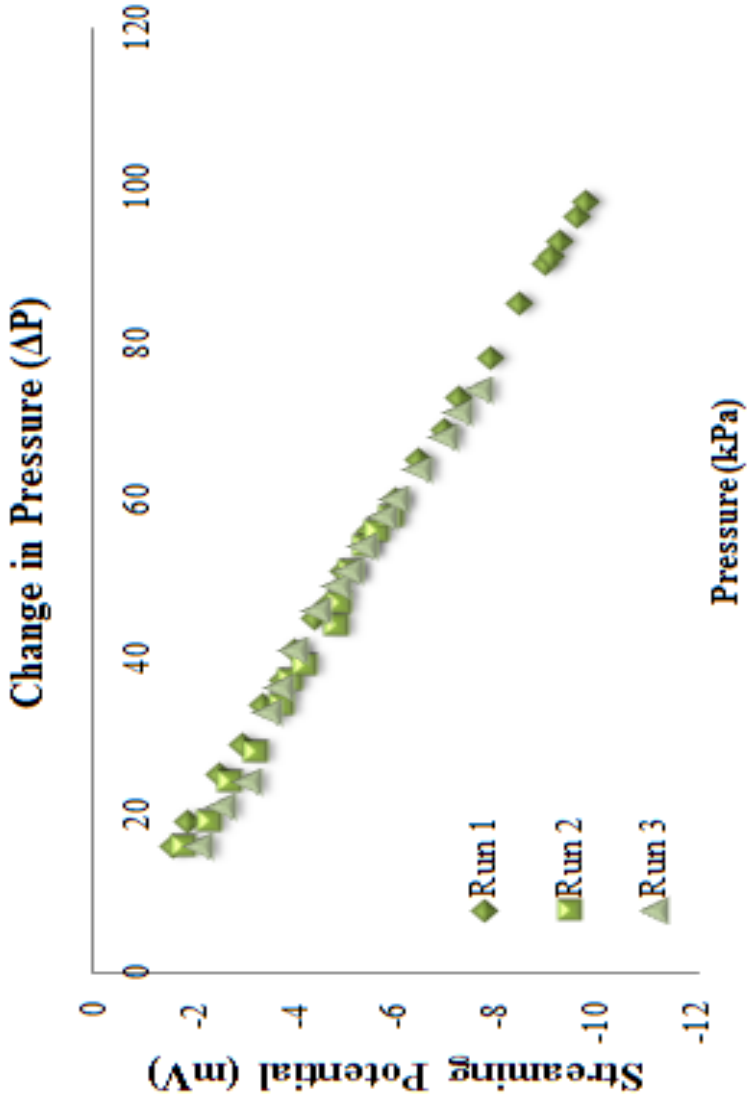

Figure 2.6| Streaming potential dependency on the employed electrolyte solution of PBS with 1.8 mS/cm and polycarbonate membranes of 0.4 μm pore size.

2.4.3 Effect of electrolyte conductivity

Our device was hence further used to evaluate the effect of different PBS conductivity since PBS was intended to be used as the electrolyte in our streaming potential measurements. The pore size and membrane type were kept constant and the conductivity was varied from 1.89 mS/cm to 5.91 mS/cm and 12.2 mS/cm.

The findings further illustrate the effect of electrolyte conductivity and ionic strength to the overall measured zeta potential. The lower the concentration and the conductivity of the electrolyte, the more accurate is the zeta potential measurement of the charged surface.

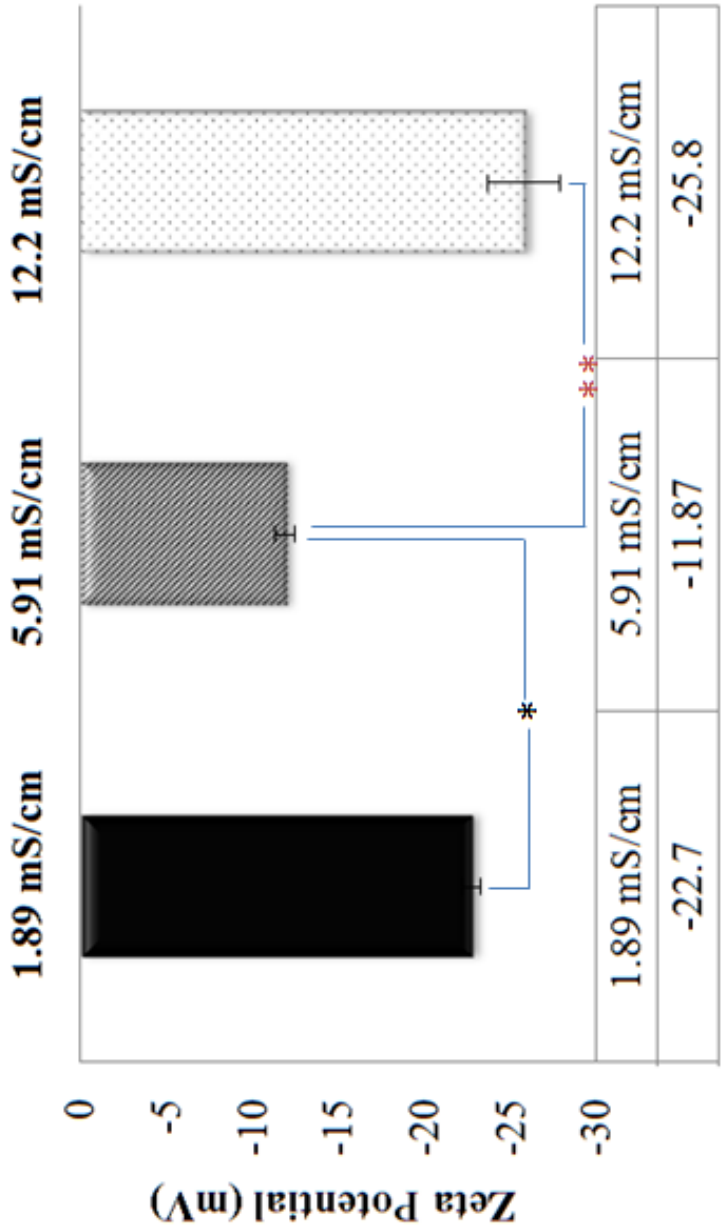

Figure 2.7| Variation of zeta potential measurements under different PBS conductivities (1.89 mS/cm, 5.91 mS/cm and 12.2 mS/cm). Throughout the experiments, polycarbonate membranes with a constant pore size oft 3µm were used.

2.4.4 Effect of soaking conditions

Although PBS will be used in all cell streaming potential measurements, the effect of the composition of the electrolyte solution was further studied. Streaming potential measurement of polycarbonate 3µm Transwell® were run using KCl (10 mM) and PBS (1.89 mS/cm). The results as shown in Figure 2.10 below show that for the same membrane with a characteristic surface charge, the measured zeta potential varies depending on the composition of the employed electrolyte. The findings further confirmed that the cell media highly leads to reductions in the magnitude of the zeta potential of the membrane from -24 mV to -13 mV (constant membrane type and pore size).

Surface charge reduction was attempted by soaking the membrane in BSA and further considering the cell media's effect. Neutralizing the polycarbonate membrane though fouling with BSA did not screen the effect of the membrane but further increased the zeta potential. The zeta potential of the polycarbonate membrane was reduced from -24 mV to -15 mV in presence of BSA and was further reduced to -3 mV when cell media was added to the system.

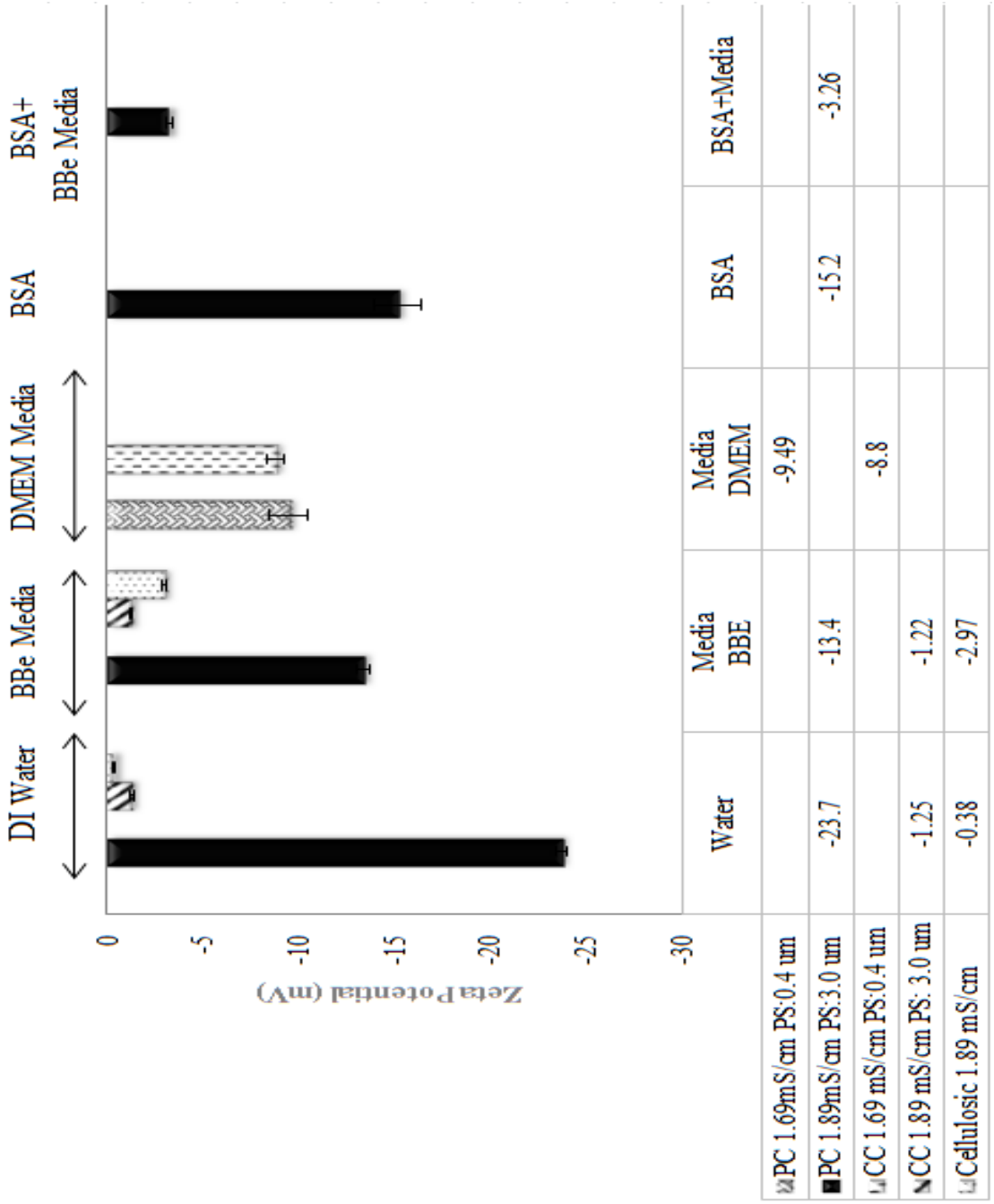

Figure 8| Zeta potential measurements for Transwell® membranes under various soaking conditions. CC (Colagen Coated membranes), PC (Polycarbonate membrane) and PS (pore size).

2.4.5 Effect of membrane composition

While variation of streaming potential measurements were expected for various membranes, a detailed study was performed to evaluate the zeta potential of polycarbonate, collagen coated PTFE membranes, and cellulosic membranes. The later were glued to the Transwell® and had an MWCO of 30K. The conductivity of the electrolyte solution was set at 1.89 mS/cm. Low conductivity was maintained in order to accurately assess the zeta potential of the membranes. Measurements were undertaken under different soaking conditions, including water and advanced DMEM media. The pore size of the polycarbonate and collagen coated membrane was maintained at 3µm.

The results showed significant differences between polycarbonate, collagen coated and cellulosic membranes with zeta potential ranging from -23.7 ± 0.25 mV to -0.38 ± 0.04 mV for cellulosic when the membranes were soaked in water versus DMEM media. Owing to a major difference in zeta potential for water soaked versus DMEM soaked membranes, we conclude that the polycarbonate membranes will capture differences in the measured streaming potential as low as 0.01 mV.

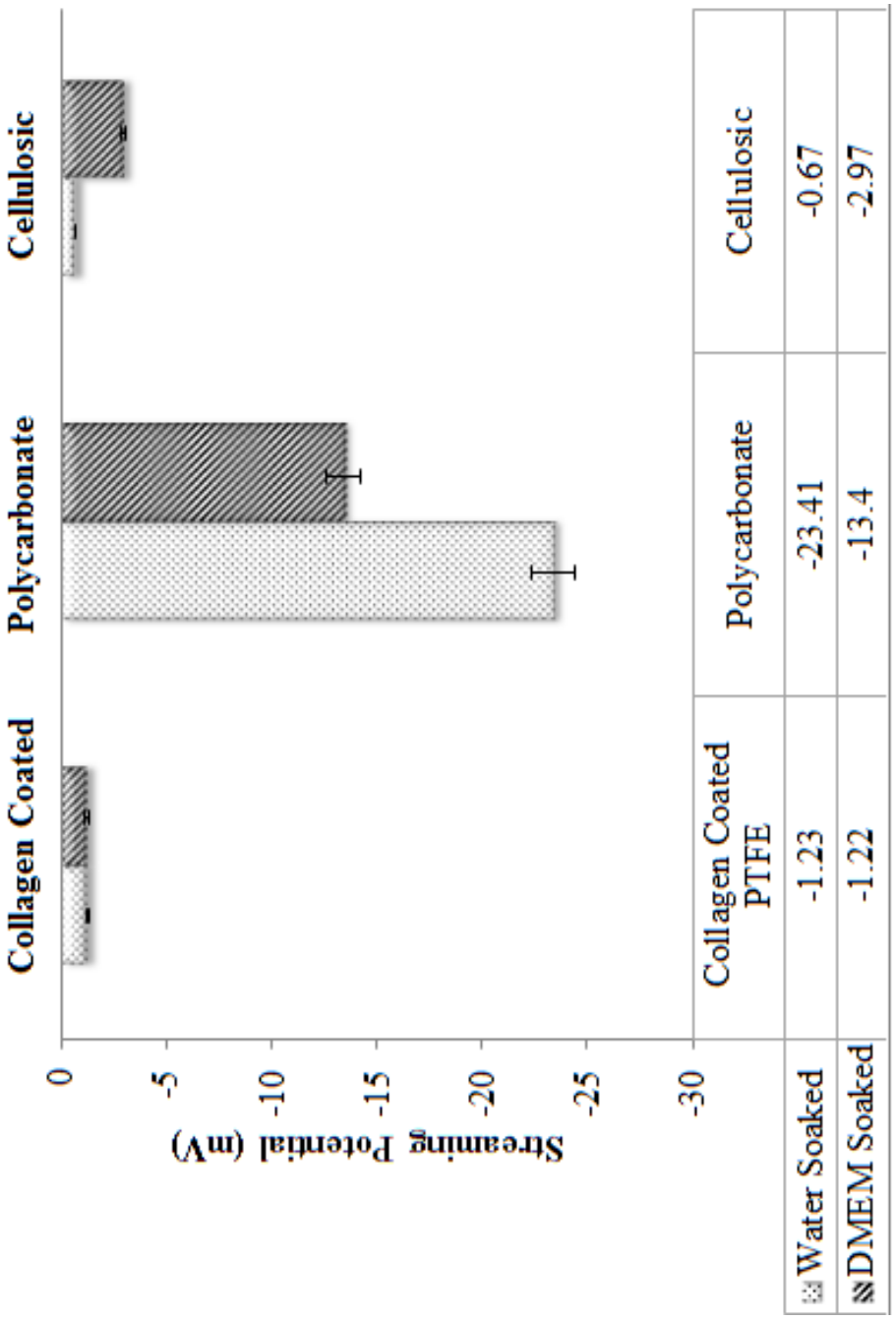

Figure 2.9| Variation of zeta potential measurements for three different membranes: polycarbonate, Collagen-coated and Cellulosic. The left data series represent measurements under water soaking conditions, whereas the right membranes were soaked in DMEM. All measurements are in mV.

2.4.6 Effect of pore size

In addition to considering the effect of membranes on the measured zeta potential, various pore sizes where considered. The pore sizes where varied from 0.4 µm, 3 µm to 8 µm. In order to eliminate additional variables, the same membrane was used (polycarbonate). Comparison of zeta potential values was done at fixed conductivity of 5.91 mS/cm in one study and 12.2 mS/cm in the other.

The findings showed no significant differences between all three pore sizes for an electrolyte conductivity of 5.91 mS/cm. The small range of differences detected for all the three pore sizes can be attributed to the fact that the pores are in fact large enough to prevent formation of a double layer overlap (expected in the nanometer scale). Meanwhile, under a higher conductivity of 12.2 mS/cm, the zeta potential measured across the 3.0 µm Transwell® varied to a higher extent.

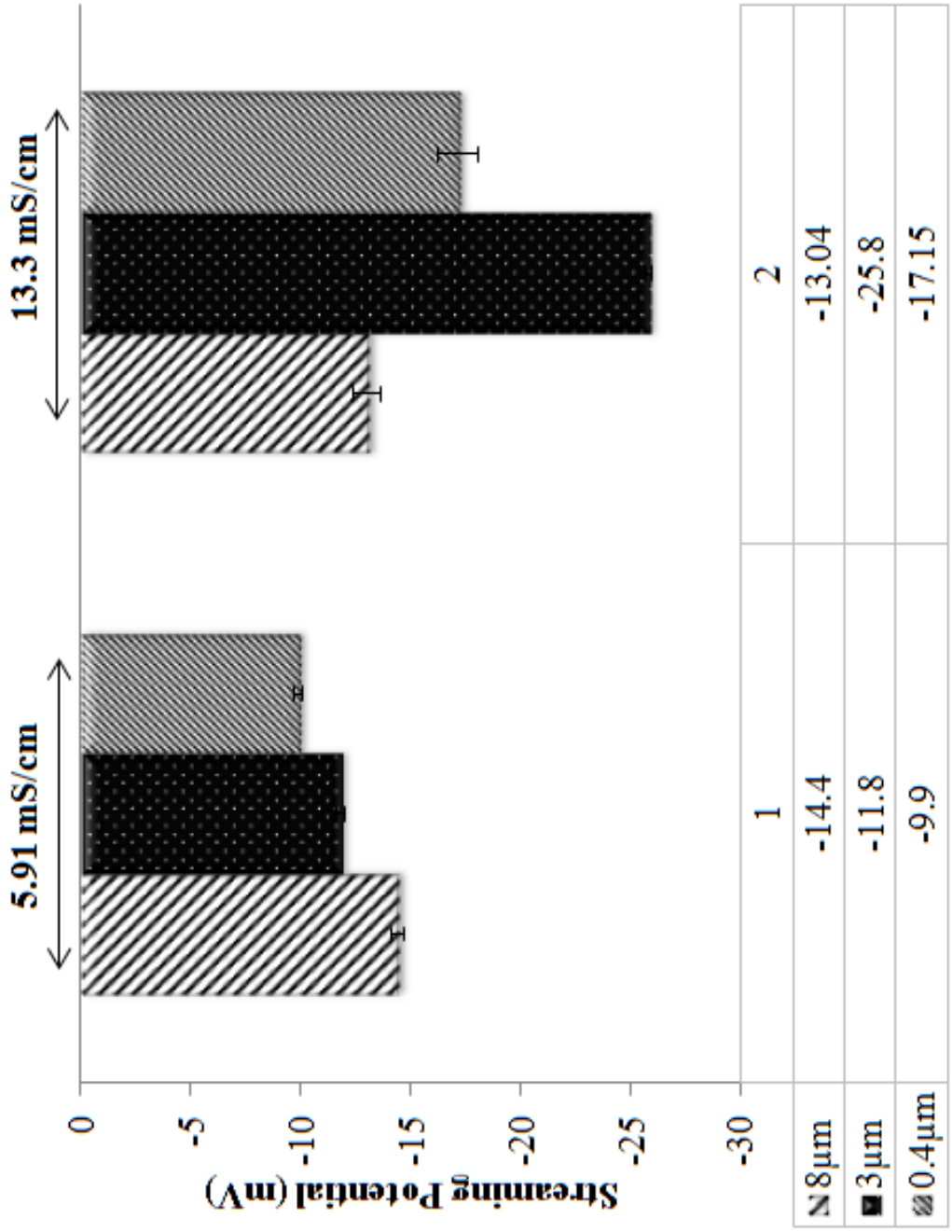

Figure 2.10| Variation of zeta potential measurements for three different pore sizes. PBS conductivity was set constant at 5.91 mS/cm for left data and 12.2 mS/cm for right data. All measurements are in mV.

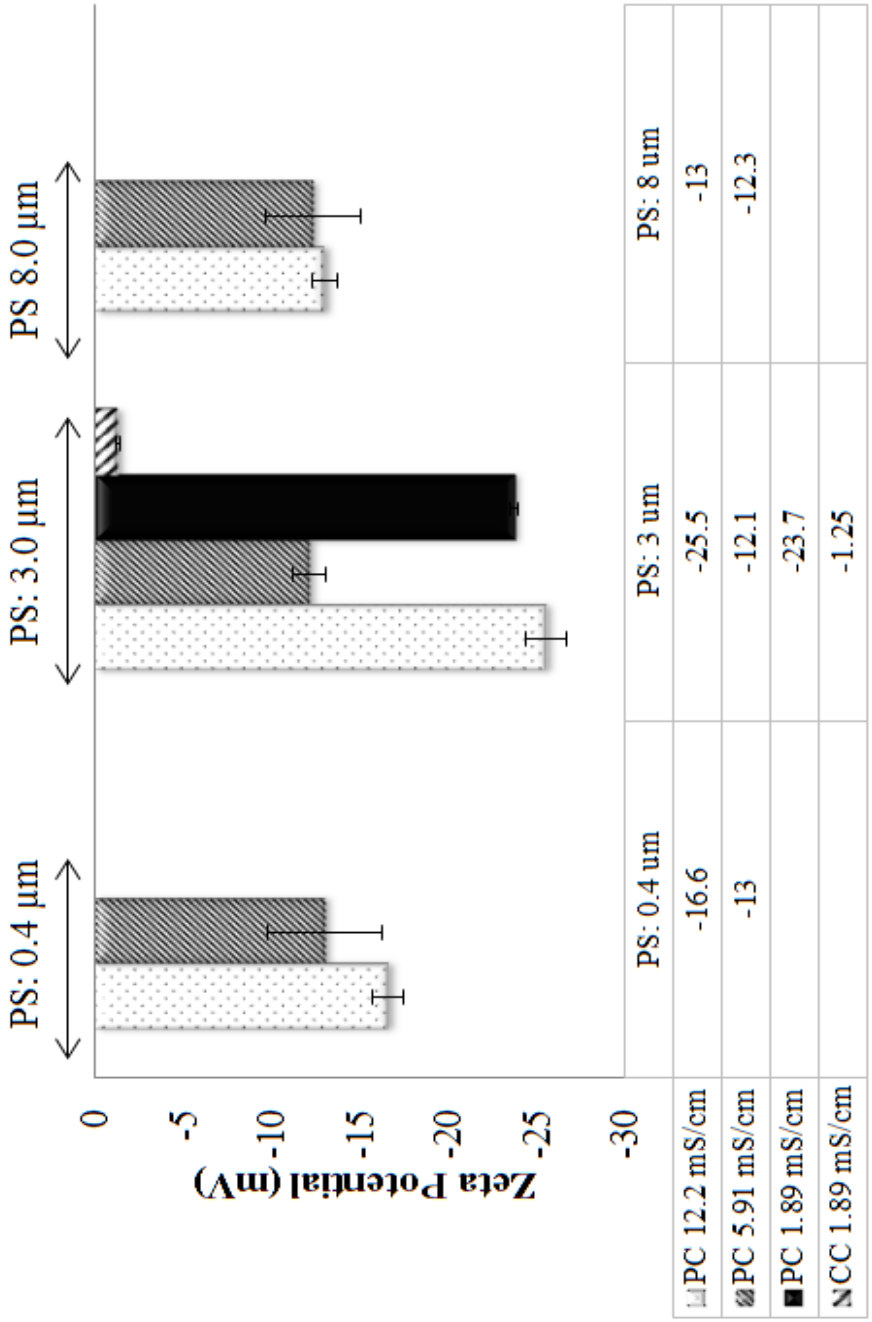

Figure 2.11| Zeta potential measurements for Transwell® membranes of different pore sizes and different electrolyte conductivities.

2.5 CONCLUSION

Zeta potential is a measured parameter that determines the charge properties of the test bed. Here, we calculate the zeta potential using the values of measured streaming potential. A device was designed and an experimental protocol was set for streaming potential measurements across 24 mm diameter Transwell® inserts. The device was tested across different membranes types, pore size, conductivity, and soaking conditions. Hence, the test bed captures the potential of both the membrane and electrolyte properties. We observed maximum change in streaming potential for polycarbonate membranes in comparision to collogen-coated PTFE, and cellulosic membranes. We further observed that membranes with pore size of 3.0 μm were more sensitive to pressure changes and subsequently the calculated streaming potential. In Chapter 3 and Chapter 4, we employ polycarbonate membranes with 3.0 μm pore size and an electrolyte solution of -1.89 mS/cm was used to capture the streaming potential of confluent cell layers seeded on Transwells®.

2.6 REFERENCES

1 Bangham A, Glover J, Hollingshead S and Pethica B (1962). The surface properties of some neoplastic cells. Biochem. J. 84: 513 – 517.

2 Burns D and Zydney A (2000). Buffer effects on the zeta potential of ultrafiltration membranes. Journal of Membrane Science 172: 39 - 48.

3 Chunga T, Wub S, Yaoc M, Lua C, Linb Y, Hungb Y, Moub C, Chena Y, Huange D (2007). The effect of surface charge on the uptake and biological function of mesoporous silica nanoparticles in 3T3-L1 cells and human mesenchymal stem cells. Biomaterials 28: 2959–2966.

4 Datta S, Conlisk A, Kanani D, Zydney A, Fissell W and Roy S (2010). Characterizing the surface charge of synthetic nanomembranes by the streaming potential method. Journal of Colloid and Interface Science 348: 85-95.

5 Drozd C and Schwartzbrod J (1996). Hydrophobic and electrostatic cell surface properties of cryptosporidium parvum. Applied and Environmental Microbiology 62 (4): 1227–1232.

6 Wilbert M, Delagah S, and Pellegrino J (1999). Variance of streaming potential measurements. Journal of Membrane Science. 161: 247-261.

7 Matsudaira PT and Burgess DR (1982). Structure and function of the brush-border cytoskeleton. Cold Spring Harbor Symposium Quantity Biology. 46: 845-854.

8 Nyström M, Pihlajamäki A, and Ehsani NC (1994). Chacterization of ultrafiltration membranes by simultaneous streaming potential and flux measurements. J. Membr. Sci. 87: 245–256.

9 Nabe A, Staude E, and Belfort G (1997). Surface modification of polysulfone ultrafiltration membranes and fouling by BSA solutions. J. Membr. Sci. 133: 57–72.

10 Nyström M, Lindström M, and Matthiason E (1989). Streaming potential as a tool in the characterization of ultrafiltration membranes. Colloids Surfaces. 36: 297–312.

11 Wilbert MC, Delagah S, and Pellegrino J (1999). Variance of streaming potential measurements. J. Membr. Sci. 161: 247–261.

12 Ricq L, Pierre A, Reggiani JC, Pagetti J, and Foissy A (1998). Use of electrophoretic mobility and streaming potential measurements to characterize electrokinetic properties of ultrafiltration and microfiltration membranes. Colloids Surfaces A, 138: 301–308.

CHAPTER 3

NOVEL *IN-SITU* NORMAL STREAMING POTENTIAL DEVICE FOR CHARACTERIZING ELECTROSTATIC PROPERTIES OF CONFLUENT CELLS

3.1 ABSTRACT

The characteristics of transport across confluent cell monolayers may often be attributed to its electrostatic properties. While tangential streaming potential is often used to quantify these electrostatic properties, this method is not effective for transport normal to the apical cell surface where the charge properties along the baso-lateral sides may be important (i.e., confluent cells with leaky tight junctions). In addition, even when cells have a uniform charge distribution, the shear stress generated by the conventional tangential flow device may dislodge cells from their confluent state. Here we introduce a novel streaming potential measurement device to characterize the normal electrostatic properties of confluent cells. Confluent monolayers of HEK and EA926 cells are used as examples. The corresponding zeta potential of the cell-membrane configuration is calculated using the Helmholtz Smochulski equation and the zeta potential of the confluent cell layer is deconvolved from the overall measurements. For these test models, the zeta potential is consistent with that determined using a commercial dispersed-cell device. This novel streaming potential device provides a simple, easy, and cost-effective methodology to determine the normal zeta potential of confluent cells cultured on Transwell® systems while keeping the cells intact. Furthermore, its versatility allows periodic measurements of properties of the same cell culture during transient studies.

Keywords: *zeta potential, streaming potential, confluent cells, electrodes*

3.2 INTRODUCTION

Transport across and through cell layers, such as endothelial cells in the vascular system or M-cells at the mucosal-systemic barrier, are important for overall system homeostasis. In particular, the transport of nanoparticles for mucosal vaccines has been recently coupled to the electrostatic properties of the solution [1]. It is speculated that the local normal electrostatic potential across cellular barriers, such as intranasal M-cells, is a critical factor for vaccine delivery and cellular regulation in general. Thus, a critical evaluation of cellular normal electrostatic potential could prove valuable in determining appropriate mucosal vaccine delivery vehicles and other relevant transport processes.

One common approach for determining cellular electrostatic properties is through a zeta potential analysis. Bangham *et al.* (1957) invented the first zeta potential (ζ) measuring device [2]. Subsequently, ζ using laser Doppler spectroscopy, light-addressable potentiometric sensors, Doppler electrophoretic light scattering techniques, ion selective field emission transistors, microchip analytical devices, and dynamic light scattering techniques have been employed [3-10]. A number of devices such as ZetaCad® and Malvern Zetasizer® have been commercially designed to measure the electrostatic properties of particulates. The limitations of the current techniques for measuring ζ are: somewhat device-dependent values, the size of the cells, the concentration of cell suspension in surrounding media, the use of tangential flow devices, and the inability to measure normal ζ for a confluent layer of cells.

But while the streaming potential is typically used to determine the electrostatic properties of confluent cell layers, these methods are often measured tangential to the

cellular surface [11-16]. Haydon (1961) provided an excellent overview of how the surface charge of living cells can be quantified using ζ [17]. Enumerous studies demonstrated that the electrostatic charges of cellular bilipid membrane layers can be correlated to the absorption and permeability of cations, particles, and preferential adhesion to bacterium, leukocytes, nanoparticles, *etc*. [18-28].

Even though the above mentioned studies capture the electrokinetic characteristics of cellular layer alone, various inter-cellular and sub-cellular layer electrostatic properties (*viz*., pore dimensions, leaky junctions, and cellular surface conductivities) cannot be captured using tangential flow alone as shown in Figure 3.1A. Hence, to substantially understand the cell layer electokinetic characteristics, employing normal or permeate flow (streams across the apical-basolatereal side) as shown in Figure 3.1B is necessary. To summarize, tangential flow streams across the apical side of the cell and normal flow streams across the apical-basolatereal side.

A

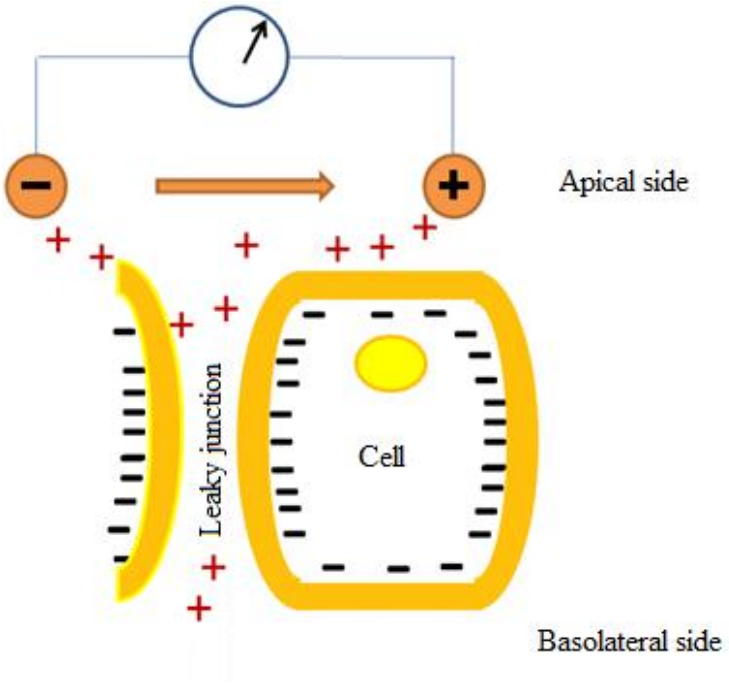

B

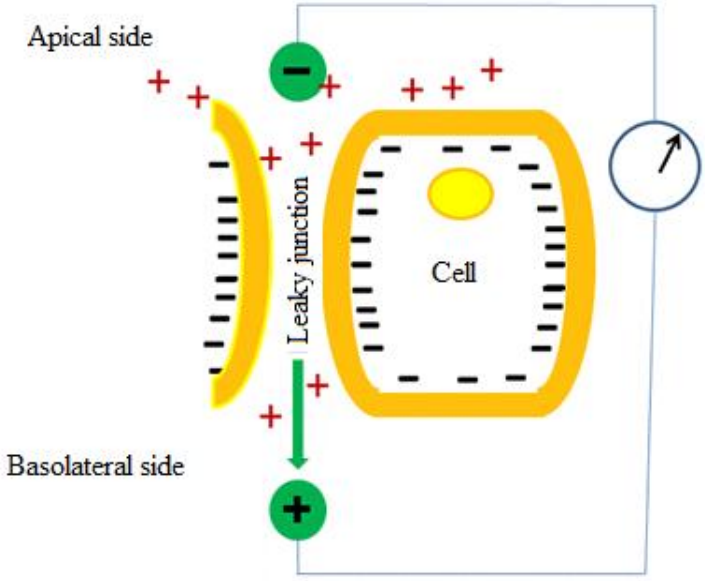

Figure 3.1| Illustration of a cell with leaky junction. The figure shows a (A) tangential flow and (B) normal flow configurations of measuring streaming potential.

While studies in Chapter 2, allowed us to evaluate the device and consider the effects of different variables in the experimental protocol, evaluation of zeta potential across cell layers was then performed. Since the presence of proteins in the cell media in which cells are soaked for different growth periods might foul the surface of the Transwell® inserts, the effect of the media was taken into account. Measurements of zeta potential under different soaking conditions were undertaken in order to first take into account the contribution of cell media to the overall measured zeta potential and second neutralize the surface charge of the membrane itself; hence eliminating any additional electrostatic contributions to cells' measured zeta potential.

In this study, we introduce a novel streaming potential device to capture the intrinsic properties of living cells by obtaining the normal ζ of a confluent monolayer of cells. As shown in Figure 3.2, an electrostatic double layer is formed along a confluent layer of cells. In our work, cells cultured on commercially available Transwell® inserts, are subjected to normal flow with varying pressure drop. The resulting membrane streaming potential is measured and the zeta potential of the cultured cell layer alone is mathematically determined.

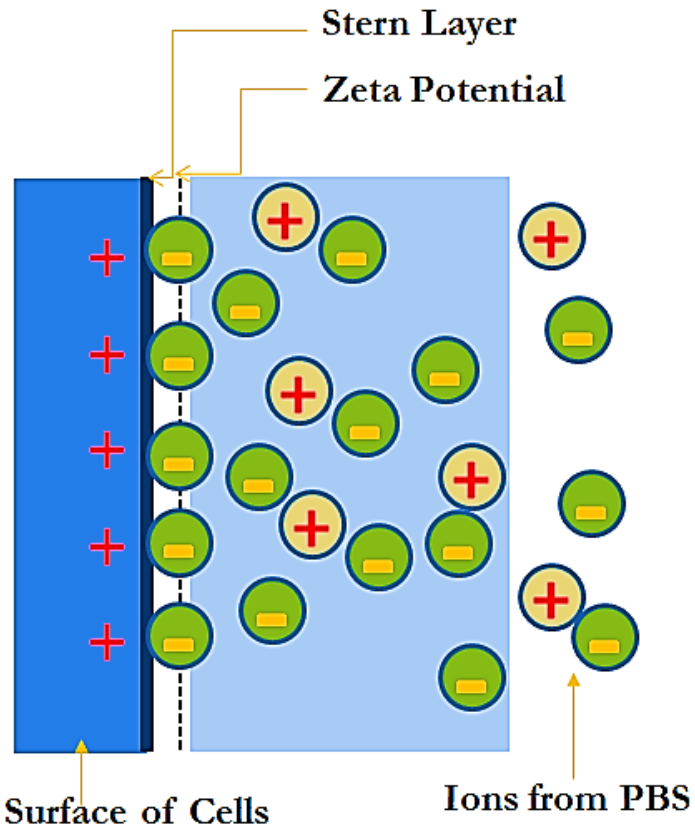

Figure 3.2| Illustration of the zeta potential layer and the stern layer that build up on the surface of cells when PBS is passed across them.

3.3 METHODS

3.3.1 Cell culture

EA926 cells and HEK cells (obtained from ATCC (Manassas, VA)) were carefully chosen to represent diverse cell lines. Cells were cultured using Dulbecco's modified Eagle's medium (DMEM, Lonza Inc.) and were supplemented with 10% FBS (Gibco Inc.) and antibiotics (Primocin, Invivogen Inc.). Freshly passaged cells were grown on Transwell® filters (24 *mm*, 3.0 μm pore sized polycarbonate Transwell®s, Corning, 3414; Lot #02011017, Corning, NY) to facilitate their insertion into the *in-situ* streaming potential device. The polycarbonate Transwell®s were pre-soaked in DMEM for two hours before being seeded with cells (with a density of 1×10^6 *cells/cm*^{2}). The cells were cultured overnight in triplicates. The polycarbonate Transwell®s pre-soaked in complete DMEM was used as the control for the experiments. The cell-cultured Transwell® filters were maintained in humidified 95% air-5% CO_2 incubator at 37°C. The integrity of the cellular layer was measured using a transcellular resistance measuring device. Cells were determined to be confluent if the transcellular resistance was greater than 1 MΩ.

3.3.2 Zeta potential measurements using Zetasizer®

The zeta potential of the HEK293 cells and EA926 cells were measured by dynamic light scattering using Zetasizer® Nano ZS90 (Malvern Instruments, UK). Samples of HEK293 cells and EA926 cells were pelleted down and dispersed in PBS buffer (pH 7.4) with 0.01% of EGTA and placed in a disposable capillary cell (DTS1061, Malvern

Instruments, UK). ζ of each sample was measured at 25^{o}C for five times and was reported as mean ± standard deviation.

3.3.3 Calculation of normal zeta potential of confluent cells

Teychene *et al.* (2011) proposed a mathematical equation to decouple the streaming potential of a chemical particulate cake layer from that of the measured cake-membrane support potential [31]. We apply a similar approach to decouple the streaming potential of the confluent cells from the cell-seeded membrane streaming potential.

Streaming potential of confluent cellular layers is considerably influenced by the number and size of their tight junctions. The proposed mathematical derivation assumes that the confluent cellular layer has low surface conductivity compared to that of the media and that the radii of tight junctions of the cellular monolayer are much larger than the Debye length of the media. This will ensure non-overlapping electrical double layers and the resulting non-linear potential which would not represent the ζ of the cell surface being considered. The proposed method also takes into consideration the deviation in the isoelectric point of the membrane when a confluent cell layer is cultured on it. The obtained ζ assumes that the flow is laminar within the tight junctions of the confluent cell layers and the pores of the membrane; that the electric double layer is very thin compared to the thickness of the pores; and that the junctions and pores are co-axial.

At a given steady state, electric charge flows through the membrane and the cellular layer seeded on the membrane:

$$I = I_c + I_m \text{, } i.e.,$$

$$I = \iint_{S_c} \rho_c \vec{V}_c \cdot dS_c + \iint_{S_m} \rho_m \vec{V}_m \cdot dS_m \quad , \tag{1}$$

where I_c and I_m denote the cell layer and membrane layer current, respectively. Here also ρ_i is the electric charge density of the cellular layer or the membrane, ds_i is the cellular surface element and membrane surface element; V_i is the velocity field of the media across the cellular layer and the membrane layer [32-34]; where i=c or m with c denotes the cell layer and m denotes the membrane layer. The resulting streaming potential is expressed as the ratio of the measured electrical potential and the pressure gradient [33]).

$$SP = \frac{\Delta\Psi}{\Delta P} \quad , \tag{2}$$

where $\Delta\Psi$ is the measured electrical potential (V) and ΔP is the transmembrane pressure drop (Pa). The streaming potential is used to calculate ζ of the cell-seeded membrane using the Helmoltz–Smoluchowsky equation [29-30]. Thus, for a given pressure drop, ζ can be determined based on the variations of streaming potential across the charged membrane layer as:

$$SP = \frac{\Delta\Psi}{\Delta P} = \frac{\varepsilon_0 \varepsilon_r \zeta}{\mu \Lambda_0} \quad , \tag{3}$$

where ε_0 is the permittivity of free space (8.854 x 10^{-12} F/m), ε_r is the relative dielectric constant of PBS (approximately that of water, 78.35 at 25 ^{O}C), μ is the viscosity of PBS (0.0098 $g/cm/s$), and Λ_0 is the conductivity of the PBS (1.69 $\mu S/m$).

In the absence of a confluent cell layer and defining R_m as the hydraulic resistance (m^{-1}) of the virgin membrane and J is the permeate flow ($m^3m^{-2}s^{-2}$), Darcy's law (Equation (2)) is expressed as,

$$J_m = L_{p\,m}\Delta P = \frac{1}{\mu R_m}\Delta P\,. \tag{4}$$

The measured electrical potential is directly linked to the ζ and the hydraulic resistance (i.e. the permeability) of the membrane. Equation (4) when combined with Equation (3) the electrical potential measured across the virgin membrane can be written as a function of the permeate flow (Equation (5)).

$$\Delta\psi = \frac{\varepsilon_0\varepsilon_r\zeta_m}{\mu\Lambda_0}\Delta P = \varepsilon_0\varepsilon_r\zeta_m\frac{R_m}{\Lambda_0}J_m\,. \tag{5}$$

As cells are cultured on the membrane (c+m), they increase the overall hydraulic resistance of the cell-seeded membrane. Assuming that there is no significant cell-membrane interaction, the permeate flux can then be written as,

$$J_{c+m} = L_{p\,c+m}\Delta P = \frac{1}{\mu\left(R_m + R_c\right)}\Delta P\,, \tag{6}$$

where $L_{p\,c+m}$ is the cell-seeded membrane permeability and R_c is the hydraulic resistance of the cellular layer. From Equation (5) and Equation (6),

$$\Delta\psi = \frac{\varepsilon_0\varepsilon_r\zeta_{c+m}}{\Lambda_0}\left(R_m + R_c\right)J_{c+m}\,. \tag{7}$$

Note that ζ_{c+m} is the zeta potential of the cell-seeded membrane. In addition, if the cultured layer of cells is considered as a hydraulic resistance with no interaction with the membrane, ζ_{c+m} can be written as a function of the zeta potential of the two layers (membrane and cultured cell layer). Applying the theoretical streaming potential of a porous medium composed of two different porous layers proposed by Szymczyk *et al.* (2001)[33], the streaming potential of a confluent layer of cells on the membrane is:

$$\psi_{m+c} = \psi_c \left(1 - \frac{L_{P_{m+c}}}{L_{P_m}} \right) + \psi_m \left(\frac{L_{P_{m+c}}}{L_{P_m}} \right). \tag{8}$$

Finally, the streaming potential of the confluent cell layer is given as:

$$\psi_c = \frac{\psi_{m+c} - \psi_m \dfrac{L_{P\,m+c}}{L_{P\,m}}}{1 - \dfrac{L_{P\,m+c}}{L_{P\,m}}}. \tag{9}$$

3.4 RESULTS AND DISCUSSION

3.4.1 Measuring streaming potential across confluent cell layers

From Equation (2), the streaming potential was determined using the slope of the streaming potential-pressure curves using least squares linear regression (SigmaPlot®, San Jose, CA). The measured streaming potentials across three membrane cases: the DMEM soaked virgin membranes, HEK confluent cell seeded membranes, and EA926 confluent cell seeded membranes were determined to be -40.5 mV, -51.4 mV, and -52.1 mV, respectively. All the graphs obtained through our streaming potential device as shown in Figure 3.3 provided linear relationships with R^2 values between 0.986 and 0.9972. The change in the slope ($\Delta\Psi/\Delta P$) captures the change in voltage measured across the membrane-cell configuration for different pressures. The voltage differences capture the variations in cellular characteristics.

3.4.2 Calculating normal zeta potential across confluent cell layers

The zeta potential for three membrane cases: (1) virgin membrane, (2) EA926 cells seeded membrane, and (3) HEK cells seeded membrane were determined using the corresponding streaming potentials calculated using Helmoltz–Smoluchowsky equation (Equation (3)). Table 3.1 summarizes the results of this work for the three membrane cases. The hydraulic permeability (L_P) for each case was calculated by measuring the flux flowing across the membrane cases for the pressure drop. Zeta potential was first

measured for membranes soaked in water, and was compared to that of membranes soaked in DMEM.

3.4.3 Variations of zeta potential across cells seeded on membranes

In order to initiate our investigation of significant electrostatic signature carried by cells, we tested zeta potential across four different cell lines: CHO, Caco2-BBE, HEK, and EA926 cells and considered the variation of the zeta potential. All measurements were performed for same membrane type and pore size (polycarbonate 3μm). The findings showed significant differences in zeta potential measurements across Caco2-BBE and CHO cells. The zeta potential of the Transwell® was reduced from -24 mV to -19 mV in presence of CHO cells and – 8 mV in presence of Caco2-BBE cells for polycarbonate membranes. The detected zeta potential for Caco2-BBE cultured on collagen coated membranes was, however, reduced – 1 mV.

3.4.4 Deconvolving zeta potential of cells from composite zeta potential of cell cultured membrane

The values for the zeta potential were deeconvolved to be -7.8±1.04 mV and -7.4±3.2 mV for the EA926 and the HEK confluent cells, respectively. Figure 3.5 compares the ζ of the virgin membrane, the composite membranes (EA926 confluent cell seeded membrane or HEK confluent cell seeded membrane) and, the ζ of the EA926 cells and HEK cells alone deconvolved from the composite ζ of cell-cultured membranes using Equation (9).

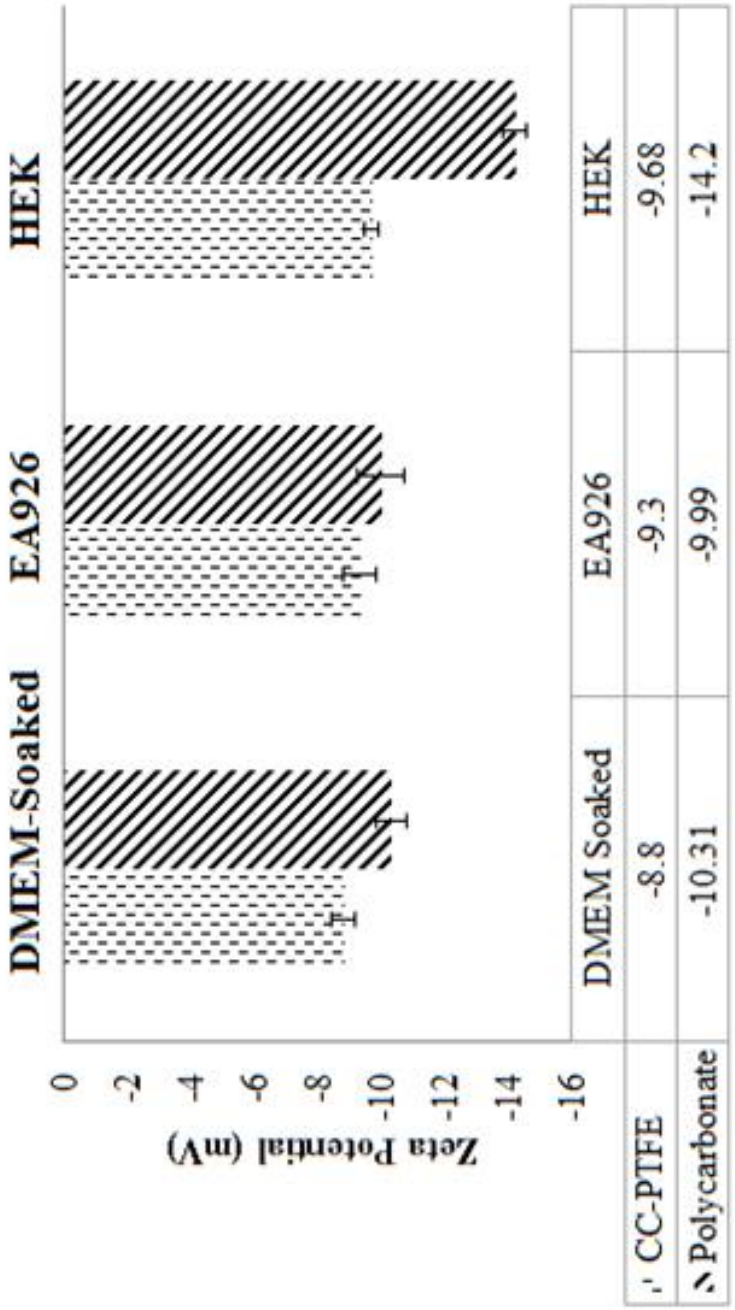

Figure 3.3| Zeta representative graphs comparing the measured zeta potential (ζ) for three membrane cases: DMEM soaked polycarbonate and collagen-coated PTFE membranes, HEK confluent cell seeded membranes and EA926 confluent cell seeded membranes. The electrolyte used was PBS (1.68 mS/cm).

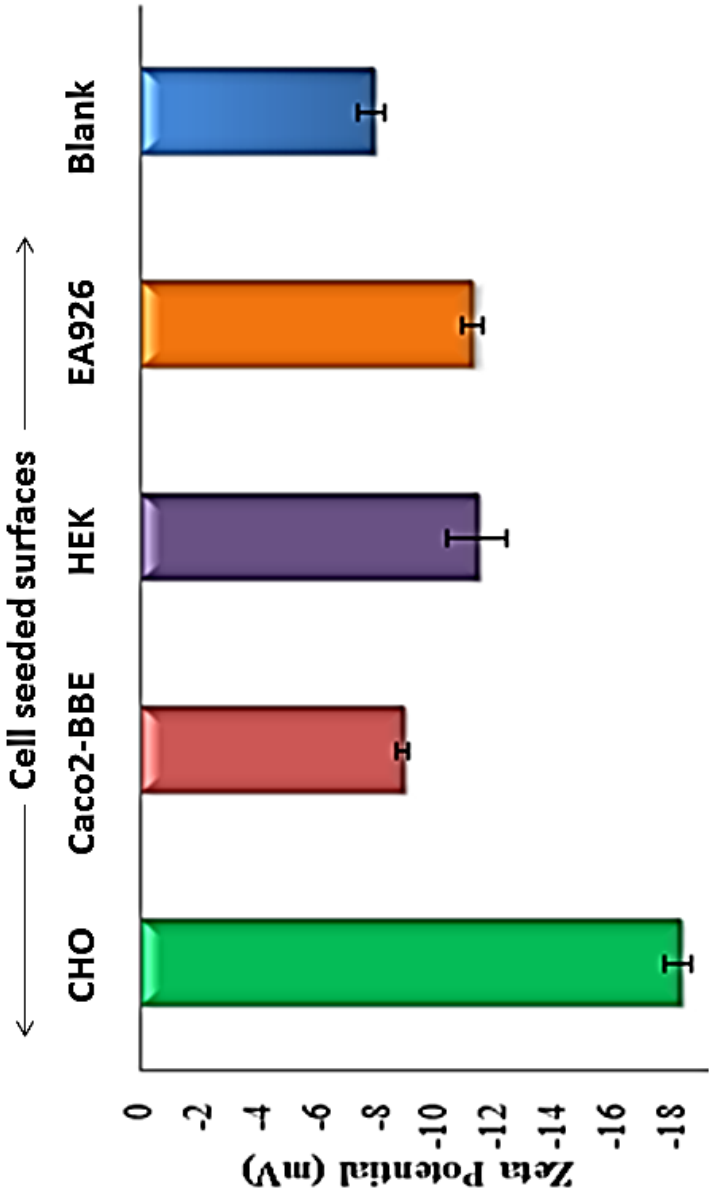

Figure 3.4| Measured and calculated Zeta potential for Cho cells, Caco2-BBE cells, HEK cells, and EA926 cells using normal *in-situ* streaming potential device. n=10.

Table 3.1. Results from normal in-situ streaming potential device. The Table shows the streaming potential, zeta potential, and hydraulic permeability for EA926 cells and HEK cells.

Case	Streaming Potential ($\Delta\Psi$) mV	Zeta Potential (ζ) mV	Range of Pressures (P) kPa	Hydraulic Permeability (L_P) 10^{-9} x cm/s
DMEM soaked (membrane only)	-36.1±2.0	-7.9±0.438	23-127	28.9±3.72
EA926 seeded with membrane	-52.1±4.6	-11.44±1	31-66	8.96±8.24
HEK seeded with membrane	-51.4±1.6	-11.29±0.343	17-66	2.18±2
EA926 cultured cells alone (decomvolved)	N/A	-7.8±1.04	N/A	N/A
HEK cultured cells alone (decomvolved)	N/A	-7.4±3.2	N/A	N/A

[a]Initial feed: Phosphate Buffer Solution (PBS)
[b]conductivity:1.81 mS/cm
[c]pH:7.4

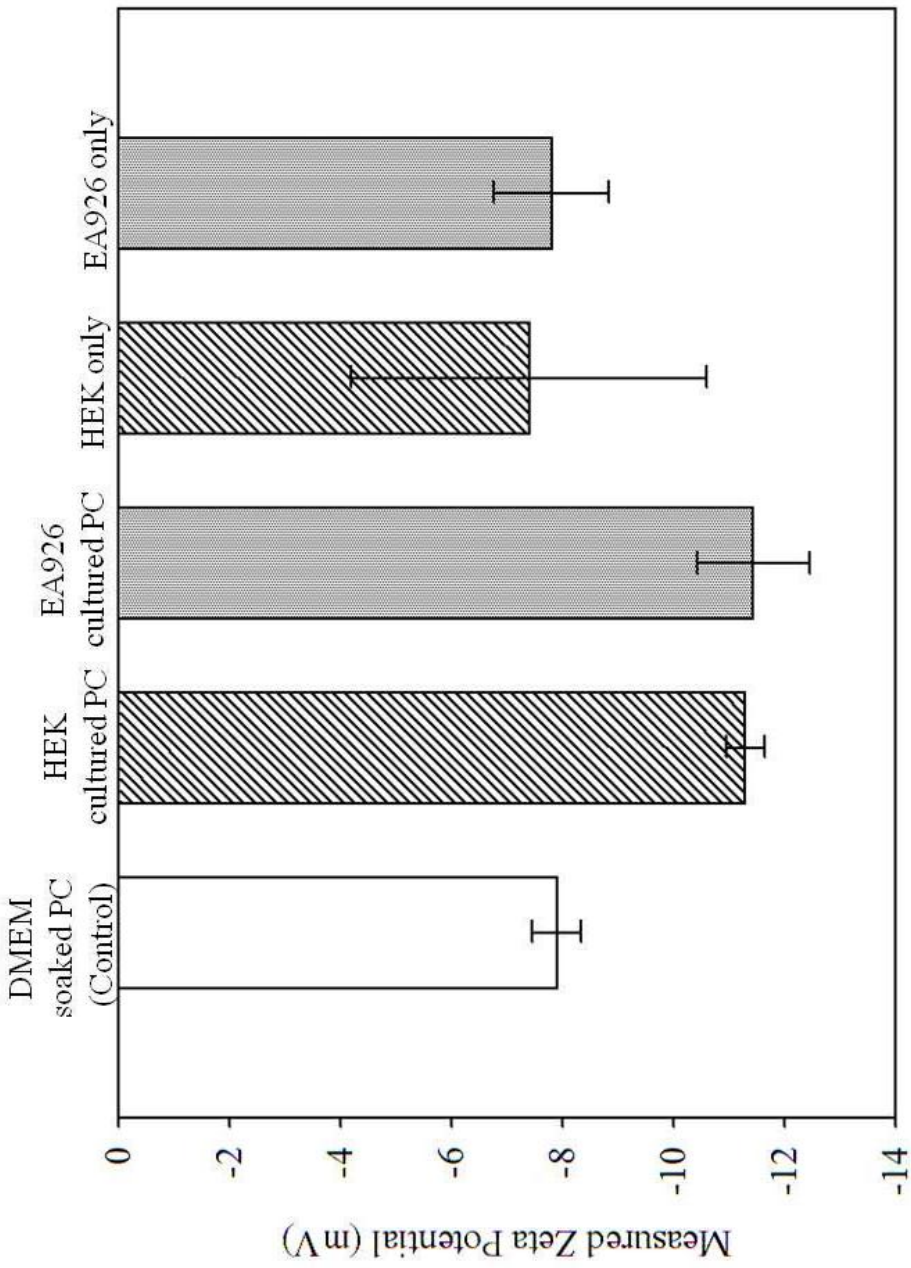

Figure 3.5| Representative graphs comparing the measured zeta potential (ζ) for three membrane cases: virgin polycarbonate membranes, HEK confluent cell seeded membrane and EA926 confluent cell seeded membrane and the deconvolved confluent cells. Using Equation (9), the the zeta potential (ζ_c) of the HEK cells and EA926 cells were deconvolved from the cell-membrane configurations.

3.4.5 Sensitivity of the calculated zeta potential of cells

The sensitity of determining the zeta potential of the cells directly corresponds to the sensitivity of the corresponding streaming potential measurements. Using Equation (9), the sensitivity of the overall streaming potential to changes in the streaming potential of the confluent cells only is approximated

$$\frac{\partial \psi_{m+c}}{\partial \psi_c} = \left(1 - \frac{L_{P_{m+c}}}{L_{Pm}}\right). \tag{10}$$

The equation clearly shows that the potential in capturing zeta potential of confluent cells from the proposed device is dependent on significant reductions in hydraulic permeability of the confluent cell seeded membrane from the virgin membrane. As the L_P of confluent cell seeded membrane increases for the same membrane, the error propagated through the system, decreases.

3.4.6 Zeta potential measurements using Zetasizer®

Although the normal zeta potential for the confluent cells does not have to correspond to the zeta potential of single cells, their comparison is instructive. Figure 3.6 compares the zeta potential measured using a Zetasizer® (for fluid dispersed cells) to that of the normal zeta potential of the corresponding confluent cell layer. The measured zeta potential for both HEK and EA926 cells, in this study, are not statistically different.

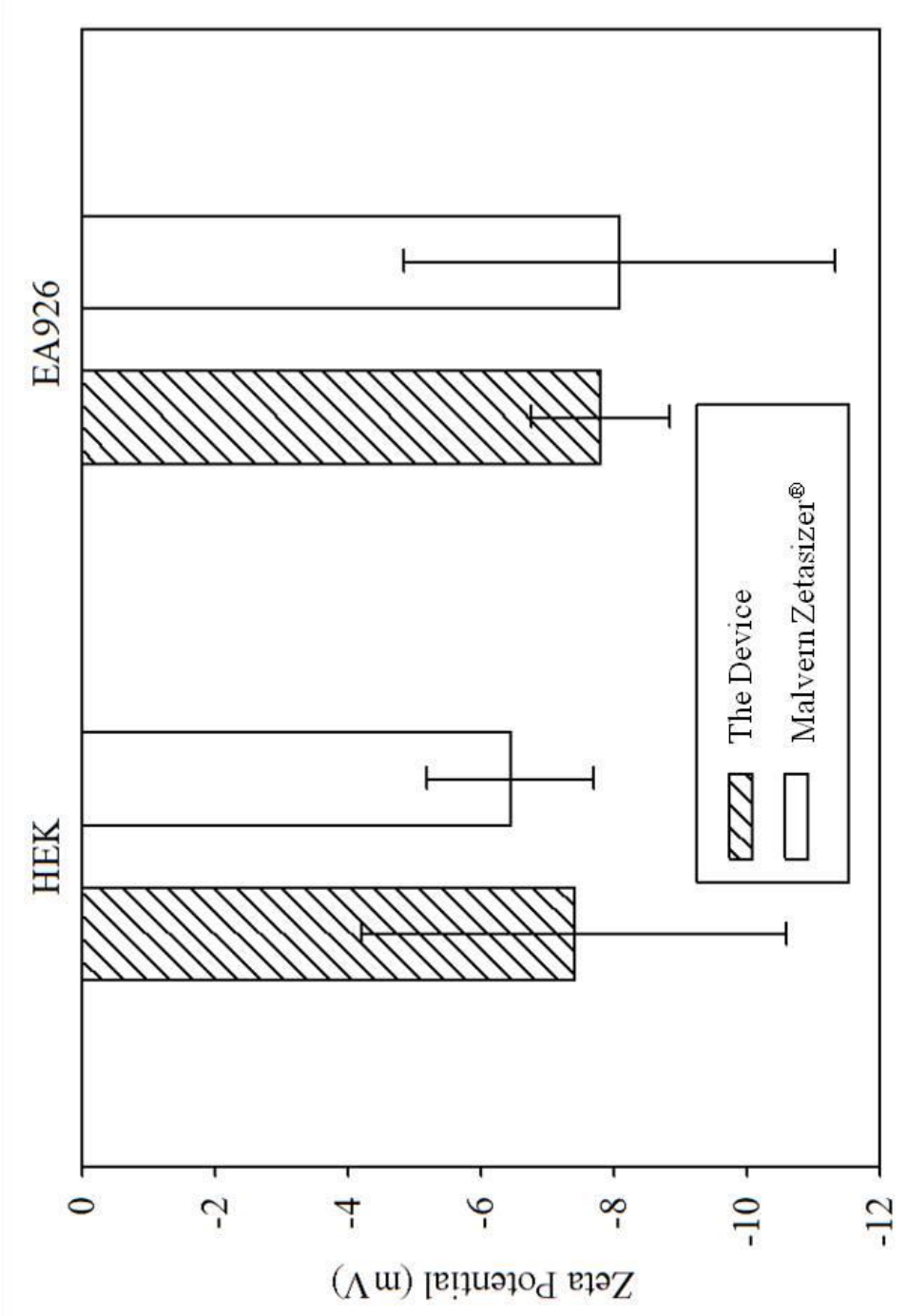

Figure 3.6| Comparing the zeta potential of EA926 and HEK cells deduced from the streaming potential measured using our streaming potential device and that measured using commercially available Malvern Zetasizer®.

3.5 CONCLUSION

Here we develop a simple and novel device to determine the normal ζ of confluent cells that are cultured on membranes. The device has the potential to be used to study cell surface interactions to identify and monitor the dynamic responses of the cells in response to administration of chemical or biological stimuli. Current ζ devices employ methodologies incorporating electrokinetic, sesimokinetic, or electroosmotic concepts, however, they are limited by the inability to measure normal zeta potential of cells and cellular monolayers.

In summary, we investigated the ζ of two different cellular (HEK cell line and EA926 cell line) monolayers on polycarbonate membranes. Using Helmholtz Smochuslky's equation and Darcy's law, we developed a methodology to deduce the zeta potential of confluent cellular layers that is derived from the work of Teychene *et al.* (2011)[31]. The proposed method assumes minimum conductivity inside the tight junctions and uses the conductivity of the bulk media flowing perpendicular to the confluent cell layer. The method is applicable when the mean size of the tight junctions is not much smaller than the Debye length of the confluent cellular layer. The results are sensitive to the ratio of the hydraulic permeability of the virgin membrane and that of the confluent cell-seeded membrane. Moreover, for isotropically charged cells that may be susceptible to removal by shear using a tangential flow device, the proposed normal flow device offers an ideal alternative that will maintain cell adherence to the membrane. We demonstrate that this ζ measurement device is a convenient laboratory approach and

show that this method can be used to quickly calculate electrostatic properties of confluent cellular surfaces.

The device provides a quick and reliable measurement for the intrinsic properties of cells in native cultures; to study the cellular interaction with drugs and cellular behavior in the presence of antigens (microbes, bacteria); and to detect abnormal cell behavior. The device can also be used as a fast and accurate first-step measurement to design drug therapy with minimal side effects. We have developed a laboratory device to directly measure streaming potential of confluent cells for measuring cellular electrostatic properties and capturing streaming potential can be attributed to cellular characteristics. Cells can be utilized for further studies after measuring streaming potential.

3.6 REFERENCES

1 TE Rajapaksa, KM Bennett, M Hamer, C Lytle, VGJ Rodgers and, DD Lo (2010) Intranasal M Cell Uptake of Nanoparticles is Independently Influenced by Targeting Ligands and Buffer Ionic Strength. The Journal of Biological Chemistry. 285: 23739-23746.

2 AD Bangham, GA Pethica, and GVF Seaman (1958) The Charged Groups at the Interface of Some Blood Cells. Biochemistry Journal. 69: 12-19.

3 A Dekkeq, K Reitsm, T Beugeling, A Bantjeq, J Feijen, CJ Kirkpatrick, and WGr. van Aken (1992) Surface Modification of Hydrophobic Polymexs for Improvement of Endothelial Cell-Surface Interactions. Clinical Material. 11:157-162.

4 LJ Bousse, S Mostarshed, and D Hafeman (1992) Combined Measurement of Surface Potential and Zeta Potential at Insulator/Electrolyte Interfaces. Sensors and Actuators B: Chemical. 10(1): 67–71.

5 ER Boevé, LC Cao, WC De Bruijn, WG Robertson, JC Romijn, FH Schröder.(1994) Zeta Potential Distribution on Calcium Oxalate Crystal and Tamm-Horsfall Protein Surface Analyzed with Doppler Electrophoretic Light Scattering. Journal of Urology.152(2):531-6.

6 S Koch a, P Woias, LK Meixner, S Drost, H Wolf (1999) Protein Detection with a Novel ISFET-based Zeta Potential Analyser. Biosensors & Bioelectronics. 14:417–425.

7 BJ Kirby, AR Wheeler, RN Zare, JA Fruetel, TJ Shepodd (2003) Programmable Modification of Cell Adhesion and Zeta Potential in Silica Microchips. Lab On a Chip. 3:5-10.

8 AS Lawrie, A Albanyan, RA Cardigan, IJ Mackie, and P Harrison (2009) Microparticle Sizing by Dynamic Light Scattering in Fresh-Frozen Plasma.Vox Sanguinis. 96: 206–212.

9 WW Wilson, MM Wade, SC Holman, FR Champlin (2001) Status of Methods for Assessing Bacterial Cell Surface Charge Q Properties Based on Zeta Potential Measurements. Journal of Microbiological Methods. 43:153–164.

10 N Guzelsu, C Wienstien, and SP Kotha (2010) A New Streaming Potential Chamber for Zeta Potential Measurements ofPparticulates. Review of Scientific Instruments. 81: 015106-1-6.

11 RJC Barry and J Eggenton (1972) Membrane Potentials of Epithelial Cells in Rat Small Intestine. J. Physiol., 227: 201-216.

12 JM Diamond and SC Harrison (1966) The Effect of Membane Fixed Charges on Diffusion Potentials and Streaming Potentials. .J. Physiol., 183: 37-57.

13 RB Gandhi and JR Robinson (1991) Permselective Characterisitics of Rabbit Buccal Muccosa. Pharmaceutical Research. 8(9): 1199-1202.

14 AB Micflikier, JP Shoenut, T Fraueneelder, and GR Grahame (1980) Potential difference of the pancreatobiliary mucosa during endoscopic retrograde cholangiopancreatography. CMA Journal, 122: 798-799.

15 Y Okada, W Tsuchiya, A Irimajiri, and A Inouye (1977) Electrical Properties and Active Solute Transport in Rat Small Intestine. J. Membrane BioI. 31: 205-219.

16 RC Rose and SG Schultz (1951) Studies on the Electrical Potential Profile across Rabbit Ileum. The Journal of General Physiology 57: 639-653.

17 DA Haydon (1961) The Surface Charge of Cells and Some Other Small Particles as Indicated by Electrophoresis. I. The Zeta Potential-Surface Charge Relationships. Biochemical Biophysical Acta. 50: 450-457.

18 L Renaud, P Kleimann, and P Morin (1974) Zeta Potential Determination by Streaming Current Modelization and Measurement in Electrophoretic Microfluidic Systems. Experimental Cellular Research. 87: 281.

19 JA Schellman (1977) Electrical Double Layer, Zeta Potential, and Electrophoretic Charge of Double-Stranded DNA. Biopolymers. 16:1415-1434.

20 S Eisenberg, S Ben-Or and F Doljanski (1962) Electrokinetic Properties of Cells in GrowthProcesses. Experimental Cell Research. 26: 45-461.

21 N Guzelsua, and WR Walsha (1990) Streaming Potential of Intact Wet Bone. Journal of Biomechanics: 23(7): 673–685.

22 AH Weerkamp HM Uyen, HJ Busscher(1988) Effect of Zeta Potential and Surface Energy on Bacterial Adhesion to Uncoated and Saliva-coated Human Enamel and Dentin. Journal of Dental Research. 67 (12): 1483-1487.

23 EH Frank, AJ Grodzinsky, TJ Koob, and DR Eyre (1987) Streaming Potentials: A Sensitive Index of Enzymatic Degradation in Articular Cartilage. Journal of Orthopaedic Research. 5497-508.

24 C Foged, B Brodin, S Frokjaer, A Sundblad (2005) Particle Size and Surface Charge Affect Particle Uptake by Human Dendritic Cells in an in -Vitro Model. International Journal of Pharmaceutics. 298: 315–322.

25 S Patil, A Sandberg, E Heckert, W Self, and S Seal (2007) Protein Adsorption and Cellular Uptake of Cerium Oxide Nanoparticles as a Function of Zeta Potential. Biomaterials. 28(31): 4600–4607.

26 K Fujisaki, S Tadano, and N Asano (2011) Relationship Between Streaming Potential and Compressive Stress in Bovine Intervertebral Tissue. Journal of Biomechanics. 44(13): 2477–2481

27 N Ferrell, J Groszek, L Li, R Smith, RS Butler, CA Zorman, S Roy, and WH Fissell (2011) Basal Lamina Secreted by MDCK Cells has Size- and Charge-Selective Properties. American Journal of Physiology - Renal Physiology 300: F86–F90.

28 C Lettmann, D Möckel, and E Staude (1999) Permeation and tangential flow streaming potential measurements for electrokinetic characterization of track-etched microfiltration membranes. Journal of Membrane Science 159 (1-2): 243-251.

29 H Helmholtz (1879) Studies of the Electrical Surface Layers. Wied. Ann. Physik Chemie Ser. 3 (7) 337–382.

30 M Smoluchowski (1903) Contribution to the Theory of Electroosmosis and Related Phenomena. Bull International Academy of Science Cracovie. 184-199.

31 B Teychene, P Loulerguea, C Guiguia, and C Cabassuda (2011) Development and Use of a Novel Method for In Line Characterisation of Fouling Layers Electrokinetic Properties and for Fouling Monitoring., Journal of Membrane Science. 370: 45–57.

32 G Tanny, E Hoffer, O Kedem (1971) Streaming Potential During Hyperfiltration. Experimental Supplement. 18:619.

33 A Szymczyk, B Aoubiza, P Fievet, J Pagetti (1999) Electrokinetic Phenomena in Homogeneous Cylindrical Pores, Journal of Colloid Interface Science. 216: 285–296.

34 A Szymczyk, C Labbez, P Fievet, B Aoubiza, C Simon (2001) Streaming Potential through Multilayer Membranes. Journal of American Institute of Chemical Engineers.47: 2349–2358.

CHAPTER 4

ELECTROSTATIC PROPERTIES OF CONFLUENT MUCOSAL CELLS CORRELATES TO THEIR MICROVILLI GROWTH AND DETERMINES UNDERLYING TRANSCELLULAR FLOW

4.1 ABSTRACT

A promising therapeutic mucosal vaccine strategy would be to recognize the features of the mucosal barrier and manipulate its' pharmaceutical nanoparticles to enhance its beneficial components. Recently, Rajapaksha *et al.* (2010) showed that the rate of uptake of potential vaccine delivery nanoparticles in the mucosal layer is a function of the electrostatic properties of the corresponding solvent. It is speculated that the electrostatic properties of mucosal cells are related to their development of brush border. Here we correlate development of brush border on a variant of human epithelial colorectal cells (Caco-2) cultured in DMEM on 3.0 μm pore sized polycarbonate membranes to their corresponding electrostatic properties characterized through measurements of zeta potential. Properties of normal streaming potential, hydraulic permeability, and brush border development (as determined by size and number) were monitored for 2, 6, and 16 days (after cells were confluent). Human endothelial cells (EA926), which lack brush border, were used as a control. Our results demonstrate that zeta potential of the Caco-2 cells significantly changed from -5.7 ± 0.11 mV to -3.4 ± 0.11 mV for a time period between 2 and 16 days, respectively. Microvilli size and number increased for 0.1 ± 0.02 μm to 0.8 ± 0.02 μm and 1.6 ± 0.2 $microvilli/\mu m$ to 7.6 ± 0.3 $microvilli/\mu m$, respectively for the same time period. The zeta potential of the control cell line, EA926 cells, stayed constant (statistically not different,$p > 0.05$) for the duration of the experiments. The zeta potential of the cell-free polycarbonate membrane was determined to be -7.93 ± 0.04 mV. These results imply that microvilli may alter the

electrostatic local environment around mucosal cells, thus, enhancing electrostatic selective transport of solute across the mucosal barrier.

Keywords: streaming potential, vaccination, drug delivery, cellular processes

4.2 INTRODUCTION

One of the largest interfaces to the microbacterial environment in most mammalian bodies is the mucosa. The mucosa is adapted to mutual endosymbiosis by mucosa-microflora and docks varied bacteria [1-3]. The mucosa-microflora mutualism occurs primarily along the mucosal surface and encompasses a single layer of epithelial cells as their barrier - the M-cells. They accurately gauge the surrounding microenvironment to identify pathogenic bacteria intruding commensal bacteria and further regulates the subsequent downstream processes by deploying immunosensory cells to the underlying lymphoid tissue [4-5]. In doing so, the M-cells are endorsed as the first-order epithelial defence machinery in the mucosal lining.

The microflora significantly affects the normal morphology and functionality of the mucosal immune system. It follows that favorably controlling the flora and effectively administering pharmabiotics and mucosal drug vaccines enhance the mucosal environment. These characteristics of the underlying microflora that positively condition mucosal homeostasis, immune responses, and uptake pharmabiotic/vaccine uptake have to be further investigated [6].

It is interesting to note that M-cells also form the rate-limiting barrier to the absorption of dissolved drugs [7]. Transport across the mucosal-systemic barrier is important to maintain overall mucosal homeostasis. In particular, the transport of nanoparticle-based drugs has been recently coupled to the electrostatic properties of their colloidal solution [8]. The authors speculate that the local electrostatic potential

across intranasal M-cells is a critical factor for drug delivery. Thus, an evaluation of cellular electrostatic potential could prove valuable in determining appropriate pharmaceutical delivery vehicles, interaction of microflora, and other relevant transport processes [9-11]. The following properties of the cells will be introduced in this study: (1) passive transcellular permeation, (2) understanding the charge of the cell membrane, (3) capturing the charge of the epithelial membrane, and (4) the overall streaming potential of the mucosal cells.

4.2.1 Paracellular transport

Transport across epithelial cells can occur through paracellular pathways or transcellular pathways. Paracellular transport is the transport of compounds across cellular monolayers via water filled pores between the cells. However, paracellular transport across epithelial cell layers is very unlikely as the dimensions of these paracellular spaces are in the range of A^0 [12]. For larger and more hydrophilic compounds (charged molecules and peptides) transcellular diffusion is often restricted or depending on the pKa of the molecules absent at physiological pH values and their molecular size. Hence, paracellular transport most likely might not contribute as much to the overall transport of most drugs *in vivo*, with the exception of small molecules (with MWCO = 200 Da) [13-14].

4.2.2 Effect of tight junction

Further, adjacent epithelial cells are separated by each other by the tight junctions. Tight junctions, as implied by the name, establish a tight closure between neighboring cells restricting solute transport through them [15]. The calculated human pore sizes for jejunum, ileum, and colon are also in the range of Å and that of colon is especially less, smaller than 2.3 Å [16]. More specifically, the effective pore radium of Caco-2 cell monolayers grown on the Transwell® system was calculated to be 12.0 ± 1.9Å [17]. Furthermore the fraction of area contributed by the junctions of the cell monolayer to the total cell surface is less than 10^{-4} [18-19]. Hence, it is not possible for large molecules to penetrate through the tight junctions.

4.2.3 Passive transcellular transport

The apical surface of the epithelial cells faces the intestinal lumen and the baso-lateral surface faces the underlying tissues, polarizing the epithelial cell layers. Both the apical and the baso-lateral surfaces have different protein and lipid compositions and hence different permeability properties [20]. Smaller molecules can more readily diffuse through the apical surface when compared to the larger biomolecules (MWCO>200 Da). The transport of a larger hydrophilic species across the epithelial layer is restricted by the hydrophobic lipid bilayer of the cell membrane. Larger hydrophilic species can be transported into the apical membrane from the lumen and further diffused across the cytoplasm, whereas, the transport of hydrophobic species involves lateral diffusion through the bi-lipid mosaic cell membrane layer. In both cases, the solutes exit through

the baso-lateral membrane to the sub-epithelial layers. Hence, the rate of passive transcellular permeability is mainly determined by the rate of transport across the cell membrane.

3.2.4 Active transcellular transport

The active transcellular route utilizes cellular ATP to drive $Cl^-/Na^+/K^+/Ca^{2+}$ pumps and hence species transport against an electrochemical potential. These ionic pumps in turn set up chemical gradients that can be used by other membrane transporters to dictate the movement of molecules in certain directions. In addition to this active transport of substances across the epithelial cells, transcellular transport generates the environment that favors the direct diffusion of other active biomolecules along the paracellular pathway [21].

4.2.5 Streaming potential

A driving force across a cell layer can be applied to measure the flux through both the transcellular and paracellular pathways, even though, our initial analysis of the transport mechanisms hints to the importance of transcellular transport (both active and passive) in the mucosal cellular systems. When a voltage drop is applied across the cellular surfaces, it results in an ionic flux inducing an ionic current across the system (Figure 4.1B). A pressure applied across the cells generates hydraulic flux across the cellular system, and defines the underlying cellular streaming potential (Figure 4.1C). The streaming potential is a cellular measurement of the overall resulting ionic contribution across cell

layers. We will be measuring the *in-situ* streaming potential of the overall cellular layers to study the effect of cellular features such as microvilli on the overall electrochemical gradient induced by the transcellular potential.

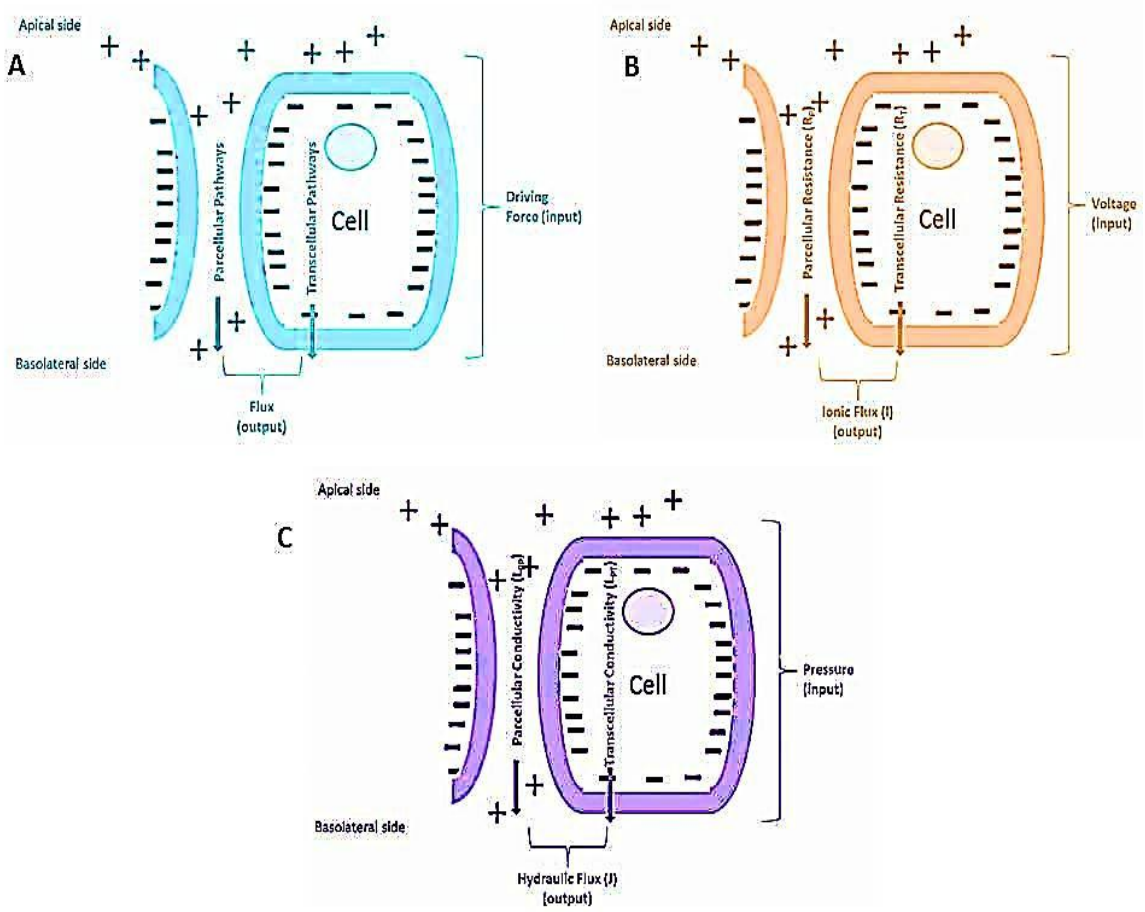

Figure 4.1| The figure shows the apical-basolateral measurements of a confluent monolayer of cells when subjected to transversal flow. (A) General schematic shows a driving force as the input and flux as the output, (B) A schematic of the electrostatic contribution shows a resultant ionic flux, I for voltage as the input, and (C) a schematic of the hydraulic contribution depicts a hydraulic flux, J for pressure as the input parameter.

Abundant studies describe the transmural transport of solutes and their accumulation in the epithelium by measuring the electrostatic properties of various cells [22-27]. Subsequently, electrical potential across the macroscopic mucosal tissue and the corresponding streaming potential were measured [28-31]. Studies were also performed to measure the permeability of the mucosa [32-33]. These studies incorporate isolated strips of the intestine or the gut tissue necessitating a clearer insight into the mechanisms of the mucosal barrier alone. Hubatsch *et al*. (2007) demonstrated successful measurement of drug permeability through cultured M-cells [34]. Subsequently, Vandrangi *et al*. (2012) introduced a novel *in-situ* measuring device to characterize the normal streaming potential and hydraulic conductivity of confluent cell monolayers [35].

Cell culture techniques predominantly employing the Caco-2 cell line have been established in the last decade as a screening and study tool of intestinal absorption. In this study, we correlate the electrostatic contribution of brush border developed on mucosal cells. The confluent monolayer of Caco-2 cells (a highly-accepted functional and morphological model of the intestinal mucosa) are grown on permeable supports to capture the effect of microvilli by measuring their *zeta potential* [36]. The permeable supports are subjected to normal flow with varying pressure drop to capture the cellular apical to basal features of the trans-mural barrier. The results demonstrate that microvilli might be an important morphological feature of the mucosal cells might contribute to their electrostatic properties.

4.3 METHODS

4.3.1 Cell culture

Caco-2 (ATCC) human colon carcinoma cells and EA926 (ATCC) immortalized human endothelial cells were carefully chosen to represent widely accepted mucosal cells and endothelial cells. Endothelial cells were chosen as they were expected to not have any microvilli. Cells were cultured using advanced Dulbecco's modified Eagle's medium (Gibco) and Dulbecco's modified Eagle's medium (DMEM, Lonza Inc.) respectively and were supplemented with 10% FBS (Gibco Inc.) and antibiotics (Primocin, Invivogen Inc.) and 15 mmol/L HEPES buffer. Freshly passaged cells were grown on Transwell® filters (24 *mm*, 3.0 μm pore sized polycarbonate Transwell®s, Corning, 3414; Lot #02011017, Corning, NY) to facilitate their insertion into the *in-situ* streaming potential device.

4.3.2 Experimental trials

The polycarbonate Transwell®s were pre-soaked in DMEM for two hours before being seeded with cells (with a density of 2×10^4 *cells/well*). The cells were cultured for two days, six days, and 16 days in triplicates. The polycarbonate Transwell®s pre-soaked in complete DMEM was used as the *blank* and the EA926-cultured polycarbonate Transwell®s were used as the control for the experiments. The cell-cultured Transwell® filters were maintained in humidified 95% air-5% CO_2 incubator at 37°C. The integrity of the cellular layer was measured using a transcellular resistance measuring device.

Cells were determined to be confluent if the transcellular resistance was greater than 10 Ω for the cell cultured Transwell® (compared to almost negligible resistance for Transwell® pre-soaked with DMEM).

4.3.3 Normal zeta potential measurements

Streaming potential experiments are performed using a novel *in-situ* streaming potential device [25]. The device measures the potential across the cells cultured on the hosted 24 *mm* Transwells® (Corning, Corning, NY). Electrolytic solution of phosphate buffered saline (PBS) (7.4 pH, 1.5 M, and 1.87 mS/cm^2) flows through the feed side of the device, normal to the Transwell® (with a known pressure drop), and exits out through the permeate side of the device[35].

4.3.4 Calculation of normal zeta potential of confluent cells

We further employed a mathematical development that used Helmholtz-Smoluchowski's equation and Darcy's law to extract the charge contribution of a confluent cellular layer from a cell-membrane configuration.[35] The streaming potential (SP) is used to calculate ζ of the cell-seeded membranes using the Helmoltz–Smoluchowsky equation [37-38].

$$SP = \frac{\varepsilon_0 \varepsilon_r \zeta}{\mu \Lambda_0}, \qquad (1)$$

where $\Delta\Psi$ is the measured electrical potential (V), ΔP is the transmembrane pressure drop (Pa)., ε_0 is the permittivity of free space (8.854 x 10^{-12} F/m), ε_r is the relative

dielectric constant of PBS (approximately that of water, 78.35 at 25 ^{O}C), μ is the viscosity of PBS (0.0098 *g/cm/s*), and Λ_0 is the conductivity of the PBS (1.69 *μS/m*). Finally, the streaming potential of the confluent cell layer is given as:

$$SP_c = \frac{SP_{m+c} - SP_m \frac{L_{P\,m+c}}{L_{P\,m}}}{1 - \frac{L_{P\,m+c}}{L_{P\,m}}}. \qquad (2)$$

where L_p is the hydraulic conductivity (cm^2-s/g), *m* represents the membrane filter insert and *m+c* represents the cells-membrane filter configuration.

4.3.5 Transmission electron microscopy

Cultures of Caco-2 cells and EA926 cells from passages were preserved for transmission electron microscopy examinations on days 2, 6 and 16. Cell cultures on membranes were rinsed three times with PBS and fixed with 2% glutaraldehyde-PBS (0.1 M sodium phosphate, pH 7.2–7.4) for one hour. The cells were again washed for at least three times with PBS and the monolayers were treated with 1% osmium tetroxide (OsO_4) in the same buffer for at least two hours to ensure good contrast. The cells were dehydrated with ethanol and embedded in an EPON-18 substitute. The embedded cultures were examined with compound microscope and ultra-thin sections of cell-covered filters were mounted for sectioning the apical-basal plane. Gold thin sections of the embedded cells were mounted on bare grids (mesh 200), stained with uranyl acetate

and lead citrate. Observations were made using a Phillips Tecnai 12 microscope at 30 kV.

3.3.6 Immunocytochemistry

Samples of Caco2 cells and EA926 cells were washed with PBS three times for five minutes each. Cell samples were fixed and permeabilized with ice cold methanol in -20 ^{o}C for 20 minutes. Samples were again washed in PBS (1X) and incubated with blocking buffer (4 g BSA +80 mL PBS + 150 µL Triton X 100) for 1 hour followed by incubation with 5 µg/ml of anti--claudin primary antibody (AbCAM) in antibody dilution buffer (4 g BSA + 40 mL PBS + 120 µL Triton X 100) for 90 minutes in room temperature. Cells were rinsed 3 times with 10 minutes PBT and incubated with 5 g/ml Alexa Fluor® 488 goat anti-rabbit secondary in antibody dilution buffer for another 60 minutes. Cells were washed three times with PBT for 5 minutes each.

4.3.7 Confocal Microscopy

Claudin 4 expressed in the cell samples were examined for all the indicated times and imaged using Leica SP2 Confocal microscope (Buffalo Grove, IL). Leica SP2 LAS software was used for image acquisition and images were processed using (ImageJ® 1.46, NIH) [39].

4.4 RESULTS AND DISCUSSION

4.4.1 Measuring hydraulic conductivity for EA926 cells and Caco-2 cells

The hydraulic conductivity defines the conductance or the permeability of the surface being studied. In cellular systems, the parameter demonstrates how confluent the cell monolayer is. The measured hydraulic permeability is an order of magnitude smaller for the cell-seeded membrane when compared to the membrane alone as shown in Figure 4.2. The hydraulic conductivity of the filters substantially decreased with a confluent layer of cells growing on the membrane filters. The formation of tight-junctions and desmosomes as the mucosal cells mature might also influence the variation measured by the hydraulic conductivity [40]. However, for the endothelial cells, the presence of leaky junctions increases their hydraulic conductivity [41].

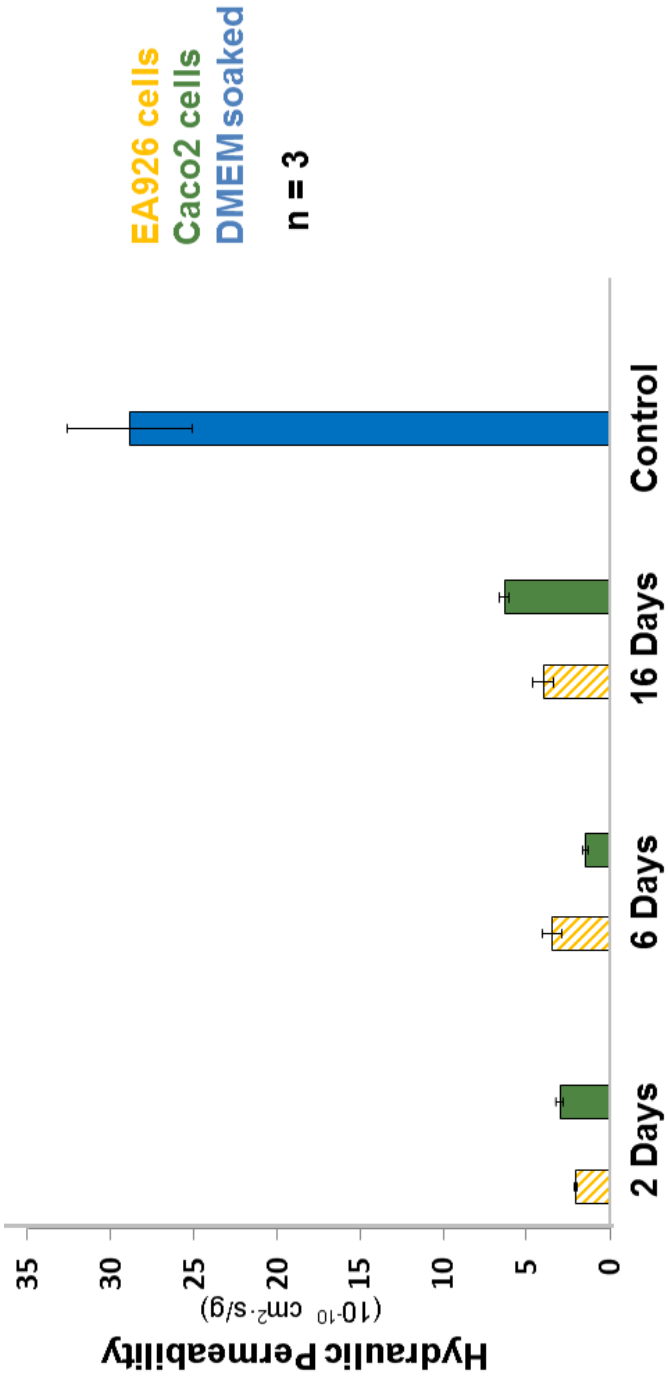

Figure 4.2| The Figure compares the hydraulic conductivity (L_P) for DMEM pre-soaked membrane, EA926 cells, and Caco-2 cells cultured membranes for 2 days, 6 days and 16 days.

4.4.2 Streaming potential measurements using streaming potential device

The polycarbonate membranes utilized in these experiments are highly charged surfaces with a ζ of -7.91 mV. We observe an increase in ζ for the Caco-2 cells cultured membranes and relatively no change in ζ for the EA926 cells cultured membranes and DMEM pre-soaked membrane. Each sample set has been statistically checked for significance. The observed change in streaming potential, as exhibited in Figure 4.3, actually captures a change in passive flux of molecules/ions in the solution, implying a selective uptake of ions. Similarly, a constant measured zeta potential demonstrates an increase in passive flux of molecules/ions in the solution corresponding to the pressure being applied. This implies a non-selective uptake of ions and charged species, implying enhanced facilitation. The phenomenon is evident in endothelial cells forming blood vessels such as capillaries and hence facilitating easy diffusion across their membranes. Furthermore, the glycocalyx of the M-cells is much thinner when compared to the glycocalyx of other cellular membranes, providing another rationale for the decrease in the measured zeta potential [40].

The developed layer of microvilli, shown in Figure 4.4, is the characteristic of mucosal cells during the differentiated state. Microvilli act as effective diffusion barriers and increase the residence time of administered pharmaceuticals. Actin based cytoskeleton of microvilli contribute to the negative decrease in streaming potential by increasing the cation concentration boundary layer at the apical surface of mucosal cells. This ability implies the importance of microvilli in intracellular signaling. Further, the

microvilli tips host functionally important integral proteins, hence guarding the influx of metabolic substrates and ions. Microvilli hence form membrane-limited systems.

4.4.3 Analyzing surface morphology

Transmission electron micrographs (TEMs) demonstrate change in the height and number of the microvilli for 2 days, 6 days and 16 days, correlating with the ζ results (shown in Figure 4.4). The density of the brush borders on the Caco-2 cells increased by 40% in the 16 days culture in comparison to the 6 days cultured cells. As shown in Figure 4.4 and Figure 4.5, the endothelial cells which do not manifest brush borders, almost have a constant zeta potential [41]. However, the absence of brush border on EA926 cells (shown in Figure 4.5) demonstrates that the brush border is a defining factor of ζ.

As depicted in Figure 4.6, change in the measured zeta potential of the brush borders with increase in length can be explained by correlating it to the difference in the surface area. The zeta potential of the EA926 cells was not statistically different for the 2 days versus 16 days with p-value > 0.05.

Furthermore, notice the development of tight junctions as cells mature (shown with arrows). Both Figure 4.4 and Figure 4.5 demonstrate the presence of leaky junctions (in 2 day cultures) and the further formation of tight junctions (starting around 6 day cultures). However, streaming potential results show a decrease in zeta potential for Caco-2 cells and not EA926 cells, hence ruling out the impact of tight junctions on the measured streaming potential across the apico-basal surface.

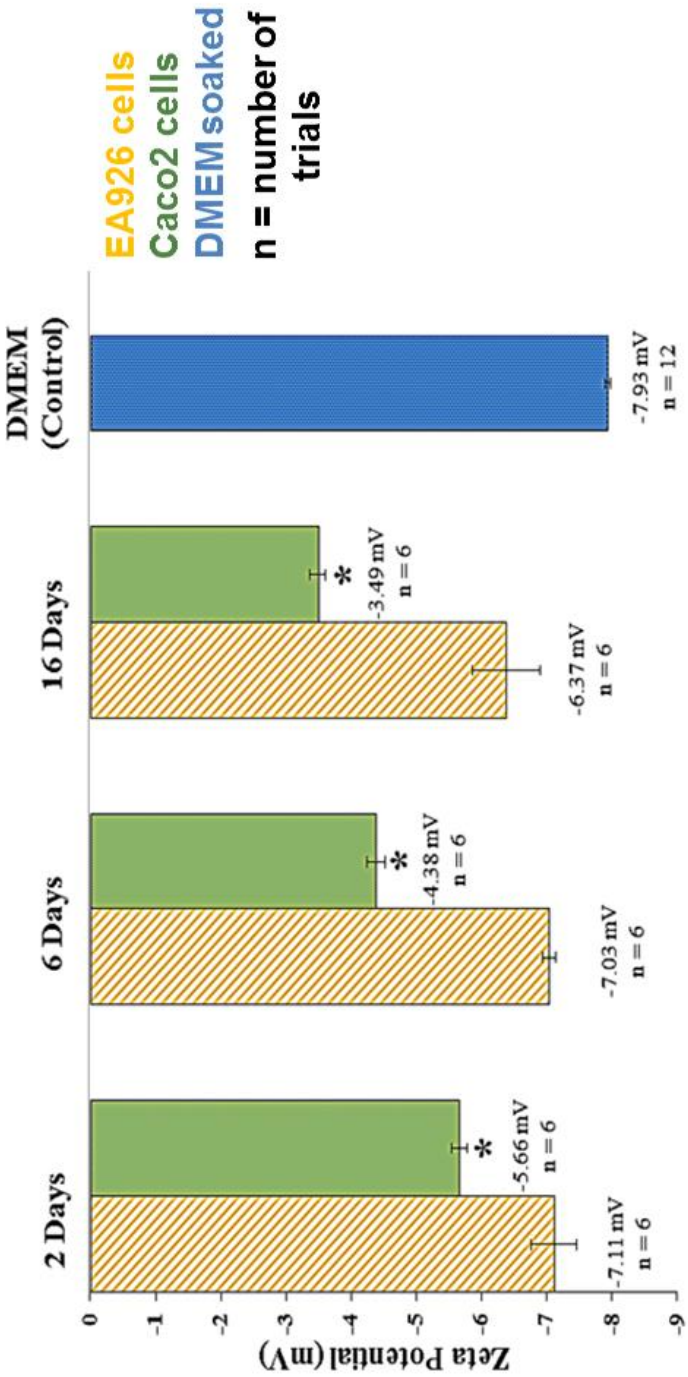

Figure 4.3| The Figure compares the zeta potential (ζ) for DMEM pre-soaked membrane and Caco-2 cells cultured membranes for 2 days, 6 days, and 16 days The p values are mentioned below the graphs. * shows that the p-value < 0.05. Hence, the measured zeta potential is significantly different.

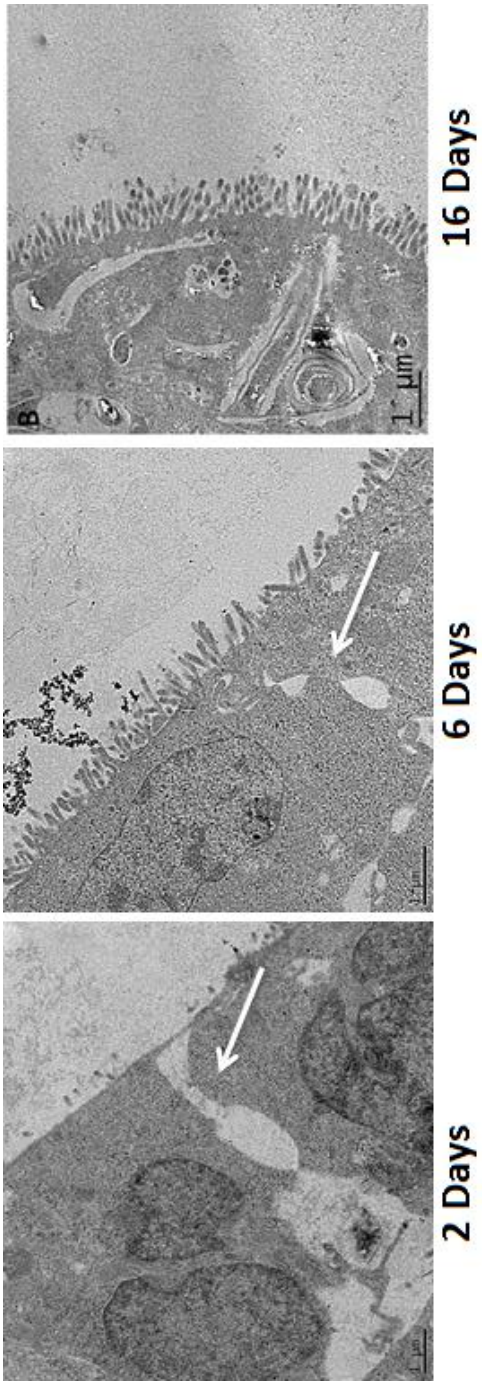

Figure 4.4| Transmission electron micrographs illustrating the cell morphology of Caco-2 cells for 2 days, 6 days and 16 days cultures. The arrows point to the leaky junctions (for 2 days) and the tight junctions (for 6 days).

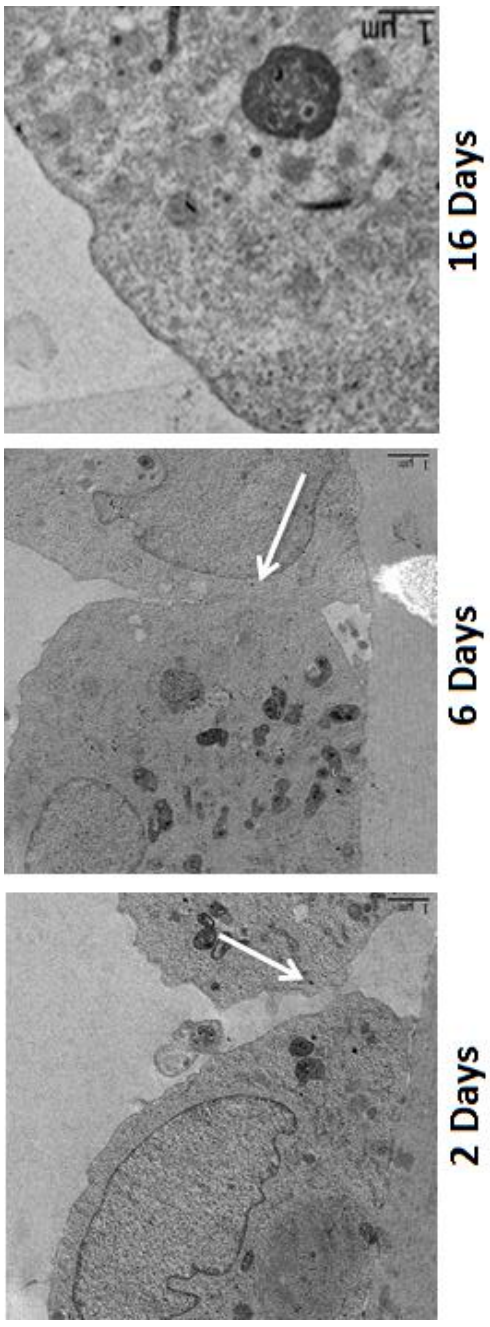

Figure 4.5| Transmission electron micrographs illustrating the cell morphology of EA926 cells for 2 days, 6 days and 16 days cultures. The presence of leaky junctions (in 2 days) and the formation of tight junctions (starting from 6 days) are shown in the figure.

4.4.4 Quantifying claudin expression for Caco2 cells

To further test the presence of tight junctions, we studied the expression of claudin 4 in Caco-2 cell cultures. claudins are the most abundant junctional proteins connecting and sealing contact sites in between epithelial and endothelial cells. They are capable of forming a tightened paracellular cleft and ion pores. Furthermore, the extracellular loops of claudins function as ion selective regions. Studying the expression of claudin 4 (the highly expressed epithelial trans-junctional protein) determined the tight junctions formed as epithelial cells matured. Studies have been shown the temporal expressions of claudin 5 as endothelial cells mature [42]. Since the expression of claudin 4 increases with time; we attribute the change in zeta potential to the microvilli growing on the Caco2 cell surface.

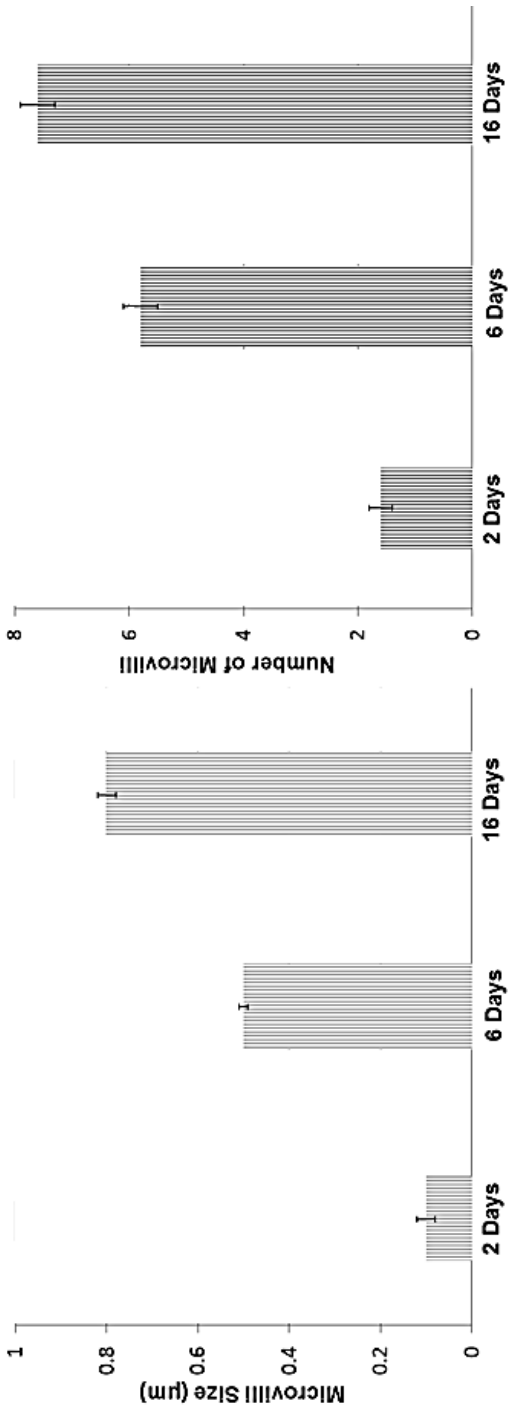

Figure 4.6| The Figures show the (A) size of microvilli and (B) number of microvilli for 2 day cultures, 6 day cultures, and 16 day cultures. n=3.

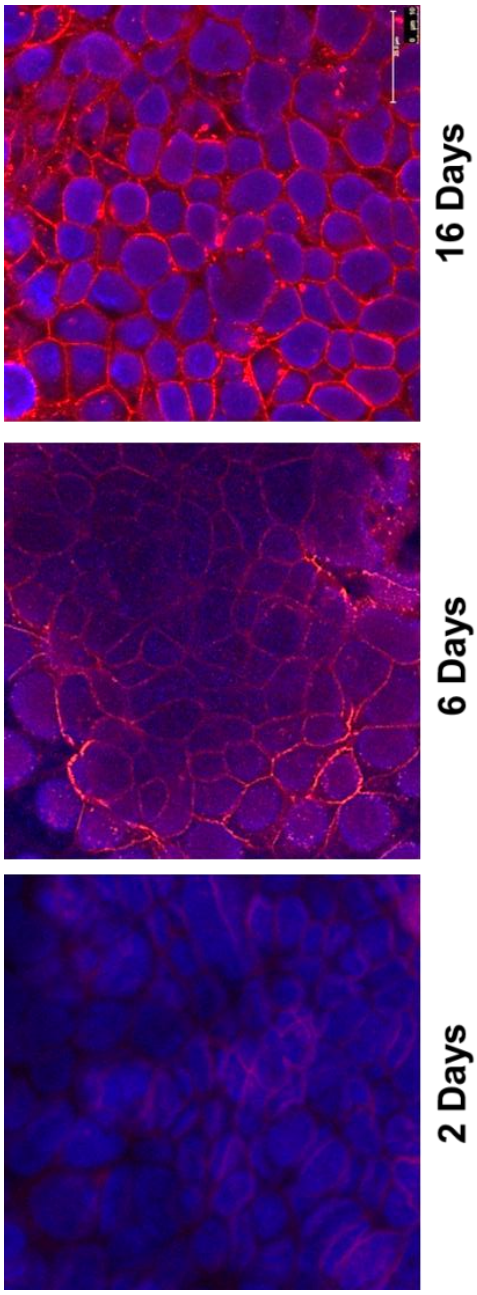

Figure 4.7| Confocal images illustrating the tight junction formation of Caco-2 cells for 2 days, 6 days and 16 days cultures. The expression for claudin 4 (the dominant tight junction protein in Caco2 cells) is shown by the Texas Red (594 nm) stain and the cell cytoplasm is stained with Hoechst 33342 (380 nm).

Table 1 summarizes the electrostatic and transport characteristics for Caco-2 Cells and the EA926 Cells measured during the time course of these studies. The trans-electrical resistance (TER) demonstrates a constant increase with cell maturity. The TER of Caco2 cells was increased substantially when compared to that of EA926 cells. ζ and TER values were almost constant for all the EA926 cell cultures. The TER of the Caco2 cell monolayers increased substantially as the cells matured.

Both the increase in ζ and the substantial increase in TER corroborate with previous studies have been shown that depict microvilli (developing on the Caco2 cell cultures) as cation exchangers [43]. They transmit electrical signals through actin filament bundles (represented by polyelectrolytes). Microvilli, physiologically arrange for restricting Ca^{2+} influx, the most versatile divalent cation that governs intercellular processes and provides moderate resistance to monovalent cations. High density of fixed cations imparts considerable resistance to ionic transduction. Hence, mucosal cells having microvilli exhibit reduced membrane potentials and higher resistance.

Table 4.1 Summary of the streaming potential, zeta potential, and hydraulic conductivity to for the DMEM soaked polycarbonate membranes, EA926 cells, and Caco2 cells seeded polycarbonate membranes with pore size of 3.0 μm.

	Streaming Potential SP (mV/kPa)	Zeta Potential ζ (mV)	Hydraulic Permeability L_P (10^{10} x $cm^2 \cdot s \cdot g^{-1}$)	Trans Electric Resistance TER ($\Omega \cdot cm^2$)
Day 2				
EA926	-32.67±1.46	-7.11±0.35	2.06±0.03	17.70±1.19
Caco2	-26.89±2.74	-5.66±0.11	3.02±0.14	28.14±1.34
Day 6				
EA926	-32.54±3.71	-7.03±0.10	3.47±0.53	24.16±4.99
Caco2	-20.78±5.37	-4.38±0.14	1.47±0.13	153.47±3.24
Day 16				
EA926	-30±1.20	-6.37±0.52	4.05±0.61	27.08±3.97
Caco2	-21.34±3.26	-3.49±0.11	6.36±0.23	282.35±10.15
DMEM	-36.13±2	-7.93±0.04	28.87±3.72	6.78±0.04

To further attribute for any correlation of claudin family expression with the measured streaming potential and TER values, we revisit their expression. We observed an increase in claudin expression in both mucosal cells (shown in Figure 4.7) and endothelial cells [42]. Hence, we analysed the charge properties of both claudin 4 (expressed in mucosal cells) and claudin 5 (expressed in endothelial cells) in their extracellular domains. Both claudin 4 and claudin 5 have 51 residues in one of their extracellular domains, out of which 11 are different from each other. A cumulative summation of the charged residues was calculated to be +4 for claudin 4 and -1 for claudin 5, providing a net charge difference of 5.

Claudin 4 MWRVTAFIGSNIVTSQTIWEGLWMNCVVQSTGQMQCKVYDSLLALPQDLQAAR 53

Claudin 5 MWQVTAFLDHNIVTAQTTWKGLWMSCVVQSTGHMQCKVYDSVLALSTEVQAAR 53

This initial analysis demonstrates the possible impact of both claudin 4 and claudin 5 in the measured streaming potential measurements and the transelectric resistance.

Our group has recently shown that the ionic strength of the buffer solution in which nanoparticles are dispersed, affects *in-vivo* uptake by the mucosal cells; suggesting that uptake might be based on electrostatic interactions [8]. In this study, we further investigated the processes underlying the interactions between the surface of mucosal cells and the invading pathogens.

We established an experimental protocol for characterization of electrostatic properties of cell layers using streaming potential methods. Zeta potential was measured across epithelial cells as well as endothelial cells. Measurements were taken for 2 days,

6 days, and 16 day cultures. 6 days and 16 days Caco2 cultures reflected developed brush border across epithelial cells. The results allowed the establishments of correlations between zeta potential measurements and the maturation state of Caco2 and EA926 cells.

4.5 CONCLUSION

The solution to many immunological and pathological conditions might be found at the port of entry or the exposed endo-symbiotic barrier. Mucosal cells transport many macromolecules and microbial organisms from the apical lumen to the underlying basal lymphoid tissue. Hence, manipulating the mucosal cells of the gut will prove to be a therapeutic and cautionary strategy for many infectious, inflammatory, and even metastatic diseases within the gut. This paper addresses the electrical properties of mucosal cells using Caco-2 as a model. We study the streaming potential resulting from concentration gradients across the mucosal cells for constant pH, salt concentration, osmolarity, and temperature. The results demonstrate that the cell membrane (composed of organic acids with a low pKa) of both epithelial and endothelial cells has a negative fixed charged. The zeta potential of the Caco2 cells decreased in their value as the cells matured and developed microvilli whereas the zeta potential of endothelial cells remained rather constant and closer to the zeta potential of the support membrane. Analyzing the TEMs and the claudin 4 expression for mucosal cells, we attribute the change in the measured zeta potential to the observed microvilli developed on the apical surface of the mucosal cells. These studies will be instrumental to develop methods to control the entry of antigens by hindering toxic foreign bodies and to facilitate the entry or uptake of oral-intranasal vaccines. It will also be possible to devise therapeutic strategies to modulate or prevent diseases that result from antigens or microorganisms invading the mucosal barrier.

4.6 REFERENCES

1 Bocci V (1992) The neglected organ: bacterial flora has a crucial immunostimulatory role. Perspectives Biology in Medicine. 35: 251–260.

2 O'Hara AM and Shanahan F (2006) The gut flora as a forgotten organ. EMBO Reports. 7: 688–693.

3 Shanahan F (2002) The host–microbe interface within the gut. Best Practices in Residential Clinical Gastroenterology. 16: 915–931.

4 Corr SC, Gahan CCGM, and Hill C (2008) M-cells: origin, morphology and role in mucosal immunity and microbial pathogenesis. FEMS Immunology and Medical Microbiology. 52: 2–12.

5 Wolf JL and Bye WA (1984) The membranous epithelial (M) cell and the mucosal immune system. Annual Review of Medicine. 35: 95-112.

6 Nicoletti C (2000) Unsolved mysteries of intestinal M cells. Gut. 47:5 735-739.

7 Clark MA, Jepson MA, and Hirst BH (2001b) Exploiting M-cells for drug and vaccine delivery. Advanced Drug Delivery Reviews. 50: 81–106.

8 Rajapaksa T, Bennett K, Hamer M, Lytle C, Rodgers VGJ and Lo DD (2010) Intranasal M cell uptake of nanoparticles is independently influenced by targeting ligands and buffer ionic strength. Journal of Biological Chemistry. 285 (31): 23739-23746.

9 Datta S, Conlisk A, Kanani D, Zydney A, Fissell W, and Roy S (2010) Characterizing the surface charge of synthetic nanomembranes by the streaming potential method. Journal of Colloid and Interface Science. 348: 85-95.

10 Wilsona W, Wadeb M, Holmana S, and Champlinb F (2001) Status of methods for assessing bacterial cell surface charge properties based on zeta potential measurements. Journal of Microbiological Methods. 43: 153–164.

11 Chung T, Wub S, Yaoc M, Lua C, Linb Y, Hungb Y, Moub C, Chena Y, and Huange D (2007) The effect of surface charge on the uptake and biological function of mesoporous silica nanoparticles in 3T3-L1 cells and human mesenchymal stem-cells. Biomaterials. 28: 2959–2966.

12 Morishita, M., Peppas, N. A. (2006). Is the oral route possible for peptide and protein drug delivery? Drug Discovery Today. 11(19-20): 905 – 910

13 Avdeef, A. (2001). Physicochemical profiling (solubility, permeability and charge state). Current topics in medicinal chemistry. 1: 277 – 351.

14 Karlsson, J., Ungell, A.-L., Gråsjö, J., Artursson, P. (1999). Paracellular drug transport across intestinal epithelia: influence of charge and induced water flux, European journal of pharmaceutical sciences. 9: 47 – 56.

15 Salama NN, Eddington ND, Fasano A. (2006). Tight junction modulation and its relationship to drug delivery. Advanced drug delivery reviews. 58(1): 15 – 28.

16 Smith DA, van de Waterbeemd H, Walker DK. (2001). Chapter 3: Absorption. In: Pharmacokinetics and metabolism in drug design. Edited by D. A. Smith, H. van de

Waterbeemd, D. K. Walker, R. Mannhold, H. Kubinyi, H.Timmerman. Wiley-VCH Verlag GmbH.

17 Ho NFH, Raub TJ, Burton PS, Barsuhn CL, Adson A, Audus, KL, Borchardt, RT (2000). Quantitative approaches to delineate passive transport mechanisms in cell culture monolayers. In: Transport processes in pharmaceutical systems. Marcel Dekker Ltd, New York. 219 – 316.

18 Nellans HN. (1991). Paracellular intestinal transport: modulation of absorption. Advanced drug delivery reviews. 7: 339 – 364.

19 Pappenheimer J and Reiss KZ. (1987). Contribution of solvent drag through intercellular junctions to absorption of nutrients by the small intestine of the rat. Journal of membrane biology. 100: 123 – 136.

20 van Meer G, Simons K.(1988). Lipid polarity and sorting in epithelial cells. Journal of cellular biochemistry. 36(1): 51 – 58.

21 Saito H, Yamamoto M, Inui K, Hori R. (1992) Transcellular transport of organic cation across monolayers of kidney epithelial cell line LLC-PK. American Journal of Physiology. 262(1.1):C59-66.

22 Bangham A, Glover J, Hollingshead S, and Pethica B (1962) The surface properties of some neoplastic cells. Biochemistry Journal. 84: 513-517.

23 Brooks DE and Seaman GVF (1973) The effect of neutral polymers on the electrokinetic potential of cells and other charged particles: I. Models for the zeta potential increase. Journal of Colloid and Interface Science. 43(3): 670-686.

24 Zhang Y, Yang M, Portney NG, Cui D, Budak G, Ozbay E, Ozkan M, and Ozkan CS (2008) Zeta potential: a surface electrical characteristic to probe the interaction of nanoparticles with normal and cancer human breast epithelial cells. Biomed Microdevices. 10(2):321-328.

25 Portney NG, Destito G, Manchester M, Ozkan M (2009) Hybrid assembly of CPMV viruses and surface characteristics of different mutants. Current Topics Microbiology Immunology. 327:59-69.

26 Drozd C and Schwartzbrod J (1996) Hydrophobic and electrostatic cell surface properties of cryptosporidium parvum. Applied and Environmental Microbiology. 62 (4): 1227–1232.

27 Foged C, Brodin B, Frokjaer S, and Sundblad A (2005) Particle size and surface charge affect particle uptake by human dendritic cells in an in vitro model. International Journal of Pharmaceutics. 298: 315–322.

28 Smyth DH and Wright EM (1966) Streaming potentials in the rat small intestine. Journal of Physiology. 182: 591-602.

29 Rose RC and Schultz SG (1971) Studies on the electrical potential profile across rabbit ileum. The Journal of General Physiology. 57:639-663.

30 Gandhi RB and Robinson JR (1991) Permaselective characteristics of rabbit buccal mucosa. Pharmaceutical Research. 8(9): 1199-1122.

31 Barry RJC and Eggenton J (1972) Membrane potentials of epithelial cells in rat small intestine. Journal of Physiology. 227: 201-216.

32 Wright EM and Diamond JM (1969) An electrical method of measuring non-electrolyte permeability. Proceedings of the Royal Society of London (B), Biological Sciences. 172(1028): 203-225.

33 Paulman SF and Thomson ABR (1981) Nonelectrolyte permeability of canine tracheal epithelium. American Physiological Society. 363-368.

34 Hubatsch I, Ragnarsson EGE, and Artursson P (2007) Determination of drug permeability and prediction of drug absorption in Caco-2 monolayers. Nature Protocols. 2(9): 2111-2119.

35 Vandrangi P, Jreij P, Rajapaksa TE, Bansal N, Lo DD, and Rodgers VGJ (2012) Novel in-situ normal streaming potential device for characterizing electrostatic properties of confluent cells. Review of Scientific Instruments. 83(7): 074302-1-5

36 Sambuy Y, De Angelis I, Ranaldi G, Scarino ML, Stammati A, Zucco F (2005) The Caco-2 cell line as a model of the intestinal barrier: influence of cell and culture-related factors on Caco-2 cell functional characteristics. Cell Biology Toxicology. 21(1):1-26.

37 Helmholtz H (1879) Studies of the electrical surface layers. Wied. Ann. Physik Chemie Ser. 3(7): 337–382.

38 Smoluchowski M (1903) Contribution of the theory of electro-osmosis and related phenomena. Bull International Academy of Science Cracovie. 184-199.

39 Schneider CA, Rasband WS, and Eliceiri KW (2012) NIH Image to ImageJ: 25 years of image analysis. Nature Methods 9:671-675

40 Matsudaira PT and Burgess DR (1982) Structure and function of the brush-border cytoskeleton. Cold Spring Harbor Symposium Quantity Biology. 46: 845-854.

41 Bazzoni G (2006) Endothelial tight junctions: permeable barriers of the vessel wall. Thrombosis Haemostasis. 95(1):36-42.

42 Morita K, Sasaki H, Furuse M, Tsukita S (1999) Endothelial claudin: claudin-5/TMVCF constitutes tight junction strands in endothelial cells. Journal of Cell Biology. 47(1):185-94.

43 Gartzke J and Lange K (2002) Cellular target of weak magnetic fields: ionic conduction along actin filaments of microvilli. American Journal of Physiology Cell Physiol. 283(5): C1333-C134.

SECTION 2

CHARACTERIZING CELL-BIOMATERIAL INTERACTIONS

PRELUDE

A material is identified as a 'biomaterial' when its microenvironment triggers favorable cellular responses. Materials that are not biocompatible can induce many complications including cytotoxic chemical build-up, chronic inflammation, trauma, and eventually scaring. Such biodegradation can be unevenly distributed *in-vivo* producing unwanted physiological trauma.

In this Section, we study the biocompatibility of titanium (Ti) substrates that have micro-patterns and nano-patterns. In Chapter 5, we investigate endothelial cell adhesion, alignment, proliferation, and spreading with rationally designed patterns on Ti surfaces composed of nano-scale grooves compared with both micro-scale grooves and no grooves at all. The results show that the nanometer grooves on the Ti surfaces demonstrate enhanced cell proliferation rate. We compare the corresponding endothelial cell response on Ti substrates and silicon (Si) substrates.

In Chapter 6, we further map the cell distribution, cell growth, migration, and underlying synthesized extracellular matrix on Ti surfaces for 2 days, 5 days, 9 days, and 12 days. We observe enhanced endothelial cell migration and extracellular matrix generation on the Ti substrates with nano-scale grooves. In Chapter 7, we study the endothelial signaling activation on endothelial nitric oxide synthase (eNOS), von Willbrand factor (vWF), vascular endothelial selectin (VE Selectin), and vascular cell adhesion molecule (VCAM1). The competitiveness of endothelial alignment with flow versus mechanical patterns is quantified and showed for the first time. We observe a higher endothelial function on the Ti substrates with nano-scale grooves.

Collectively, this suggests that nano-patterning biomaterials would be good for enhancing neovascularization and endothelialization. More specifically, Ti nano-patterns would be a preferred substrate. As demonstrated in our results, enhanced native morphology, functionality, extra cellular matrix synthesis on Ti substrates suggests the potential for long-term biocompatibility. The results also demonstrate the utilization of Ti substrates in areas that need neovascularization or angiogenesis.

Further *in-vivo* experiments are necessary to study the bio-response of the nanopatterned biomaterial prosthetic devices in animal models. The underlying mechanism of the observed improved endothelial cell response to these nano-featured patterns has yet to be explored. We can dictate the design of biomimicking prosthetics using the local distribution of favorable topographical cues.

CHAPTER 5

COMPARATIVE ENDOTHELIAL CELL ADHESION, PROLIFERATION, AND ALIGNMENT ON MICRO-PATTERNED AND NANO-PATTERNED TITANIUM AND SILICON

ABSTRACT

In this work, we evaluate the response of human endothelial cells (EA926) *in vitro* to variation in substrate materials and variation in precisely defined micro-scale and nano-scale surface topography. Specifically, we compare EA926 cell responses on two different substrate materials, titanium (Ti) and silicon (Si), both of which possess identically patterned surfaces. These surfaces are composed of substrates with no patterns and with patterns with groove sizes ranging from 0.50 to 50 μm. In our studies, we observe only minor variation in EA926 cell adhesion with substrate material and pattern feature size. However, we observe considerable enhancement of proliferation on Ti relative to Si, as well as with decreasing feature size on both substrates. Moreover, we observe that EA926 cells on sub-micrometer scale patterned surfaces of both materials remain in their exponential growth phase over the entire 5 day study period. In comparison, EA926 cells on smooth, unpatterned surfaces of both materials did not proliferate as much. Finally, significant elongation and alignment are observed on the sub-micrometer scale patterned surfaces from 1 day onwards. Collectively, these observations suggest that nano-patterned, Ti-based implantable micro-devices would be preferred in applications where rapid neovascularization and/or reestablishment of the endothelium are paramount.

Keywords: endothelial cells, titanium, silicon, nano-pattern, micro-pattern

5.2 INTRODUCTION

A material is identified as a 'biomaterial' when its *in-vivo* microenvironment triggers favorable cellular responses. Materials that are not biocompatible can induce many complications including cytotoxicity, chronic inflammation, trauma, and eventually scaring [1-6]. Bio-incompatibility can also be unevenly distributed *in-vivo* producing unwanted physiological trauma [7-14].

Many potential biomaterials have been studied to understand their working in the body at sites of injury, stent therapy, prosthetics, and neovascularization [15-17]. In the present market, stainless steel, gold, cobalt-chromium alloys, titanium, tantalum, silicone, polymer-based polyethylene/polyurethane and ninitol have been employed for stent applications [18-21]. These materials are agonists of immuno-response and understanding their responses to cellular environments can facilitate their modulations to obtain the desired host response.

One such biomaterial - Ti - has been studied rigorously as an attempt to be employed for novel biomedical applications [22-24]. When implanted, tissue repair around the Ti substrate critically depends on the inflammatory and osseous response triggered in that area [25-28]. Another biomaterial - Si - has also been employed as wafers in varied biomedical applications including implantable microdevices, drug delivery, ocular implants, neural electrodes, sensors, and renal deplacement devices [29-34]. However the interaction of endothelial cells (ECs) with Ti and Si is not completely understood [35-41].

Present nano-fabrication and micro-fabrication techniques can allow the development of nanostructured devices and substrates at a very precise and controllable manner [42-44]. Previous studies have shown the effect of employing micro-patterned biomaterials *in-vitro* [45-50]. Grating-based surface patterns potentially induce elongated cellular morphologies reminiscent of the native endothelium. Islands of extracellular matrix coated surfaces have been employed to obtain endothelial cells with specific features [51-52].

In this study, we chose Ti and Si due to their relevance for implantable microdevice application as mentioned above. We study the EC interaction to the micro-scale and nano-scale patterns on Ti and Si. Patterns composed of 0.5 μm – 50 μm were carefully and uniformly micro-fabricated and nano-fabricated on the Ti and Si substrates. We demonstrate that ECs adhere to Ti and Si *in vitro*, however endothelial cells on Ti substrates proliferate at a higher rate. Further, a confluent EC layer was quickly obtained on the nanoscale patterned Ti substrates without any coating or surface treatment. The results also show that ECs align in the direction of nano-scaled patterns on Ti substrates.

5.3 MATERIALS AND METHODS

5.3.1 Fabrication of patterned titanium and silicon substrates

Figure 5.1 schematically illustrates the layouts of the patterned Ti and Si substrates used in this study. Figure 5.1 schematically illustrates the layouts of the patterned Ti and Si substrates used in this study. The substrates share identical dimensions and patterning; however, the Ti substrate is a mirror image of the Si substrate, due to the use of the latter in the fabrication of the former, as will be discussed later. In each substrate, there are nine distinct 5 x 5 mm^2 sub-patterns. One of the sub-patterns is left unpatterned as a control (i.e. blank), while the remainder are composed of groove-based gratings with groove widths ranging from 0.5 to 50 μm and pitch twice the groove width. Each grating sub-pattern is orthogonally-oriented with respect to its neighbors, and is surrounded by a 100 μm wide unpatterned border. This substrate layout was chosen to provide opportunity for simultaneous evaluation of a broad parameter space within the same sample, and therefore, within the same cell culture conditions. However, in the current work, attention was focused solely on the 0.5 μm, 0.75 μm, 50 μm, and unpatterned sub-patterns, since our earlier studies focused on endothelial cell response to similar substrates with 0.75 μm and larger features [47]. It is important to note, however, that only patterned Ti substrates were considered in our earlier studies, and rat aortic endothelial cells (RAECs) were used rather than the human endothelial cells (HECs) used herein.

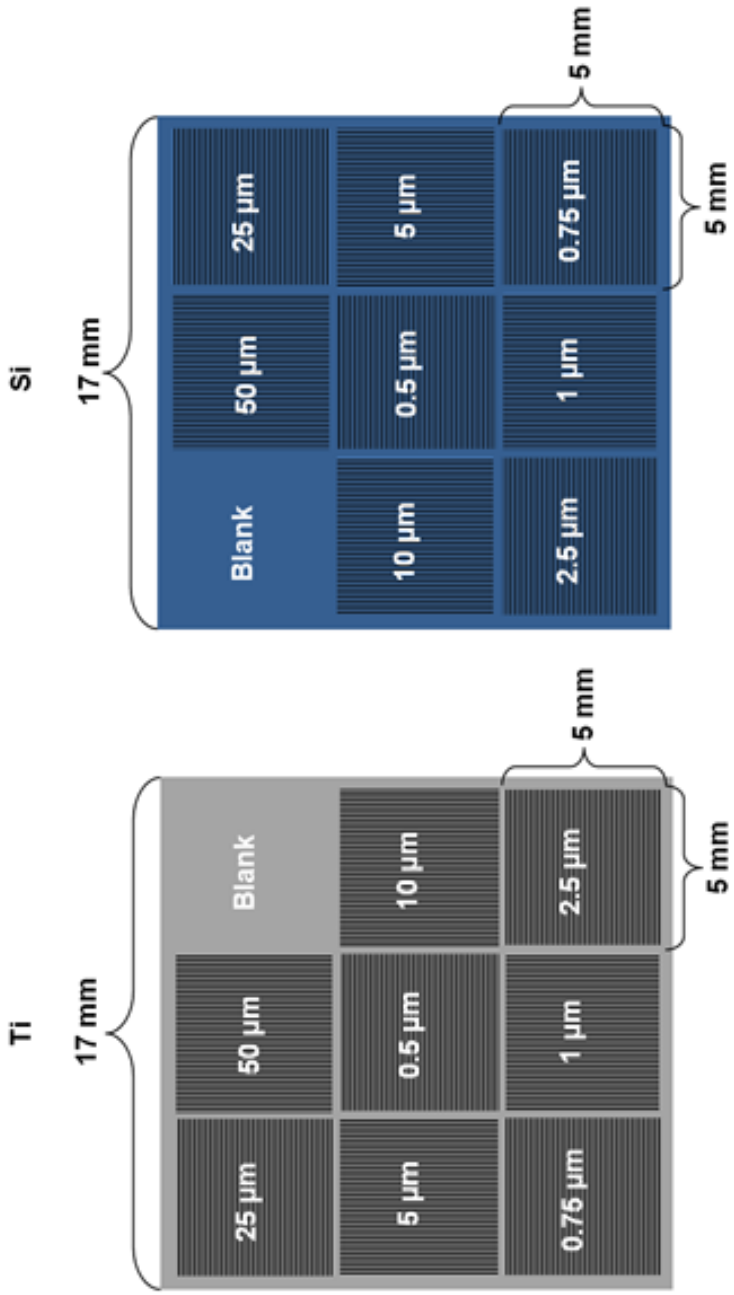

Figure 5.1| Schematic of patterned Ti (left) and Si (right) substrates used in this study.

Figure 5.2 outlines the fabrication processes for the patterned Ti and Si substrates. In both cases polished substrates were first cleaned by a standard solvent cleaning procedure consisting of sequential sonication in acetone and isopropanol, followed by rinsing in deionized (DI) water, and drying with N_2 gas. For the patterned Si substrate fabrication, single crystal Si wafers were used (100 mm diameter, P/B, <1-0-0>, 525±25μm thickness, Silicon Quest International, R_A ~ 0.5 nm). Following cleaning, the wafers were dipped in buffered hydrofluoric acid (BHF), rinsed with DI, dried with N_2, and dehydration baked. Hexamethyldisilazane (HMDS) was applied as an adhesion promoter, followed by spin-coating of photoresist (PR) (AZ nLOF 5510, Clariant). After lithographic patterning using projection lithography (GCA Autostep 200 i-line Wafer Stepper, 3C Technical), the substrates were subjected to descuming by O_2 plasma (PE-IIA, Technics). The PR patterns were then transferred into the underlying Si substrate using fluorine–based dry etching (Plasmatherm SLR 770, Unaxis). Using this process, patterned Si substrates were produced for two purposes: 1) Substrates with grating depths of 1.3 μm were used for the cell studies; and 2) Substrates with grating depths of ~ 0.3 μm served as imprint masters in the fabrication of the patterned Ti substrates. For the latter, a coating of perflourodecyltricholorsilane (FDTS) was applied using molecular vapor deposition (MVD 100E, Applied Microstructures Inc.) to minimize resist adhesion during imprinting.

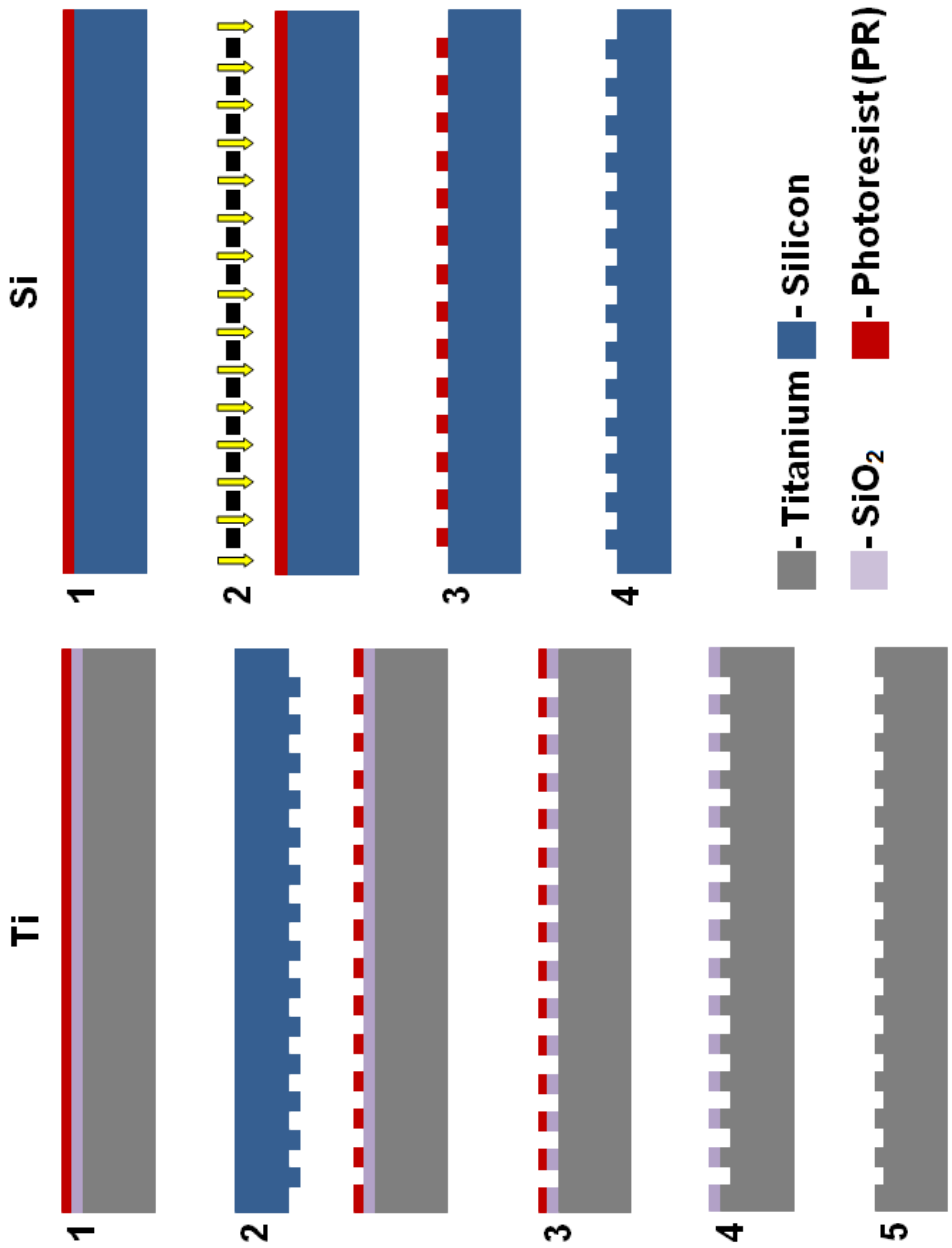

Figure 5.2| Fabrication processes for the patterned Si (left) and Ti (right) substrates. Patterned Si substrate fabrication: 1) PR application; 2) Lithographic patterning via projection lithography; 3) PR development and O_2 plasma descum; and 4) F-based dry etching and PR removal. Patterned Ti substrate fabrication: 1) SiO_2 deposition by PECVD, followed by PR application; 2) Lithographic patterning via thermal NIL with patterned Si imprint master; 3) Pattern transfer to SiO_2 by F-based dry etching; 4) PR removal and Ti DRIE etch; and 5) Final SiO_2 removal by F-based dry etching.

For the patterned Ti substrate fabrication, polycrystalline Grade 1 Ti wafers were used (99.6% Ti, Tokyo Stainless Grinding Co., R_A ~ 5 nm). Following cleaning, an etch mask of 200 nm SiO_2 was deposited using plasma enhanced chemical vapor deposition (PECVD) (VLR, Unaxis). The wafers were then spin-coated with PR (mr-I 7020, Micro Resist Technology). Afterwards, the PR was patterned using the Si imprint masters and thermal nanoimprint lithography (NIL) (NX2000, Nanonex Inc.). Oxygen-based dry etching was used to remove the residual layer at the base of the features after imprinting (E620-R&D, Panasonic Factory Solutions). This was followed by transfer of the PR patterns into the underlying SiO_2 etch mask by fluorine-based dry etching (E620-R&D). The etch mask patterns were then transferred into the underlying substrate using a modified version of the Ti DRIE process optimized for nanoscale features. Finally, fluorine-based dry etching was used to remove the remaining etch mask [44].

5.3.2 Patterned substrate characterization

The fidelity and uniformity of the surface patterning was characterized using scanning electron microscopy (SEM) (SUPRA 55, Leo). Imaging was performed at 5 kV accelerating voltage without need for application of conductive coatings on either substrate. The surface roughness of the patterned substrates was characterized using atomic force microscopy (AFM; DimensionTM 3100, NanoscopeIIIa, Vecco Meterology Group). Commercially-available, silicon-nitride tips were used (tip radius of curvature < 10 nm, tip height = 14 - 16 µm, and cantilever spring constant = 1.2 - 6.4 $N \cdot m^{-1}$; Bruker

AFM Probes). Imaging was performed in tapping mode with 1 Hz scan rate. The depth of the gratings on the patterned Ti substrates was characterized using focused ion beam milling (CrossBeam XB1540, Carl Zeiss Microscopy), since the intrinsic toughness of these substrates precluded cross sectioning by cleaving. This was not necessary for the patterned Si substrates, since their intrinsic brittleness allowed cross sectioning by cleaving. Finally, the depths in the larger gratings of both substrates were also measured using a surface profilometer with 12 μm tip diameter stylus (Dektak 8, Veeco).

5.3.3 Endothelial cell culture

EA926, a variant of human endothelial cells were obtained from ATCC (Manassas, VA). Cells were cultured using Dulbecco's modified Eagle's medium (DMEM, Lonza Inc.) and were supplemented with 10% FBS (Gibco Inc.) and antibiotics (Primocin, Invivogen Inc.). Freshly passaged cells were maintained in humidified 95% air-5% CO_2 incubator at 37°C.

5.3.4 Endothelial cell adhesion and proliferation assays

Prior to all assays, the patterned substrates were subject to standard solvent cleaning, followed by sterilization by autoclaving at 121 °C for 15 minutes and cooled at 110 °C for 20 minutes and UV light exposure overnight. To study EA926 cell adhesion, cells were seeded at a density of 1050 cells/cm^2 on the patterned substrates. The cells were

cultured for 4 h, after which non-adherent cells were removed by rinsing twice in phosphate buffered solution (PBS), while cells that remained on the surface were visualized by staining (Rhodamine 123, Life Technologies). To study proliferation of endothelial cells, cells were seeded at a density of 1050 cells/cm^2 on the patterned substrates. The cells were cultured for 4 h, 1 d, 3 d, and 5 d, after which non-adherent cells were removed by rinsing in PBS, while cells that remained on the surface were again visualized by Rhodamine 123 staining.

5.3.5 Endothelial cell imaging

Optical and fluorescent imaging of EA926 cells on the patterned substrates was performed using a fully apochromatic corrected stereomicroscope with 12.5:1 zoom (M125, Leica). Images were acquired with a 10X objective lens, binning of 4 x 4, gain of 8.0, and brightness of 1.2. Commonly-available software was used for image acquisition (Spot Imaging Software®, Spot Imaging Solutions) and processing (ImageJ® 1.46, NIH)[53]. SEM imaging of ECs on the patterned substrates was also performed. Prior to imaging, cells were fixed with 4% glutaraldehyde and postfixed with 0.5% OsO_4 for 1 h each, dehydrated through a graded series of alcohol, and dried in a critical point dryer (Balzer CPD 030, Liechtenstein). Imaging was performed at 5 kV accelerating voltage without need for application of conductive coatings on either cell seeded substrate.

5.3.6 Statistical analyses

All experiments were conducted for four to five times and repeated at three different times. Experimental data were analysed statistically using ANOVA (with single factor) and commercially-available statistical packages (Excel®, Microsoft; and SigmaPlot® 5.0, Systat Software Inc.).

5.4 RESULTS AND DISCUSSION

5.4.1 Patterned substrate characterization

Figure 5.3 shows SEM micrographs of the patterned Ti and Si substrates. Precisely defined and highly uniform patterning is observed on both substrates across the entire feature size range. Moreover, the unpatterned control surfaces are observed to be featureless, thus demonstrating that there is no significant roughnening produced by the fabrication process. It is important to note that the 0.5 μm gratings on the Ti substrates represent the smallest features produced by the Ti DRIE process to date.

Figure 5.4 shows cross section SEM micrographs of the 0.5 μm gratings on the Ti and Si substrates. As can be seen, nearly identical grating patterns have been produced in both substrates. Moreover, groove cross section profiles are observed to be nearly rectangular. Finally, grating depths are observed to be 1.3 μm for both substrates. Results from surface profilometry measuresments of wider grooves elsewhere on the patterned substrates returned similar depths (data not shown), thus indicating that grating depth is uniform across all patterns on the substrates.

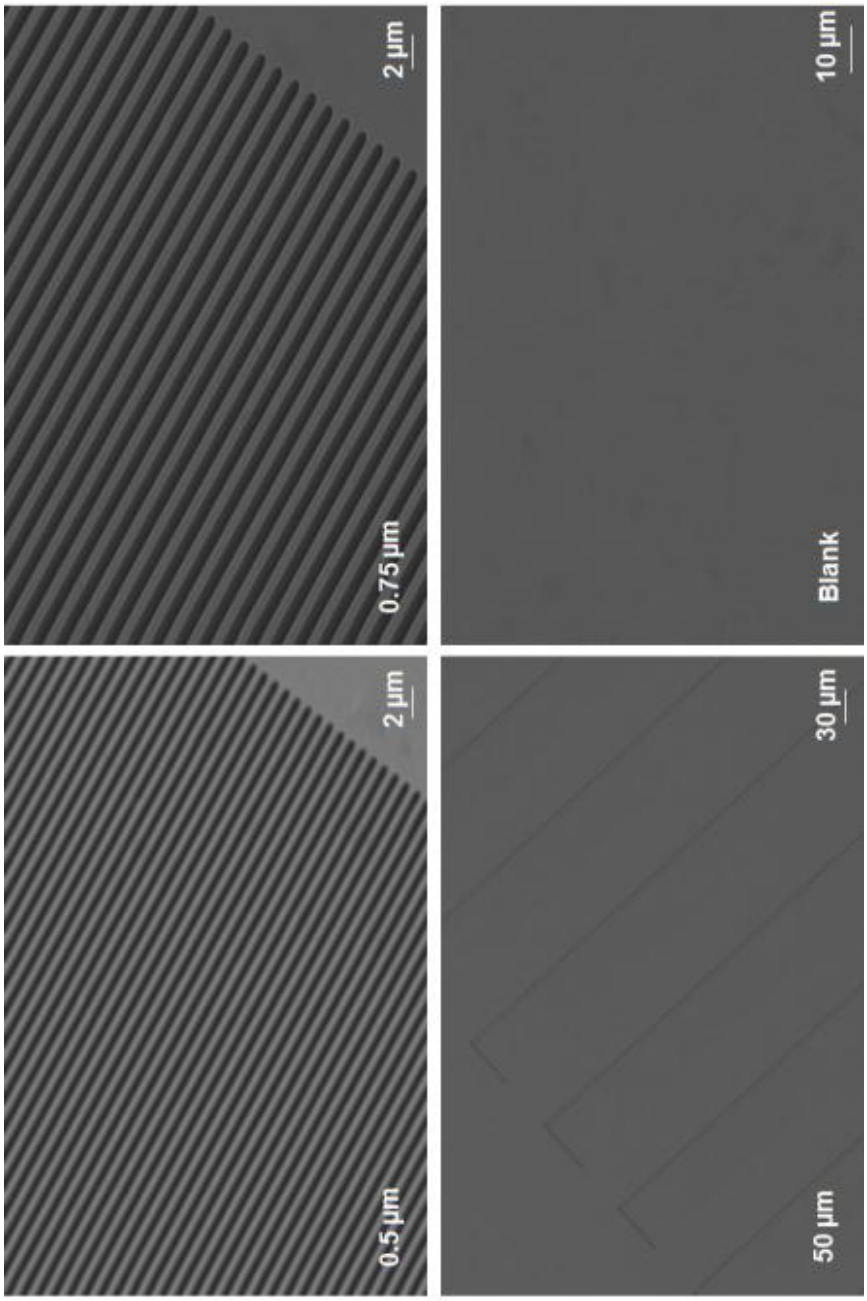

Figure 5.3| Scanning electron microscope (SEM) micrographs of patterned Ti substrates with 0.5 µm, 0.75 µm, and 50 µm gratings, as well as unpatterned control surfaces (i.e. blank).

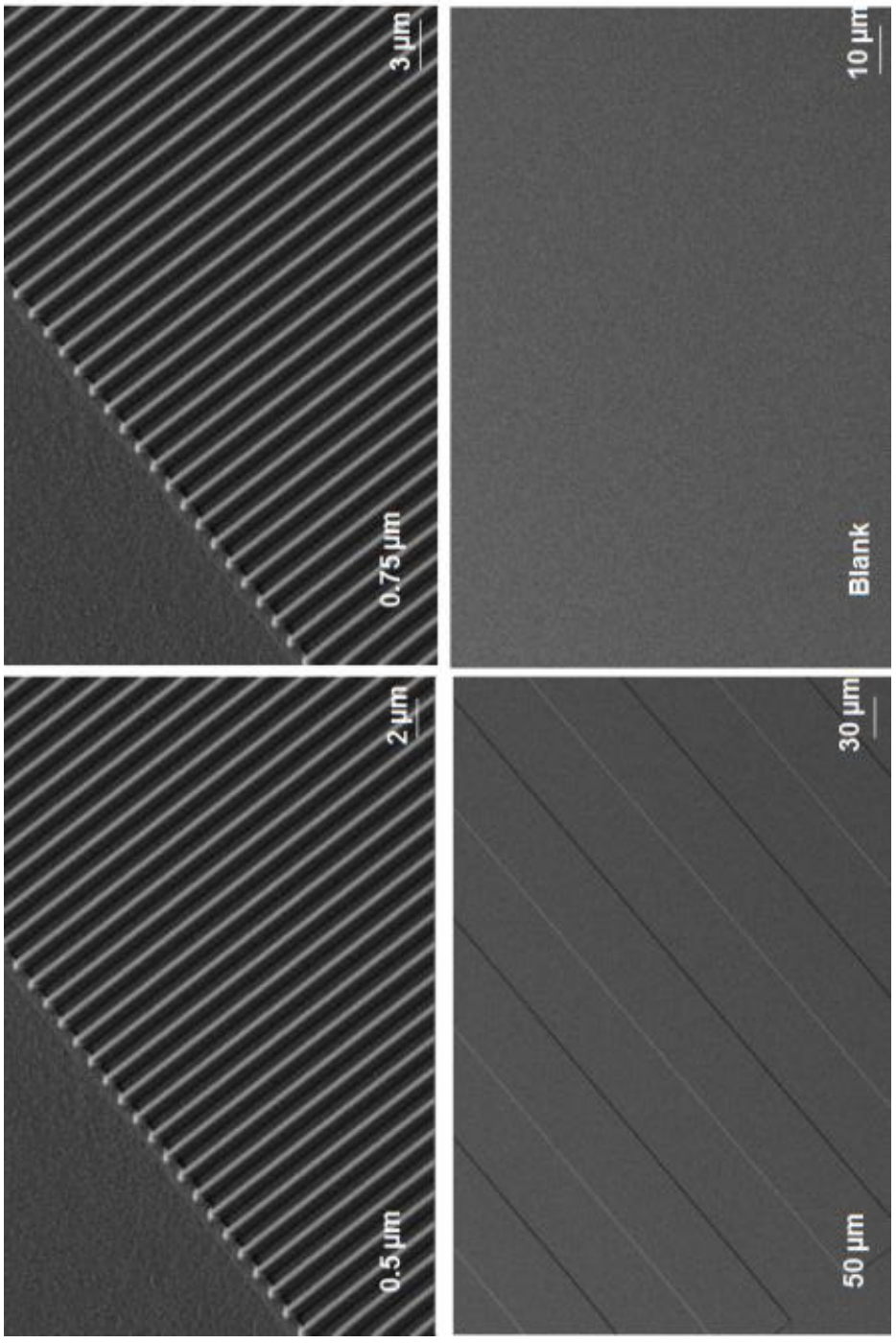

Figure 5.4| Scanning electron microscope (SEM) micrographs of patterned Si substrates with 0.5 µm, 0.75 µm, and 50 µm gratings, as well as unpatterned control surfaces (i.e. blank).

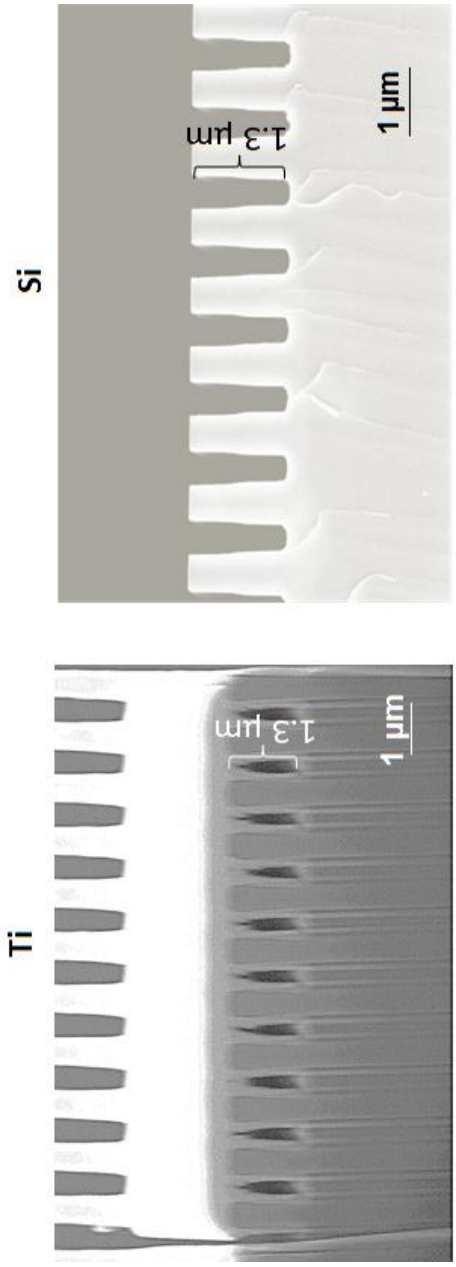

Figure 5.5| Scanning electron microscope (SEM) micrographs of 0.5 μm grating cross sections from patterned Ti (left) and Si (right) substrates. Notes: The bright layer covering the Ti grating is a Pt film deposited prior to focused ion beam (FIB) milling to protect the underlying structures from sputtering-induced faceting. The vertically-oriented contrast variations observed beneath the grating in the patterned Ti substrate are "curtain effect" artifacts produced by differential sputtering during milling [48].

Table 5.1 shows AFM-based surface roughness measurements from various sub-patterns on the patterned Ti and Si substrates. Measurements were taken on the ridge-tops of the grating sub-patterns, and the reported values are averages of measurements made at five different regions (center, and four corners) on each sub-pattern. Measurements were made over 200 x 200 nm^2 areas within the middle of the ridge-tops for the 0.5 and 0.75 μm gratings (0.04 μm^2 measurement area). For the 50 μm gratings and upatterned sub-patterns, measurements were made over 530 x 530 nm^2 areas (0.28 μm^2 measurement area). Average roughness, R_a, represents the average height of the roughness irregularities, while root mean squared roughness , R_{sq}, is more sensitive to low and high points, and maximum roughness, R_{max}, reports the highest abberations. In most cases, surface roughness is observed to be greater on Ti than Si. However, in all cases, roughness is less than 15 nm, and far less than the smallest pattern size – 0.5 μm. This suggests that the surface roughness has negligible influence on cellular responses. Surprisingly, the unpatterned surface of Ti was smoother than the Si.

Table 5.1. Atomic force microscope (AFM) surface roughness measurements of specific sub-patterns on the patterned Ti and Si substrates. Reported values are averages of 4 measurements taken at various locations within each sub-pattern.

	Ti					Si				
Area (μm^2)	0.04		0.28			0.04		0.28		
	0.5 µm	0.75 µm	50 µm	Unpatterned		0.5 µm	0.75 µm	50 µm	Unpatterned	
R_a (nm)	0.88±0.19	0.62±0.05	0.43±0.04	0.56±0.03		0.39±0.01	0.60±0.07	0.30±0.03	1.60±0.15	
R_{sq} (nm)	1.15±0.18	0.77±0.28	0.56±0.05	0.74±0.06		0.52±0.01	0.91±0.22	0.40±0.07	2.01±0.19	
R_{max} (nm)	10.48±4.23	5.06±0.41	7.89±2.19	7.05±1.08		5.30±1.58	11.56±2.38	5.21±1.63	14.23±1.27	

5.4.2 Endothelial cell adhesion

Figure 5.6 shows EC densities after 4 h on patterned Ti and Si substrates, as characterized by fluorescence imaging. Although variations in adhesion with feature size and substrate material are observed, most are relatively minor. The ECs on Ti substrates showed greater adhesion with the nano-scale patterns. These results corroborate with our earlier studies, which showed 2 – 3 fold higher RAEC adhesion on 0.75 μm Ti gratings compared to 50 μm Ti gratings and unpatterned Ti control surfaces [47]. However, on the Si substrates, endothelial cells adhered to a similar extent on patterned as well as non-patterned surfaces.

5.4.3 Endothelial cell proliferation

Our results show greater proliferation with decreased feature sizes. We observe the previously seen trend for Ti [47] and observe a similar trend on Si, albeit at lower cell densities. It is also interesting to note that ECs on sub-micron patterns are in a continued growth phase, while ECs on unpatterned surfaces move on to the subsequent phases in the growth cycle. ECs on sub-micron patterns adhered to the surface, spread and proliferated and within 1 d forming a sub-confluent monolayer.

More specifically, Figure 5.7 – Figure 5.9 show EC densities after time points ranging from 4 h to 5 d on the patterned Ti and Si substrates. At comparable time points and feature sizes, greater proliferation is typically observed on Ti compared to Si, e.g. cell densities on the 0.5 μm Ti patterns are nearly 40% greater at 5 d than those on

comparable Si gratings. Moreover, at most time points, greater proliferation is observed with decreasing feature sizes for both materials, e.g. cell densities on the 0.5 μm Ti patterns are nearly 5 times greater than unpatterned Ti at 5 d, and nearly 3 times greater for 0.5 μm Si gratings compared to unpatterned Si. In summary, after 1 day, we observed increased cell density and after 5 days we observed a confluent and dense cell monolayer.

ECs on sub-micrometer scale gratings in both Ti/Si are observed to remain in their exponential growth phase over the entire 5 d study period. EC confluence occurred most quickly on the Ti/Si surfaces with groove sizes in the nano-scale range (0.5 μm and 0.75 μm). Cell layer is said to be confluent when approximately 90% of its surface is covered with cells. The endothelial cells reach confluence on 0.5 μm as quickly as within 2 days whereas in 50 μm Ti substrates and unpatterned Ti substrates, the endothelial cells do not grow to confluence.

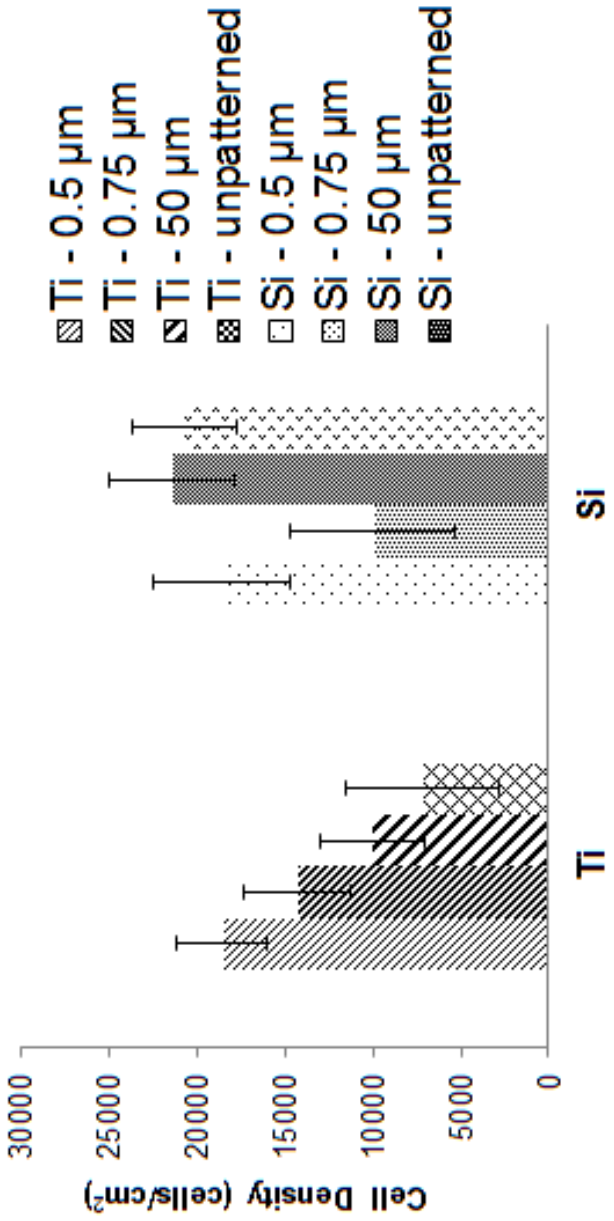

Figure.5. 6. Human endothelial cells (EA926) densities on patterned Ti and Si substrates after 4 hour culture. n=5. No statistical difference is seen at $p<0.5$.

Cells over the unpatterned surface maintained their morphological patterns without any significant volume variation. Finally, as shown in Figure 5.9, ECs on sub-micrometer scale gratings in both Ti/Si are observed to remain in their exponential growth phase over the entire 5 d study period. In summary, cell confluence occurred most quickly on the Ti/Si surfaces with groove sizes in the nano-scale range (0.5 μm and 0.75 μm). To remind ourselves, a cell layer is confluent when approximately 90% of its surface is covered with cells. The endothelial cells reach confluence on 0.5 μm as quickly as within 2 days whereas in 50 μm Ti substrates and unpatterned Ti substrates, the endothelial cells do not grow to confluence. Figure 5.9 shows the number of cells attached to Ti/Si and unpatterned surfaces after the different growing periods.

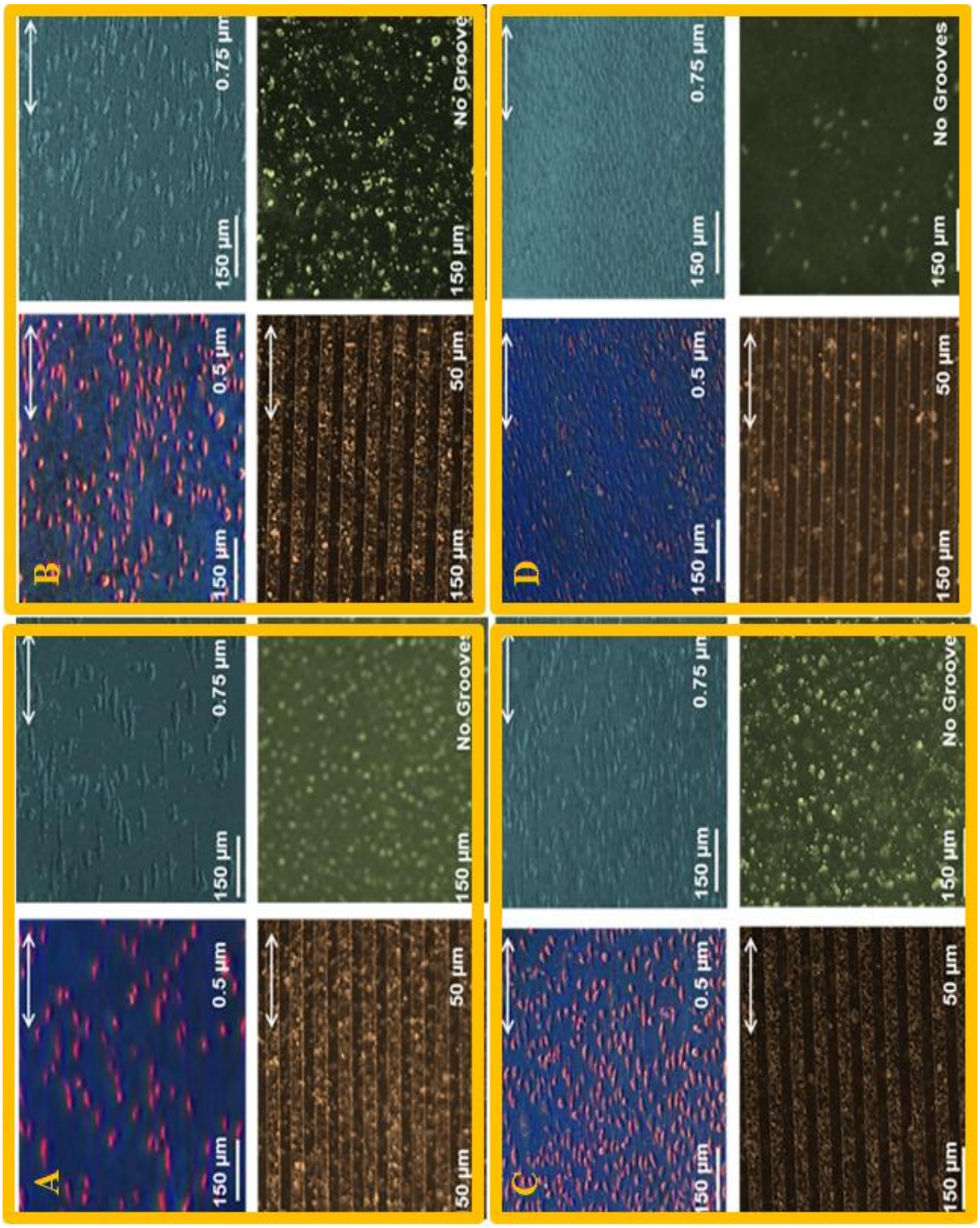

Figure 5.7| Human endothelial cells (EA926) on patterned Ti substrates for 0.5 µm, 0.75 µm, 50 µm, and unpatterned substrates at varying time points ranging from 4 hours to 5 days. Cell densities for (A) 4 hours, (B) 1 day, (C) 3 days, and (D) 5 days have been quantified.

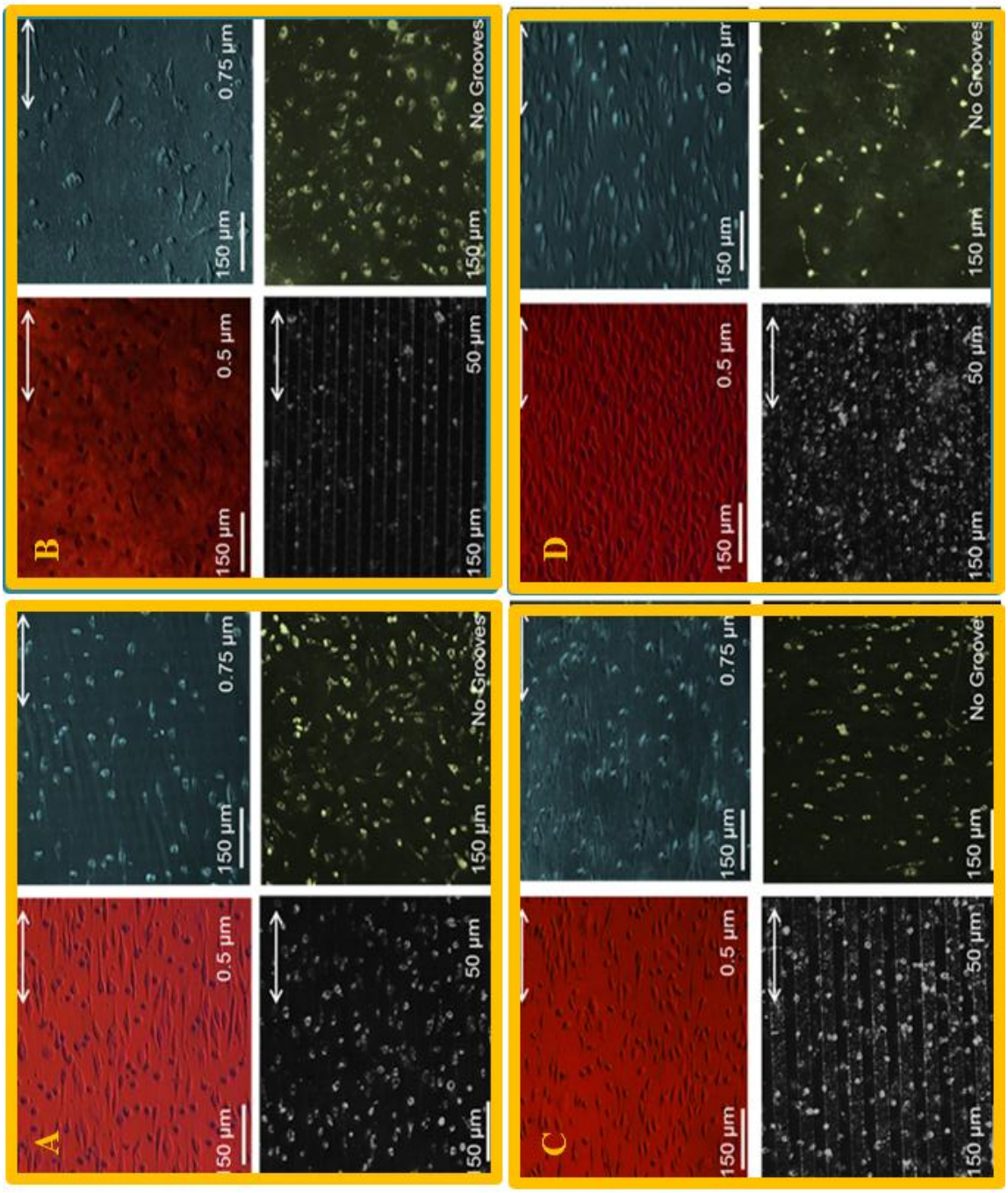

Figure 5.8| Human endothelial cells (EA926) on patterned Si substrates for 0.5 µm, 0.75 µm, 50 µm, and unpatterned substrates at varying time points ranging from 4 hours to 5 days. Cell densities for (A) 4 hours, (B) 1 day, (C) 3 days, and (D) 5 days have been quantified.

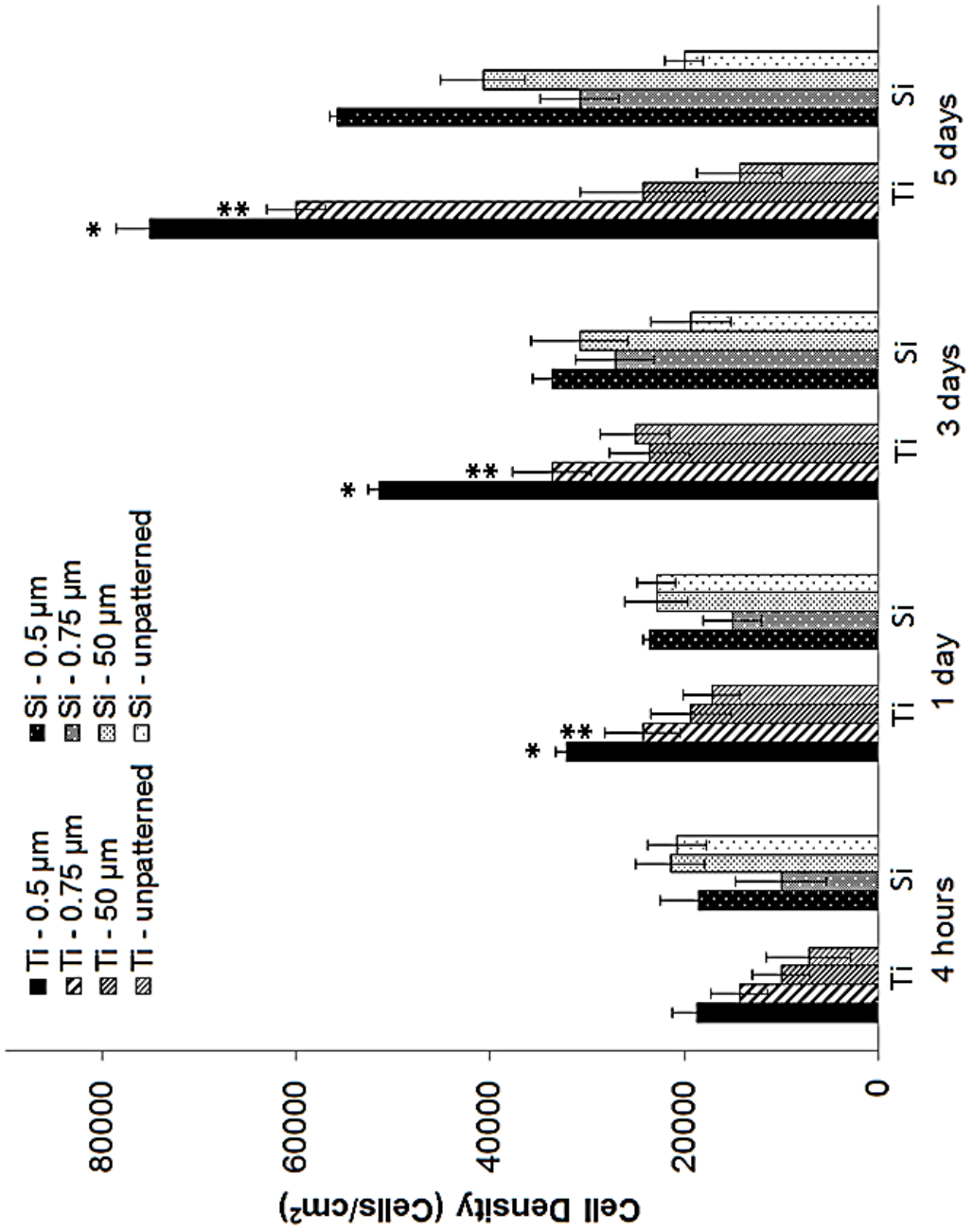

Figure 5.9| Human endothelial cell (EA926) densities on patterned Ti and Si substrates at varying time points ranging from 4 hours to 5 days. Data = mean ± SEM (*p=0.001; unpaired samples T-test, n = 5).

5.4.4 Endothelial cell alignment and morphology

The morphological observations indicated that ECs seeded on Ti were flat, elongated and oriented along the direction of the Ti grooves. These cells adhered on the surfaces with maximum cytoskeletal focal points. Figure 5.10 shows SEM micrographs of ECs on 0.5 μm grating sub-patterns on both Ti and Si substrates after 1 d. Strong alignment and elongation is observed on both materials, as is the presence of cellular extensions of filopodia and lamellipodia, which demonstrate an intrinsic tendancy of paracellular signaling. The signaling can be attributed directly to the tensegrity of the cell structure [45]. However, more favorable cellular morphology is observed on the Ti gratings, as evidenced by greater flattening and spreading and hence greater focal point adhesion. On the unpatterned surfaces, ECs do not morph to their normal cell shapes. Instead, we observe that the ECs were more spherical.

Figure 5.11 shows optical micrographs of ECs on 0.5 μm Ti gratings and commercially available polystyrene cell culture dishes after 5 d. The salient feature that can be observed on the 0.5 μm Ti grating is the elongated cellular morphology within the nearly confluent monolayer, which is reminiscent of the native endothelium. Cells on unpatterned Ti surfaces and polystyrene culture dish did not reached confluence and are observed to proliferate in a largely random manner. These results demonstrate that sub-micro gratings elicit faster confluence than unpatterned, and Ti specifically elicits more favorable morphology (as evidenced by flattening & spreading) than Si.

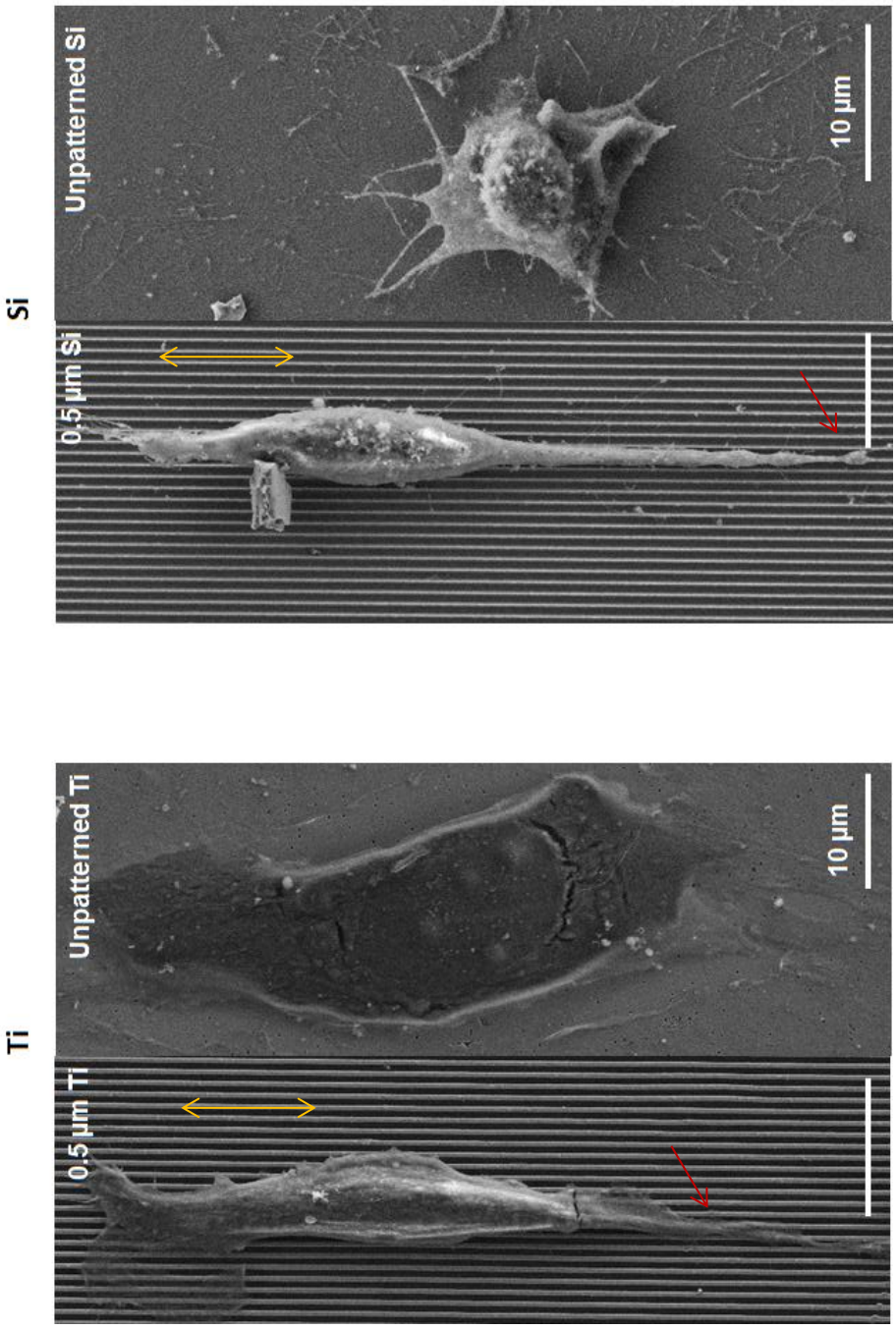

Figure 5.10| Scanning electron microscope (SEM) micrographs of human endothelial cells (EA926s) after 1 day culture on 0.5 µm grating sub-patterns of Ti (left) and Si (right) substrates. Double arrow in Ti image indicates grating direction, while single arrows in both images indicate filopodia and lamellipodia.

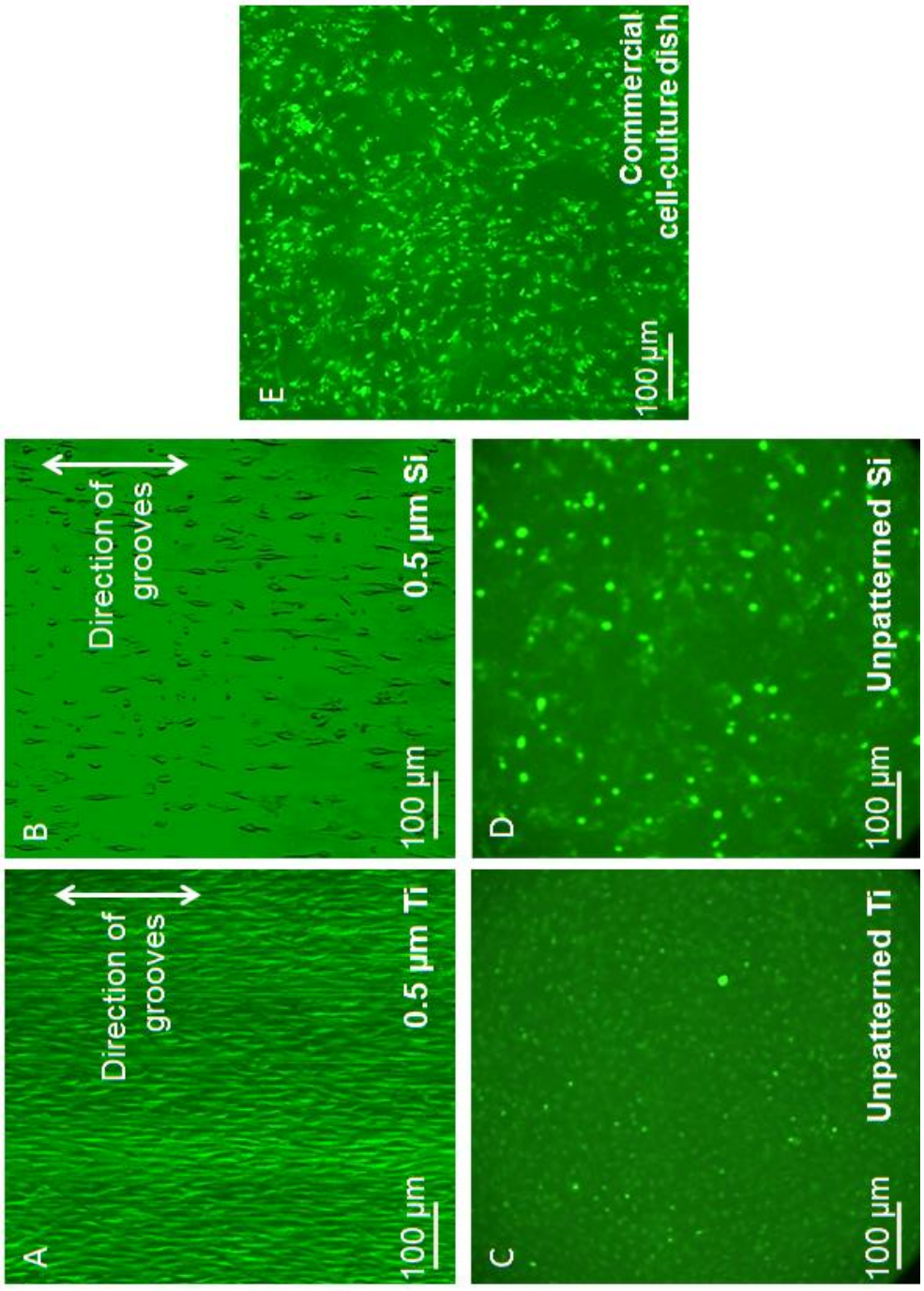

Figure 5.11| Optical microscope micrographs of human endothelial cells (HECs) after 5 day culture on: 0.5 µm grating sub-pattern of (A) Ti substrate and (B) Si substrate; unpatterned (C) Ti substrate and (D) Si substrate; and (E) Commercially-available polystyrene cell culture dish. Note: Double arrows indicate grating direction.

Figure 5.12 shows a SEM micrograph of ECs on a patterned Ti and Si substrates after 5 d. The images are taken at the boundary of 0.5 μm and 50 μm sub-patterns, which are orthogonally oriented with respect to one another, and are separated by a 100 μm wide unpatterned border. As in Figure 5.8, a confluent monolayer of elongated and aligned cells is observed on the 0.5 μm grating Ti sub-pattern substrate. However, cell density and alignment are observed to decrease in the neighbouring unpatterned border and 50 μm grating sub-pattern substrate. Similar trends were observed for ECs on the patterned Si substrates at comparable locations.

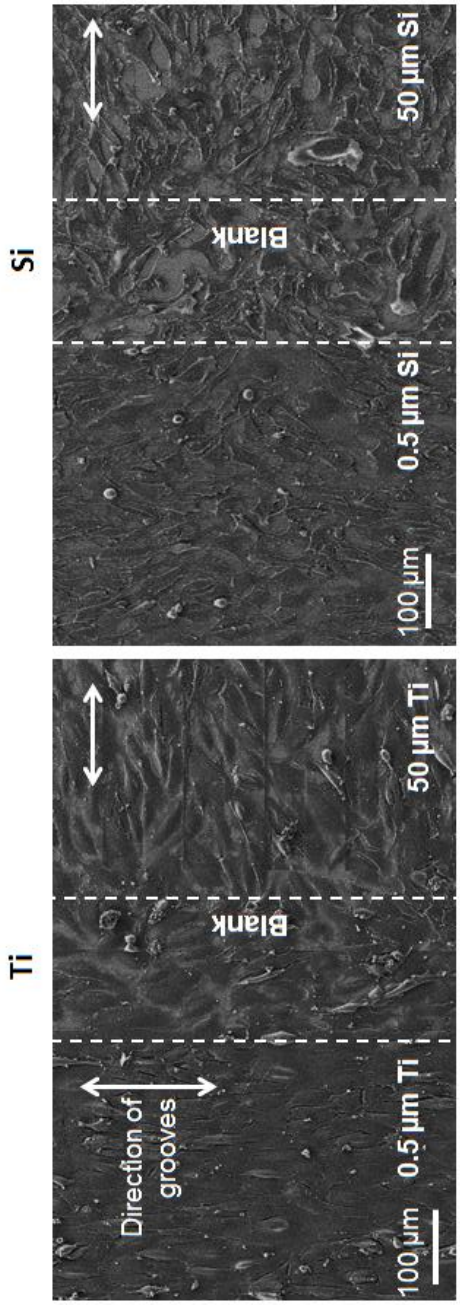

Figure 5.12| Scanning electron microscope (SEM) micrograph of human endothelial cells (EA926s) after 5 day culture on patterned Ti substrate. Imaged region is at boundary between 0.5 µm (left) and 50 µm (right) grating sub-patterns, which are orthogonally oriented and separated by 100 µm unpatterned border (middle). Note: Dotted lines indicate boundaries of the sub-patterns and double arrows indicate grating direction.

The results demonstrate the importance of controlled nano-scale gratings, which may mimic the physical topography of the subendothelium, and hence successfully maintain the underlying environment for ECs. These *in-vitro* studies explore EC adhesion and proliferation on rationally designed patterned Ti and Si surfaces including, and for the first time, a groove size as small as 0.5 μm. The salient feature of these studies is the utilization of a novel technique that meticulously produces nanometer to micrometer-scale surface features on biomaterials. Moreover, the data demonstrates superior EC adhesion, alignment, and proliferation on patterned Ti and Si surfaces with nano-sized grooves compared to unpatterned Ti and Si panels, micropatterned Ti and Si, and commercially available cell culture substrates.

These *in-vitro* studies explore endothelial cell adhesion and proliferation on rationally designed patterned Si and Ti surfaces including, and for the first time, a groove size as small as 0.5 μm. The salient feature of these studies is the utilization of a novel technique that meticulously produces nanometer to micrometer-scale surface features on biomaterials. Moreover, the data demonstrate superior endothelial cell adhesion, alignment, and proliferation on patterned Ti and Si surfaces with nano-sized grooves compared to blank Ti and Si panels, micropatterned Ti and Si, and commercially available cell culture substrates.

Controlled nano-patterns on Ti and Si surfaces are favorable to endothelial cell growth. The data also demonstrates a direct correlation of neo-vascular benefits with decreasing pattern feature sizes, thus suggesting that even greater promise may lie in

further feature size reduction. An added advantage of using the proposed nanopatterned stent model is the non-intervention of any pharmaceutical drugs they might lead to less complications or side-effects than the currently employed pharamaceutical modified biomimetic surfaces in the market.

Further *in-vivo* experiments are necessary to be performed to study the bio-response of the nanopatterned biomaterial prosthetic devices in animal models. The rationale of the observed improved endothelial cell response to these nano-featured patterns has yet to be explored. Additionally, the local distribution of physical and chemical cues within the substrate dictates the design of biomimicking prosthetics.

5.5 CONCLUSIONS

Precise nano-patterned features were fabricated on Ti and Si substrates using novel plasma etching techniques - NIL and TIDE. In this work, we show that Ti and Si substrates with nano-patterns promote the formation of an endothelial monolayer. We observed a non-preferential EC adhesion on Ti and Si substrates for 4 hours, however, over longer time periods. ECs readily proliferate on Ti substrates compared to Si substrates. The results further propose that contact-guided neovascularization can be enhanced on substrates with nano-grooves. More studies are necessary to corroborate the benefits of nanopatterned Ti/Si for prosthetic applications. The data also demonstrates a direct correlation of endothelial proliferation rate with decreasing pattern feature sizes, thus suggesting that even greater promise may lie in further feature size reduction. An added advantage of using the proposed nanopatterned stent material is the non-intervention of any pharmaceuticals that might lead to less complications or side-effects than the commercially available biomimetic devices. It will be interesting to observe the endothelial behavior on nanopatterned substrates of smaller dimensions.

5.6 REFERNCES

1 Ratner BD *et al*. 2004 Biomaterials science: an introduction to materials in medicine (Academic Press)

2 Mitragotri S and Lahann J 2009 Nature Mater. 8, 15–23

3 Ratner DR and Bryant SJ 2004 Biomaterials: where we have been and where we are going. Annu. Rev. Biomed. Eng. 6:41–75

4 Navarro M, Michiardi A, Castano O, and Planell JA 2008 Biomaterials in ortheopedics. J. R. Soc. Interface 5(27): 1137-1158

5 Mieszawska AJ and Kaplan DM 2010 Smart biomaterials – regulating cell behavior through signaling molecules. BMC Biology 8:59

6 Wang Y, Kim, HJ, Novakovic VG, and Kaplan DL 2006 Stem cell-based tissue engineering with silk biomaterials. Biomaterials 27(36): 6064-6082

7 P Moreno, M Molina, G Avila, HF Rios, P Cortés, and HL Wang 2011 Complications associated with implant migration into the maxillary sinus cavity. Clinical oral implants research.

8 W Zimmerli and A Trampuz. 2012 Biomaterial-Associated infection: a perspective from the clinic. biomaterials associated infection: immunological sspects and antimicrobial strategies, 1.

9 ISO 2002 Biological evaluation of medical devices: Part 4— Selection of tests for interactions with the blood.

10 Place ES, Evans ND, and Stevens MM 2009 Complexity in biomaterials for tissue engineering. Nature Mater. 8, 457-470

11 Hench LL and Thompson I 2010 Twenty-first century challenges for biomaterials. J. R. Soc. Interface 7(4): S379-S391

12 Rakin M and Sedmak A 2006 Biomaterials – joints and problems of contact interfaces. FME Transactions 34: 81-86

13 Ueno H, K Kakihata, Y Kaneko, S Hashimoto, and A Vinogradov 2011 Enhanced fatigue properties of nanostructured austenitic SUS 316L stainless steel. Acta Materialia, 59(18): 7060-7069.

14 Fintan MT, Sebastian AM, and Henk BJ 2013 Biomaterials associated infection. Springer.

15 Ruberti JW, Roy AS, and Roberts CJ. 2011 Corneal biomechanics and biomaterials. Ann. Rev. Biomed. Eng. 13: 269-295.

16 Hollinger JO. 2011 An introduction to biomaterials. CRC Press.

17 Brien O, Fergal J. 2011 Biomaterials and scaffolds for tissue engineering. Mat Today 14(3): 88-95.

18 Sionkowska A. 2011 Current research on the blends of natural and synthetic polymers as new biomaterials: Review. Progress in Polymer Science 36(9): 1254-1276.

19 Li Z and Masakazu K. 2011 Current progress in inorganic artificial biomaterials. Journal of Artificial Organs 14(3): 163-170.

20 Burdick JA and Mauck RL 2011 Biomaterials for tissue engineering applications: a review of the past and future trends. Springer.

21 Katti K 2004. Biomaterials in total joint replacement. Colloids and Surfaces B: Biointerfaces. 39(3): 133-142

22 Mediaswanti K., Wen C, Ivanova EP, Berndt CC, Malherbe F, and Wang J. 2012. Biological performances of titanium scaffolds: a review. Advanced Materials Research, 535: 1634-1637.

23 Rack HJ and Qazi JL 2006. Titanium alloys for biomedical applications. Materials Science and Engineering: C, 26(8):1269-1277.

24 Valiev RZ, Irina PS, Vladimir VL, Henry R, Terry CL Jiri P, Ludek D, Daniel H, and Jarmila S. 2008 Nanostructured titanium for biomedical applications. Advanced engineering materials 10(8):B15-B17.

25 Manivasagam G, Dhinasekaran D, and Rajamanickam A 2010 Biomedical implants: corrosion and its prevention-a review. Recent patents on corrosion science. 2:40-54.

26 Özcan M and Hämmerle C 2012 Titanium as a Reconstruction and Implant Material in Dentistry: Advantages and Pitfalls. Materials 5(9):1528-1545.

27 Januairo AL, Sallum EA, Toledo S, Sallum AW, Nociti FH 2001 Effect of calcitonin on bone formation around titanium implant. A histometrics study in rabbits. Braz Dent J. 12(3): 158-162

28 Fox SC, Moriarty JD and Kusy RP 1990 The effects of scaling a Titanium implant surface with metal and plastic instruments: an in vitro study. 61(8): 485-490

29 Desai TA, Hansford D, and Ferrari M 1999 Characterization of micromachined silicon membranes for immunoisolation and bioseparation applications. J. Membr. Sci. 159:221–231.

30 ErlenkötterA., Endres P, Nederlof B, Hornig C, and Vienken J 2008. Score model for the evaluation of dialysis membrane hemocompatibility. Artif. Organs 32:962–969

31 Muthusubramaniam L, Lowe R, Fissell WH, Li L, Marchant RE, Desai TA, and Roy S 2011 Hemocompatibility of silicon-based substrates for biomedical implant applications. Annals of Biomed. Eng. 39(4): 1296-1305

32 Fissell WH., Dubnisheva A, Eldridge AN, Fleischman AJ, Zydney AL, and Roy S. 2009 High-performance silicon nanopore hemofiltration membranes. J. Membr.Sci. 326:58–63.

33 Bisi O, Ossicini S, and Pavesi L 2000 Porous silicon: a quantum sponge structure for silicon based optoelectronics. Surf. Sci. Rep. 38: 1-126

34 Stewart MP and Buriak JM 2000 Chemical and biological applications of porous silicon technology. Adv. Mater. 12, 859-869

35 Feng B, Weng J, Yang BC, Qu SX, and Zhang XD 2003 Characterization of surface oxide films on titanium and adhesion of osteoblast. Biomaterials. 24(25): 4663-4670.

36 Ziebart T, Schnell A, Walter C, Kämmerer PW, Pabst A, Lehmann KM, Ziebart J, Klein MO, Al-Nawas B 2012 Interactions between endothelial progenitor cells (EPC) and titanium implant surfaces. Clin. Oral. Investig. 1-9.

37 de Mel A., Jell G, Stevens MM, and Seifalian AM 2008. Biofunctionalization of biomaterials for accelerated in situ endothelialization: a review. Biomacromolecules, 9(11): 2969-2979.

38 Keller JC, Stanford CM, Wightman JP, Draughn RA, and Zaharias R 2004 Characterizations of titanium implant surfaces. III. Journal of biomedical materials research, 28(8): 939-946.

39 Fiorillo AS 2012 Deposition of zeolite thin layers onto silicon wafers for biomedical use. Nanotechnology, IEEE Trans. Nanotech. 11(4): 654-656.

40 Westerhoff HV, Malkhey V, Frank JB, Alexey K, Maciej S, Neil H, Maria N, Barbara MB, and Jacky LS. 2011 From silicon cell to silicon human. BetaSys 437-458.

41 Dvir T, Timko BP, Kohane DS, and Langer R 2010 Nanotechnological strategies for engineering complex tissues. Nature nanotechnology 6(1): 13-22.

42 Kaji H, Camci-Unal G, Langer R and Khademhosseini A 2011 Engineering systems for the generation of patterned co-cultures for controlling cell–cell interactions. Biochimica et Biophysica Acta (BBA)-General Subjects. 1810(3):239-250.

43 Martinez AW and Chaikof EL 2011 Microfabrication and nanotechnology in stent design. WIREs Nanomedicine and Nanobiotechnology 3:256-268

44 Parker ER, Thibeault BJ, Aimi MF, Rao MP, MacDonald NC 2005 Inductively coupled plasma etching of bulk Ti for MEMS applications. J Electrochem Soc. 152(10):675-83

45 Mohan CC, Sreerekha PR, Divyarani VV, Nair S, Chennazhi K and Menon D 2012 Influence of titania nanotopography on human vascular cell functionality and its proliferation in vitro. J Mat. Chem. 22:1326-1340

46 Palmaz JC, Benson A, Sprague EA. 1999 Influence of surface topography on endothelialization of intravascular metallic material. J Vasc Interv Radiol 10:439–444

47 Lu J, Rao MP, MacDonald NC, Khang D, Webster TJ. 2008 Improved endothelial cell adhesion and proliferation on patterned titanium surfaces with rationally designed, micrometer to nanometer features. Acta Biomater 4(1):192-201

48 Choudhary S, Haberstroh KM, Webster TJ. 2007 Enhanced functions of vascular cells on nanostructured Ti for improved stent applications. Tissue Eng. 13:1421–1430

49 Fine E, Zhang L, Fenniri H, Webster TJ 2009 Enhanced endothelial cell functions on rosette nanotube-coated titanium vascular stents International Journal of Nanomedicine.4 91–97

50 Kipshidze N, Dangas G, Tsapenko M, Moses J, Leon MB, Kutryk M, and Serruys P. 2004 Role of the endothelium in modulating neointimal formation. J Am Coll Cardiol 44:733-739

51 RS Kane, S Takayama, E Ostuni, DE Ingber, GM Whitesides 1999 Patterning proteins and cells using soft lithography. Biomaterials. 20(23-24): 2363-2376

52 CS Chen, M Mrksich, S Huang, GM Whitesides, DE Ingber 2008 Micropatterned surfaces for control of cell shape, position, and function. Biotechnology Progesss. 14(3): 356-363

53 Schneider CA, Rasband WS, and Eliceiri KW 2012 NIH Image to ImageJ: 25 years of image analysis. Nature Methods 9:671-675

54 Orloff J, Utlaut M, Swanson L 2002 High resolution focused ion beams: FIB and its applications. Kluwer Academic, Dordrecht

CHAPTER 6

COMPARITIVE ENDOTHELIAL CELL GROWTH, MIGRATION, AND EXTRACELLULAR MATRIX SYNTHESIS ON MICRO-PATTERNED AND NANO-PATTERNED TITANIUM

ABSTRACT

In this work, we patterned titanium (Ti) surfaces with periodic arrays of grooves and spacings ranging from 50 μm to 500 nm. We explore the effect of nano-patterned Ti on the yield of endothelial cells in an effort to restore vascular endothelium. Our results demonstrate the superior response of endothelial cells cultured on nanopatterned Ti with smaller groove sizes. More specifically, we compare the growth, migration, and extracellular matrix sunthesis, and growth arrest of endothelial cells seeded on 500 nm, 0.75 μm, 50 μm Ti surface patterns, and unpatterned Ti. We observe that the cells intuitively migrate from substrates with the smallest nanopatterned groves (500 nm). Considering the enhanced endothelial extracellular matrix synthesis and migration, composed of elongated vascular endothelial cells aligned with the direction of blood flow, it has been speculated that rationally designed, nanopatterned Ti surface features could further enhance endothelial cell functions by promoting a more native cellular morphology.

Keywords: stents; endothelium; titanium

6.2 INTRODUCTION

Neovascularization defined as the formation of nascent blood vessels plays a critical role in tissue growth and homeostasis, as well as in the pathogenesis of many diseases such as cancer, diabetic retinopathy, and rheumatoid arthritis [1]. Inhibition and liberation of neovascularization can be utilized to either prevent the growth of tumors in pathological conditions or accelerate the formation of tissue in wound healing respectively [2-3]. The goal of using biomaterials is to obtain the desired neovascularization with minimal or no side effects.

While neovascularization is the development of novice circulation as a response to multiple biomolecules, the endothelial cell responses to these factors that dictate the cell state (growth-differentiation-death-senescence). The cell cycle control, an important extension of the routine proliferation, is crucial for studying developmental and tumor biology [4-6].The mechanism by which ECM exerts this control remains controversial.

6.2.1 Cell cycle control

Cell-cycle control is intimately associated with differentiated cell function and many current biocompatibility tests for biomaterials involve some kind of determination of cell numbers [19–21]. Cell numbers themselves result from the balance between cell proliferation and cell death; i.e., they are dependent on cell cycle control. The study of cell-cycle control is an important extension of routine proliferation assays and has extensive roots in developmental and tumor biology. Control of the cell cycle involves decision making about the fate of damaged cells. An increasing number of tumor-

suppressor genes and oncogenes have been identified, the expression of which is somehow directly or indirectly associated with cell-cycle control [22-23]. One prominent example of a directly involved gene product is p53 [24-25]. Overexpression as well as mutations in this gene is associated with a substantial fraction of a large number of human cancers, indicating its crucial role in physiological control mechanisms [26-28].

6.2.2 Extracellular matrix

Previous *in vitro* studies have established that varying the density of ECM molecules such as fibronectin immobilized on dishes can switch endothelial cells between growth and differentiation in the presence of soluble plasma biomolecules. This switch appears to be regulated through the changes in cell spreading that directly result from varying the density of immobilized ECM molecules [8-9]. Changes in ECM density also influence the efficiency of binding and activation of cell surface integrin receptors which can trigger intracellular signaling pathways [10-13] and alter gene expression [9] required for growth. Thus, it is unclear whether the switch between cellular programs is caused by the change in cell geometry or a change in ECM-integrin receptor binding,

Even though ECM is known to play a key role in angiogenesis regulation, the underlying mechanism by which ECM exerts this effect remains unclear. Integrin receptor binding has been shown to stimulate chemical signaling events involved in this process [14-16]. Other studies have suggested that mechanical determinants, such as cytoskeletal tension-dependent changes in cell shape, also play a role in dictating between growth and differentiation during angiogenesis [13,15-16].

The cell integrates information from both the extracellular matrix and growth factor receptors to regulate cell migration through signaling intermediates [21]. The size of cellular extensions determines the number of adhesions between the cell and ECM molecules, thereby increasing the degree of signaling initiated by the ECM to the cell. Additionally, protrusive forces mediate migration by propelling a cell forward, are regulated depending on the degree of cell extension or retraction in the local microenvironment.

6.2.3 Cell-substrate contact points

The initial contact between a cell and the ECM is mediated by the adhesion of the cell to the extracellular matrix via integrin receptors present on the cell surface [30]. Integrin ligand binding is followed by the extension of pseudopodia from the cell body. As the cell begins to flatten against the substrate, it forms additional bonds with the ECM, rearranging its cytoskeleton to form actin bundles and focal adhesions [31]. To spread, a cell must exert force against its membrane and its substrate to allow for pseudopodial extension and the stabilization of nascent contacts. The resultant net force is a balance between the extensional and contractile forces exerted by the cytoskeletal machinery [29]. This balance of forces and the resultant degree of spreading, in part, controls cell physiology.

6.2.4 Micropatterned surfaces

Recent work with micropatterned surfaces demonstrated that cell shape--the degree to which an endothelial cell extends and flattens--is a key determinant of whether a cell enters the growth cycle or undergoes apoptosis [(2,12].

In the present study, we engineered nano-scale and micro-scale titanium substrates composed of different pattern sized islands. We are interested in seeing if the high density of grooves promotes optimal iutegrin clustering. We observed that the size and shape of the grooves controlled the degree to which the cells spread. We also demonstrate that the endothelial cells can be switched between growth, differentiation, and final apoptosis. Our results demonstrate that the mechanical interactions between endothelial cells and extracellular matrices govern the formation of neovascularization.

6.3 MATERIALS AND METHODS

6.3.1 Endothelial cell culture

EA926 cells are obtained from ATCC (Manassas, VA). Cells are cultured using Dulbecco's modified Eagle's medium (DMEM, Lonza Inc.) and are supplemented with 10% FBS (Gibco Inc.) and antibiotics (Primocin, Invivogen Inc.). Freshly passaged cells are grown on Ti coupons. The cell-cultured nano-grooved Ti substrates will be maintained in humidified 95% air-5% CO_2 incubator at 37°C.

6.3.2 Immunostaining

Ti samples seeded with EA926 cells will be washed with PBS three times for five minutes each. The Vybrant Apoptosis Assay Kit #4 detects apoptosis on the basis of changes that occur in the permeability of cell membranes. This kit contains ready-to-use solutions of both YO-PRO-1 and propidium iodide nucleic acid stains. YO-PRO-1 stain selectively passes through the plasma membranes of apoptotic cells and labels them with moderate green fluorescence. Necrotic cells are stained red-fluorescent with propidium iodide.

6.3.3 Confocal imaging

EA926 cells seeded on the Ti surfaces were examined for all the indicated times and imaged using Leica M125 (Buffalo Groove, IL, USA) fully apochromatic corrected stereomicroscope with 12.5:1 zoom. Fluorescent images and transmitted images with

10X objective lens, binning of 4 x 4, gain of 8.0, and brightness of 1.2 were acquired. The seeded endothelial cells on the Ti surfaces are examined for all the indicated times and imaged using Leica SP2 (Buffalo Groove, IL, USA) Confocal microscope is used to image the cells for the Adhesion experiments. Spot Imaging Software® (Sterling Heights, MI, USA) and ImageJ® 1.46 (NIH, Bethesda, USA) is used to acquire and process the images.

6.3.4 Scanning electron microscope

SEM imaging of EA926 cells on the patterned substrates was performed. Prior to imaging, cells were fixed with 4% glutaraldehyde and post fixed with 0.5% OsO_4 for 1 h each, dehydrated through a graded series of alcohol, and dried in a critical point dryer (Balzer CPD 030, Liechtenstein).

6.4 RESULTS AND DISCUSSION

6.4.1 Extracellular matrix synthesis

After 1 day culture of endothelial cells on titanium (see Figure 6.1 and Figure 6.2), a strong synthesis of extracellular matrix was observed by endothelial cells on 0.5 μm Ti substrates. Conversely, on unpatterned, 50 μm, and 0.75 μm grooved substrates, the development of extracellular matrices was not observed to that extent. Cells seeded on 0.75 μm grooves formed cell-cell contacts but remained flattened on the culture substrate and did not readily differentiate. Even though the micropatterned surfaces described here have identical chemistry and the cells were cultured in the same serum (growth factors) containing medium; the variation of the cellular behavior can be solely attributed to the mechanical structural aspects of different nano-scale and micro-scale grooves.

In Chapter 5, we observed that the cells proliferated and aligned to a better extent on the 0.5 μm patterned Ti surfaces. In this Chapter, we observe that the cells on 0.5 μm Ti surfaces synthesize a denser extracellular matrix. The ECM produced and released by the endothelial cells can be directly correlated to the observed behavior of the endothelial cells on Ti surfaces with 0.5 μm groove sizes. Simultaneously, linear ECM tendrils accumulated underneath and between the cells; this decreased the area of cell substrate adhesion and promoted formation of continuous monolayer.

A

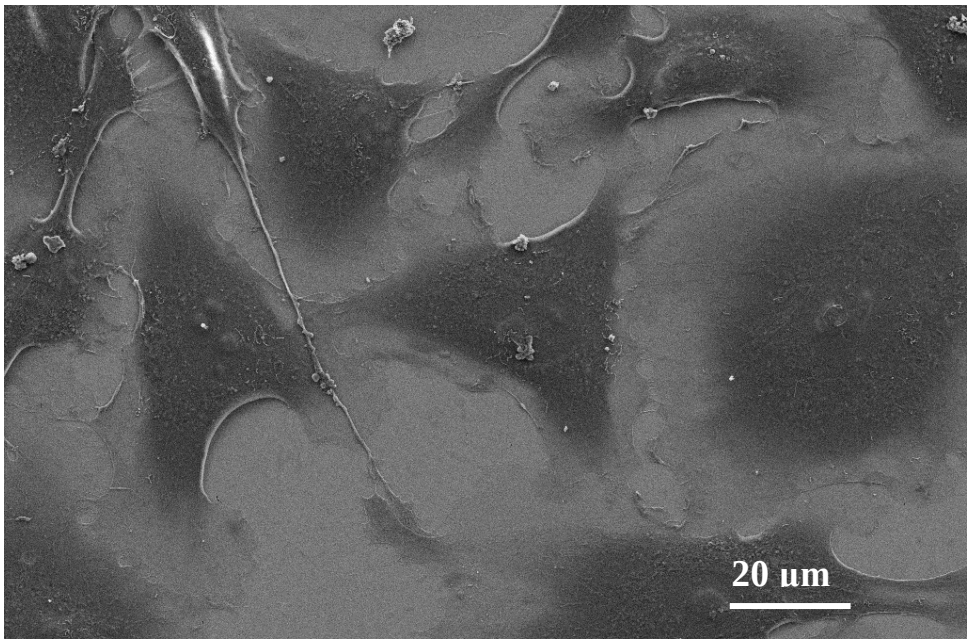

B

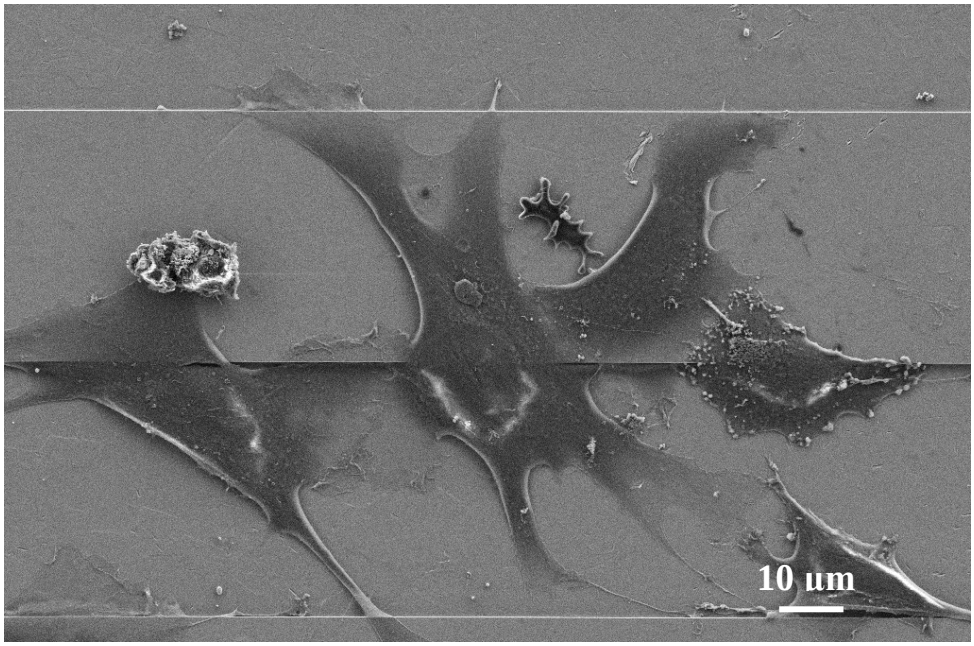

Figure 6.1| Scanning electron micrographs of Ti grooves showing a minimal synthesis of extracellular matrices for (A) unpatterned Ti material and (B) 50 μm Ti material for two days.

A

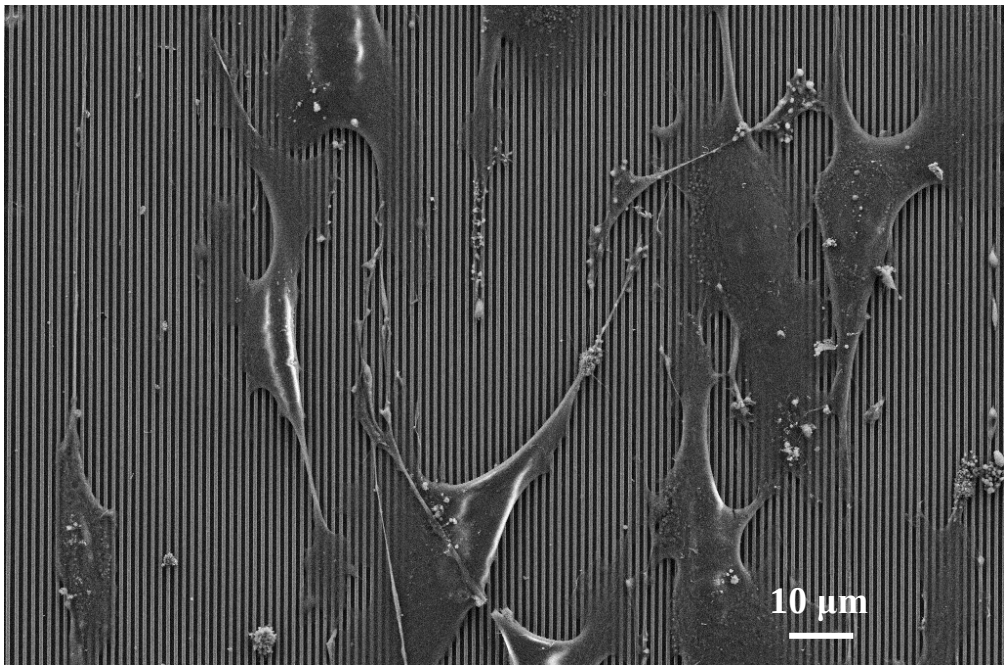

B

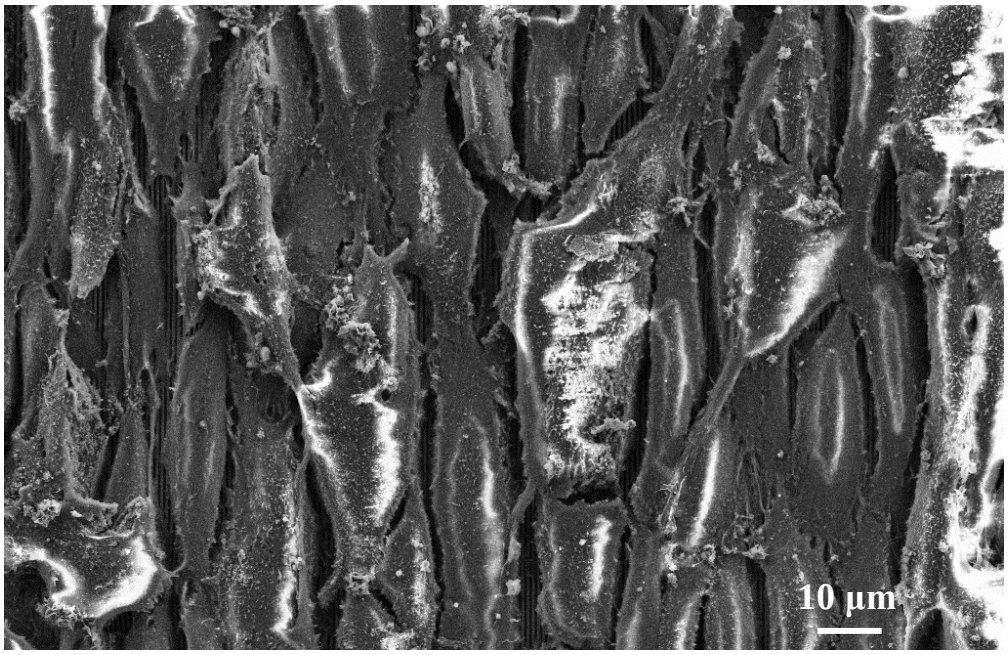

Figure 6.2| Scanning electron micrographs of Ti grooves showing a minimal synthesis of extracellular matrices on (A) 0.75µm grooved and (B) 0.5 µm grooved Ti material for two days.

6.4.2 Quantifying cell growth

Apoptosis is a carefully regulated process of cell death that occurs as a normal part of development. Inappropriately regulated apoptosis is implicated in disease states, such as Alzheimer's disease and cancer. Apoptosis is distinguished from necrosis, or accidental cell death, by characteristic morphological and biochemical changes, including compaction and fragmentation of the nuclear chromatin, shrinkage of the cytoplasm and loss of membrane asymmetry.

Furthermore, during apoptosis the cytoplasmic membrane becomes slightly permeant. Certain dyes, such as the green fluorescent YO-PRO®-1 dye can enter apoptotic cells, whereas other dyes, such as the red fluorescent dye, Propidium iodide (PI), cannot. Thus, use of YO-PRO®-1 dye and PI together provide a sensitive indicator for apoptosis.

As shown in Figures 6.3- 6.6, endothelial cells proliferate (higher extent on 0.5 μm substrates) on all the grooved substrates. We observe apoptosis to a higher extent on the substrates with no grooves and 0.75 μm grooved Ti substrates.

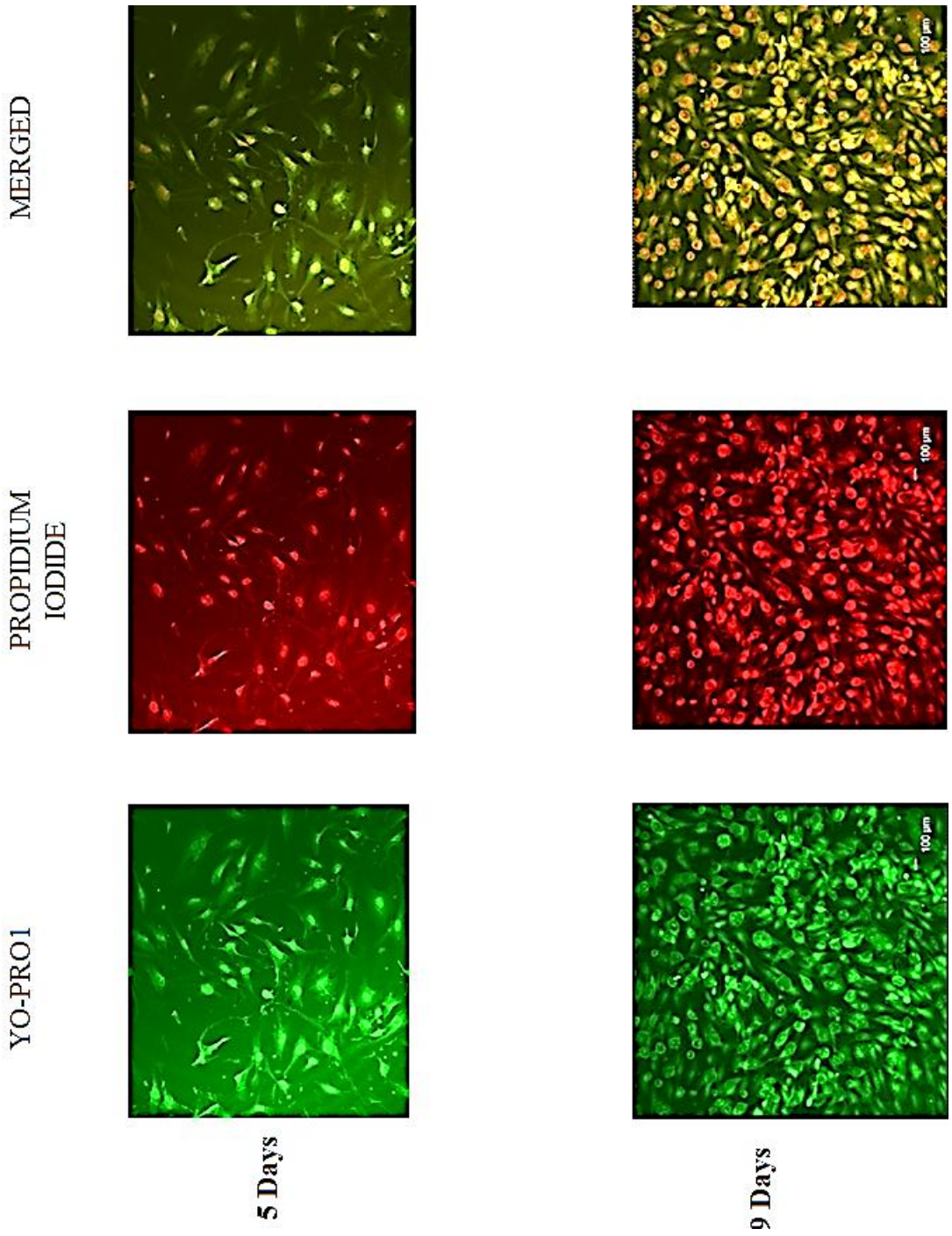

Figure 6.3| Endothelial cells are stained with YoPro-1 and Propidium Iodide and the cell seeded Ti substrate was imaged for unpatterned substrate.

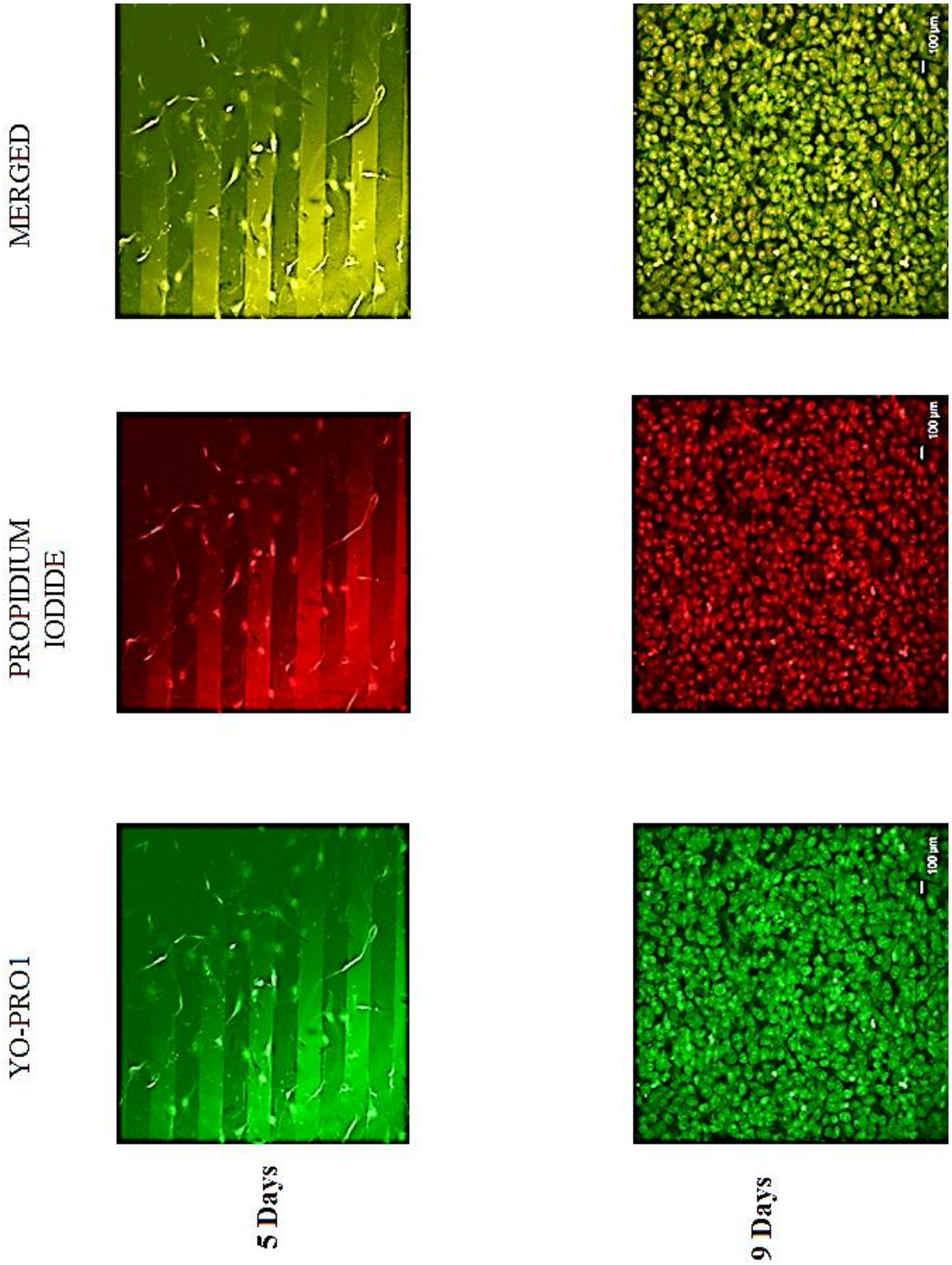

Figure 6.4| Endothelial cells are stained with YoPro-1 and Propidium Iodide and the cell seeded Ti substrate was imaged for 50 µm grooved surface.

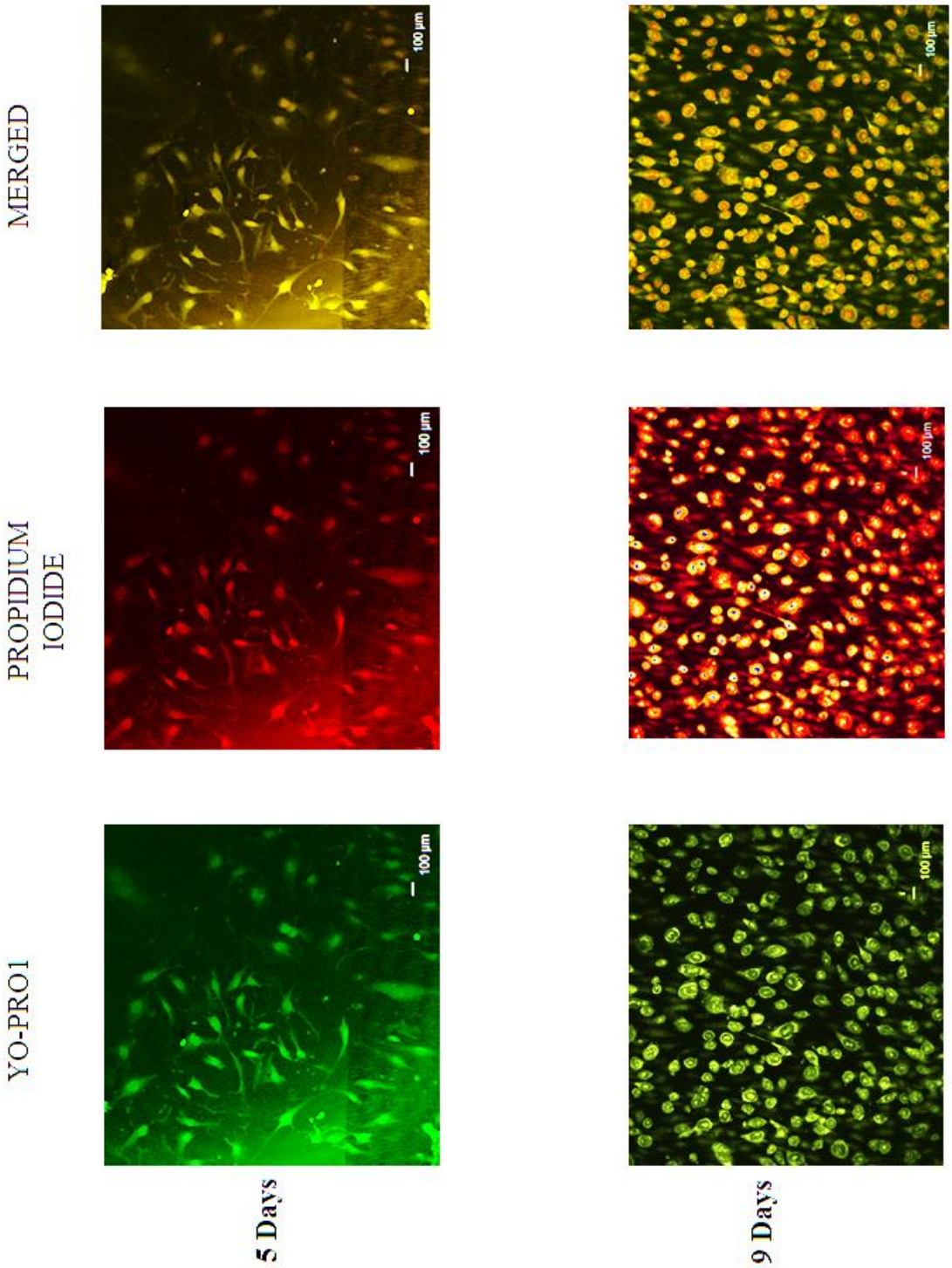

Figure 6.5| Endothelial cells are stained with YoPro-1 and Propidium Iodide and the cell seeded Ti substrate was imaged for 0.75 µm grooved surface.

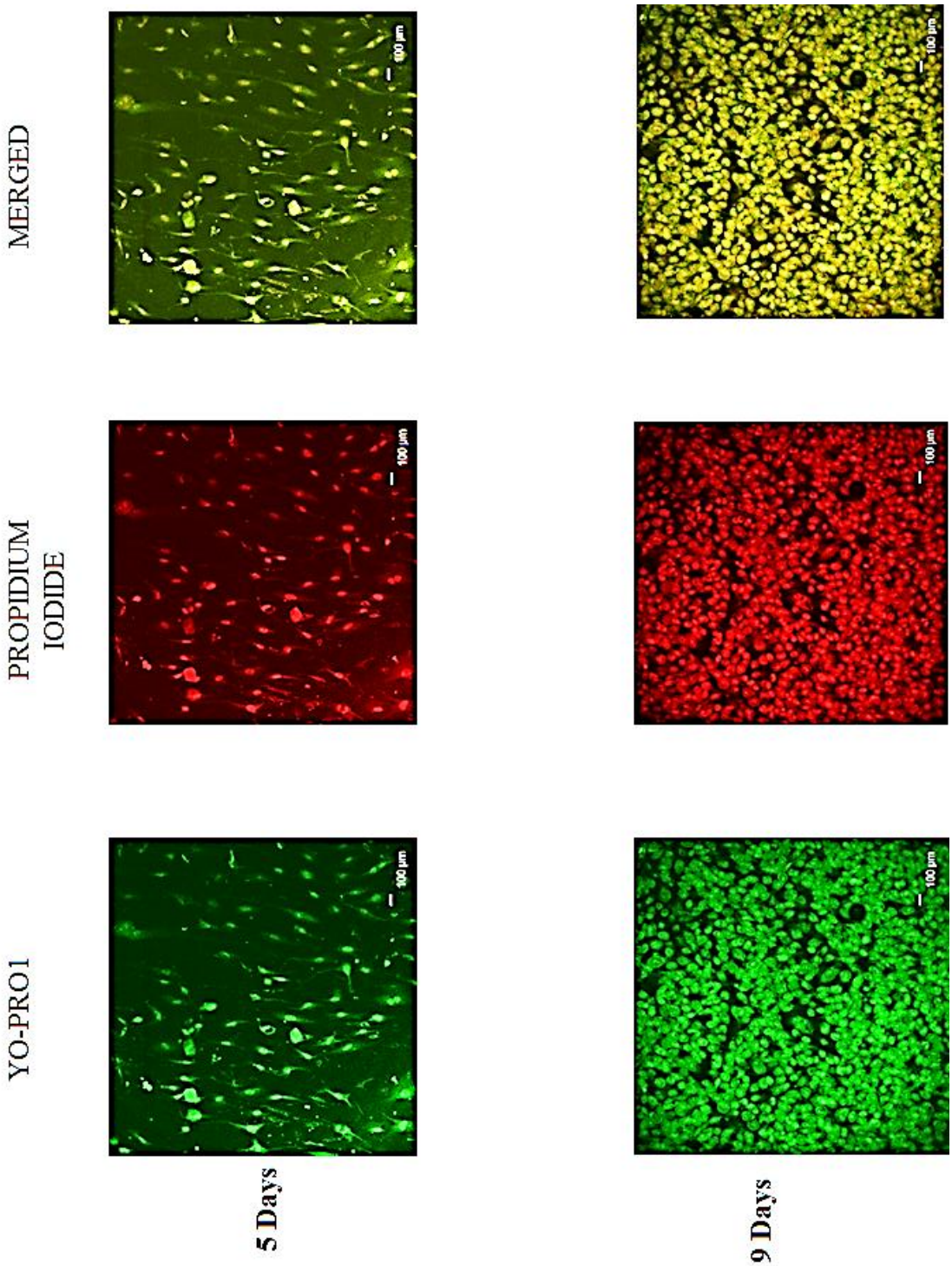

Figure 6.6| Endothelial cells are stained with YoPro-1 and Propidium Iodide and the cell seeded Ti substrate was imaged for 0.75 μm grooved surface.

6.4.3 Detecting migration of cells

As shown in Figure 6.7, we observe a high density of endothelial cells at the 0.5 μm groove Ti substrates compared to the 50 um grooved substrates. When we looked closer, we observed that a protrusion (identified as pseudopodia) is made at the leading edge. At the trailing edge of the cells, we observe reminiscent of the developed pseudopodia (shown in Figure 6.8). These events are the initial events of the migratory cycle. To migrate, cells must establish dynamic and highly regulated adhesive interactions with the extracellular matrix. Similar endothelial cell behavior can be observed in unpatterned structures (Figure 6.9). In Figure 6.8, we observe a greater extent of migration of the endothelial cells in 0.75 μm grooved size substrates. The summary of the above events is shown in Figure 6.10 where we observe cells migrating towards the 50 μm substrates and unpatterned substrates from 0.5 μm grooved substrates.

The concentration of the extracellular matrix molecule on the substrate and the concentration of the growth factor in solution regulate the migratory responses of endothelial cells. Cells coordinate the formation of lamellipodia at the leading edge and retraction at the trailing edge to move forward. Lack of rear release decreases cell migration. The balance of extensional and contractile forces that mediate processes such as cell migration and ECM remodeling are thought to also control the dynamic changes in cell spreading that occur when an initially spherical cell flattens against a surface; thus, an examination of cell spreading should inform us about the basic mechanisms of cell-substrate interactions.

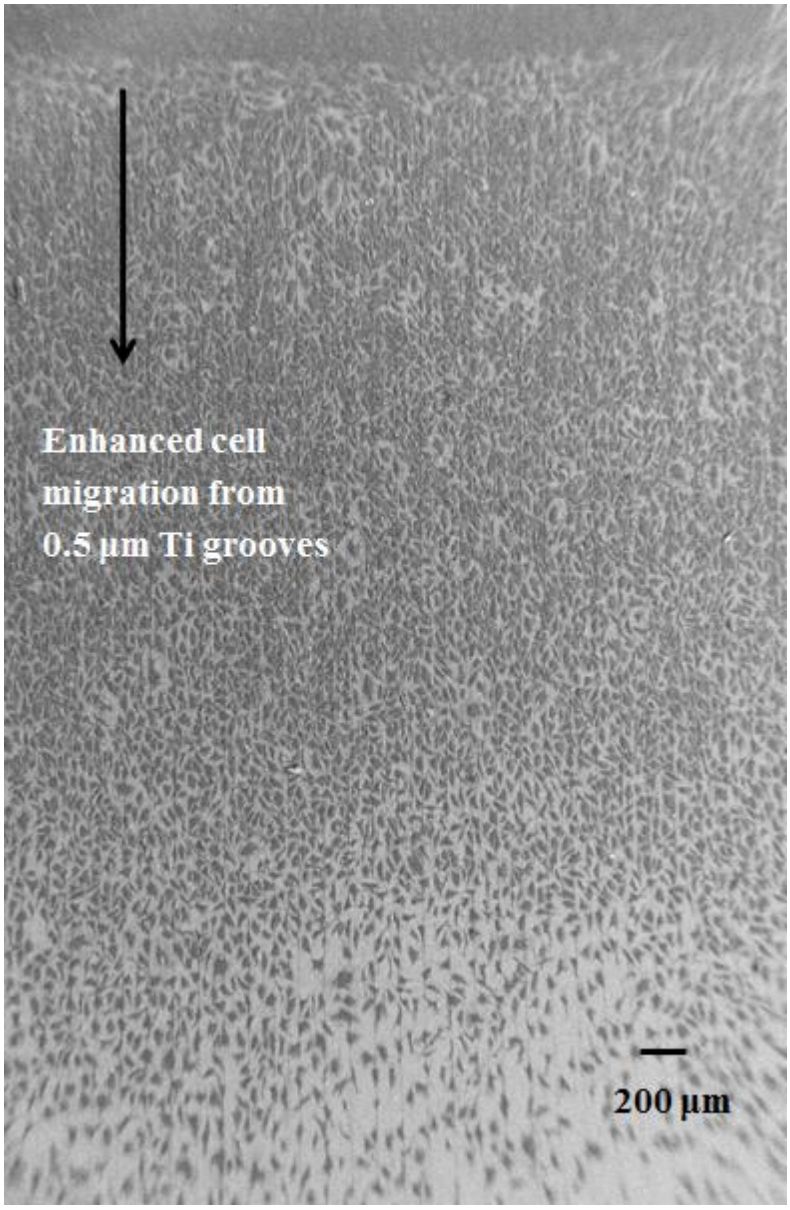

Figure 6.7| Scanning electron micrographs of a 50 µm Ti grooves depicting the migration of endothelial cells towards 0.5 µm grooves.

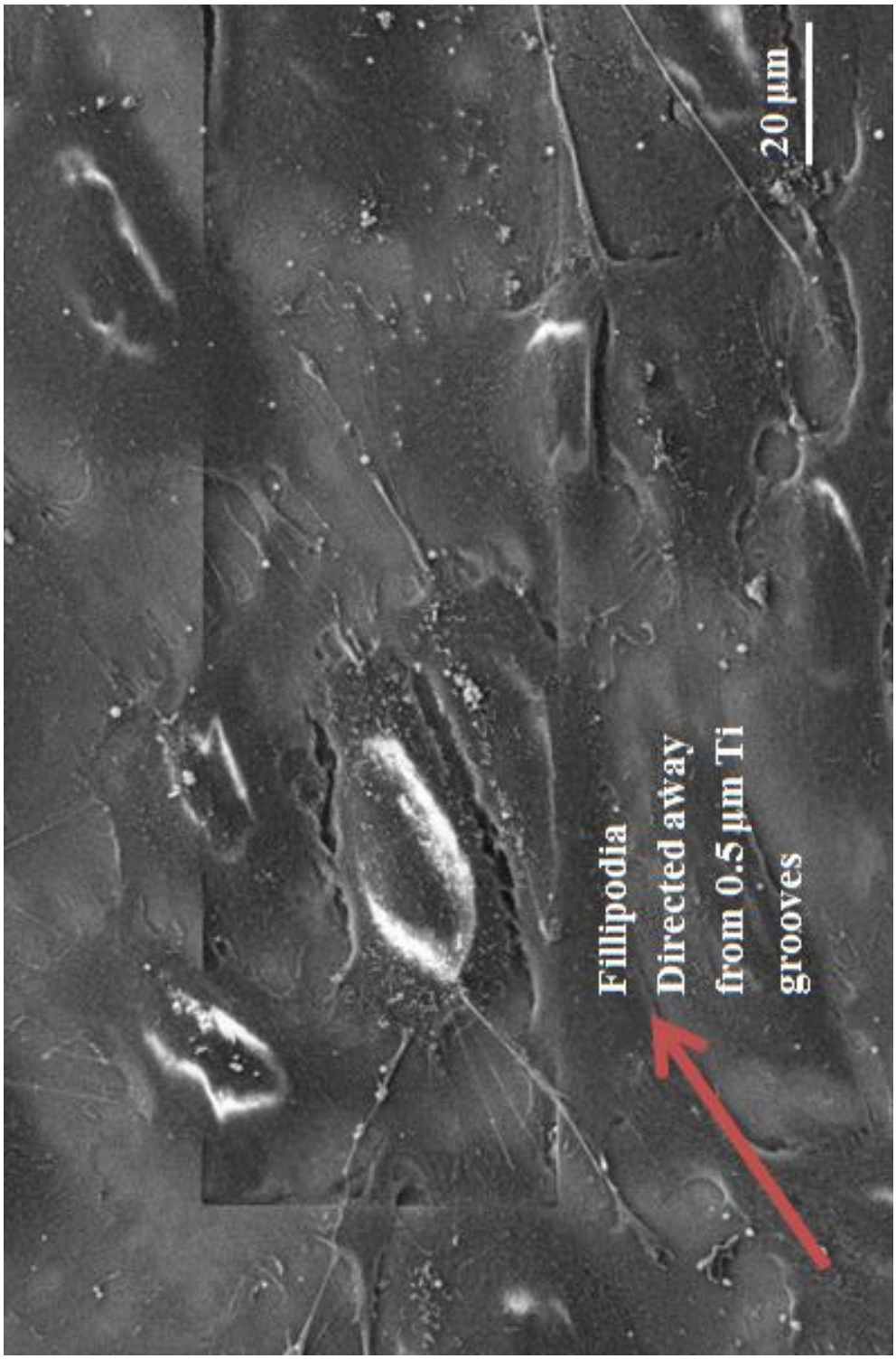

Figure 6.8| Scanning electron micrographs of a 50 µm Ti grooves depicting the migration of endothelial cells towards 0.5 µm grooves.

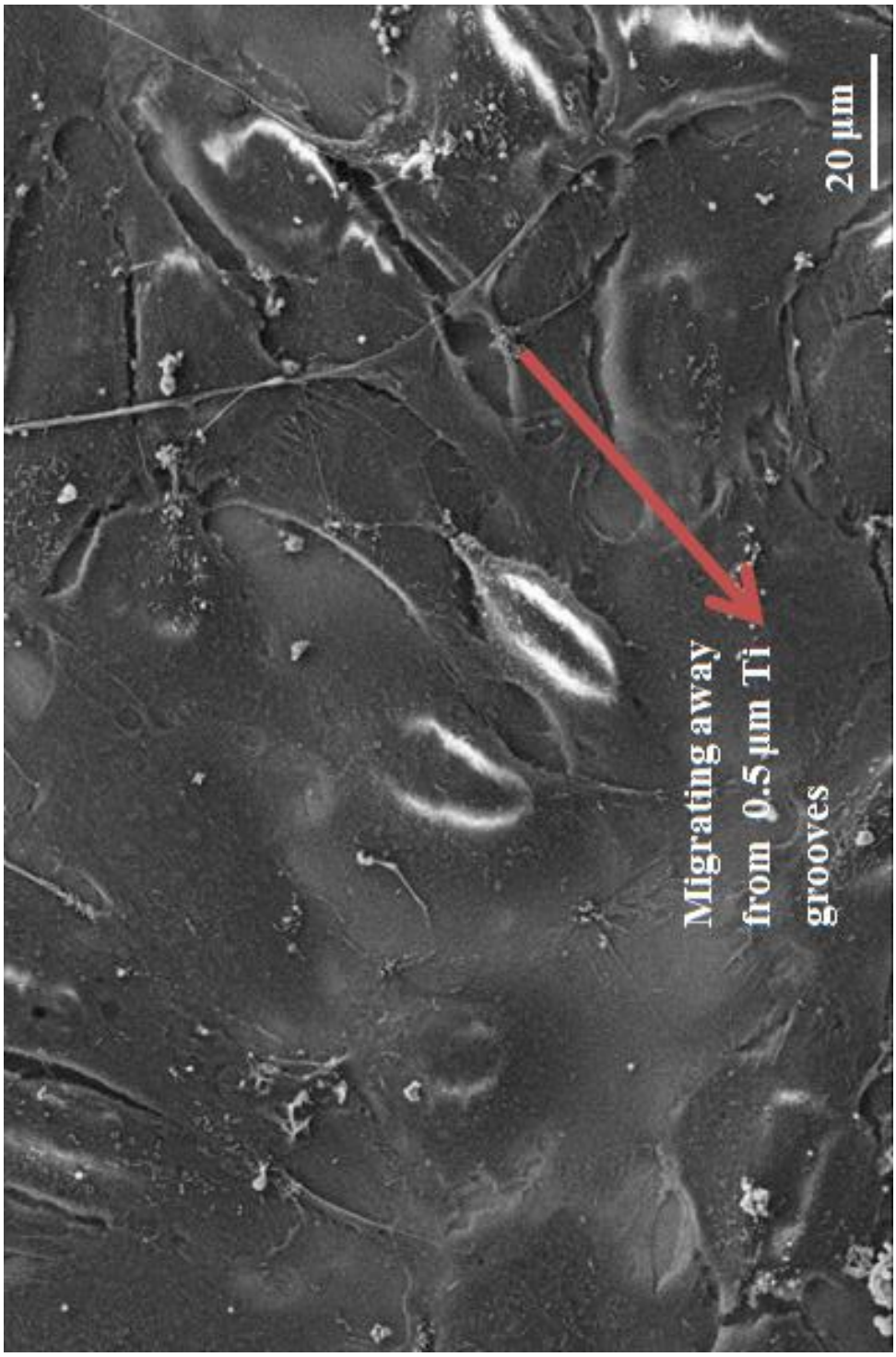

Figure 6.9| Scanning electron micrographs of unpatterned Ti material depicting the migration of endothelial cells towards 0.5 µm grooves.

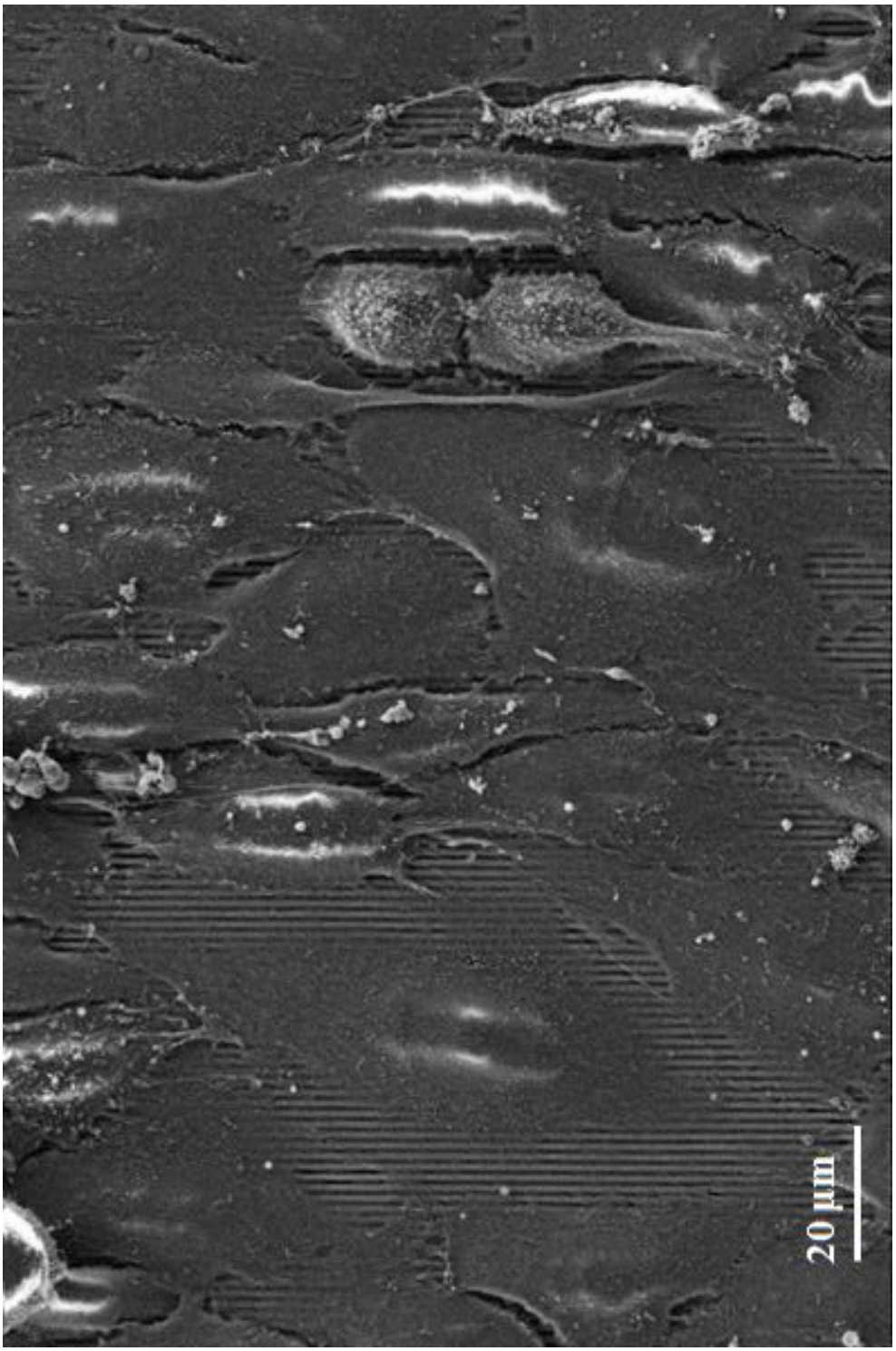

Figure 6.10| Scanning electron micrographs of unpatterned Ti material depicting the migration of endothelial cells towards 0.5 µm grooves.

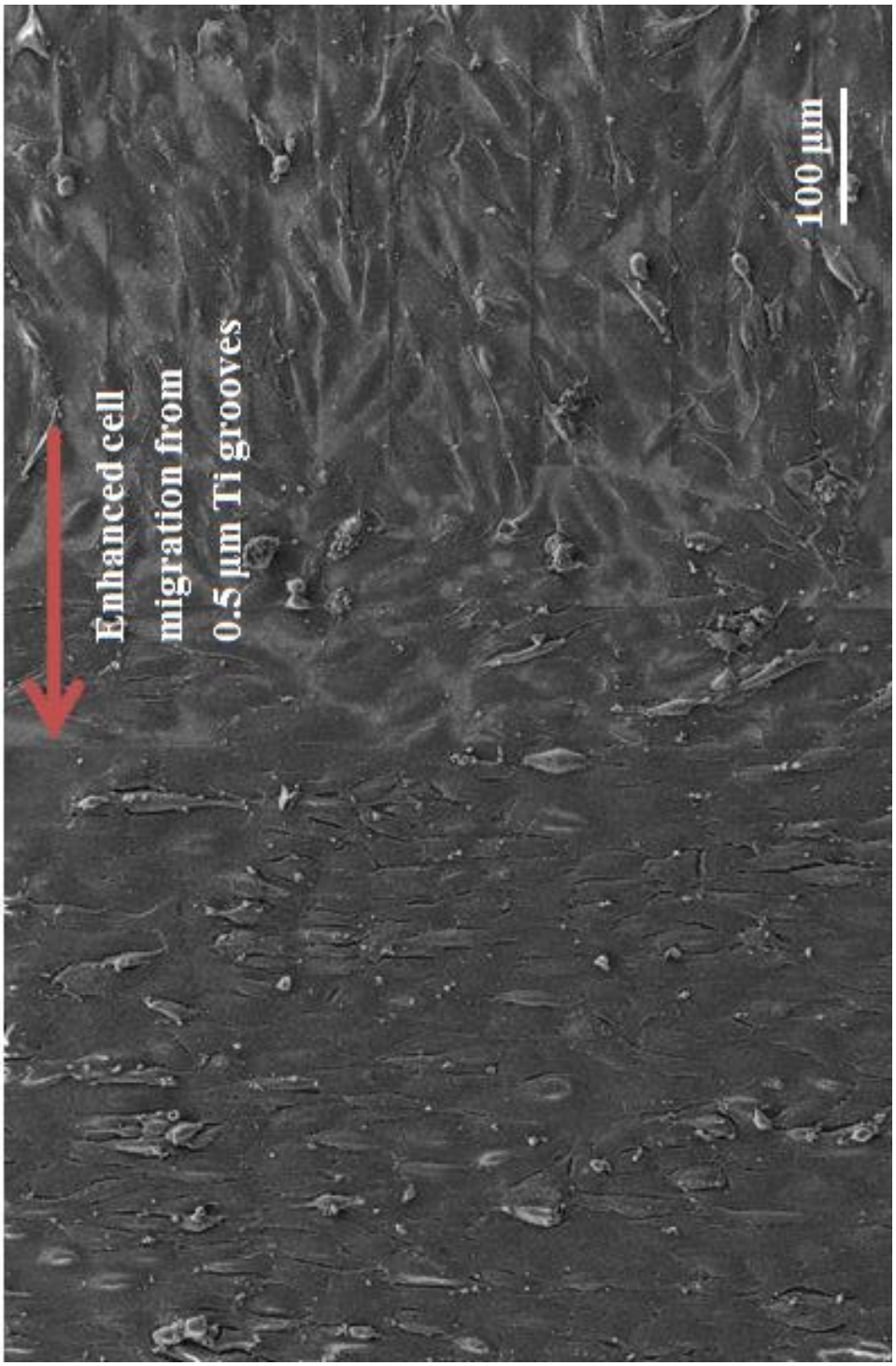

Figure 6.11| Scanning electron micrographs of Ti grooves depicting the migration of endothelial cells towards 0.5 μm grooves.

6.4.4 Capturing cells in growth arrest

The culture of endothelial cells differed only in a single parameter: the geometric difference in the width of the grooves. However, growth and apoptosis in cells cultured on these substrates revealed that endothelial differentiation occurs at a moderate degree of cell spreading that neither supports DNA synthesis nor apoptosis as shown in Figure 6.11 (A-B) and Figure 6.12(A-B) – and hence, entering a subsequent growth arrest. The endothelial cells were cultured for a period of 12 days.

This observation suggests that a common pathway may exist that regulates these major gene cascades, rather than a model in which each program is independently regulated. Such a mechanism would ensure concomitant switching between different cell fates while preventing mitosis or apoptosis from being initiated simultaneously.

Patterns composed of 50 μm grooves moderately restricted the extent of cell spreading such that neither growth nor apoptosis was induced. At the same time, the 0.5 μm and 0.75 μm grooves promoted mutti-cellular interactions enabling cell-cell signaling and linear junctional seals along the formed monolayer.

A

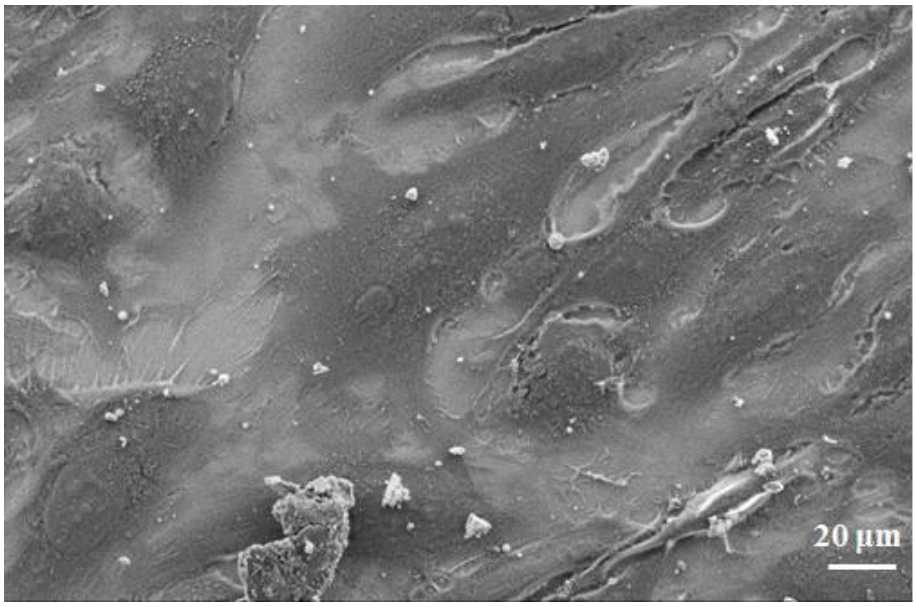

B

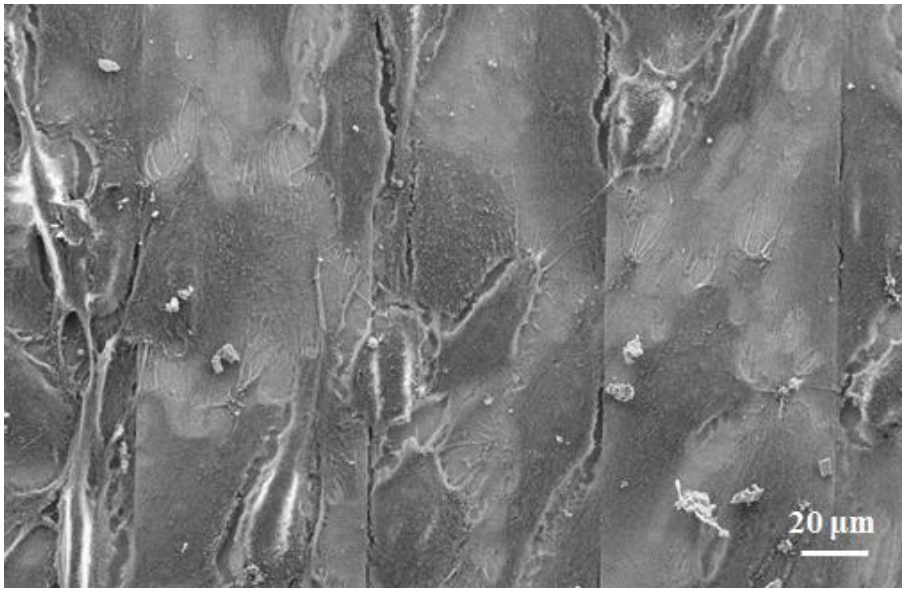

Figure 6.12| Scanning electron micrographs of Ti grooves showing a minimal synthesis of extracellular matrices on 0.75µm grooved Ti material for 12 days.

A

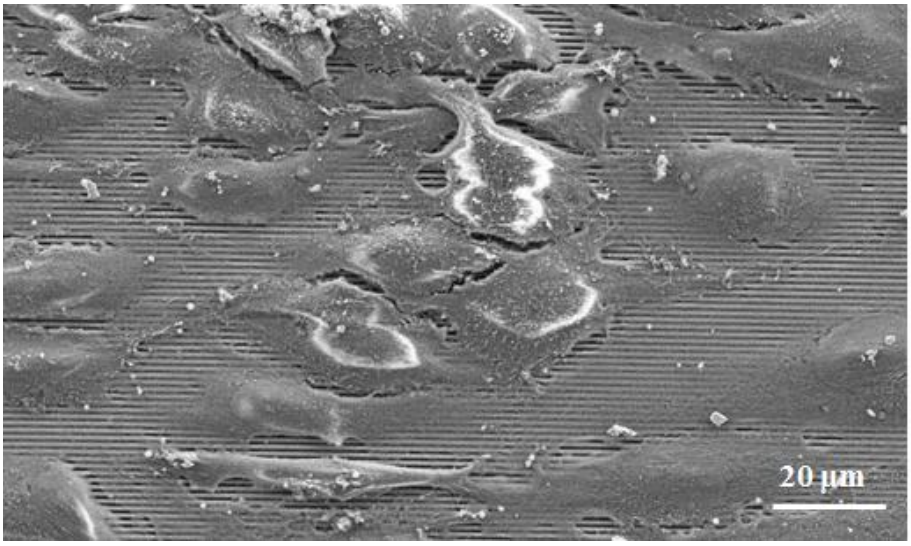

B

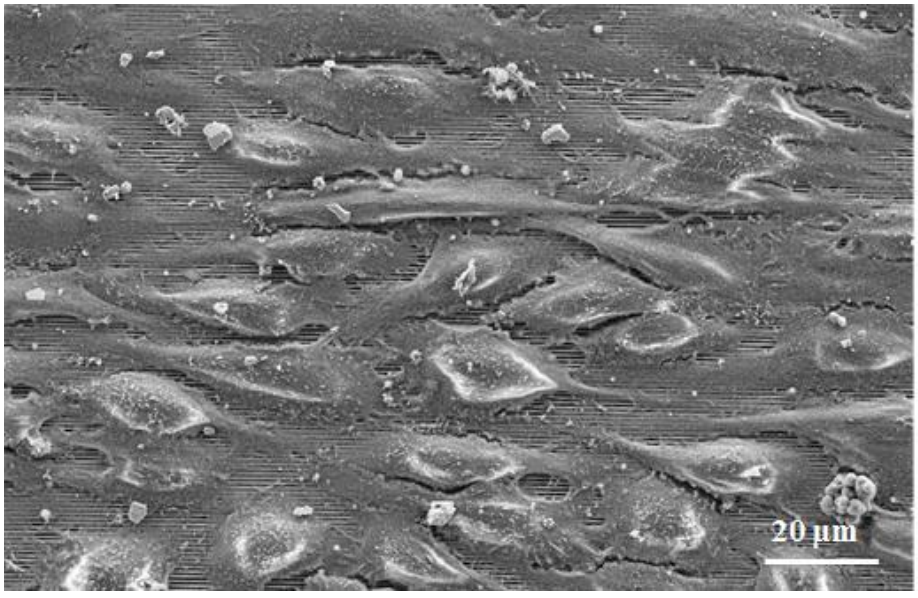

Figure 6.13| Scanning electron micrographs of Ti grooves showing a minimal synthesis of extracellular matrices on 0.75µm grooved Ti material for 12 days.

6.5 CONCLUSION

Biomaterials promoting neovascularization play an important role in the delivery of cells to the sites of trauma, wound healing, and inflammation. In these areas, chemotaxis, cell adhesion, and extravasation play key roles, involving different cell types with a plethora of released chemical mediators. In this chapter, we took into account other regulatory parameters – extracellular matrix synthesis, cell growth, and cell sensesence to evaluate the interaction of endothelial cells on the Ti substrates. In summary, our results demonstrate that the endothelial extracellular matrix synthesis promotes the triggering of the cells between growth, differentiation, and apoptosis. These extracellular matrices synthesized by the cells are in turn governed by the presence of geometric topographies eliciting different signaling cascades and downstream gene transcription, even in the presence of the same set of chemical signals (e.g., growth factors, integrin binding). Our results demonstrate that this central mechanism of cellular control is regulated by changes in the subendothelial microenvironment. The mechanism by which cell shape regulates these genetic programs has yet to be elucidated. The integrity of the cytoskeleton and its ability to generate tension against the resisting Ti substrate through integrin-ECM interaction has to be further studied. It will also be interesting to capture the signaling specific to these cell fates (namely, growth: vascular endothelial growth factor; apoptosis: p53; and cell cycling: CDK-cyclin).

6.6 REFERENCES

1. Folkman J (1971) Tumor angiogenesis: therapeutic implications. N. Engl. J. Med. 285:1182.

2. O'Reilly MS, Holmgren L, Shing Y, Chen C, Rosenthal RA, Moses M, Lane WS, Cao Y, Sage EH, Folkman J (1994) Angiostatin: a novel angiogenesis inhibitor that mediates the suppression of metastasis by a Lewis lung carcinoma. Cell 79:315-328; 1994.

3. O'Reilly MS, Holmgren L, Chen C, Folkman J (1996) Angiostatin induces and sustains dormancy of human primary tumors in mice. Nat. Med. 2:689-692.

4. Folkman J, Klagsburn M (1987) Angiogenic factors. Science. (Wash DC) 235:442-447; 1987.

5. lngber DE, Dike LE, Hansen L, Karp, S., et al. (1994) Cellular tensegrity: exploring how mechanical changes in the cytoskeleton regulate cell growth, migration, and tissue pattern during morphogenesis. Int. Rev. Cytol. 150:173-220.

6. Ingber DE and Folkman J (1989) How does extraeellular matrix control capillary morphogenesis? Cell 58:803-805.

7. lngber DE (1990) Fibronectin controls capillary endothelial cell growth by modulating cell shape. Proc. Natl. Acad. Sci. USA 87:3579-3583.

8. Ingber DE, Dike LE, Hansen L, Karp S., et al. (1994) Cellular tensegrity: exploring how mechanical changes in the cytoskeleton regulate cell growth, migration, and tissue pattern during morphogenesis. Int. Rev. Cytol. 150:173-220.

9. Ingber DE and Folkman J (1989) How does extraeellular matrix control capillary morphogenesis? Cell 58:803-805.

10. Ingber DE and Folkman J (1989) Meehanoehemical switching between growth and differentiation during fibroblast growth factor-stimulated angiogenesis in vitro: role of extraeellular matrix. J. Cell Biol. 109:317- 330.

11. McNamee HP, Ingber DE, Schwartz MA (1993) Adhesion to fibronectin stimulates inositol lipid synthesis and enhances PDGF-induced inositol lipid breakdown. J. Cell Biol. 121:673-678.

12. Ploppel GE, McNamee HP, Dike LE, Bojanowski C et al. (1995) Convergence of integrin and growth factor receptor signaling pathways within the focal adhesion complex. Mol. Biol. Cell 6:1349-1365.

13. Schwartz MA, Ingber DE, Lawrence M, Springer, TA., et al. (1991) Multiple integrins share the ability to induce elevation of intracellular pH. Exp. Cell Res. 195:533-535.

14. Schwartz MA, Lechene C, Ingber DE (1991) Insoluble fibronectin activates the Na/H antiporter by clustering and immobilizing integrinalpha 5 beta 1, independent of cell shape. Proc. Natl. Acad. Sci. USA. 88:7849-7853.

15. Schwartz MA, Schaller MD, Ginsberg MH (1995) Integrins: emerging paradigms of signal transduction. Annu. Rev. Cell Dev. Biol. 1t:549-599.

16. Sheibani N, Newman PJ, Frazier WA (1997) Thrombospondin-1, a natural inhibitor of angiogenesis, regulates platelebendothelial cell adhesion molecule-1 expression and endothelial cell morphogenesis. Mul. Biol. Cell 8:1329-1341; 1997.

17. Singhvi R, Kumar A, Lopez GP, Stephanopoulos GN., et al. (1994) Engineering cell shape and function. Science (Wash DC) 264:696-698.

18. Chen CS, Mrksich M, Huang S,Whitesides GM et al. (1997) Geometric control of cell life and death. Science (Wash DC) 276:1425-1428.

19. Chen CS, Mrksich M, Huang S.; Whitesides, G. M., et al. (1998) Micropatterned surfaces for control of cell shape, position and function. Biotechnol. Prog. 14:356-363.

20. Ciapetti G, Stea S, Cenni E, Sudanese A, Marraro D, Toni A, Pizzoferrato A (1994) Cytotoxicity testing of cyanoacrylates using direct contact assay on cell cultures. Biomaterials. 15:63–67.

21. Storck J, Ab Del RH, Zimmermann ER (1996) Effect of polyvinyl chloride plastic on the growth and physiology of human umbilical vein endothelial cells. Biomaterials 17:1791–1794.

22. Wilke A, Orth J, Lomb M, Fuhrmann R, Kienapfel H, Griss P, and Franke RP (1998) Biocompatibility analysis of different biomaterials in human bone marrow cell cultures. J Biomed Mater Res. 40:301–306.

23. Schafer KA (1998) The cell cycle: A review. Vet Pathol. 35:461–478.

24. Smith KJ, Barrett TL, Smith WF, and Skelton HM (1998) A review of tumor suppressor genes in cutaneous neoplasms with emphasis on cell cycle regulators. Am J Dermatopathol. 20:302–313.

25. Wynford-Thomas D (1997) Proliferative lifespan checkpoints: Cell type specificity and influence on tumour biology. Eur J Cancer 1997;33:716–726.

26. Prives C and Hall PA (1999) The p53 pathway. J Pathol.187:112–126.

27. Sauter ER, Cleveland D, Trock B, Ridge JA, and Klein-Szanto AJ (1994) p53 is overexpressed in fifty percent of pre-invasive lesions of head and neck epithelium. Carcinogenesis.15:2269–2274.

28. Brennan JA, Boyle JO, Koch WM, Goodman SN, Hruban RH, Eby YJ, Couch MJ, Forastiere AA, and Sidransky D (1995) Association between cigarette smoking and mutation of the p53 gene in squamous-cell carcinoma of the head and neck. N Engl J Med. 332:712–717.

29. Lauffenburger DA and Horwitz AF (1996) Cell migration: a physically integrated molecular process. Cell. 84:359–369.

30. Hynes RO (1987) Integrins: a family of cell surface receptors. Cell. 48:549–554.

31. Burridge K, Fath K, Kelly T, Nuckolls G, and Turner C (1988) Focal adhesions: transmembrane junctions between the extracellular matrix and the cytoskeleton. Annu. Rev. Cell Biol. 4:487–525.

CHAPTER 7

TRIGGERED SMART ENDOTHELIAL SIGNALING PATHWAYS IN RESPONSE TO NANOFABRICATED TITANIUM SUBSTRATES

ABSTRACT

One of the major problems of in-vivo metallic implants remains to be related to restenosis. Titanium (Ti) is a favorable biomaterial that can be used for neo-vascularization by as yet unknown mechanisms. This work aims to characterize the Ti substrates by studying their antithrombotic yet vasodilatory properties. In this work, we attempt to identify the activation of key biomolecules in the endothelial cells. We investigate eNOS, AMPK, VCAM-1, Von Willebrand factor, and KLF2 activation as a systemic response to varied nano-patterns on titanium in static conditions. We further study the competitiveness of endothelial cell alignment when cells are parallel and perpendicular to the direction of blood flow. These results demonstrated the growth of a healthy endothelial cell layer on Ti substrates with nano-patterns. When patterns were oriented in the parallel direction of flow, we observed favorable adhesion of cells and when patterns were oriented perpendicular to flow, we observed that cells unadhered from the surface and were washed away into the media. Calculating the critical shear force that causes the dislodging of cells from the substrate is an important factor to be considered when the substrates are deployed *in-vivo*. In conclusion, these benifical effects of using nano-patterned Ti substrates demonstrate their efficacy in sites of neo-vascularization.

Keywords – titanium, signaling, endothelium

7.2 INTRODUCTION

Often transplantable biomedical devices are placed in the vascular system which consists of endothelial and smooth muscle cells. It is well known that the subsequent cell signaling is intimately coupled to the presence of these devices. Signaling proteins such as eNOS, AMPK, VCAM-1, VE-Cadherin, von Willebrand factor, and KLF2 have been shown to be key players in maintaining vascular homeostasis [1-5]. Further, disease states are biomarked by varied expression of extracellular proteins. In addition, the altered composition of extracellular matrix (ECM) can lead to a dysfunctional endothelium [6-7].

Thus, prosthetic device features such as material composition or structure will significantly impact vascular cell signaling. Alterations in signaling will dramatically dictate the homeostasis of the local cellular environment which could adversely lead to severe device limitations such as restenosis. Conversely, understanding the signalling processes of cells in contact with engineered materials can be utilized to enhance system performance.

Titanium (Ti) has been used for many in-vivo transplantable applications, including but not limited to, vascular grafts, heart valves, hip and knee prostheses, percutaneous devices, stents, contact lenses, dental implants, chest walls, and catheters [8-13]. Recently micro-scale and nano-scale surface topography on titanium has been shown to exert profound influence on cell-substrate interaction [14]. Moreover, the monolithic nature of surface patterning may provide greater reliability than coatings-based approaches. Many studies have shown that precisely-defined, periodic surface topographies (i.e. nanopatterned surfaces) can exert stronger influence than randomly

structured surfaces with similar morphological length scales [15-17]. In addition, nanopatterned gratings can elicit desirable cellular responses (e.g. elongation and alignment), that are not possible with other periodic structures (e.g. arrays of pits or posts) [18-19]. It is conceivable that the mechanical properties and surface topography of these biomaterials play a key role for biocompatibility.

We demonstrate for the first time nanopatterning-enhanced endothelialization in materials of immediate relevance to prostheses. Our studies establish enhanced competitive endothelial proliferation over vascular smooth muscle cells on nanopatterned surfaces[20]. Further, we have shown that p-eNOS, a critical protein for vasodilatation, was significantly enhanced when cells, under physiological flow conditions, were seeded on 500 nm nanopattern grooved titanium. The endothelium is the inner most layer of the blood vessels [21].

It is a flat monolayer of cells that communicates with the dynamic mechanical stimuli such as shear stress and hydrostatic pressure, and chemical stimuli such as vasoactive factors in the blood [22-28]. In response to these stimuli, the endothelial cells trigger various gene responses via biochemical molecules that regulate vascular functions and hence modulate vascular homeostasis [29-31]. Vascular homeostasis is a synergistic effect that is defined by the orchestra of anti-thrombotic, anti-proliferative, anti-constrictive, and anti-adhesive signals. Table 1 summarizes some important vascular biomolecules and their role in endothelial functioning. Decreased NO production, increased oxidative stress and suppressed production of the hyperpolarizing factors could account for the decreased vasodilatory response in endothelial dysfunction [32-36].

Table 1: Table summarizing the vascular roles and affiliated biomolecules.

Vascular roles	Biomolecules	References
Anti-thrombotic	vWF, thrombomodulin, KLF2, AMPK	[37-48]
Anti-adhesive	VCAM1, ICAM1	[49-51]
Anti-inflammatory	E-selectin, VCAM1, MCP1, PAI1	[52-56]
Anti-proliferative	eNOS, prostacyclin	[57-62]
Para cellular communication	VE cadherin, claudin	[63-65]
Vaso-dilatory	eNOS, KLF2, prostacyclin	[66-67]

Our previous work demonstrates enhanced adhesion, proliferation, migration, and extracellular matrix synthesis on nano-patterned Ti when compared to endothelial cells on materials such as silicon (Si). Our goal is to understand the biomolecular mechanism(s) by which vascular blood flow elicits nano-patterned Ti substrates that alter the activation of signaling pathways and define the integrity and functionality of endothelial cells. Here we investigate activation of eNOS, VCAM-1, VE-Cadherin, and Von Willebrand factor as a systemic response to varied nano-patterns.

As shown in Figure 7.1, we propose to explore not only the macroscopic cell fate processes (differentiation, migration, apoptosis) on different nano-featured Ti substrate, but also, the molecular dynamics that define the function of the endothelial cells to maintain vascular homeostasis. The molecules that we will be studying are eNOS, AMPK, VCAM-1, claudin 5, vWF, and KLF2. In the process, we will also study the competitive nature of the endothelial cells versus smooth muscle cells and probe for the five above-mentioned biomolecules to capture a more realistic behavior of endothelial cells in-vivo.

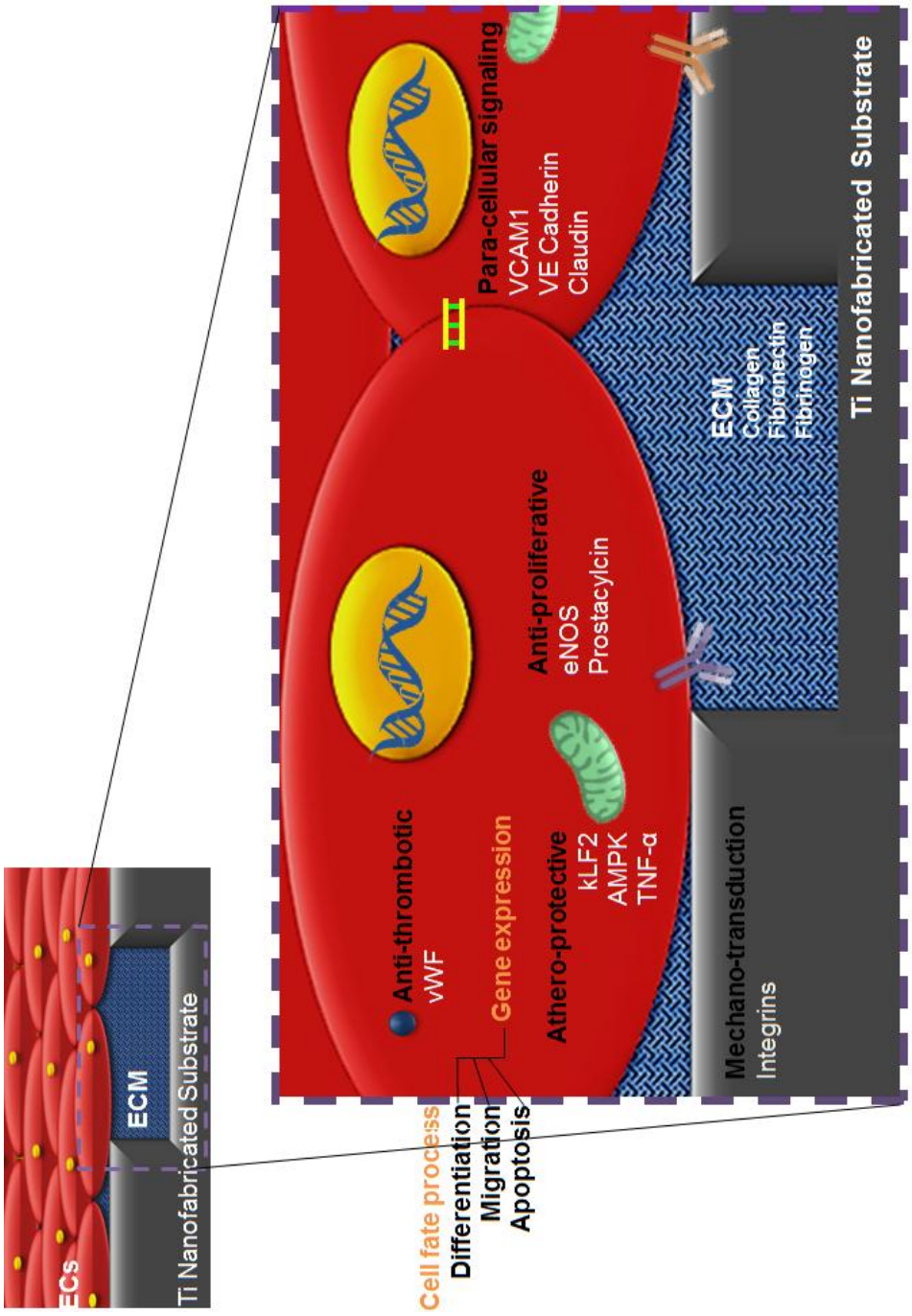

Figure 7.1| Interaction of the endothelial cells and extracellular matrix with the Ti substrate. The anti-proliferative, anti-thrombotic, vaso-dilating, athero-protective, and para-cellular signaling molecules will be probed.

7.3 MATERIALS AND METHODS

7.3.1 Endothelial cell culture

EA926 cells are obtained from ATCC (Manassas, VA). Cells are cultured using Dulbecco's modified Eagle's medium (DMEM, Lonza Inc.) and are supplemented with 10% FBS (Gibco Inc.) and antibiotics (Primocin, Invivogen Inc.). Freshly passaged cells are grown on Ti coupons. The cell-cultured nano-grooved Ti substrates will be maintained in humidified 95% air-5% CO2 incubator at 37°C.

7.3.2 Flow circuit

For each experiment, the flow circuit will be sterilized in an autoclave and assembled in a laminar flow hood. As shown in Figure 7.11, a stage will be machined into the chamber to accommodate the nanofabricated Ti stent coupon. The flow system will be maintained at 37 °C, ventilated with 95% humidified air - 5% CO_2. The flow channel will be used to impose laminar flow with shear stress of 12 dynes/cm^2 on confluent monolayer of endothelial cells cultured on the coupon. Care will be taken to avoid entrapment of air bubbles in the flow channel.

7.3.3 Immunocytochemistry

Ti Samples seeded with EA926 cells will be washed with PBS three times for five minutes each. Cell samples will be fixed and permeabilized with ice cold methanol in -20 ^oC for 20 minutes. Samples will be again washed in PBS (1X) and incubated with

blocking buffer (4 g BSA +80 mL PBS + 150 µL Triton X 100) for 1 hour followed by incubation with 5 µg/ml of rabbit polyclonal anti-peNOS (Ser1177), rabbit polyclonal anti-VCAM1, rabbit monoclonal p-AMPK, rabbit monoclonal anti-VWF, monoclonal VE Cadherin, and KLF2 primary antibodies (AbCAM, Cambridge, MA) in antibody dilution buffer (4 g BSA + 40 mL PBS + 120 µL Triton X 100) for 90 minutes in room temperature. Cells will be rinsed 3 times with 10 minutes PBT and incubated with 5 µg/ml Alexa Fluor® 488 goat anti-rabbit secondary antibody or Texas Red 598® donkey anti-rabbit secondary antibody in antibody dilution buffer for another 60 minutes. Cells will be washed three times with PBT for 5 minutes each.

7.3.4 Confocal imaging

EA926 cells seeded on the Ti surfaces were examined for all the indicated times and imaged using Leica M125 (Buffalo Groove, IL, USA) fully apochromatic corrected stereomicroscope with 12.5:1 zoom. Fluorescent images and transmitted images with 10X objective lens, binning of 4 x 4, gain of 8.0, and brightness of 1.2 were acquired. The seeded endothelial cells on the Ti surfaces are examined for all the indicated times and imaged using Leica SP2 (Buffalo Groove, IL, USA) Confocal microscope is used to image the cells for the Adhesion experiments. Spot Imaging Software® (Sterling Heights, MI, USA) and ImageJ® 1.46 (NIH, Bethesda, USA) is used to acquire and process the images [73].

7.4 RESULTS AND DISCUSSION

7.4.1 Expression of signaling molecules

Endothelial nitric oxide (NO) is an endothelial-derived relaxing factor (EDRF) and is a crucial messenger molecule responsible for multiple physiological and pathological processes in the mammalian body [68-69]. NO is generated by the action of nitric oxide synthase (eNOS) on L-arginine amino-acid. Once produced from the endothelium, NO diffuses to the smooth muscle layer of the vessel wall which consequently leads to smooth muscle relaxation and therefore vasodilatation [70-72].

Von Willebrand factor (vWF) maintains homeostasis through binding to FVIII, to platelet surface glycoproteins, and to constituents of connective tissue. VWF initiates platelet aggregation via binding to exposed structures of injured vessel walls at physiological high arterial shear rates [44-48]. Furthermore, VWF is thought to assist during platelet aggregation by bridging adjacent platelets at high shear rates. The function of VWF is strongly shear rate dependent, whereas fluid dynamic conditions as well as mechanical forces are crucial for the conformational transition of VWF to develop its interaction with endothelial matrix proteins as well as platelets in case of vessel injury.

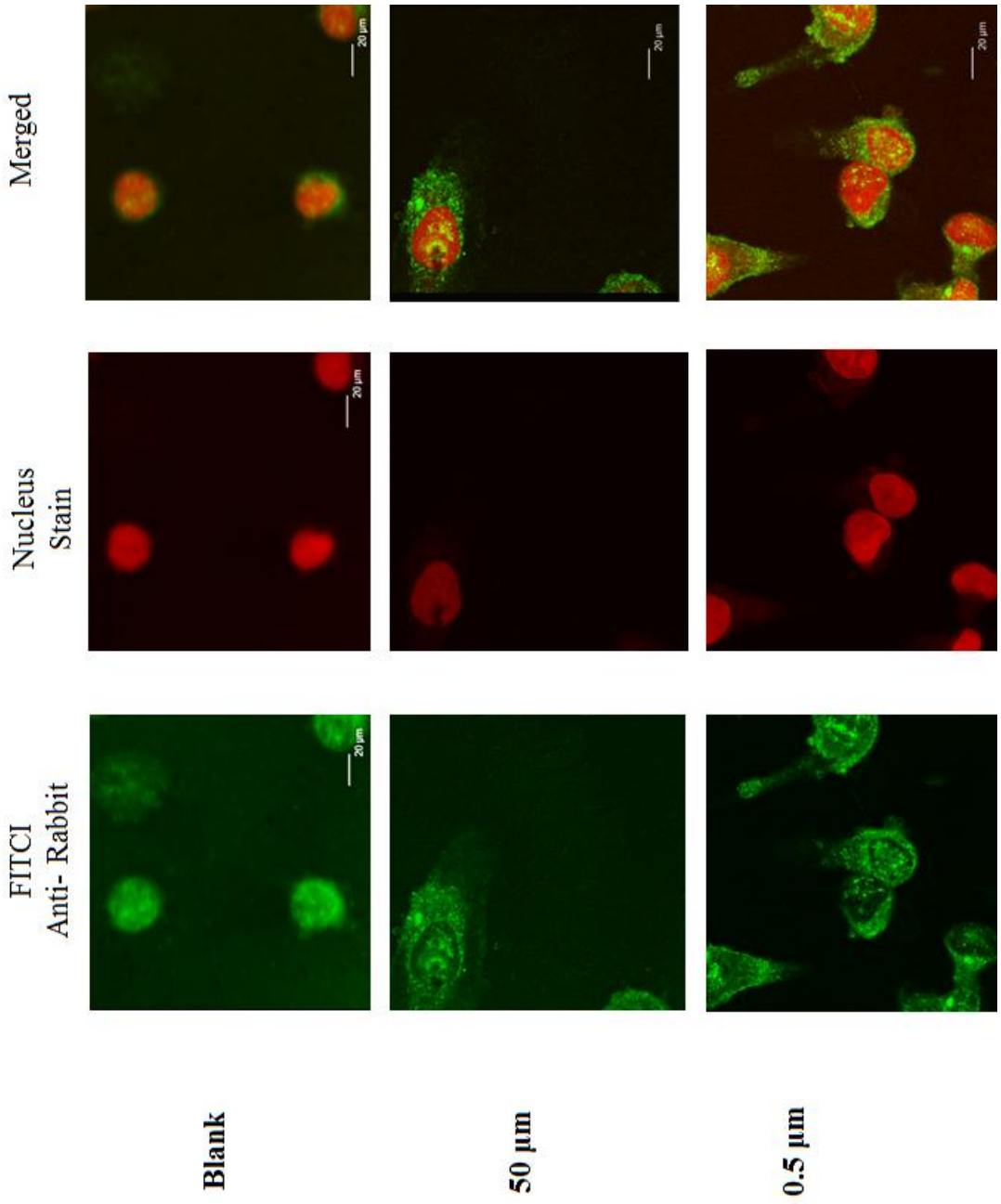

Figure 7.2| Confocal imaging of activation on von-Willbrand Factor on unpatterned, 50 um, and 0.5 um Ti substrates. The permeabilized cell nuclei is stained with PI and the vWF is imaged using FITCI secondary antibody.

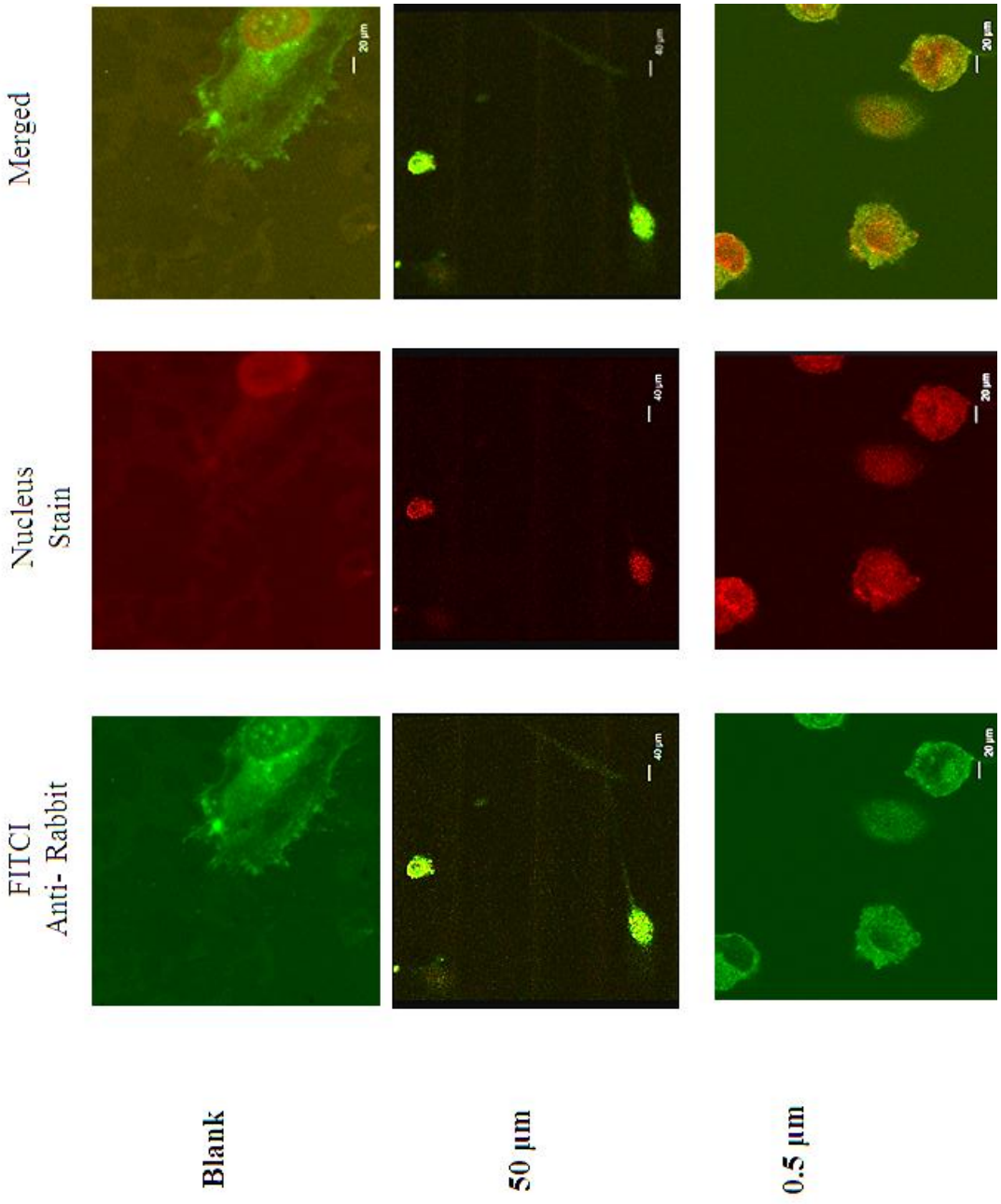

Figure 7.3| Confocal imaging of activation on p-eNOS on unpatterned, 50 um, and 0.5 um Ti substrates. The permeabilized cell nuclei is stained with PI and the p-eNOS is imaged using FITCI secondary antibody.

7.4.2 Competitiveness of flow versus pattern orientation

In this work, we exposed endothelized nano-patterned Ti substrates of 0.5 μm to 12 dynes/cm^2 (within the physiological range of shear stress) for a period of ten hours. Endothelized nano-patterened Ti substrates were aligned parallel and perpendicular to the direction of flow. We observed that an increased intracellular tensile stress occurred on endothelized substrates perpendicular to the flow direction. However, when cells were aligned parallel to the direction of flow, the cells overcame the applied shear stress. These results demonstrate that endothelial cells on nano-patterned surfaces are guided by the orientation of the patterns. The findings demonstrate that the observed increase in intracellular tension in the former case (patterns perpendicular to flow) is a result of a complex interaction of mechani-chemical cues as they respond to flow and pattern orientation.

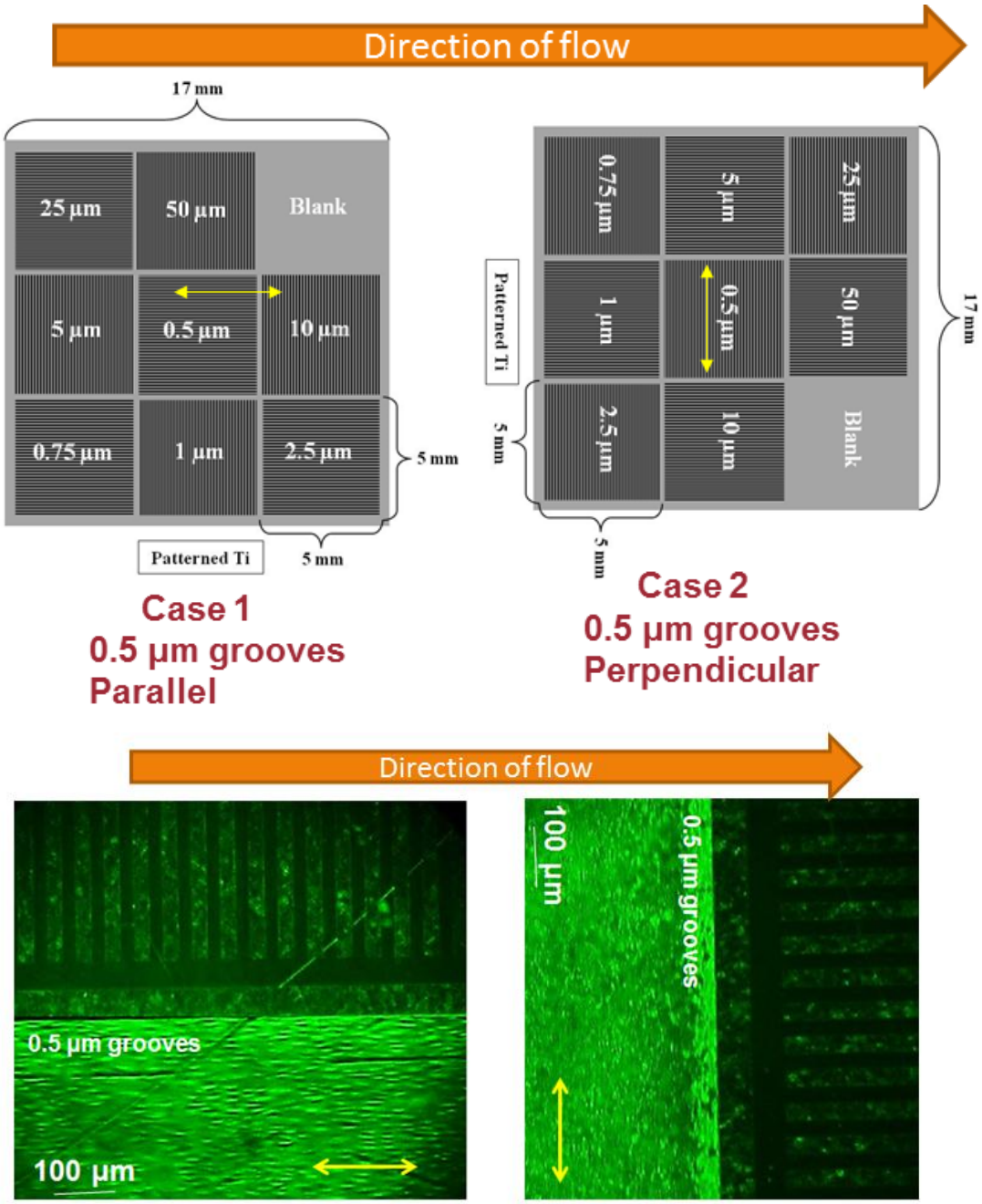

Figure 7.4| Optical micrographs demonstrating the importance of orientation of TI patterns to determine the direction of flow. In case 1, 0.5 um patterns are parallel to the orientation of flow. In case 2, 0.5 um patterns are perpendicular to the orientation of flow.

7.5 CONCLUSION

The results of these *in-vitro* studies indicate that TIDE generated Ti nano-patterns efficiently interacts with endothelial cells for achieving rapid endothelization without altering their native functionality. The activation of eNOS and vWF on these structures demonstrates the anti-proliferative and anti-coagulant properties of the endothelial cells and hence the vascular system. Further, nanostructured Ti surfaces seeded with endothelial cells indicated the maintenance of antithrombogenic phenotype of the cells. When exposed to vascular laminar flow of 12 dynes/cm^2, we observed that endothelized nano-patterned Ti in the parallel direction of flow is favorable compared to when it is in the perpendicular direction. In the future, it will be interesting to study the subendothelium and identify the integrin pairs that communicate these paracellular and extracellular signals to the endothelized nano-patterns. In conclusion, we demonstrate that the nano-patterned Ti substrates are cytofriendly and improve cellular functions. Hence, these substrates could serve as a suitable alternative to limit problems such as restenosis and thrombosis associated with current stenting.

7.6 REFERENCES

1 Cines DB, Pollak ES, Buck CA, Loscalzo J, Zimmerman, McEver RP, Pober JS, Wick TM, Konkle BA, Schwartz BS, Barnathan ES, McCrae KR, Hug BA, Schmidt AM, and Stern DM (1998) Endothelial cells in physiology and in the pathophysiology of vascular disorders. Blood 91:3527-3561

2 Furchgott RF and Vanhoutte PM (1989) Endothelium-derived relaxing and contracting factors. FASEB J. 3(9):2007-18.

3 Cooke JP (2000) The endothelium: a new target for therapy. Vasc Med. 5: 49-53

4 Chiu JJ and Chien S (2011) Effects of disturbed flow on vascular endothelium: pathophysiological basis and clinical perspectives. Physiol Rev. 2011 Jan;91(1):327-87.

5 Moses MJ, Leon MB, Kutryk M, and Serruys P (2004) Role of the endothelium in modulating neointimal formation. J Am Coll Cardiol. 44:733-739

6 Aird WC Endothelium as an organ system. (2004) Crit Care Med. 32(5):S271-9.

7 Vestweber D (2007) Adhesion and signaling molecules controlling the transmigration of leukocytes through endothelium. Immunol Rev. 218:178-96.

8 Bessler M, Teaneck NJ, Chuter TAM (1999) Artificial heart valve and method and device for implanting the same.' Patent No. 5855601.

9 Nyman S, Lang NP, Buser D, and Bragger U (1990) Bone regeneration adjacent to titanium dental implants using guided tissue regeneration: a report of two cases. The Inter. J. Oral Maxillo. Impl. 5(1):9-14.

10 Long M, Rach HJ (1998) Titanium alloys in total joint replacement – A materials science perspective.' Biomat. 19(18): 1621-1639.

11 Franco D, Labianca M, Smadja C, Fragoso J, Halabi S (2008) Titanium catheter tip for peritoneovenous shunts. Artificial Organs. 12(1): 81-82

12 Berthet JP, Annoville TD, Canaud L and Marty-Ané CH (2011) Use of the titanium vertical ribs osteosynthesis system for reconstruction of large posterolateral chest wall defect in lung cancer.' Interact CardioVasc Thorac Surg 13(2): 223-225.

13 Patrick TM, Kevin JO and Masaru PR (2011) Robust penetrating microelectrodes for neural interfaces realized by titanium micromachining. Biomedical Microdevices (2011) 13(3): 503-515

14 Yeh H, Lu S, Tian T, Hong R, Lee W, and Tsai C (2006) Comparison of endothelial cells grown on different stent materials. J Biomed Mater Res 76A: 835–841.

15 Palmaz JC, Benson A, and Sprague EA (1999) Influence of surface topography on endothelialization of intravascular metallic material. J Vasc. Interv. Radiol. 10:439–444.

16 Chandini CM, Sreerekha PR, Divyarani VV, Shantikumar N, Krishnaprasad C and Deepthy M (2012) Influence of titania nanotopography on human vascular cell functionality and its proliferation in vitro. J Mat. Chem. 22:1326-1340

17 Lu J, Rao MP, MacDonald NC, Khang D, Webster TJ (2008) Improved endothelial cell adhesion and proliferation on patterned titanium surfaces with rationally designed, micrometer to nanometer. Acta Biomater. 4(1):192-201

18 Choudhary S, Haberstroh KM, Webster TJ (2007) Enhanced functions of vascular cells on nanostructured Ti for improved stent applications. Tissue Eng. 13:1421–1430.

19 Fine E, Zhang L, Fenniri H, Webster TJ (2009) Enhanced endothelial cell functions on rosette nanotube-coated titanium vascular stents. Int. J. Nanomed. 4:91–97.

20 Rao MP, Lu J, Aguilar HP, MacDonald NC, and Webster TJ (2008) Solid-State Sensor, Actuator, and Microsystems Workshop, Hilton Head Island, SC, Jun. 1-5.

21 Davies PF (1995) Flow-mediated endothelial mechanotransduction. Physiological Reviews.75(3):519-560.

22 Boon RA and Horrevoets AJG (2009) Key transcriptional regulators of the vasoprotective effects of shear stress. Hämostaseologie 39-43.

23 Harrison DG (2005) The shear stress of keeping arteries clear. Nat Med.; 11(4): 275-376.

24 Chien S (2008) Effects of disturbed flow on endothelial cells. Annals of Biomedical Engineering. 36(4):554-562.

25 Bakker SJL and Gans ROB (2000) About the role of shear stress in atherogenesis. Cardiovascular Research. 45:270-272.

26 Konstantopoulos K, Kukreti S, and McIntire LV (1998) Biomechanics of cell interactions in shear fields. Adv. Drg. Del. Rev. 33(1-2):141-64.

27 Garcia-Cardena G, Comander J, Anderson KR, Blackman BR and Gimbrone MA (2001) Biomechanical activation of vascular endothelium as a determinant of its functional phenotype. PNAS-USA 98(8):4478-85.

28 Gimbrone MA, Nagel T, and Topper JN (1997) Biomechanical activation: an emerging paradigm in endothelial adhesion biology. J. Clin. Invest. 100(11):S61-S65.

29 Vandrangi P, Shyy JYJ, Rodgers VGJ (2012) "Flow-Dependent Mass Transfer May Trigger Endothelial Signaling Cascades", PLoS One, 7(4): e35260.

30 Chien S, Li S, and Shyy JYJ (1998) Effects of mechanical forces on signal transduction and gene expression in endothelial cells. Hypertension. 31(1):162-9.

31 Fisher AB, Chien S, Barakat AI, and Nerem RM (2001) Endothelial cellular response to altered shear stress. AJP-Lung Cell. Mol. Phys. 281(3):L529-L33.

32 Resnick N and Gimbrone MA (1995) Hemodynamic forces are complex regulators of endothelial gene-expression. FASEB 9(10):874-82.

33 Malek AM, Izumo S (1994) Molecular aspects of signal-transduction of shear-stress in the endothelial-cell. Journal of Hypertension. 12(9):989-99.

34 Gibson CM, Diaz L, Kandarpa K, Sacks FM, Pasternak RC, Sandor T, et al. (1993) Relation of vessel wall shear-stress to atherosclerosis progression in human coronary-arteries. Arteriosclerosis and Thrombosis 13:310-315.

35 Feldman CL, Ilegbusi OJ, Hu ZJ, Nesto R, Waxman S, and Stone PH. (2002) Determination of in-vivo velocity and endothelial shear stress patterns with phasic flow in human coronary arteries: A methodology to predict progression of coronary atherosclerosis. American Heart Journal 143:931-939.

36 J Davignon and P Ganz (2004) Role of endothelial dysfunction in atherosclerosis. Circulation 109,27-32.

37 Lin Z, Kumar A, SenBanerjee S, Staniszewski K, Parmar K, Vaughan DE, Gimbrone MA, Balasubramanian V, García-Cardeña G, Jain MK (2005) Kruppel-Like factor 2 (KLF2) regulates endothelial thrombotic function. Circ. Res. 96: e48-e57.

38 Dekker RJ, Boon RA, Rondaij MG, Kragt A, Volger OL, Elderkamp YW, Meijers JCM, Voorberg J, Pannekoek H, and Horrevoets AJG (2006) KLF2 provokes a gene

expression pattern that establishes functional quiescent differentiation of the endothelium Blood 107(11): 4354-4363.

39 Parmar KM, Larman HB, Dai G. (2005) Integration of flow-dependent endothelial phenotypes by Kruppel- like factor 2'. J Clin Invest 2005; 116: 49–58.

40 Senbanerje S, Lin Z, Atkins GB et al. (2004) KLF2 Is a novel transcriptional regulator of endothelial proinflammatory activation. J Exp Med.199: 1305–1315.

41 Boon RA, Fledderus JO, Volger OL et al. (2007) KLF2 suppresses TGF-beta signaling in endothelium through induction of Smad7 and inhibition of AP-1. Arterioscler Thromb Vasc Biol. 27: 532–539.

42 Ruggeri ZM and Ware J (1993) von Willebrand factor. FASEB J 1993; 7:308-16

43 Sakariassen KS, Bolhuis PA and Sixma JJ (1979) Human blood platelet adhesion to artery subendothelium is mediated by factor VIII–Von Willebrand factor bound to the subendothelium. Nature 279, 636-638

44 Vischer UM (2006) von Willebrand factor, endothelial dysfunction, and cardiovascular disease. Journal of Thrombosis and Haemostasis. 4(6): 1186–1193

45 Jaffe EA, Hoyer LW and Nachman RL (1974) Synthesis of von Willebrand factor by cultured human endothelial cells. PNAS-USA 71(5): 1906-1909

46 Sadler JE (1998) Biochemistry and Genetics of von Willebrand Factor. Annual Review of Biochemistry 67: 395-424

47 Hardie DG, Salt IP, Hawley SA, and Davies SP (2008) AMPK: a key regulator of energy balance in the single cell and the whole organism, Nature: International Journal of Obesity. 32:S7–S12

48 Chen Z, Peng IC, Sun W, Su MI, Hsu PH, Fu Y, et al. (2009) AMP-Activated Protein Kinase functionally phosphorylates Endothelial Nitric Oxide Synthase Ser633. Circulation Research. 104:496-U159.

49 Hwang SJ, Ballantyne CM, Sharrett AR, Smith LC, Davis CE, Gotto AM, and Boerwinkle E (1997) Circulating adhesion molecules VCAM-1, ICAM-1, and E-selectin in carotid atherosclerosis and incident coronary heart disease cases: the atherosclerosis risk in communities (ARIC) study. Circulation. 96:4219-4225.

50 Cybulsky MI, Iiyama K, Li H, Zhu S, Chen M, Iiyama M, Davis V, Gutierrez-Ramos JC, Connelly PW, and Milstone DS (2001) A major role for VCAM-1, but not ICAM-1, in early atherosclerosis. J *Clin Invest.* 107(10):1255–1262

51 Cybulsky MI, Motamed MA, and Collins T (1993) Structure of the murine VCAM1 gene' Genomics. 18(2): 387–391

52 Mori N, Horie Y, Gerritsen ME, Anderson DC, Granger DN (1999) Anti-inflammatory drugs and endothelial cell adhesion molecule expression in murine vascular beds. Gut 44:186-195.

53 Silverman MD, Zamora DO, Pan Y, Texeira PV, Planck SR, and Rosenbaum JT (2001) Cell adhesion molecule expression in cultured human iris endothelial cells IOVS, 42(12): 2861-2866.

54 Boer OJ, van der Wal AC, Teeling P, Becker AE. (1999) Leucocyte recruitment in rupture prone regions of lipid-rich plaques: a prominent role for neovascularization? Cardiovascular Research 41: 443–449.

55 Labbe K, Danialou G, Gvozdic D, Demoule A, Divangahi M, Boyd JH, Petrof BJ. (2010) Inhibition of monocyte chemoattractant protein-1 prevents diaphragmatic inflammation and maintains contractile function during endotoxemia. Critical Care 14(R187):1-11.

56 Odrowąż-Sypniewska G (2007) Markers of pro-inflammatory and pro-thrombotic state in the diagnosis of metabolic syndrome. Advances in Medical Sciences 52: 46-250.

57 Lin H, Lee JL, Hou HH, Chung CP, Hsu SP, Juan SH. (2008) Molecular mechanisms of the antiproliferative effect of beraprost, a prostacyclin agonist, in murine vascular smooth muscle cells. J Cell Physiol. 214(2):434-41.

58 Vane J and Corin RE. (2003) Prostacyclin: a vascular mediator. Eur J Vasc Endovasc Surg. 26(6): 571-8.

59 Moncada S. (2006) Adventures in vascular biology: a tale of two mediators', Phil. Trans. R. Soc. B 361(1469): 735-759.

60 Fetalvero KM, Martin KA, Hwa J. (2007) Cardioprotective prostacyclin signaling in vascular smooth muscle, Prostaglandins & Other Lipid Mediators. 82(1-4): 109-118.

61 Ignarro J. (2002) Nitric oxide in the regulation of vascular function. an historical overview' J Cardiol. 17:301-306.

62 Fukumura D, Gohongi T, Kadambi A, Izumi Y, Ang J, Yun CO, Buerk DG, Huang PL, and Rakesh KJ (2001) Predominant role of endothelial nitric oxide synthase in vascular endothelial growth factor-induced angiogenesis and vascular permeability. PNAS 98 (5) 2604-2609.

63 Dejanaa E, Bazzonia G, and Lampugnani MG (1999) Vascular endothelial (VE)-cadherin: only an intercellular glue? Exp. Cell Res. 252(1): 13-19.

64 Gavard J and Gutkind JS (2008) VE-cadherin and claudin-5: it takes two to tango. Nat Cell Biol. 10(8): 883–885.

65 Tsukita S and Furuse M (1999) Occludin and claudins in tight-junction strands: leading or supporting players? Trends Cell Biol. 9(7): 268-273.

66 Wu W, Xiao H, Fernandez AL, Villarreal G, Wang KC, Geary GG, Zhang Y, Wang WC, Huang HD, Zhou J, Li YS, Chien S, Cardena GG, and Shyy JYJ. (2011) Flow-dependent regulation of Krüppel-Like Factor 2 is mediated by MicroRNA-92a. Circulation.124: 633-641.

67 Mees B, Wagner S, Ninci E, Tribulova S, Martin S, Haperen RV, Kostin S, Heil M, Crom RD, and Schaper W (2007) Endothelial nitric oxide synthase ativity is essential for vasodilation during blood flow recovery but not for arteriogenesis. Arterioscler Thromb Vasc Biol. 27:1926-1933.

68 Beckman JS and Koppenol WH. (1996) Nitric oxide, superoxide, and peroxynitrite: The good, the bad, and the ugly. American Journal of Physiology-Cell Physiology. 271:C1424-C1437.

69 Balligand JL, Feron O, and Dessy C. (2009) eNOS activation by physical forces: from short-term regulation of contraction to chronic remodeling of cardiovascular tissues. Physiol Rev. 89: 481–534.

70 Uematsu M, Ohara Y, Navas JP, Nishida K, Murphy TJ, Alexander RW et al. (1995) Regulation of endothelial cell nitric oxide synthase mrna expression by shear stress. American Journal of Physiology-Cell Physiology. 269(6):C1371-C8.

71 Liu XP, Yan QT, Baskerville KL, and Zweier JL. (2007) Estimation of nitric oxide concentration in blood for different rates of generation - evidence that intravascular nitric oxide levels are too low to exert physiological effects. Journal of Biological Chemistry 282:8831-8836.

72 Nagel T, Resnick N, Atkinson WJ, Dewey CF, Gimbrone MA. (1994) Shear stress selectively up-regulates intercellular-adhesion molecule-1 expression in cultured human vascular endothelial-cells. Journal of Clinical Investigation. 94(2):885-91.

73 Schneider CA, Rasband WS, and Eliceiri KW (2012) NIH Image to ImageJ: 25 years of image analysis. Nat Methods 9:671-675.

SECTION 3

DELINEATING MASS TRANSFER FROM MECHNOTRANSDUCTION AT THE VASCULAR ENDOTHELIUM

PRELUDE

In the debate over whether mechanotransduction or mass transfer is most dominant in providing the fundamental mechanism for hemodynamic force modulated endothelial signaling pathways and their downstream gene products, mechanotransduction has been declared the clear winner. But this conclusion may be premature. In our work, we computationally simulate *in-vitro* experiments of parallel flow chambers using laws of multi-physics. Here we show that the underpinning criteria used previously to determine whether mechanotransduction is more significant than mass transfer is, in fact, also observed in models using a basic mass transfer mechanism. Our results imply that the role of mechanical transduction in endothelial signaling may be overstated and mass transfer considerations should be carefully examined when studying triggering methods in signaling cascades.

Chapter 8 describes the qualitatively deduced their conclusions by looking at viscosity dependency. They demonstrated that a modification of viscosity clarified the mechanism behind the triggering of endothelial signaling pathways. The significance of mass transport was exhibited by shear rate dependency, whereas a mechanotransduction mechanism was observed by shear stress dependency. They concluded that since shear stress illustrated viscosity-independency, the signaling mechanism was coupled to mechanotransduction.

In Chapter 9, we model vascular atheroma in diseases such as atherosclerosis, we simulate the *in-vitro* experiments using vertical step-flow channel by Chiu *et al*. (1998) and the step-flow simulations by Choi *et al.* (2007). The authors correlate the increase in

DNA (deoxyribonucleic acid) replication in the disturbed flow region, and a sudden spike of ATP generation distal to the step to mechanotransduction respectively.

As evident from our results, the use of viscosity variation relative to shear rate and shear stress are not enough to eliminate mass transfer in determining the signaling mechanism in endothelium processes. Thus, it remains plausible that biomolecular mass transfer may be significant in vascular signaling pathways. This work shows that a more cautious analysis that delineates endothelial mechanotransduction from mass transfer remains warranted. Carefully examining the effect of mass transfer will prove to play a quintessential role in elucidating endothelial flow-dependent signaling.

We propose a novel *in-vitro* experimental methodology using membrane separations technology in Chapter 10. The proposed technique can decouple mechanotransduction effects from mass transfer in flow-induced studies. The methodology takes advantage of modest alterations of the transmembrane pressure normal to cells seeded on membranes that can make tremendous variations in concentration gradients at the membrane surface (and thus mass transfer) but offers virtually little change in the associated fluid shear stress experienced by the cells. The methodology is flexible and robust, in can be used with mass transfer-limited and reaction-limited processes and can address a number of controllable scenarios.

CHAPTER 8

REVISITING THE CRITERIA FOR ASSUMING MECHANOTRANSDUCTION AS THE PRIMARY MECHANISM IN TRIGGERING ENDOTHELIAL FLOW-DEPENDENT SIGNALING CASCADES

ABSTRACT

It is well known that fluid mechanical forces directly impact endothelial signaling pathways. But while this general observation is clear, less apparent are the underlying mechanisms that initiate these critical signaling processes. This is because fluid mechanical forces can offer a direct mechanical input to possible mechanotransducers as well as alter critical mass transport characteristics (i.e. concentration gradients) of a host of chemical stimuli, present in the blood stream. However, it has recently been accepted that mechanotransduction (direct mechanical force input), and not mass transfer, is the fundamental mechanism for many hemodynamic force-modulated endothelial signaling pathways and their downstream gene products. This conclusion has been largely based, indirectly, on accepted criteria that correlate signaling behavior and shear rate and shear stress, relative to changes in viscosity. However, in this work, we investigate the negative control for these criteria. Here we computationally and experimentally subject *mass transfer-limited systems*, independent of mechanotransduction, to the purported criteria. The results showed that the negative control (*mass transfer-limited system*) produced the same trends that have been used to identify mechanotransduction-dominant systems. Thus, the widely used viscosity-related shear stress and shear rate criteria are insufficient in determining mechanotransduction-dominant systems. Thus, research should continue to consider the importance of mass transfer in triggering signaling cascades.

Keywords

mechanotransduction │ hemodynamic forces │ mass transfer │ signaling cascades

8.2 INTRODUCTION

Understanding the mechanistic behavior of endothelial signaling pathways is crucial to the search for therapeutic drug delivery targeting vascular diseases. Endothelial signaling pathways continuously respond to varying blood flow parameters and govern downstream DNA synthesis, mRNA transcription, and protein translation. Often generally called, mechanotransduction, these fluid mechanical forces trigger cytoskeletal focal adhesions and subsequent signaling molecules such as Shc-Grb-SOS-Rho-RAS [1-3].

However, fluid mechanical forces actually offer two significantly different, but coupled, mechanisms that may impact signaling. These include mechanotransduction and mass transfer. In this more formal description, mechanotransduction consists of the direct interaction of mechanical forces on cellular transducers. Mass transfer, on the other hand, is the result of fluid mechanical forces modifying concentration gradients of signaling chemicals that also impact the subsequent signaling cascade. Both mechanotransduction and mass transfer are significant throughout cellular systems [4-7]. However, the underlying factors that stimulate changes in endothelial signaling processes due to fluid mechanical forces remain unclear and have been debated for nearly half-a-century. Schwartz *et al*. (1995-2011) demonstrated that shear stress is a determinant of endothelial signaling (activated by triggering of focal adhesions), but while assuming that the mechanisms of mechanotransduction is significant, they concede that identifying the mechanism for this process remains unresolved [8-10]. Thus a fundamental interest in the

mechanism of signaling processes in the endothelium due to fluid mechanics, whether mechanotransduction, mass transfer or both remains an important topic of interest [1-10].

In order to develop an inferential method for determining the importance of mechanotransduction and mass transfer in endothelial signaling processes, Ando *et al*. (1988) used viscosity-related tangential flow studies to evaluate signaling results as compared to fluid shear rate and shear stress. The authors used these results to establish criteria for discerning whether mechanotransduction or mass-transfer was dominant in endothelial signaling processes [11]. Their criteria was, if the signaling process was *viscosity-dependent* when plotted against shear rate, but was *viscosity-independent* when plotted against shear stress, then the process was mechanotransduction. While the authors performed both mathematical order-of-magnitude analysis and experiments to arrive at this conclusion, they did not discuss negative controls (*i.e*., the possibility of not having mechanotransducers or mass transfer). These criteria have been used to conclude the mechanism of fluid mechanical forces on a number of signaling processes [11-21].

In this paper, we evaluate a negative control for the above criteria (a system without mechanotransduction) through both computational modeling and *in-vitro* experiments and evaluated these results to the purported criteria above. We revisit the experiments previously performed by Ando *et al.* (1988-2009) that have provided the criteria that separate the significance of mechanical transducers and mass transfer on signaling at the endothelium [11-21]. We use a negative control where the system *is mass transfer-limited* and is independent of any possible mechanotransducers. We assume that chemical signaling may be proportional to mass transfer of the triggered species, and we

directly consider the viscosity dependency for the *mass transfer-limited* systems with respect to shear rate and shear stress in both experimental and computational conditions.

To define a negative control consisting of no mechanotransduction, we mathematically simulate a parallel flow chamber experiment to study the mass transfer of triggered species for varying flow parameters. We additionally perform experiments in a non-cellular environment. This eliminates any possible role of biomolecular complexes that could be identified as mechanotransducers. We compare the experimental and simulated *mass transfer-limited* results relative to viscosity dependence with previously published results by Ando *et al.* (1988-2009) that were used to establish mechanotransduction dependency for endothelial flow-dependent signaling based on the viscosity-dependence criteria [11-21].

8.2.1 Initial consideration of mass transfer and mechanotransduction in endothelial signaling

Fry *et al*. (1968) showed the effect of velocity gradients on the morphology of endothelial cells by demonstrating the enhanced uptake of Evans blue dye as a result of elevated wall shear rate [22]. Their findings supported the advanced theories that account for shear rate-dependent mass transport by Caro *et al.* [23-24]. Caro and Nerem attempted to quantify the transport of C-4-cholestrol between blood serum and arterial wall in the perfused canine carotid artery [25]. Their results suggested that mass flux might be a possible means of transport of biomolecules between the blood fluid phase and the arterial walls. The authors recommended the necessity for better experimental techniques

to ascertain the role of wall shear rate as a plausible mechanism to explain endothelial functions.

In the following years, studies on the endothelial cell function and morphology were performed by a number of researchers [26-53]. These authors independently demonstrated that shear stress and blood flow parameters were coupled to the endothelial signaling process.

In 1995, Davies wrote an extensive review where he discussed the mechanotransduction mechanisms that might lead to biochemical, biophysical, and gene regulatory effects of endothelial cells as a direct response to shear stress [54]. The review also suggested the necessity in solving the confounding, yet difficult, problem of decoupling endothelial chemical mass transport from mechanotransduction.

8.2.2 Establishment of viscosity-dependent criteria for mechanotransduction processes

At about the same time, Ando *et al*. (1988) designed experimental work to differentiate the effects of wall shear stress (τ) from shear rate ($\dot{\gamma}$) by exploiting their relationship: $\tau = \mu\dot{\gamma}$ [11]. The authors proposed that by altering the viscosity, they could separate the mechanisms of mass transfer and mechanotransduction by investigating the signaling dependency on $\dot{\gamma}$ and τ, respectively. Endothelial cells were perfused with growth media having high and low viscosities. Ultimately, they established criteria that the significance of mass transport would be exhibited by shear rate viscosity-independency, whereas mechanotransduction would be observed by shear stress viscosity-independency. The

authors observed that the increase in intracellular Ca^{2+} was viscosity dependent with varying shear rates and viscosity independent with varying shear stresses. Hence, they concluded that mass transfer of molecules (previously postulated by Fry *et al*. and Caro *et al*. [22-23]) might not be dominant at the endothelium. Interpreting their results, they concluded that mechanotransduction was the most significant mode of endothelial signaling.

2.3 Consequence of the viscosity-dependent criteria

The work of Ando *et al.* (1988-2009) led to the search of mechanical transducers or/and mechanical sensors at the endothelium. Since then, several pivotal publications have addressed the significance of mechanotransduction in their *in-vitro* shear stress experiments and determined the impact of mechanotransducers on cellular processes such as mRNA expression, Ca^{2+} influx, lymphocyte adhesion, and cell differentiation [11-21]. Although seminal work emerged, the decoupling of mass transfer and mechanotransduction in endothelial signaling pathways was not further addressed [1-6, 55-63]. However in 1999, Ross again attributed atherosclerosis as a result of both mass transfer and mechanical transduction [64]. Later, Ethier suggested the possible role of mass transport in vascular pathologies which was earlier shown not to play an important role through the experiments of Ando *et al*.(1988) [65, 11].

In recent years, a number of experimental and numerical studies have been carried out to analyze the arterial flow field, flow parameters, and biomolecules that contribute to vascular diseases such as atherosclerosis [66-76]. Numerical and mathematical models

have been developed for 2D parallel plate flow chambers for steady as well as disturbed flow to study ATP and ADP concentrations [66-67]. Further, hemodynamic flow has been correlated to endothelial vasoactive agents [68-76].

8.3 MATERIALS AND METHODS

8.3.1 Computer simulations

8.3.1.1 Problem definition

Simulations are performed using a 2-D rectangular flow chamber of dimensions 0.0254 cm x 0.25 cm. Critical dimensions, fluid density, viscosities and maximum velocity are consistent with previously reported work [11]. The length is selected to minimize computational time with fully-developed laminar flow (entry length is 0.027 cm). Wall effects are assumed to be negligible.

8.3.1.2 Governing equations

The fluid phase is governed by the continuity equation for incompressible fluid (1) and the Navier-Stokes equation (2). The chemical species flowing through the system follows the equation of conservation of mass and Fick's law of diffusion (3),

$$\nabla \cdot v = 0, \tag{1}$$

$$\rho \frac{\partial v}{\partial t} + \rho v \cdot \nabla v = \mu \nabla \cdot \left[\left(\nabla v + (\nabla v)^{T} \right) \right] - \nabla P, \tag{2}$$

and

$$\frac{\partial C}{\partial t} + D_{ij} \nabla^{2} C = v \cdot \nabla C. \tag{3}$$

8.3.1.3 Boundary equations

The transport of biologically active species such as ATP, O_2, Ca^{2+}, and NO in arteries are characterized by a high Damköhler number, *Da*, as shown in Table 1. This implies that their transport mechanisms are mass transfer-limited. Similarly, Tarbell *et al*., postulated the importance of mass transport for these species in the arteries [71]. In this paper, we analyze the effect of viscosity dependence on transport for species with relevant properties to these biologically active molecules.

The entrance flow is modeled as parabolic and laminar with a species concentration of 1 μM [78]. The diffusivities of the species relative to viscosities are calculated using Stokes-Einstein's equation as shown in Table 1. Convection and diffusion are selected as the transport mechanism for the species between the fluid and the simulated cell-seeded surface. For ATP, a surface reaction rate constant, *k*, of 1.47 x 10^{-3} cm·s^{-1} and a diffusion coefficient, $D_{B,ATP}$, of 5 x 10^{-6} cm^2·s^{-1} is used [66,72]. The *Da* is calculated as the ratio of the reaction rate to the mass transfer rate,

$$Da = \left(\frac{k}{k_f} \right), \tag{4}$$

where k_f is the mass transfer coefficient. Hence a mass transfer-limited boundary condition at the endothelial cell surface is used (5),

$$N_{y=0} = -k_f \left(\Delta C \right) = -k_f \left(C_0 - C_{y=0} \right), \tag{5}$$

where C_0 and $C_{y=0}$ are the concentration of the species in the bulk and at the endothelial cell surface, respectively.

The estimated *Da* of ATP, oxygen and NO are 17.7, 49 and 173, respectively (Table 1). In addition, the *Da* of Ca^{2+} is expected to be directly related to its dynamic relationship with the ADP/ATP concentration at the endothelium [79-81]. Thus, the transport of these small molecular-weight species under these conditions is mass transfer-limited.

Comsol Multiphysics® (Version 3.5, Burlington, MA, USA) is used to numerically simulate the parallel flow chamber. Sparse object oriented linear equations solver (SPOOLES), a library for solving sparse real and complex linear systems of equations, provided by COMSOL Multiphysics® is used to simulate the steady flow model of the parallel plate chamber.

Table 1: Transport characteristics of O_2, ATP, and NO in the simulated finite element model. Density, diffusivity, viscosity, mass transfer coefficient, and Damkoḧler number for the growth media with the two different viscosities are listed.

Parameters	Units	Symbol	Medium 1	Medium 2	Reference
Density	$g \cdot cm^{-1} \cdot s^{-1}$	ρ	1.024	1.024	Ando *et al.*[11]
Kinematic viscosity	$cm^{2} \cdot s^{-1}$	υ	0.0096	0.037	Ando *et al.* [11]
ATP diffusivity	$cm^{2} \cdot s^{-1}$	D_{ATP}	5.0×10^{-6}	1.35×10^{-6}	Dull *et al.* [72] calculated*
ATP mass transfer coefficient	$cm \cdot s^{-1}$	kf_{ATP}	1.47×10^{-3}	6.02×10^{-4}	Dull *et al.* [72] calculated**
Damkhöler number	Dimensionless	Da_{O_2}	49	> 49	Tarbell *et al.* [71]
		Da_{ATP}	17.7	> 17.7	Tarbell *et al.* [71]
		Da_{NO}	173	> 173	Chen *et al.* [81]

* $D_{ij} = \dfrac{kBT}{6\pi\mu R}$

** $k_t = 1.4674 D_v \left(\dfrac{\langle v \rangle}{D_v La} \right)^{\frac{1}{3}}$

8.3.1.4 Mesh analysis

A mesh independent model shown in Figure 8.1 is simulated and selected by increasing mesh elements until wall shear stress have a relative error of 0.002%. In order to test the accuracy of the grid size, studies are performed with models having mesh elements of 5,876 and 12,776. A parabolic inlet velocity with a Reynolds number, *Re*, of 91 is used for comparing the convergence tolerance. The results imply that the grid size of 6,776 elements is appropriate for this study. Better resolution of the large velocity and concentration gradients at the boundary layers is obtained by implementing a quadrilateral boundary layer mesh that provides a dense element distribution in the normal direction along the boundary where endothelial cells are simulated.

8.3.1.5 Post analysis

The concentration obtained for each mesh element at the inlet, outlet, and the endothelial cell surface is integrated and averaged. The normalized consumed mass flux at the endothelial cell surface is calculated using

$$\dot{M}_C = 1 - \dot{M}_O / \dot{M}_i , \tag{5}$$

where $\dot{M}_C$, $\dot{M}_O$, and $\dot{M}_i$ are the mass rate for the consumed species, the mass rate of species flowing out of the chamber, and the mass rate of the species flowing into the chamber, respectively.

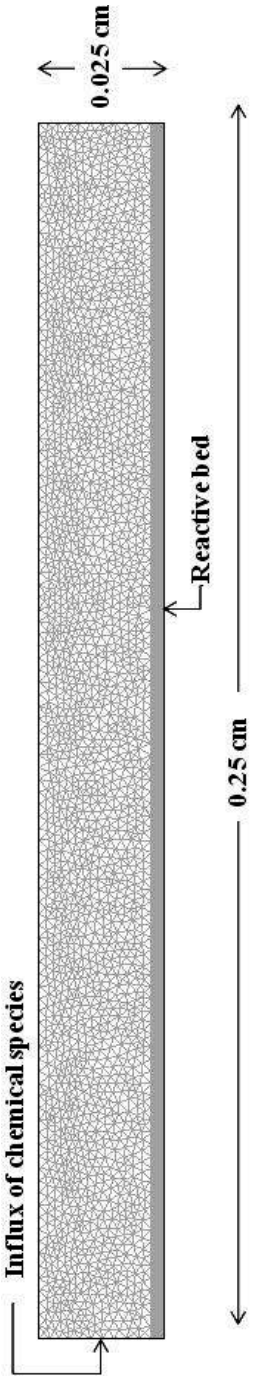

Figure 8.1| Representation of the quadrilateral boundary layer mesh used for computational modeling of the parallel flow chamber near the region representing the fluid/solid interface. In this example 6776 mesh elements are used with 2500 in the boundary layer. This mesh application improves computational representations of momentum and mass transfer gradients in the boundary layers.

8.3.2 Experimental method

We experimentally study the effects of flow parameters and fluid properties on an engineered mass transfer system. Mass transfer experiments are performed using an aqueous mixture containing measured quantities of Yellow #5 and #6 dyes, delivered through a rectangular tangential-flow diafiltration module. Water and dye solutions are introduced into the module by two inlets and co-currently delivered on the other side of the module while invoking zero transmembrane pressure. The diafiltration module consists of an upper and lower chamber and is divided by a hydrophilic membrane (Durapore 125 μm, Millipore Inc.,).

A separate set of mass transfer experiments introduce an aqueous solution of 40% glycerol and 40% glycerol-dye solution into the engineered mass transfer system. The experimental protocol for glycerol experiments are the same as that of water and dye experiments. The membrane is pre-soaked for ten minutes and the system is primed and pressurized by the corresponding non-dye solution before and after each trial. The dye concentration of the inlet streams for the experiments is 0.25 g/L. Special care is taken while handling the glycerol samples by gently stirring them to obtain spatially uniform concentrations of dye.

Samples are taken at different intervals for a time period of 10 minutes. The concentration of the dye is quantified using a VIS (500 nm) spectrophotometer. SigmaPlot (Version 10.0.1.25) is used to analyze the data from the spectrophotometer. The resultant mass transport of dye is correlated to varied shear stresses and shear rates. Experiments are performed in triplicate.

8.4 RESULTS AND DISCUSSION

8.4.1 Viscosity-independent shear stress results

Using a computational fluid dynamics (CFD) model and species mass balance as described in *Materials and Methods*, we show that a mass transfer-limited model follows the same trends as observed by others who deduced that similar trends indicated mechanotransduction [11-21]. The viscosity-independent trends observed in Figure 8.2(A) were previously interpreted to demonstrate the dominance of mechanotransduction at the vascular endothelium. The negative or positive slope is related to the consumption or production of the measured species at the endothelium. As seen in Figure 8.2(B), the CFD simulation and the *in-vitro* experimental setup using a *mass transfer-limited system* demonstrate similar viscosity-independent trends.

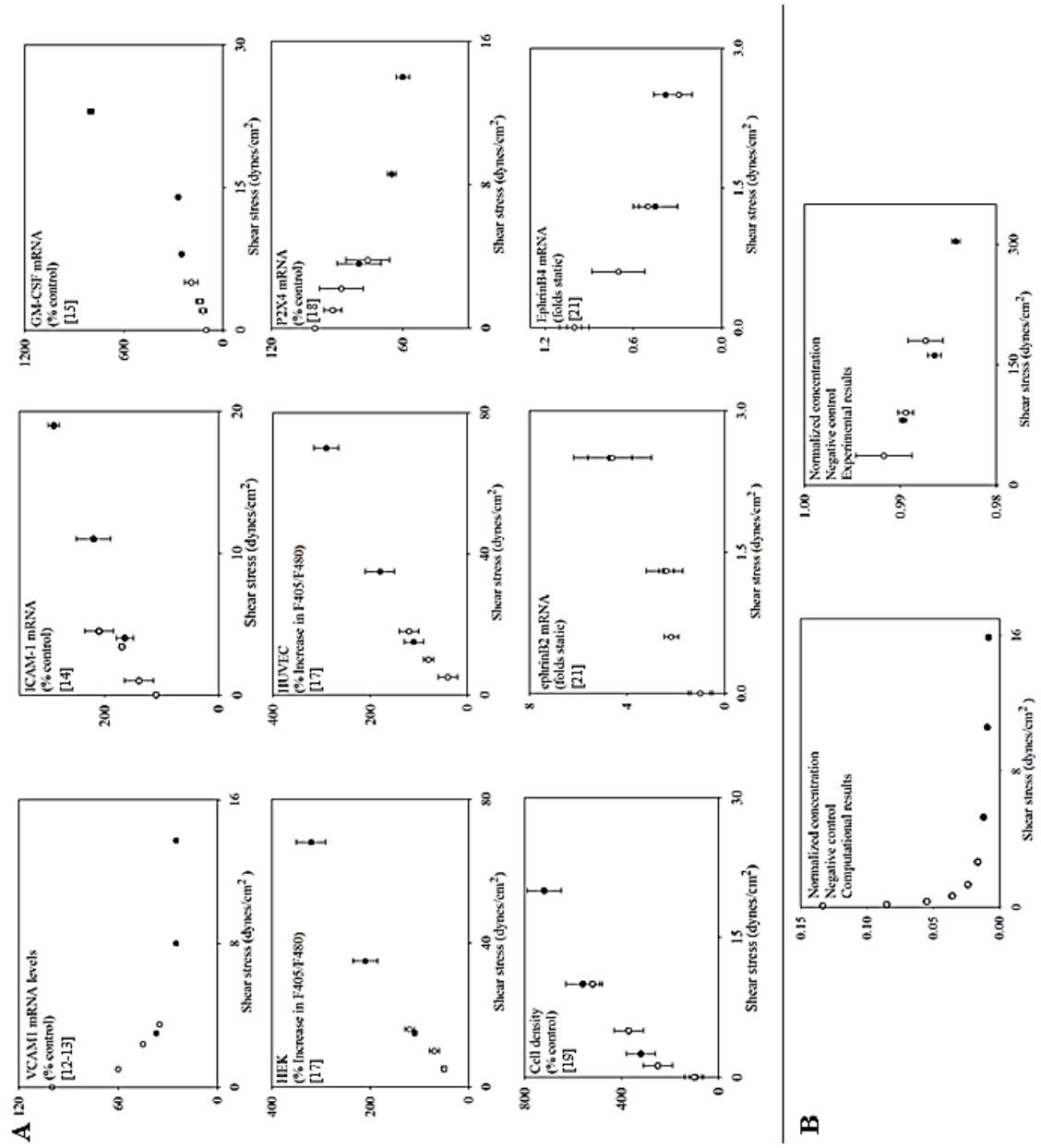

Figure 8.2| Comparison of viscosity-dependent expression with respect to shear stress from previous *in-vitro* experimental results (Panel A) and viscosity-dependent mass transfer with respect to shear stress simulation and *in-vitro* experimental results (Panel B). Panel A shows the expression of various molecules, cell density, and mRNA levels. Note that all the graphs are plotted against shear stress for high viscosity (●) and low viscosity (○) media and demonstrate a similar trend - viscosity independence. This observed viscosity-independent behavior has been previously correlated to mechanotransduction [11-21]. However, the results shown in Panel B, obtained from our computational simulations and *in-vitro* flow experiments for mass transfer-limited studies, demonstrate similar trends.

8.4.2 Viscosity-dependent shear rate results

Figure 8.3 shows the shear rate versus normalized mass flux for two viscosities. Figure 8.3(A) shows the results obtained previously by others through their *in-vitro* experiments [11-21]. Again, the negative or positive slope of the measured species is related to its consumption or production at the endothelium. The greater/lower y-axis for higher/lower viscosity media is dependent on whether the reactants or products are analyzed in their respective signaling cascade. Figure 8.3(B) shows the results of the CFD simulations and the *in-vitro* experiments, demonstrating similar viscosity-dependent relationships.

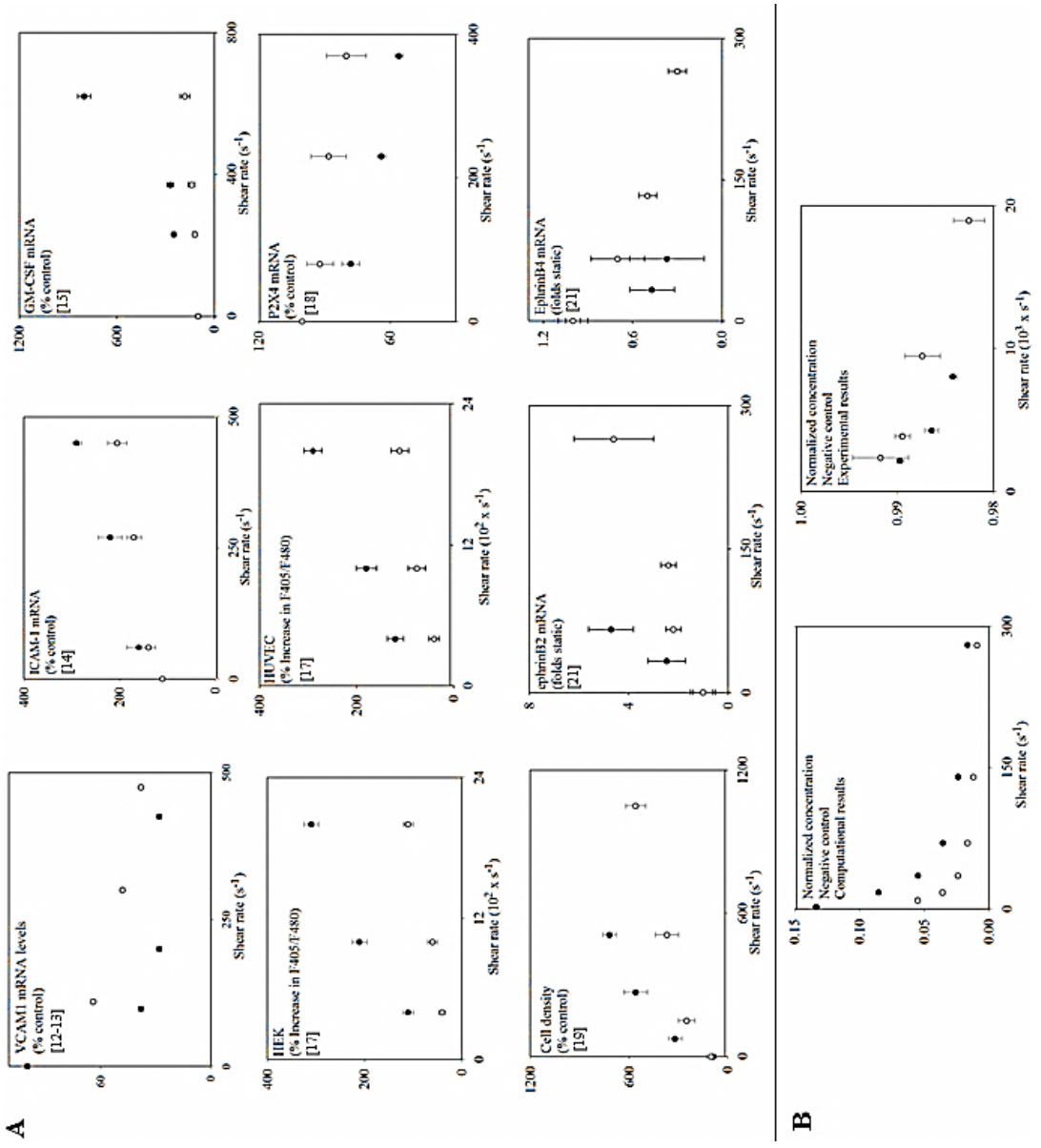

Figure 8.3| Comparison of viscosity-dependent expression with respect to shear rate from previous in-vitro experimental results (Panel A) and viscosity-dependent mass transfer with respect to shear rate simulation and in-vitro experimental results (Panel B). Panel A shows the expression of various molecules, cell density, and mRNA levels. Note that all the graphs are plotted against shear rate for high viscosity (●) and low viscosity (○) media and demonstrate a similar trend - viscosity dependence. This observed viscosity-dependent behavior has been correlated to mechanotransduction [11-21]. However, the results shown in Panel B, obtained from our computational simulations and *in-vitro* flow experiments for mass transfer-limited studies, demonstrate similar trends.

8.4.3 Differences in computational and experimental models

While comparing and analyzing the results, it is important to consider the differences in the dimensions of the typical parallel plate flow chamber used in our computer simulations (based on Ando *et al*. [11]) and the dimensions of the in-house parallel flow chamber used for the experimental results. Despite these differences in dimensions, we observe that the trends observed in both the graphs are similar when the system is mass transfer-limited. More importantly, irrespective of the range of shear rate or shear stress examined, the relevant relationship between viscosity and transport is prevalent across the investigated range for all mass transfer-limited studies and are the same relationships originally used as the criteria for determining whether the transport system was mechanotransduction-dependent. Thus, it appears that the observed trends also scale across dimensions for these flow systems.

8.5 CONCULSION

As evident from our results, the criteria of viscosity variation relative to shear rate and shear stress by Ando *et al*. (1988-2009) are not enough to eliminate mass transfer in determining the signaling mechanism in endothelium processes [11-21]. Thus it remains plausible that biomolecular mass transfer may be significant in vascular signaling pathways. This work shows that a more cautious analysis that delineates endothelial mechanotransduction from mass transfer remains warranted and that researchers should return to efforts such as those of Caro *et al*. [23-25, 82] that considered both mass transfer and mechanotransduction when investigating the endothelial flow-dependent signaling mechanisms.

8.6 REFERENCES

1. Chien S, Li S, Shyy JYJ (1998) Effects of mechanical forces on signal transduction and gene expression in endothelial cells. *Hypertension* 31(1): 162-169.

2. Chen KD, Li YS, Kim M, Li S, Yuan S *et al*. (1999) Mechanotransduction in response to shear stress - roles of receptor tyrosine kinases, integrins, and Shc. *J Biol Chem.* 274(26): 18393-18400.

3. Tzima E, Pozo MAD, Kiosses WB, Mohamed SA, Li S, Chien S, and Schwartz MA (2002) Activation of Rac1 by shear stress in endothelial cells mediates both cytoskeletal reorganization and effects on gene expression. EMBO J., 21(24): 6791–6800.

4. Jaalouk DE, Lammerding J (2009) Mechanotransduction gone awry. Nature Rev. Mol. Cell Bio.10: 63-73.

5. Wozniak MA, Chen CS (2009) Mechanotransduction in development: a growing role for contractility. Nature Rev. Mol. Cell Bio.10: 34-43.

6. Chalfie M (2009) Neurosensory mechanotransduction. Nature Rev. Mol. Cell Bio. 10, 44-52.

7. Ingber DE (2006) Cellular mechanotransduction: putting all the pieces together again. FASEB Journal. 20: 811-827.

8. Schwartz MA (1995) Integrins: emerging paradigms of signal transduction. Annu. Rev. Cell Dev. Bioi. 1: 549-599

9. Katsumi A, Orr AW, Tzima E, and Schwartz MA (2004) Integrins in mechanotransduction. J. Biol. Chem., 279: 12001-12004.

10. Hoffman BD, Grashoff C, and Schwartz MA (2011) Dynamic molecular processes mediate cellular mechanotransduction. Nature. 475: 316–323.

11. Ando J, Komatsuda T, Kamiya A (1988) Cytoplasmic calcium response to fluid shear-stress in cultured vascular endothelial-cells. *In Vitro Cell Dev Biol* 24(9): 871-877.

12. Ando J, Tsuboi H, Korenaga R, Takada Y, Toyamasorimachi N *et al*. (1994) Shear stress inhibits adhesion of cultured mouse endothelial cells to lymphocytes by downregulating VCAM-1 expression. *Am J Physiol* 267(3): C679-C687.

13. Korenaga R, Ando J, Kosaki K, Isshiki M, Takada Y *et al*. (1997) Negative transcriptional regulation of the vcam-1 gene by fluid shear stress in murine endothelial cells. *Am J Physiol Cell Physiol.* 273(5): C1506-C1515.

14. Tsuboi H, Ando J, Korenaga R, Takada Y, Kamiya A (1995) Flow stimulates ICAM-1 expression time and shear-stress dependently in cultured human endothelial-cells. *Biochem Biophys Res Commun* 206(3): 988-996.

15. Kosaki K, Ando J, Korenaga R, Kurokawa T, Kamiya A (1998) Fluid shear stress increases the production of granulocyte-macrophage colony-stimulating factor by endothelial cells via mRNA stabilization. *Circ Res.*82(7): 794-802.

16. Yamamoto K, Korenaga R, Kamiya A, Ando J (1998) Fluid shear stress activates Ca^{2+} influx into human endothelial cells via P2X4 purinoceptors. *Circ Res*. 87(5): 385-391.

17. Yamamoto K, Korenaga R, Kamiya A, Qi Z, Sokabe M, Ando J (2000) P2X(4) receptors mediate ATP-induced calcium influx in human vascular endothelial cells. *Am J Physiol Heart Circ Physiol* 279(1): H285-H292.

18. Korenaga R, Yamamoto K, Ohura N, Sokabe T, Kamiya A *et al*. (2001) SP1-mediated downregulation of p2x(4) receptor gene transcription in endothelial cells exposed to shear stress. *Am J Physiol Heart Circ Physiol* 280(5): H2214-H2221.

19. Yamamoto K, Sokabe T, Watabe T, Miyazono K, Yamashita J *et al.* (2005) Fluid shear stress induces differentiation of Flk-1-positive embryonic stem cells into vascular endothelial cells invitro. *Am. J. Physiol. Heart Circ Physiol* 288: H1915–H1924.

20. Nakatsuka H, Sokabe T, Yamamoto K, Ando J (2006) Shear stress induces hepatocyte PAI-1 gene expression through cooperative Sp1/Ets-1 activation of transcription. *Am J Physiol Gastrointest Liver Physiol* 291(1): G26-34.

21. Obi S, Yamamoto K, Shimizu N, Kumagaya S, Masumura T *et al.* (2009) Fluid shear stress induces arterial differentiation of endothelial progenitor cells. *J Appl Physiol* 106: 203–211.

22. Fry DL (1968) Acute vascular endothelial changes associated with increased blood velocity gradients. *Circ Res.* 22(2): 165-197.

23. Caro CG, Fitzgerald JM, Schroter RC (1969) Arterial wall shear and distribution of early atheroma in man. *Nature.* 223(5211): 1159-1161.

24. Caro CG, Fitzgerald JM, Schroter RC (1971) Atheroma and arterial wall shear - observation, correlation and proposal of a shear dependent mass transfer mechanism for atherogenesis. *Proc R Soc Lond [Biol]*.177(1046): 109-133.

25. Caro CG, Nerem RM (1973) Transport of c-14-4-cholesterol between serum and wall in perfused dog common carotid-artery. *Circ Res.* 32(2): 187-205.

26. Kamiya A and Togawa T (1980) Adaptive regulation of wall shear-stress to flow change in the canine carotid-artery. *Am J Physiol* 239(1): H14-H21.

27. Dewey CF, Bussolari SR, Gimbrone MA, Davies PF (1981) The dynamic-response of vascular endothelial-cells to fluid shear-stress. *J Biomech Eng* 103(3): 177-185.

28. Frangos JA, Eskin SG, McIntire LV, Ives CL (1985) Flow effects on prostacyclin production by cultured human-endothelial cells. *Science* 227(4693): 1477-1479.

29. Ku DN, Giddens DP, Zarins CK, Glagov S (1985) Pulsatile flow and atherosclerosis in the human carotid bifurcation - positive correlation between plaque location and low and oscillating shear-stress. *Arteriosclerosis* 5(3): 293-302.

30. Levesque MJ, Nerem RM. (1985) The elongation and orientation of cultured endothelial-cells in response to shear-stress. *J Biomech Eng* 107(4): 341-347.

31. Levesque MJ, Liepsch D, Moravec S, Nerem RM (1986) Correlation of endothelial-cell shape and wall shear-stress in a stenosed dog aorta. *Arteriosclerosis* 6(2): 220-229.

32. Levesque MJ, Nerem RM, Sprague EA (1990) Vascular endothelial-cell proliferation in culture and the influence of flow. *Biomaterials* 11(9): 702-707.

33. Diamond SL, Eskin SG, McIntire LV (1989) Fluid-flow stimulates tissue plasminogen-activator secretion by cultured human-endothelial cells. *Science* 243(4897): 1483-1485.

34. Diamond SL, Sharefkin JB, Dieffenbach C, Frasierscott K, McIntire LV, Eskin SG (1990) Tissue plasminogen-activator messenger-RNA levels increase in cultured human endothelial-cells exposed to laminar shear-stress. *J Cell Physiol* 143(2):364-371.

35. Sharefkin JB, Diamond SL, Eskin SG, McIntire LV, Dieffenbach CW (1991) Fluid-flow decreases preproendothelin messenger-RNA levels and suppresses Endothelin-1 peptide release in cultured human endothelial-cells. *J Vasc Surg* 14(1): 1-9.

36. Ranjan V, Xiao ZS, Diamond SL (1995) Constitutive NOS expression in cultured endothelial-cells is elevated by fluid shear-stress. *Am J Physiol-Heart C* 269(2): H550-H555.

37. Nollert MU, Hall ER, Eskin SG, McIntire LV (1989) The effect of shear-stress on the uptake and metabolism of arachidonic-acid by human-endothelial cells. *Biochim Biophys Acta* 1005(1): 72-78.

38. Nollert MU, Eskin SG, McIntire LV (1990) Shear-stress increases inositol trisphosphate levels in human endothelial-cells. *Biochem Biophys Res Commun* 170(1): 281-287.

39. Nollert MU, Diamond SL, McIntire LV (1991) Hydrodynamic shear-stress and mass-transport modulation of endothelial-cell metabolism. *Biotechnol Bioeng* 38(6): 588-602.

40. Patrick CW, McIntire LV (1995) Shear-stress and cyclic strain modulation of gene-expression in vascular endothelial-cells. *Blood Purificat* 13(3-4): 112-124.

41. Sampath R, Kukielka GL, Smith CW, Eskin SG, McIntire LV (1995) Shear stress-mediated changes in the expression of leukocyte adhesion receptors on human umbilical vein endothelial-cells *in-vitro*. *Ann Biomed Eng* 23(3): 247-256.

42. Uematsu M, Ohara Y, Navas JP, Nishida K, Murphy TJ *et al*. (1995) Regulation of endothelial cell nitric oxide synthase mRNA expression by shear stress. *Am J Physiol Cell Physiol* 269(6): C1371-C1378.

43. Nerem RM, Levesque MJ, Cornhill JF (1981) Vascular endothelial morphology as an indicator of the pattern of blood-flow. *J Biomech Eng* 103(3): 172-176.

44. Nerem RM, Sato M, Levesque MJ (1985) Elongation, orientation and effective shear modulus of cultured endothelial-cells in response to shear. *Fed Proc* 107(4): 341-347.

45. Nerem RM (1992) Vascular fluid-mechanics, the arterial-wall, and atherosclerosis. *J Biomech Eng* 114(3): 274-282.

46. Nerem RM, Harrison DG, Taylor WR, Alexander RW (1993) Hemodynamics and vascular endothelial biology. *J Cardiovasc Pharmacol* 21:S6-S10.

47. Mitsumata M, Fishel RS, Nerem RM, Alexander RW, Berk BC (1993) Fluid shear-stress stimulates platelet-derived growth-factor expression in endothelial-cells. *Am J Physiol* 265(1): H3-H8.

48. Resnick N, Collins T, Atkinson W, Bonthron DT, Dewey CF *et al.* (1993) Platelet-derived growth factor-b chain promoter contains a cis-acting fluid shear-stress-responsive element. *P Natl Acad Sci USA* 90(10): 4591-4595.

49. Nagel T, Resnick N, Atkinson WJ, Dewey CF, Gimbrone MA (1994) Shear stress selectively up-regulates intercellular-adhesion molecule-1 expression in cultured human vascular endothelial-cells. *J Clin Invest* 94(2): 885-891.

50. Resnick N, Gimbrone MA (1995) Hemodynamic forces are complex regulators of endothelial gene-expression. *FASEB J* 9(10): 874-882.

51. Malek AM, Gibbons GH, Dzau VJ, Izumo S (1993) Fluid shear-stress differentially modulates expression of genes encoding basic fibroblast growth-factor and platelet-derived growth factor-b chain in vascular endothelium. *J Clin Invest* 92(4): 2013-2021.

52. Malek AM, Izumo S (1994) Molecular aspects of signal-transduction of shear-stress in the endothelial-cell. *J Hypertens* 12(9): 989-999.

53. Malek AM, Jackman R, Rosenberg RD, Izumo S (1994) Endothelial expression of thrombomodulin is reversibly regulated by fluid shear-stress. *Circ Res* 74(5): 852-860.

54. Davies PF (1995) Flow-mediated endothelial mechanotransduction. *Physiol Rev* 75(3): 519-560.

55. Shyy JYJ, Chien S (1997) Role of integrins in cellular responses to mechanical stress and adhesion. *Curr Opin Cell Biol* 9(5): 707-713.

56. Fisher AB, Chien S, Barakat AI, Nerem RM (2001) Endothelial cellular response to altered shear stress. *Am J Physiol-Lung C* 281(3): L529-L533.

57. Gimbrone MA, Nagel T, Topper JN (1997) Biomechanical activation: An emerging paradigm in endothelial adhesion biology. *J Clin Invest* 99(8): 1809-1813.

58. Garcia-Cardena G, Comander J, Anderson KR, Blackman BR, Gimbrone MA (2001) Biomechanical activation of vascular endothelium as a determinant of its functional phenotype. *P Natl Acad Sci USA* 98(8): 4478-4485.

59. Garcia-Cardena G, Comander JI, Blackman BR, Anderson KR, Gimbrone MA (2001) Mechanosensitive endothelial gene expression profiles - scripts for the role of hemodynamics in atherogenesis. *Ann NY Acad Sci* 947: 1-6.

60. Konstantopoulos K, Kukreti S, McIntire LV (1998) Biomechanics of cell interactions in shear fields. *Adv Drug Delivery Rev* 33(1-2): 141-164.

61. Seliktar D, Nerem RM, and Galis ZS (2001) The role of matrix metalloproteinase-2 in the remodeling of cell-seeded vascular constructs subjected to cyclic strain. *Ann Biomed Eng* 29(11): 923-934.

62. Schmidt C, Pommerenke H, Durr F, Nebe B, Rychly J (1998) Mechanical stressing of integrin receptors induces enhanced tyrosine phosphorylation of cytoskeletally anchored proteins. *J Biol Chem* 273(9): 5081-5085.

63. Urbich C, Walter DH, Zeiher AM, Dimmeler S (2000) Laminar shear stress upregulates integrin expression - role in endothelial cell adhesion and apoptosis. *Circ Res* 87(8): 683-689.

64. Ross R (1999) Mechanisms of disease - Atherosclerosis - An inflammatory disease. *New Engl J Med* 340(2): 115-126.

65. Ethier CR (2002) Computational modeling of mass transfer and links to atherosclerosis. *Ann Biomed Eng* 30(4): 461-471.

66. John K, Barakat AI (2001) Modulation of ATP/ADP concentration at the endothelial surface by shear stress. Effect of flow-induced ATP release. *Ann Biomed Eng* 29: 740-751.

67. David T (2003) Wall shear stress modulation of ATP/ADP concentration at the endothelium. *Ann Biomed Eng* 31: 1231-1237.

68. Olgac U, Kurtcuoglu V, Poulikakos D (2008) Computational modeling of coupled blood-wall mass transport of LDL: effects of local wall shear stress. *Am J Physiol Heart Circ Physiol* 294: H909-H919.

69. Quarteroni A, Veneziani A, Zunino P (2002) Mathematical and numerical modeling of solute dynamics in blood flow and arterial walls. *SIAM J Numer Anal* 39: 1488-1511.

70. Rappitsch G, Perktold K, Pernkopf E (1997) Numerical modeling of shear-dependent mass transfer in large arteries. *Int J Numer Meth Fl* 25: 847-857.

71. Tarbell JM (2003) Mass transport in arteries and the localization of atherosclerosis. *Annu Rev Biomed Eng* 5: 79-118.

72. Dull RO, Tarbell JM, Davies PF (1992) Mechanisms of flow-mediated signal transduction in endothelial cells: kinetics of ATP surface concentrations, *J Vasc Res* 29: 410-419.

73. Plank MJ, Wall DJN (2006) Atherosclerosis and calcium signaling in endothelial cells. *Prog Biophys Mol Bio* 91(3): 287-313.

74. Fadel AA (2009) A Computational model of nitric oxide production and transport in a parallel plate flow chamber. *Ann Biomed Eng* 37: 943-954.

75. Adams DJ, Barakeh J, Laskey R, Vanbreemen C (1989) Ion channels and regulation of intracellular calcium in vascular endothelial cells. *FASEB J* 3: 2389-2400.

76. Comerford A, Plank MJ, David T (2008) Endothelial nitric oxide synthase and calcium production in arterial geometries: An integrated fluid mechanics/cell model. *J Biomech Eng-T ASME* 130(1).

77. Shi Z-D, Abraham G, Tarbell JM (2010) Shear stress modulation of smooth muscle cell marker genes in 2-D and 3-D depends on mechanotransduction by Heparan Sulfate Proteoglycans and ERK1/2. *PLoS ONE* 5(8): e12196.

78. Backx PH, Tombe PPDe, Deen JHKV, Mulder BJM, *et al.* (1989) A model of propagating calcium-induced calcium release mediated by calcium diffusion. *J Gen Physiol* 93(5): 963-977.

79. De S, Guilak F, Mofrad M (2010) Computational Modeling in Biomechanics. *Dordrecht: Springer*. 49-67.

80. Qin KR, Cheng X, Xu Z, Cao LL, Ge SS, Jiang ZL (2008) Dynamic modeling for shear stress induced ATP release from vascular endothelial cells. *Biomech Model Mechanobiol* 7(5): 345-353.

81. Chen K, Pittman RN, Popel AS (2007) Vascular smooth muscle NO exposure from intraerythrocytic SNOHb: A mathematical model. *Antioxid Redox Sign* 9(8): 1097-1110.

82. Wiesner TF, Berk BC, Nerem RM (1996) A mathematical model of cytosolic calcium dynamics in human umbilical vein endothelial cells. *Am J Physiol* 270(5): C1556-1569.

CHAPTER 9

DELINEATING MASS TRANSFER AT THE VASCULAR ENDOTHELIUM - A COMPUTATIONAL STUDY

ABSTRACT

Previous literature has suggested that mechanical transduction, via shear stress, plays a dominant contribution in vascular intima signaling. Cellular processes such as gene transcription, DNA replication in the disturbed flow region, and a sudden spike of ATP generation distal to plaque formation have been correlated to mechanotransduction. We hypothesize that mass transfer of a chemical species plays an important role in signal transduction. Here, we computationally model the significance of mass transfer relative to shear gradients on chemical species under the same experimental conditions prescribed by the work of Chiu *et al*. (1998), and Choi *et al.* (2007). The results demonstrate that mass transfer modifications of chemical species are in excellent agreement with the published observations. The results imply that the role of mechanical transduction in similar signaling may be overstated and mass transfer considerations should be carefully examined when studying triggering methods in signaling mechanisms.

Keywords Restenosis, back-step, mass transfer, mechanotransduction

9.2 INTRODUCTION

Physiologically, endothelial cells, the inner most layer of the vascular system, experience blood flow. The mechanism by which vascular blood flow elicits signalling in the endothelial cells remains vague. Mechanotransduction of hemodynamic forces into signaling cascades has been extensively studied during the past decade [2]. Along with hemodynamic forces such as shear stress, endothelial cells might be triggered by a biochemical response such as mass transfer leading to a variation in concentration gradients of molecules such as NO and LDL at the endothelium. Ironically, the subsequent role of mass transfer in arteriosclerosis, arrhythmias, and other disease states has, however, received relatively little attention [3].

9.2.1 Previous work

Several pivotal publications have addressed the significance of mechanotransduction and mass transfer in their *in-vitro* study of shear stress regulation on mRNA expression, Ca^{2+} influx, lymphocyte adhesion, and cell differentiation [1-11]. Interpreting their results, these scientists showed that cell behavior was dependent on shear stress and concluded that mechanotransduction was the most significant mode of signaling.

It has also been shown through experimental data from various laboratories that blood flow variations modulate endothelial cell functions by activating mechanosensors, signaling pathways, and downstream gene-protein expressions [12-17]. When endothelial cells experience shear stress resulting from laminar pulsatile or steady flow with a net unidirection, the mechanotransducers communicate with the signaling pathways,

transiently activating pro-inflammatory and proliferative pathways. These signaling pathways are down-regulated when exposed to such sustained and well-directed flow parameters. In contrast, shear flow without a definite direction (e.g., disturbed flow in regions of arterial bifurcations or in regions distal to plaque build-up) causes the mechanotransducers to trigger sustained molecular signaling of pro-inflammatory and proliferative pathways.

To demonstrate the above hypothesis, Chiu *et al*. (1998) performed *in-vitro* experiments to emulate the physiological response of endothelial cells exposed to disturbed flow in the regions of atherosclerotic lesions [12-13]. The authors qualitatively showed an enhanced rate of endothelial cell duplication in the disturbed flow zone than that in the laminar flow zone. These results qualitatively showed an increase in the activity of mechanotransducers and the resulting downstream DNA replication. It might be worth noting that considering the impact of mass transfer implications on these signaling pathways has not been investigated.

9.2.2 Flow parameters and atherosclerosis

The endothelium regulates arterial health by responding to transient flow parameters. These flow parameters activate many signaling pathways. For example, the JNK pathway in endothelial cells is activated by flow parameters via heterotrimeric G proteins ($G_{\beta\gamma}$) and trigger Phosphoinositol 3-kinaseγ (PI3Kγ). PI3Kγ has been implicated in a myriad of cellular processes including anti-apoptosis, vesicle transport, and cytoskeleton rearrangement [16].

The blood flow parameters can be attributed to velocity (v), viscosity (μ), pulse amplitude (b), and pulse frequency of the blood (f). In two dimensions (2D), the velocity profile, is defined as a function of the artery's height (h). Assuming that the healthy artery has a parabolic profile, the velocity profile for a laminar flow,

$$v = 6v_{max}\frac{y}{h}\left(1 - \frac{y}{h}\right) \qquad \text{----------(1)}$$

For a pulsatile flow,

$$v_{pulsatile} = 6v_{max}\left(\frac{y}{h}\left(1 - \frac{y}{h}\right)\right)(1 + (b \times \sin 2\pi f t)) \qquad \text{----------(2)}$$

where $b < 1$.

Shear stress (τ) is defined as the tangential force of the blood at the endothelial bed. It is the product of shear rate ($\dot{\gamma}$) and viscosity of the blood.

$$\tau = \mu\dot{\gamma} = \mu\frac{\partial v}{\partial x} \qquad \text{----------(3)}$$

9.2.3 Considering mass transfer

The controlling rate of mass transfer of a molecular substance is determined by: (1) the shear rate and (2) the chemical reaction involving the production or consumption of the chemical species. Mass transfer is coupled to shear stress and shear rate by the hydrodynamic and concentration boundary layers (δ_H and δ_C). As the velocity increases,

the shear rate increases, steepening the slope of the concentration gradient, and increasing the concentration flux of the species. This is illustrated in Figure 8.4.

Convective flux accounts for the chemical species moving in the medium. Convective mass transport entraps most biologically active molecules in the concentration boundary layer near the wall. Consequently, convective mass transfer may be a limiting factor for small molecules (e.g., NO, O_2, Ca^{2+}, ATP) flowing through the blood. Systems which are dependent wholly on the convection of these molecules are termed as mass transfer limited systems. In vascular areas prone to atherosclerosis (characterized by areas of low shear stress), the thick concentration boundary layer on the endothelial surface inhibits mass transport of biomolecules.

Along with the abovementioned flow parameters, flow patterns can also have a direct effect on cell morphology and vascular functioning. Two distinct flow patterns experienced by tunica intima are: (1) 'atheroprotective flow' attributed to laminar flow and (2) 'atherogenic flow' attributed to turbulent flow. Integrins hosted on the endothelium respond to these flow patterns differently and elicit various signaling pathways. In the quiescent state, the endothelium experiences laminar flow (characterized by steady or pulsatile flow), during which the JNK pathway is not triggered. On the other hand, a sustained integrin-JNK pathway is triggered when the endothelium experiences turbulent flow (characterized by reversed, stagnant, recirculatory and oscillatory flow) [17]. Regions that have turbulent flow up-regulate the JNK pathway --as a consequence increase the permeability to LDL, promote foam

cell formation, and develop lesions-- a characteristic feature of atherosclerotic endothelial dysfunction [18].

9.2.4 Computational modelling

In recent years, a number of experimental and numerical studies have been carried out to analyze the arterial flow field, flow parameters, and biomolecules that contribute to atherosclerosis. Atherosclerotic plaques initiate in areas of low shear stress where the concentration of LDL and cholesterol is high [29]. Numerical and mathematical models have been developed for 2D parallel plate flow chambers to study ATP and ADP concentrations [30, 31]. Steady as well as disturbed flow parameters were considered in these models. In yet another study, the relation of solute flux (albumin) to flow regimes was modelled and the results showed considerable variations between steady flow and time averaged flux for pulsatile flow [32]. Rappitsch *et al*. numerically simulated mass transfer and permeability of the endothelial wall as a function of the blood flow rate [33]. Fadel *et al*. developed a mathematical model to investigate the transport of NO generated by a monolayer of cultured endothelial cells exposed to flow in a parallel plate flow chamber [34]. An integrated systems approach was obtained by coupling Navier Stokes equation to Advection-Diffusion equation to numerically model solute absorption process by arterial walls and to understand the relationships between local features of blood flow, the solutes that nourish the arterial wall and the pathologies that may appear [35].

In this work, we capture the variation of mass transfer of ions through the growth medium owing to transient changes in the shear field. We develop a computer

model that will emulate the *in-vitro* flow experiments. Preliminary results of our work show the importance of species mass transfer in triggering signal transduction pathways. In this work, we also modelled the effect of steady, pulsatile, and oscillatory flow on the generation of a chemical species. To model vascular plaque, we simulate the *in-vitro* experiments using backward facing step (BFS). We subsequently showed the effect of stagnant and recirculation flow on the velocity field and the transport of a chemical species.

We mathematically simulate a 2-D parallel flow chamber experiment to simulate the biochemical or mass transfer response of the vascular endothelium to varying blood flow parameters. The corresponding effect of amplitude and frequency of pulsatile and oscillatory blood flow on mass flux is studied.

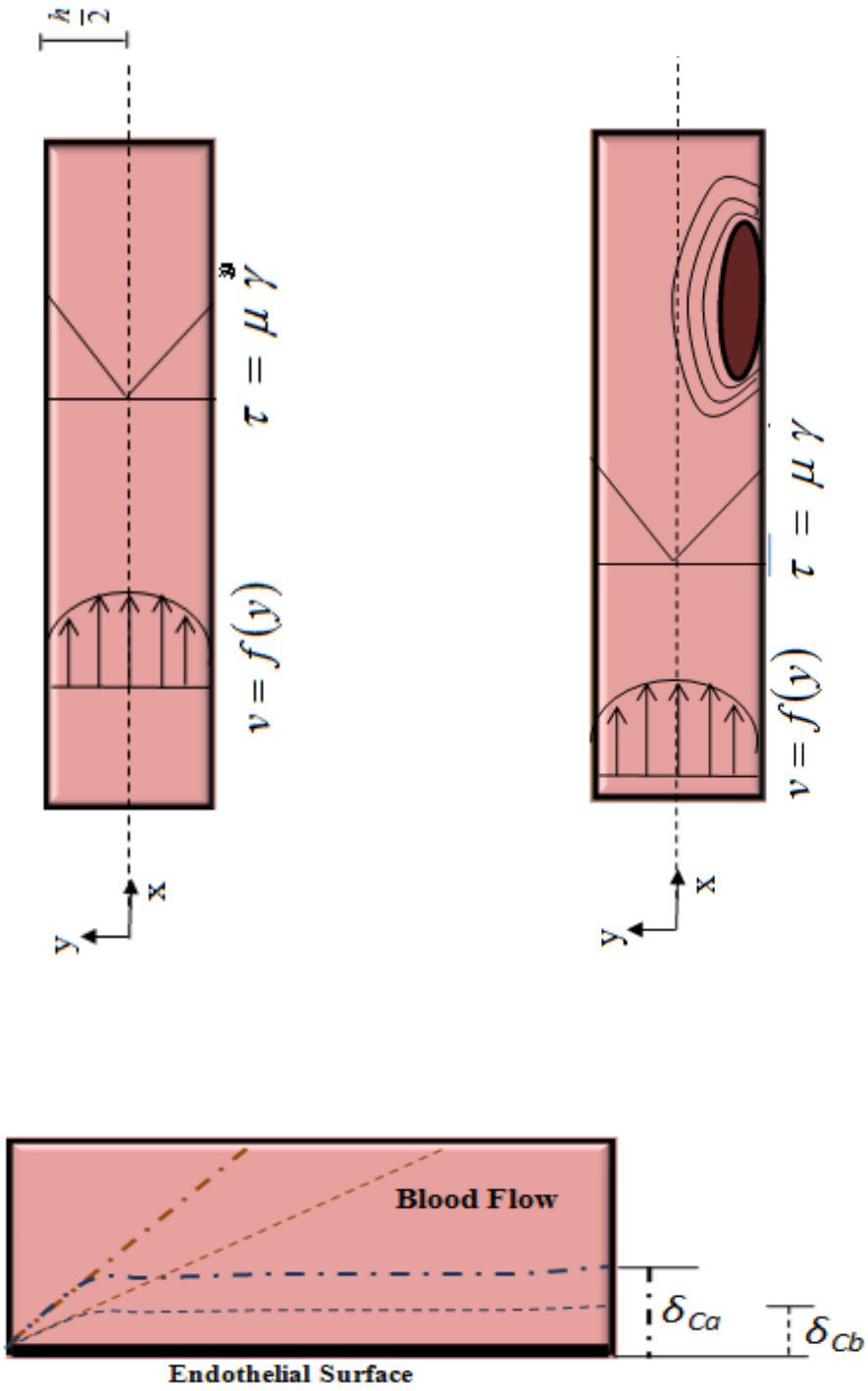

Figure 9.1| A blood vessel showing its velocity profile and shear stress experienced by the endothelial cell surface. Boundary layer concentration profiles for two scenarios - low shear (δ_{Ca}) and high shear (δ_{Cb}). Notice the steepened slope for a high shear concentration boundary layer.

9.3 MATERIALS AND METHODS

9.3.1 Computer simulations

Comsol Multiphysics® (Version 5.1, Burlington, MA, U.S.A) was used to numerically simulate the parallel flow chamber. Parameters from Table 2, Table 3 and Table 4 was used as the input values for the simulations. The diffusion coefficient of Ca^{2+} was obtained from Ando *et al*. [37]. The dimensions of the flow chamber and the viscosities of the growth medium were obtained from Korenaga *et al*. [1].

9.3.1.1 Governing equations

The Newtonian DMEM fluid phase is governed by the (1) continuity equation to ensure the mass conservation and the (2) incompressible Navier-Stokes equation to describe the momentum conservation.

$$\nabla \cdot v = 0 \tag{1}$$

$$\rho \frac{\partial v}{\partial t} + \rho v \cdot \nabla v = \nabla \cdot \left[\mu \left(\nabla v + (\nabla v)^T \right) \right] \tag{2}$$

where, v is velocity field, μ is viscosity, and ρ is density.

The Ca^{2+} flowing through the system follows the (1) equation of conservation of mass flowing through an incompressible medium and (2) Fick's Law of Diffusion.

$$\frac{\partial C_o}{\partial t} + \nabla.\left(-D\nabla C_o\right) = v.\nabla C_o \tag{3}$$

where, C_o is concentration of Ca^{2+}.

The consumption of Ca^{2+} from the DMEM occurs at the BAEC seeded surface. DMEM flows over the endothelial surface and Ca^{2+} in the fluid are transported to the surface by convection and diffusion. The flux, $N_{y=0}$ of Ca^{2+} at the endothelial cell surface can be equated to the consumption rate of Ca^{2+} by a first order reaction.

$$N_{y=0} = -k'\left(C_o\right) \tag{4}$$

where, $C_{y=0}$ is the concentration of the Ca^{2+} at the endothelial cell surface and k' is the first order rate coefficient (cm/s)

For our system, *Da*

$$Da = \frac{mass\ transfer\ time}{consumption\ time} > 1 \tag{5}$$

The values of *Da* for flow rates and viscosities of the growth medium are shown in Table 3. When *Da* » 1, the mass transfer time of the Ca^{2+} is much longer than its consumption time. The rate of consumption is limited by the time that is required to transport the Ca^{2+} to the endothelial bed. Since the reaction rate depends on the amount of Ca^{2+} transported to the endothelial surface, our system will be considered to be mass transfer limited.

For steady flow conditions, the cells were subjected to a mean shear of 10 dynes/cm^2. For pulsatile flow conditions, the cells were subjected to a maximum-minimum shear stress of 12-10 dynes/cm^2 respectively and a frequency of 1 Hz. For near zero flow conditions, the cells were exposed to 0.02 dyne/cm^2.

We computationally simulate mass transfer experiments by defining a reaction at the endothelial cells of Model 1.

$$C_1 \rightarrow C_2$$

where, C_1 and C_2 are species being consumed and generated at the endothelial cells respectively.

To capture the effects of laminar flow and turbulent flow, the mass transfer coefficient, k_f is defined as a function of *Re* and *Sc* [43].

$$k_f = 0.037\left(\frac{D^{0.66}V^{0.8}}{L^{0.2}\upsilon^{1.4}}\right) - 871\left(\frac{D^{0.66}\upsilon^{0.33}}{L}\right) \tag{6}$$

The consumption of C_1 and generation of C_2 are defined as

$$N_1\big|_{y=0} = -k'(C_1) \tag{7}$$

$$N_2\big|_{y=0} = k(C_1) \tag{8}$$

For a pulsatile flow, **a**ssuming that the healthy artery has a parabolic profile, the velocity profile for a laminar flow,

$$v_{pulsatile} = 6v_{max}\left(\frac{y}{h}\left(1-\frac{y}{h}\right)\right)(1 + (b \times \sin 2\pi f t)) \tag{9}$$

where $b < 1$. b is the pulse with and f is the frequency of pulse.

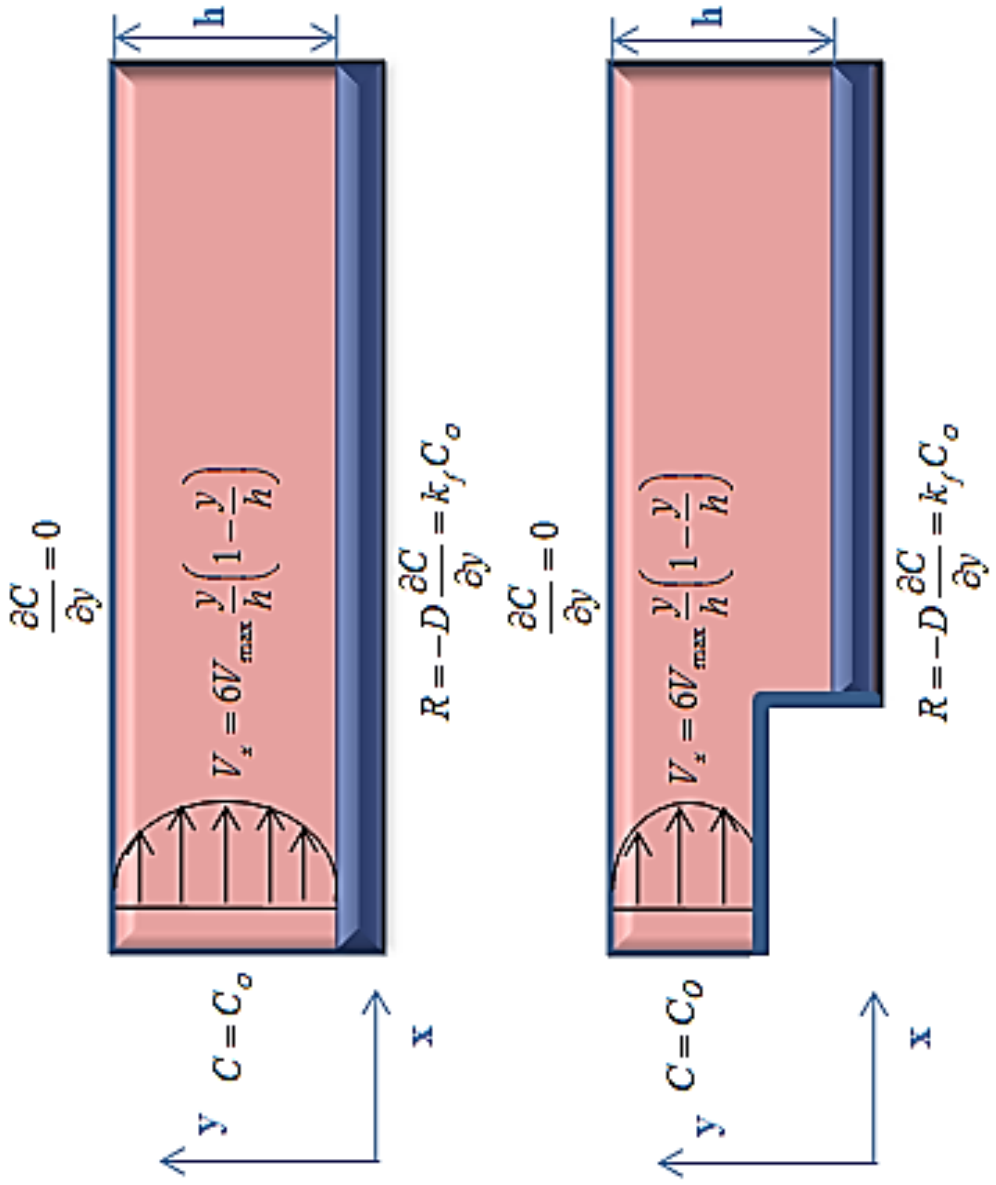

Figure 9.2| A blood vessel showing its velocity profile and shear stress experienced by the endothelial cell surface. Boundary layer concentration profiles for two scenarios - low shear (δ_{Ca}) and high shear (δ_{Cb}). Notice the steepened slope for a high shear concentration boundary layer.

9.3.3 Mathematical solver

Sparse object oriented linear equations solver (SPOOLES), a library for solving sparse real and complex linear systems of equations, provided by COMSOL Multiphysics ® has been used to simulate the steady flow model of the parallel plate chamber.

9.3.4 Mesh analysis

The boundary layer mesh tool provided by Comsol Multiphysics® was used to model the hydrodynamic and concentration boundary layers of the underlying system. Quadrilateral boundary layer mesh was incorporated to provide dense element distribution in the normal direction along the boundary where endothelial cells are seeded.

9.4 RESULTS AND DISCUSSION

The backward facing step (BFS) is a simple model of flow disturbance and has formed the basis for the design of flow chambers that allow studies of EC responses to shear stress during diseased conditions such as atherosclerosis [1]. In our work, we modeled a flow chamber within which cultured endothelial cell layer is exposed to complex flows.

9.4.1 Mesh analysis

Figure 9.3 shows the structured computational mesh used in simulations. Notice the finer mesh distribution at the endothelial bed and near the steps. This allows for a better resolution of the large velocity and concentration gradients within the recirculation region downstream of the step and adjacent to the walls. Three different cases of vertical steps have need simulated: Case 1, Case 2, and Case 3 have dimensions of 0.005, 0.010, and 0.015 cm respectively. We compare our results to those of Chiu *et al.* (1998) and Choi *et al.* (2007).

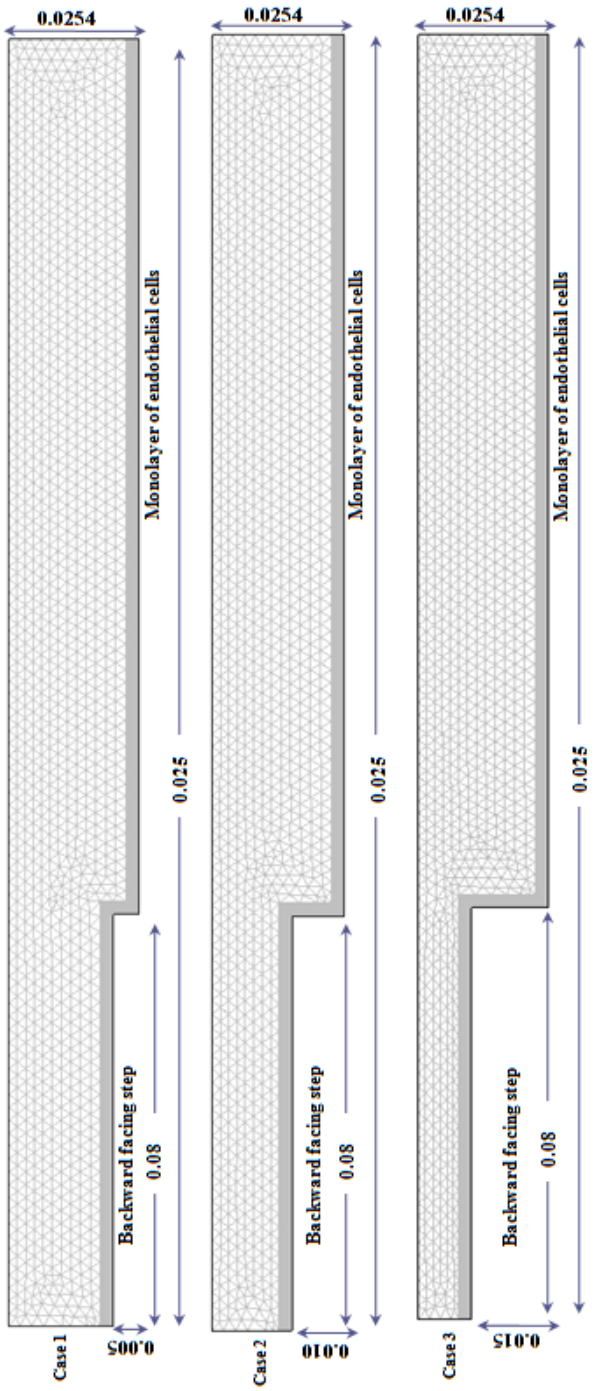

Figure 9.3| The generated mesh for Model 3 and Model 4. The figure shows a simulated parallel flow chamber with a backward facing step of 0.005, 0.010, and 0.015 cm and the endothelial cells seeded at the bottom surface.

9.4.2 Dimensionless numbers

The Reynolds Number (*Re*), Schmidt Number (*Sc*), and Damkohler Number (*Da*) were calculated for growth medium of two viscosities and are shown in Table 3. The corresponding hydrodynamic and concentration boundary layer heights were determined. Table 3 shows the dimensionless numbers and boundary layer heights for four velocities and two viscosities. *Re* increases with an increase in velocity. *Sc* is constant for a particular viscosity. *Da* increases as the velocity increases and viscosity is kept constant. As the velocity increases, we observe a decrease in the concentration boundary layer height. As the viscosity increases, the Da increases and the concentration boundary layer decreases.

9.4.3 Pulsatile flow

For a pulsatile flow, the characteristic time of the pulse is proportional to the reciprocal of the frequency ω. We study the effect of pulse frequencies by taking into account the Womersely number (α) which scales the characteristic time of the pulse with the characteristic time of momentum transport. Table 4 shows the Womersely number (α) for pulse frequencies. As ω increases, we observe an increase in α. We observe a decrease in α as the diffusivity increases. Notice that the Womersely number is independent of the velocity.

Table 9.1. Velocity, dimensionless numbers, and boundary layer heights for the modeled parallel flow chamber.

Velocity (cm/s)	*Reynolds Number, Re*	*Schmidt Number, Sc*		*Damkohler Number, Da*		*Boundary layer heights ($X10^2$ cm)*			
						Hydrodynamic		*Concentration*	
		v_1	v_2	v_1	v_2	v_1	v_2	v_1	v_2
0.0725	0.35	1361	20883	5	12.26	7.8	7.8	0.70	0.283
0.29	1.40	1361	20883	3.125	7.764	3.9	3.9	0.35	0.142
1.16	5.86	1361	20883	1.923	4.92	1.9	1.9	1.71	0.069
4.63	21.73	1361	20883	1.282	3.11	1.0	1.0	0.09	0.036

Table 9.2. Physiologically relevant frequencies and corresponding Womersely numbers (α) for two viscosities.

Frequency (beats per minute)	*Frequency (rad/s)*	*Womersely Number* α	
		ν_1	ν_2
40	4.18	0.533	0.267
60	6.28	0.653	0.327
80	8.38	0.754	0.378
100	10.47	0.843	0.423
120	12.56	0.924	0.463

We studied the effect of pulse amplitudes and pulse frequencies on normalized consumed mass flux. Figures 9.4(A) and 9.4(B) show the normalized consumed mass flux at the endothelium for pulse amplitudes and pulse frequencies. For our simulations, we used Equation (9) as the inlet velocity, and Table 4 as the pulse amplitude (*b*) and the pulse frequency (*f*).

With increasing pulse amplitude, we observe an increase in normalized consumed mass flux as the species mass flux is directly related to the velocity of the blood. However, with an increase in Womersely number (or) an increase in pulse frequency, we observe a decrease in normalized consumed mass flux. As the Womersely number increases, the species being transferred stays for relatively less time at the endothelium and the species cannot be consumed.

These findings may have important implications for different signaling in endothelial cells subjected to different types of flow. Figure 9.5 shows the velocity profile, the concentration map of C_1 and the concentration map of C_2 of a BFS with height 0.015 cm. Notice the streamlines of the velocity field. The areas of recirculation are seen distal to the step.

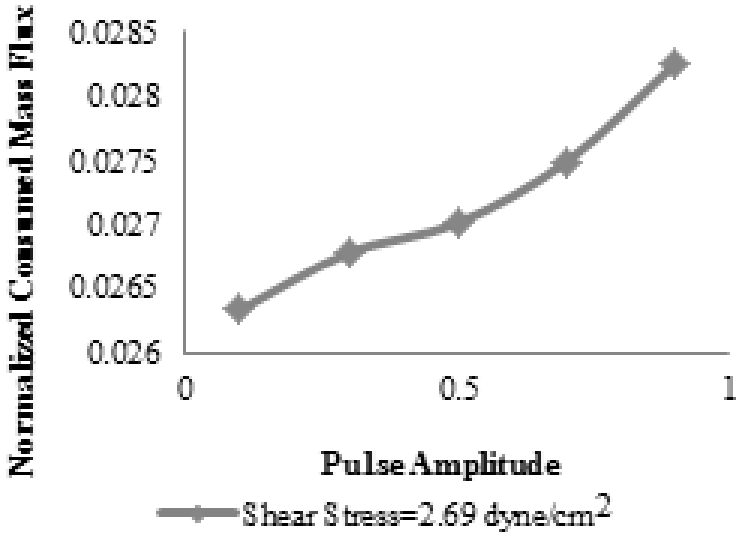

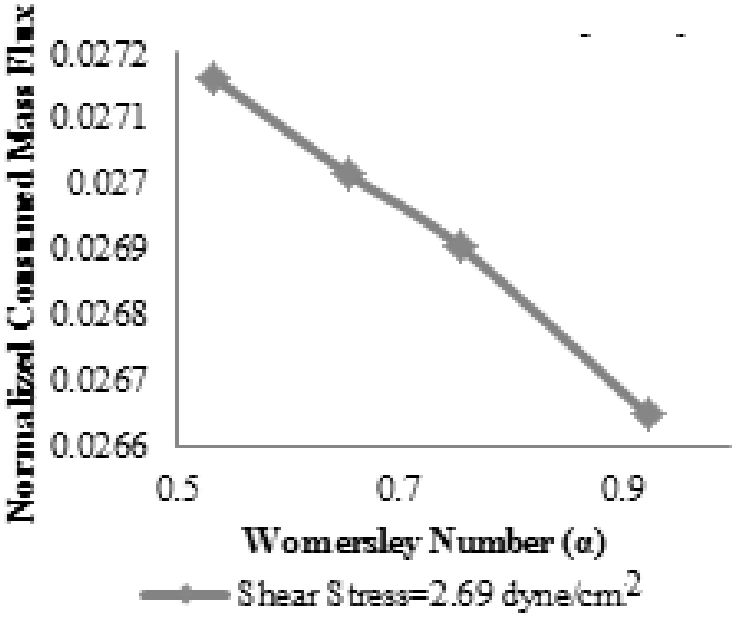

Figure 9.4| Results from the computer simulations showing normalized concentration flux for a velocity corresponding to a shear stress of 2.6 dynes/cm^2 and (A) pulse amplitudes (B) and pulse frequencies.

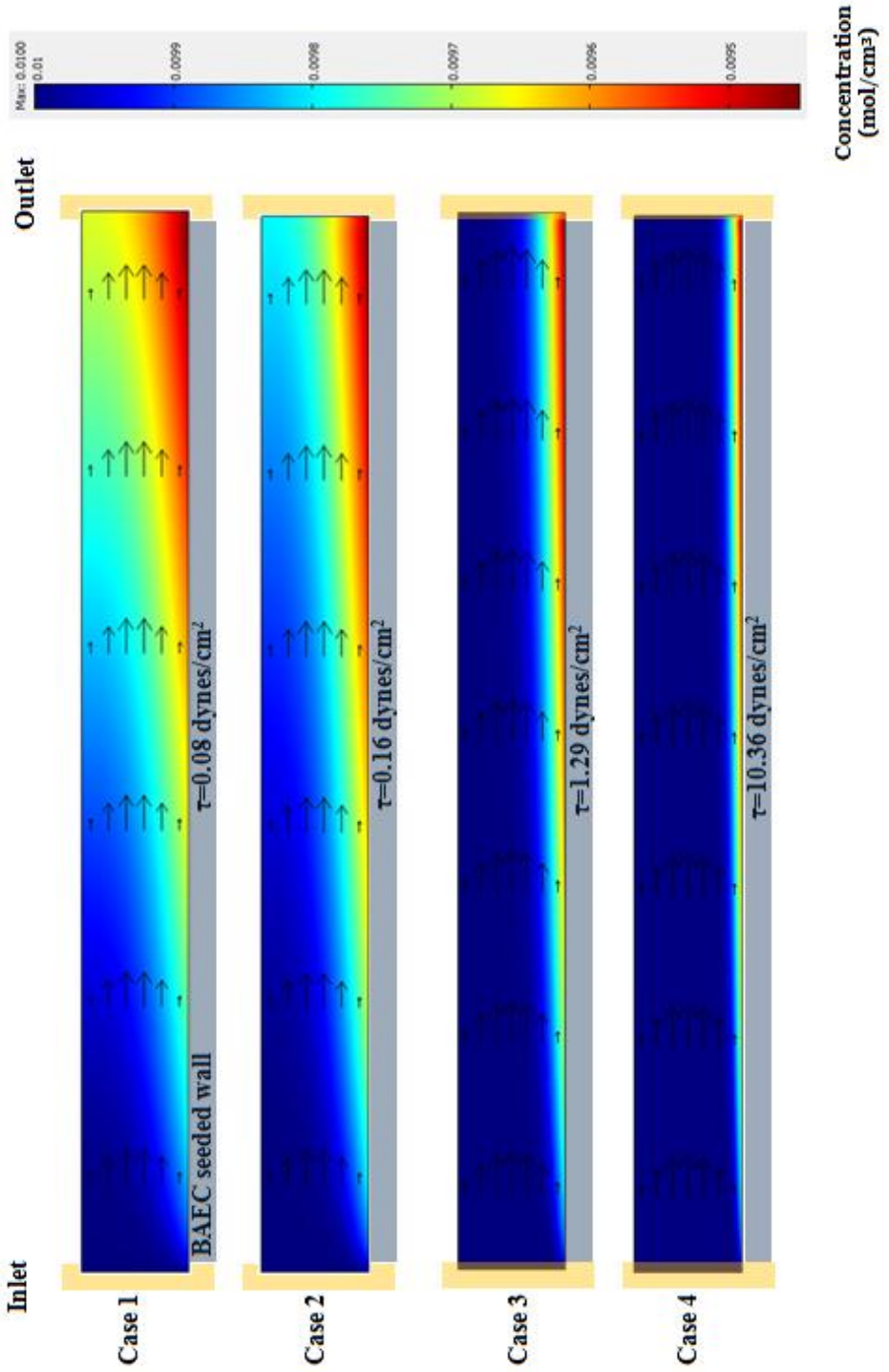

Figure 5| Concentration profiles of consumed species for four cases of shear stress. A mass balance for the system is performed at the inlet and at the outlet. Notice that as the flow loading (shear stress) increases, the boundary layer height decreases at the endothelial cell wall.

9.4.4 Mass transfer on cells seeded on the bottom surface in restenosis

Figure 9.6 shows the velocity profile, the concentration map of C_1 and the concentration map of C_2 of a vertical step with height 0.015 cm. Notice the streamlines of the velocity field in Figure 9.6. The endothelial cell layer is seeded on the bottom plate. The areas of recirculation are seen distal to the step.

Figure 9.6 compares the concentration of the generated species, C_2 at the endothelial cell surface in a parallel flow chamber emulating a healthy artery and that emulating an advanced and initial atheroma of 0.015 cm and 0.005 cm thickness respectively. We see an increase in the consumption of C_1 at the disturbed flow region. This increase in mass transfer of C_1 might provide the rationale for the increase in DNA replication shown by Chiu *et al.* (1998) [3].

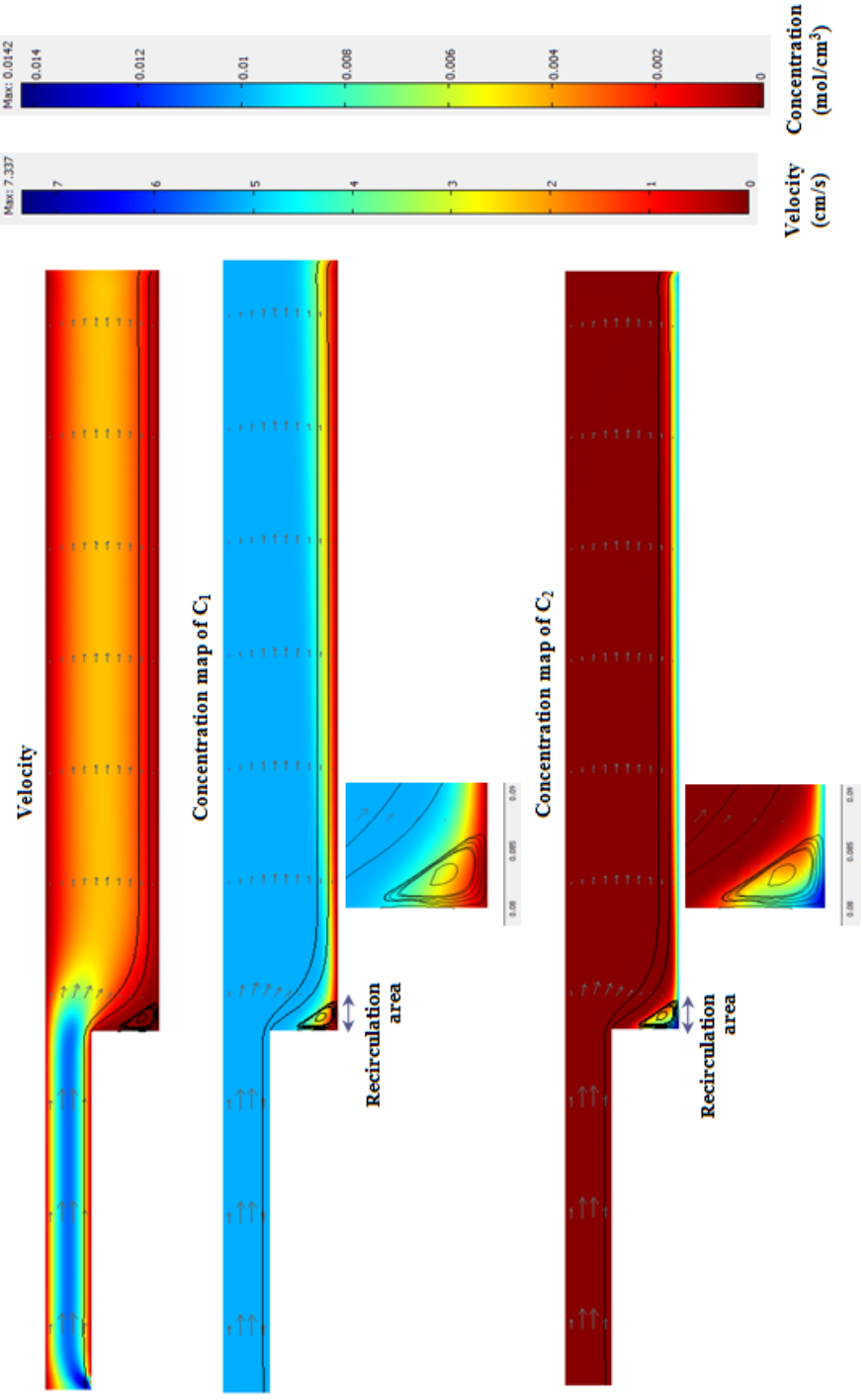

Figure 9.6| Velocity profile and concentration profiles of C_1 and C_2 when cells are exposed to a shear stress of 10 dynes/cm^2 in a parallel flow chamber having a back step of 0.015 cm. The recirculation area is marked and zoomed out for clarity. Cells are seeded only at the bottom of the flow chamber.

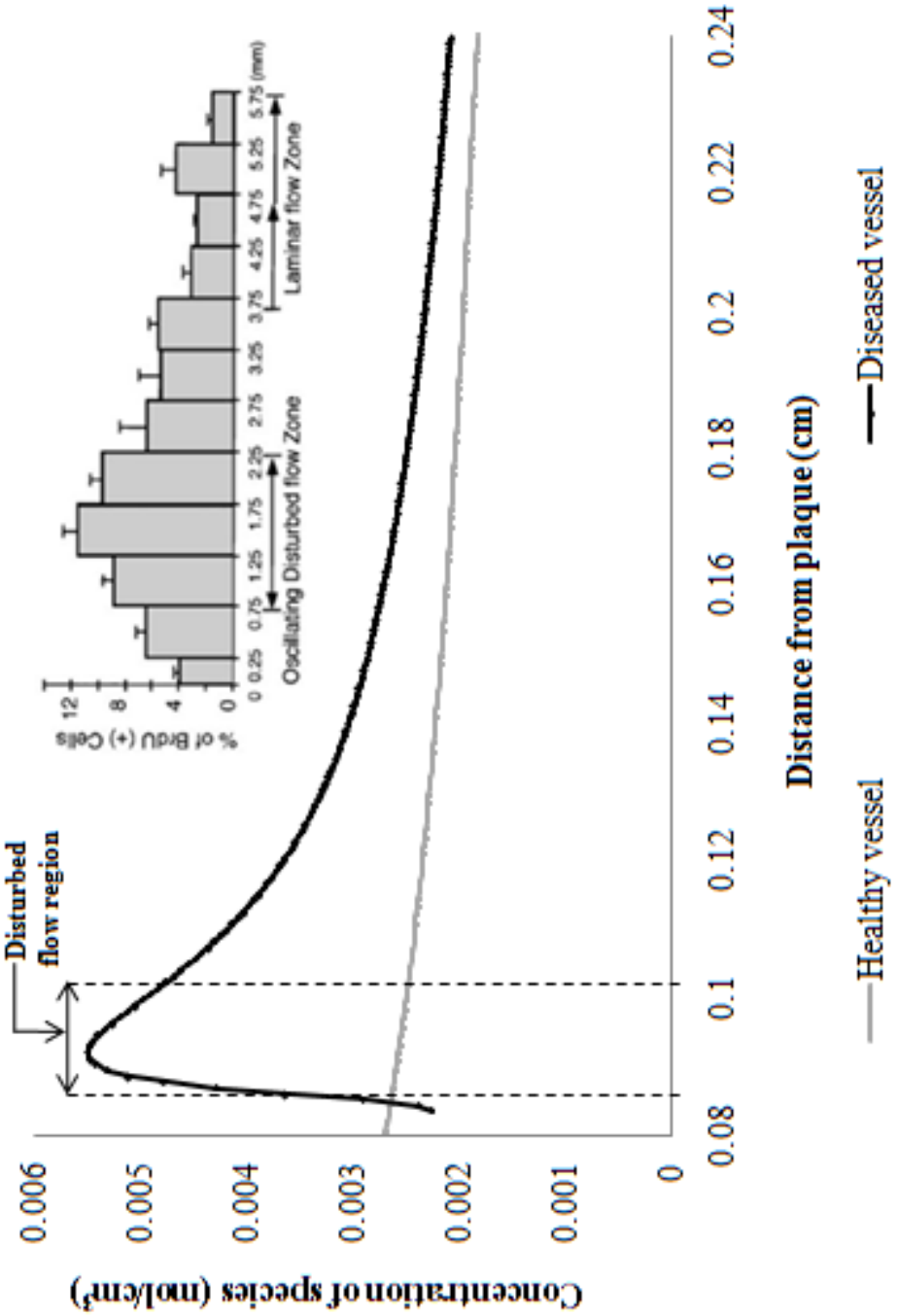

Figure 9.7| Comparing the concentration of the consumed species at the endothelial cell surface. We observe an increased consumption of species in the disturbed flow region similar to the *in-vitro* studies of Chiu *et al.* (1998) as shown in the inset.[3]

4.5 Effect of mass transfer on cells seeded on the bottom surface along with the step in restenosis

Figure 9.8 shows the velocity profile, the concentration map of C_1 and the concentration map of C_2 of a vertical step with height 0.015 cm. The endothelial cell layer is seeded on the step in addition to the bottom plate. Notice the streamlines of the velocity field in the three Figures. The areas of recirculation are seen distal to the step.

Figure 9.8 compares the concentration of the generated species, C_2 at the endothelial cell surface in a parallel flow chamber emulating a healthy artery and that emulating an advanced and initial atheroma of 0.015 cm and 0.005 cm thickness respectively. To compare our results to Choi *et al*. (2007), we seed the backstep with endothelial cells [4]. We observe a sudden burst in the production of C_2 where the atheroma ends (0.08 cm).

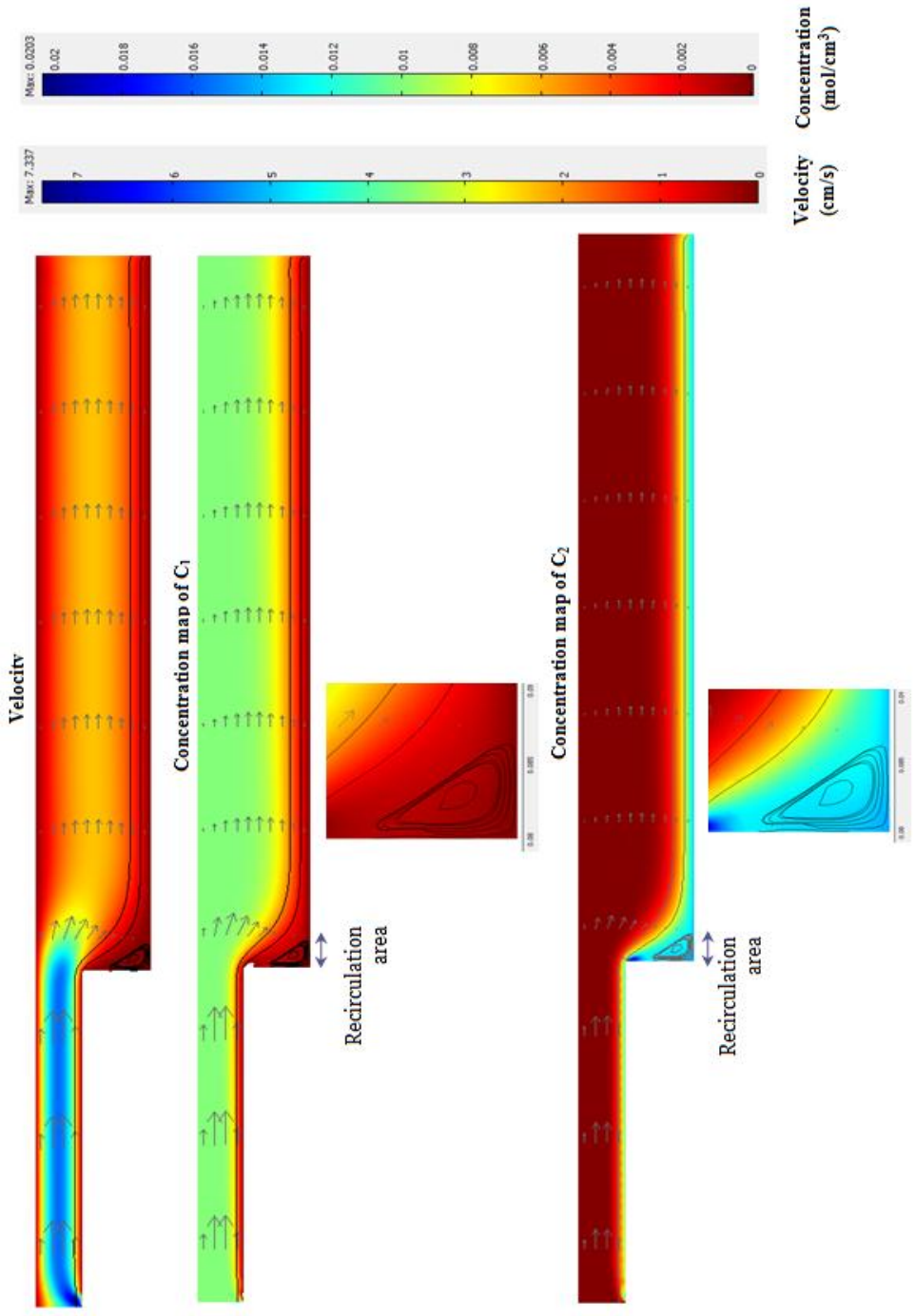

Figure 9.8| Concentration of generated species at the endothelial bed diseased versus healthy vasculature using a reaction system. The plaque ends at 0.08 cm where we observe a sudden burst in the production of the species. In the inset, a similar peak is observed in the work by Choi *et al.* (2007).[4]

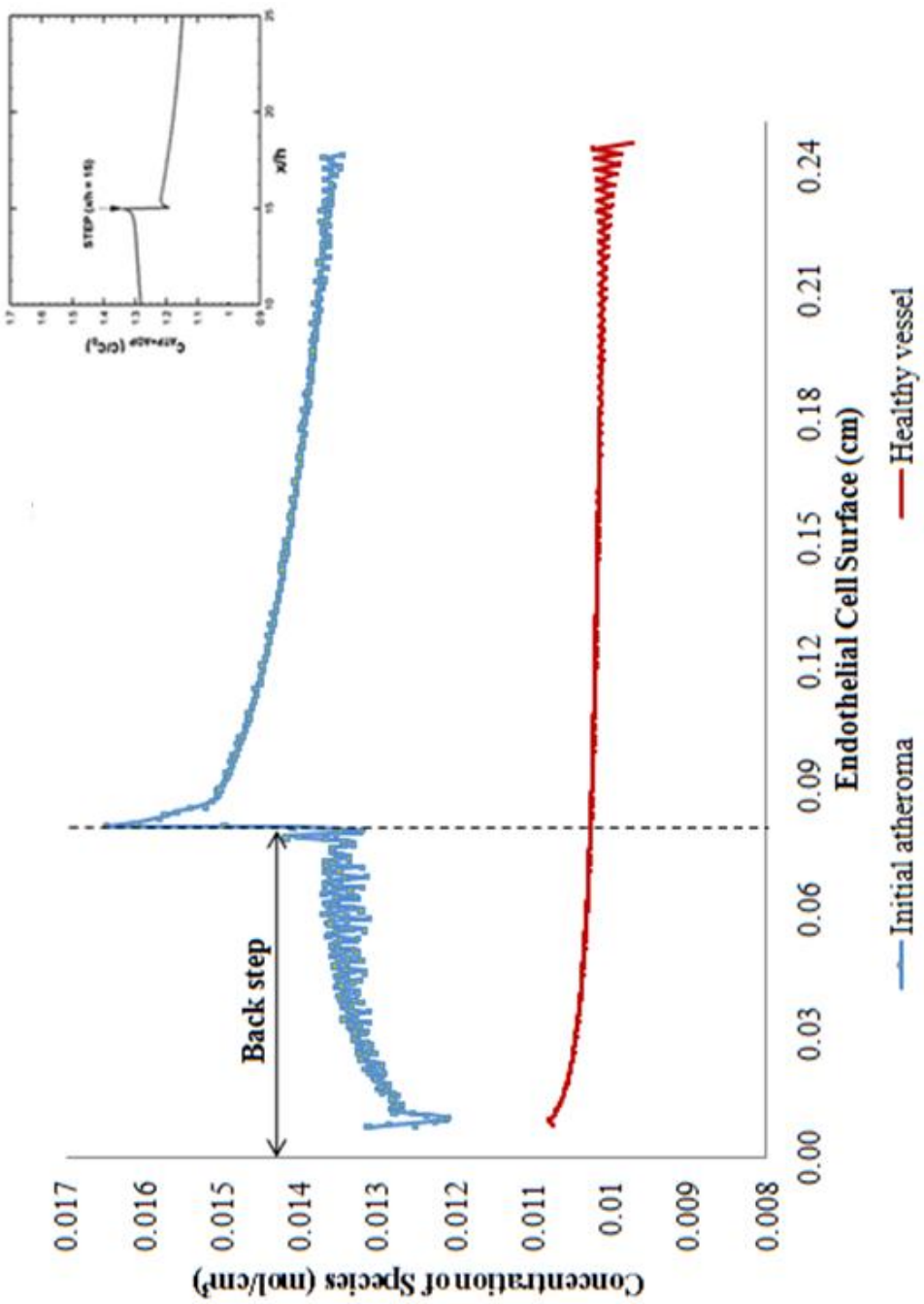

Figure 9.9| Concentration of generated species at the endothelial bed diseased versus healthy vasculature using a mass transfer limited system. Comparing the concentration of the generated species at the endothelial cell surface. The plaque ends at 0.08 cm where we observe a sudden burst in the production of the species. In the inset, a similar peak is observed in the work by Choi *et al.* (2007).[4]

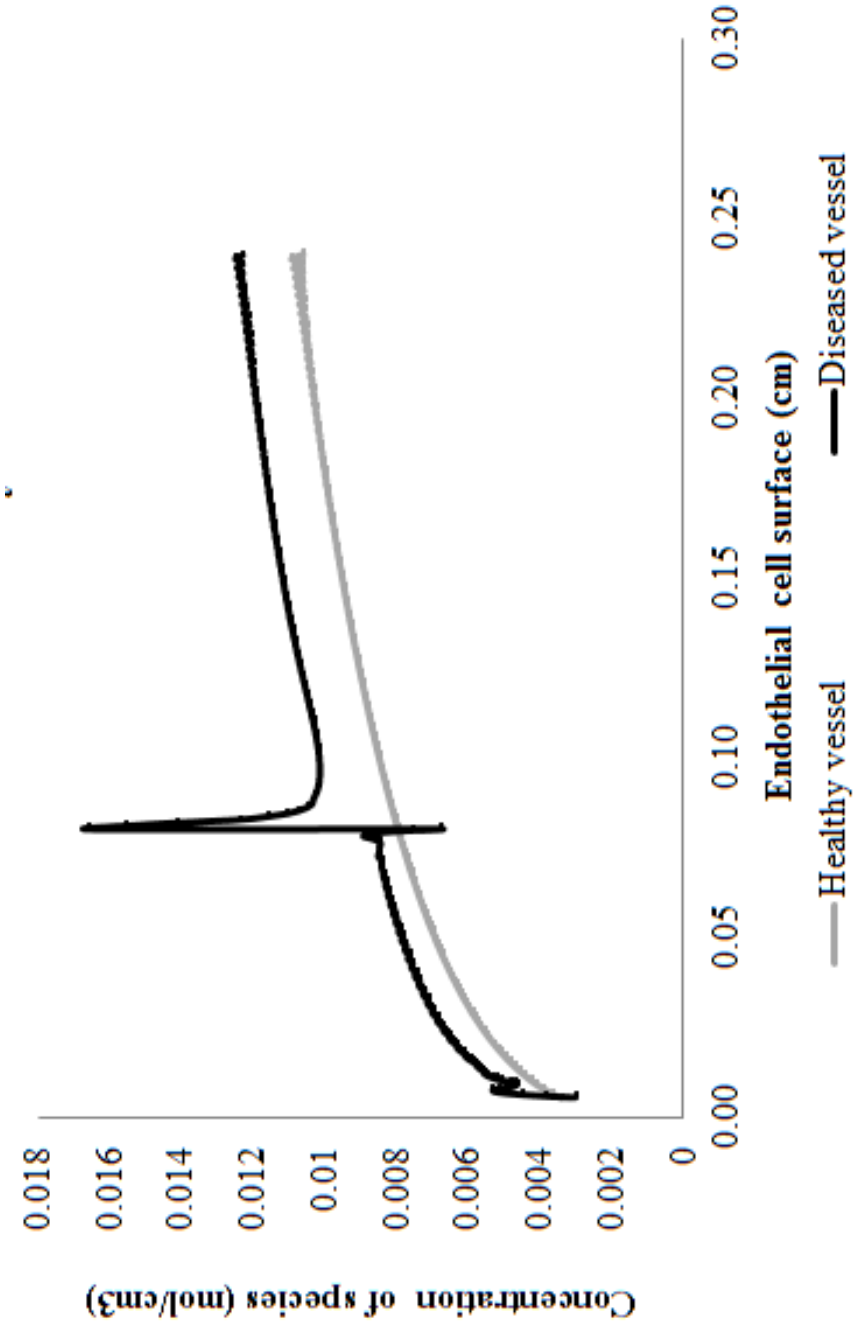

Figure 9.10| Concentration of generated species at the endothelial bed diseased versus healthy vasculature using a reaction system. The plaque ends at 0.08 cm where we observe a sudden burst in the production of the species. In the inset, a similar peak is observed in the work by Choi *et al.* (2007).[4]

9.5 CONCLUSION

Steady and pulsatile laminar flow of growth medium having two viscosities will be simulated. We compare mass transfer-limited simulation results with previous results used to establish mechanotransduction dependency for endothelial flow-dependent signaling. In our work, simulated models are based on the representative experiments performed by Choi *et al.* (2007) and Chiu *et al*. (1998) [1,12]. We mathematically simulate a parallel flow chamber experiment to obtain the biochemical or mass transfer response of the vascular endothelium to varying blood flow parameters. A more cautious analysis is warranted that specifically addresses the predicted outcomes for a mass-transfer limited system. We hypothesize that a pure mass transfer system might explain the characteristic behavior exhibited by endothelial signaling pathways which have been shown to be a result of only mechanotransducers.

In our work, these characteristic behaviors of endothelial cell signaling pathways, which have been demonstrated to be a resultant of mechanotransducers, are revisited using a mass transfer-limited system only. Our work shows persuasive results that emphasize the necessity of considering the role of mass transfer while deducing inferences of the dynamic vascular environment.

The findings from our computer simulations have important implications for signaling in endothelial cells when subjected to different flow parameters. By comparing the results of Korenaga *et al.* (1997), Frangos *et al.* (1985), Chiu *et al.* (1998), and Choi *et al.* (2007) with the results of our computer simulations, we can confidently say that we devised the computational tools to mimic the physiological conditions of endothelial cells

in atheroprotective and atherogenic vasculature. We will be employing these tools throughout this work. Our computer simulations explicitly show that species mass transfer in the vasculature plays a significant role in signaling pathways.

9.6 REFERNCES

1 Korenaga R, Ando J, Kosaki K, Isshiki M, Takada Y, and Kamiya A. Negative transcriptional regulation of the VCAM-1 gene by fluid shear stress in murine endothelial cells. American Journal of Physiology-Cell Physiology 1997;273:C1506-C1515.

2 Ando J, Ohtsuka A, Korenaga R, Kawamura T, and Kamiya A. Wall Shear-Stress Rather Than Shear Rate Regulates Cytoplasmic Ca^{2+} Responses to Flow in Vascular Endothelial-Cells. Biochemical and Biophysical Research Communications 1993;190:716-723.

3 Chien S. Effects of Disturbed Flow on Endothelial Cells. Annals of Biomedical Engineering 2008;36:554-562.

4 Ku DN. Blood Flow In Arteries. Annual Review of Fluid Mechanics 1997;29:399-434.

5 Frangos JA, Eskin SG, McIntire LV, and Ives CL. Flow Effects on Prostacyclin Production By Cultured Human-Endothelial Cells. Science 1985;227:1477-1479.

6 Caro CG, Fitzgera JM, and Schroter RC. Atheroma and Arterial Wall Shear - Observation, Correlation and Proposal of a Shear Dependent Mass Transfer Mechanism for Altherogenesis. Proceedings of the Royal Society of London Series B-Biological Sciences 1971;177:109.

7 Dull RO and Davies PF. Flow Modulation of Agonist (ATP)-Response (Ca^{2+}) Coupling in Vascular Endothelial-Cells. American Journal of Physiology 1991;261:H149-H154.

8 Topol EJ. Textbook of cardiovascular medicine. Lippencott-Raven. 1998. p 3

9 Beckman JS and Koppenol WH. Nitric oxide, superoxide, and peroxynitrite: The good, the bad, and the ugly. American Journal of Physiology-Cell Physiology 1996;271:C1424-C1437.

10 Kakolyris S, Karakitsos P, Tzardi M, and Agapitos E. Immunohistochemical Detection of Fibronectin in Early and Advanced Atherosclerosis. In Vivo (Attiki) 1995;9:35-40.

11 Nakashima Y, Fujii H, Sumiyoshi S, Wight TN, and Sueishi K. Early Human Atherosclerosis - Accumulation of Lipid and Proteoglycans in Intimal Thickenings Followed by Macrophage Infiltration. Arteriosclerosis Thrombosis and Vascular Biology 2007;27:1159-1165.

12 Hynes RO. Integrins - Versatility, Modulation, and Signaling in Cell-Adhesion. Cell 1992;69:11-25.

13 Jalali S, del Pozo MA, Chen KD, Miao H, Li YS, Schwartz MA, Shyy JYJ, and Chein S. Integrin-Mediated Mechanotransduction Requires its Dynamic Interaction with Specific Extracellular Matrix (ECM) Ligands. Proceedings of the National Academy of Sciences of the United States of America 2001;98:1042-1046.

14 Hahn C, Orr AW, Sanders JM, Jhaveri KA, and Schwartz MA. The Subendothelial Extracellular Matrix Modulates JNK Activation by Flow. Circulation Research 2009;104:995-U180.

15 Iiyama K, Hajra L, Iiyama M, Li HM, DiChiara M, Medoff, Myron IC. Patterns of Vascular Cell Adhesion Molecule-1 and Intercellular Adhesion Molecule-1

Expression in Rabbit and Mouse Atherosclerotic Lesions and at Sites Predisposed to Lesion Formation. Circulation Research 1999;85:199-207.

16 Go Y-M, Park H, Maland MC, Darley-Usmar VM, Stoyanov B, Wetzker R, Jo H. Phosphatidylinositol 3-Kinase Gamma Mediates Shear Stress-Dependent Activation of JNK in Endothelial Cells. American Journal of Physiology 1998;275:H1898-H1904.

17 Shyy JYJ. Extracellular Matrix Differentiating Good Flow versus Bad Flow. Circulation Research 2009;104:931-932.

18 Ricci R, Sumara G, Sumara I, Rozenberg I, Kurrer M, Akhmedov A, et al. Requirement of JNK2 for Scavenger Receptor A-Mediated Foam Cell Formation in Atherogenesis. Science 2004;306:1558-1561.

19 Carling D. The AMP-Activated Protein Kinase Cascade - a Unifying System for Energy Control. Trends in Biochemical Sciences 2004;29:18-24.

20 Hardie DG, Salt IP, Hawley SA, and Davies SP. AMP-Activated Protein Kinase: an Ultrasensitive System for Monitoring Cellular Energy Charge. Biochemical Journal 1999;338:717-722.

21 Hardie DG, Carling D, and Sim ATR. The Amp-Activated Protein-Kinase - a Multisubstrate Regulator of Lipid-Metabolism. Trends in Biochemical Sciences 1989;14:20-23.

22 Sanders MJ, Grondin PO, Hegarty BD, Snowden MA, and Carling D. Investigating the Mechanism for AMP Activation of the AMP-Activated Protein Kinase Cascade. Biochemical Journal 2007;403:139-148.

23 Arad M, Seidman CE, and Seidman JG. AMP-activated protein kinase in the heart - Role during health and disease. Circulation Research 2007;100:474-488.

24 Levesque MJ and Nerem RM. The Elongation and Orientation of Cultured Endothelial-Cells in Response to Shear-Stress. Journal of Biomechanical Engineering-Transactions of the Asme 1985;107:341-347.

25 Nagata D, Mogi M, and Walsh K. AMP-Activated Protein Kinase (AMPK) Signaling in Endothelial Cells is Essential for Angiogenesis in Response to Hypoxic Stress. Journal of Biological Chemistry 2003;278:31000-31006.

26 Chen Z, Peng IC, Sun W, Su MI, Hsu PH, Fu Y, et al. AMP-Activated Protein Kinase Functionally Phosphorylates Endothelial Nitric Oxide Synthase Ser633. Circulation Research 2009;104:496-U159.

27 Adams DJ, Barakeh J, Laskey R, Vanbreemen C. Ion Channels and Regulation of Intracellular Calcium in Vascular Endothelial-Cells. Faseb Journal 1989;3:2389-2400.

28 Nollert MU, Diamond SL, and McIntire LV. Hydrodynamic Shear-Stress and Mass-Transport Modulation of Endothelial-Cell Metabolism. Biotechnology and Bioengineering 1991;38:588-602.

29 Libby P. Inflammation in atherosclerosis. Nature 2002;420:868-874.

30 John K and Barakat AI. Modulation Of ATP/ADP Concentration at the Endothelial Surface by Shear Stress: Effect of Flow-Induced ATP Release. Annals of Biomedical Engineering 2001;29:740-751.

31 David T. Wall Shear Stress Modulation of ATP/ADP Concentration at the Endothelium. Annals of Biomedical Engineering 2003;31:1231-1237.

32 Olgac U, Kurtcuoglu V, and Poulikakos D. Computational Modeling of Coupled Blood-Wall Mass Transport of LDL: Effects of Local Wall Shear Stress. American Journal of Physiology-Heart and Circulatory Physiology 2008;294:H909-H919.

33 Rappitsch G, Perktold K, and Pernkopf E. Numerical Modeling of Shear-dependent Mass Transfer in Large Arteries. International Journal for Numerical Methods in Fluids 1997;25:847-857.

34 Fadel AA. A Computational Model of Nitric Oxide Production and Transport in a Parallel Plate Flow Chamber. Annals of Biomedical Engineering 2009;37:943-954.

35 Quarteroni A, Veneziani A, and Zunino P. Mathematical and Numerical Modeling of Solute Dynamics in Blood Flow and Arterial Walls. Siam Journal on Numerical Analysis 2002;39:1488-1511.

36 Schetz AE and Fuhs AE. Fundamentals of Fluid Mechanics. Wiley 1999. p 486

37 Ando J, Komatsuda T, and Kamiya A. Cytoplasmic Calcium Response to Fluid Shear Stress in Cultured Vascular Endothelial Cells. In Vitro Cellular & Developmental Biology 1988;24:871-877.

38 Wang YX, Miao H, Li S, Chen KD, Li YS, Yuan SL, et al. Interplay Between Integrins and FLK-1 in Shear Stress-Induced Signaling. American Journal of Physiology-Cell Physiology 2002;283:C1540-C1547.

39 Rosen LA, Hollis TM, and Sharma MG. Alterations in Bovine Endothelial Histidine Decarboxylase Activity Following Exposure to Shearing Stresses. Experimental and Molecular Pathology 1974;20:329-343.

40 Truskey GA, Yuan F, and Katz DF. Transport Phenomena in Biological Systems. Pearson Hall 2009. (p 449-584)

41 Heinrich R, Neel BG, and Rapoport TA. Mathematical Models of Protein Kinase Signal Transduction. Molecular Cell 2002;9:957-970.

42 Buettner GR, Ng CF, Wang M, Rodgers VGJ, and Schafer FQ. A New Paradigm: Manganese Superoxide Dismutase Influences the Production of H_2O_2 in Cells and Thereby Their Biological State. Free Radical Biology and Medicine 2006;41:1338-1350.

43 Asthagiri AR and Lauffenburger DA. A Computational Study of Feedback Effects on Signal Dynamics in a Mitogen-Activated Protein Kinase (MAPK) Pathway Model. Biotechnology Progress 2001;17:227-239.

44 Ross R. Mechanisms of Disease - Atherosclerosis - An Inflammatory Disease. New England Journal of Medicine 1999;340:115-126.

45 Stary HC, Chandler AB, Dinsmore RE, Fuster V, Glagov S, Insull W, et al. A Definition of Advanced Types of Atherosclerotic Lesions and a Histological Classification of Atherosclerosis. Circulation 1995;92:1355-1374.

46 Raines EW, Koyama H, and Carragher NO. The Extracellular Matrix Dynamically Regulates Smooth Muscle Cell Responsiveness To PDGF. Atherosclerosis V: The Fifth Saratoga Conference 2000;902:39-52.

47 Stenman S, Vonsmitten K, and Vaheri A. Fibronectin and Atherosclerosis. Acta Medica Scandinavica 1980:165-170.

48 Levenson J, Giral P, Razavian M, Gariepy J, and Simon A. Fibrinogen and Silent Atherosclerosis in Subjects with Cardiovascular Risk-Factors. Arteriosclerosis Thrombosis and Vascular Biology 1995;15:1263-1268.

49 Heino J. The Collagen Receptor Integrins have Distinct Ligand Recognition and Signaling Functions. Matrix Biology 2000;19:319-323.

50 Schwarzbauer JE and Sechler JL. Fibronectin Fibrillogenesis: a Paradigm for Extracellular Matrix Assembly. Current Opinion in Cell Biology 1999;11:622-627.

51 Vinogradova O, Velyvis A, Velyviene A, Hu B, Haas TA, Plow EF, et al. A Structural Mechanism of Integrin Alpha(Iib)Beta(3) "Inside-Out" Activation as Regulated by its Cytoplasmic Face. Cell 2002;110:587-597.

52 Bakker SJL and Gans ROB. About the Role of Shear Stress in Atherogenesis. Cardiovascular Research 2000;45:270-272.

53 Gibson CM, Diaz L, Kandarpa K, Sacks FM, Pasternak RC, Sandor T, et al. Relation of Vessel Wall Shear-Stress to Atherosclerosis Progression in Human Coronary-Arteries. Arteriosclerosis and Thrombosis 1993;13:310-315.

54 Feldman CL, Ilegbusi OJ, Hu ZJ, Nesto R, Waxman S, and Stone PH. Determination of In-vivo Velocity and Endothelial Shear Stress Patterns with Phasic Flow in Human Coronary Arteries: A Methodology to Predict Progression of Coronary Atherosclerosis. American Heart Journal 2002;143:931-939.

55 Lowe GDO, Drummond MM, Lorimer AR, Hutton I, Forbes CD, Prentice CRM, et al. Relation Between Extent of Coronary-Artery Disease and Blood-Viscosity. British Medical Journal 1980;280:673-674.

56 Liu XP, Yan QT, Baskerville KL, and Zweier JL. Estimation of Nitric Oxide Concentration in Blood for Different Rates of Generation - Evidence that Intravascular Nitric Oxide Levels are Too Low to Exert Physiological Effects. Journal of Biological Chemistry 2007;282:8831-8836.

57 Wang YP, Shin WS, Kawaguchi H, Inukai M, Kato M, Sakamoto A, et al. Contribution of Sustained Ca^{2+} Elevation for Nitric Oxide Production in Endothelial Cells and Subsequent Modulation of Ca^{2+} Transient in Vascular Smooth Muscle Cells in Coculture. Journal Of Biological Chemistry 1996;271:5647-5655.

58 Loudon, C., Tordesillas, A., 1998. The use of the dimensionless Womersley number to characterize the unsteady nature of internal flow. Journal of Theoretical Biology 191, 63–78.

CHAPTER 10

DESIGN OF A TRANSMEMBRANE DEVICE FOR DELINEATING MASS TRANSFER FOR A CONSTANT SHEAR PROFILE

ABSTRACT

As evident from our previous results, the use of viscosity variation relative to shear gradients are not enough to eliminate mass transfer in determining the signaling mechanism in endothelium processes. In this Chapter, we propose a novel, *in-vitro* experimental methodology using membrane separations technology. The proposed method of analysis will take advantage of the potential for tangential membrane processes to modify mass transfer characteristics, in particular the concentration gradients of species, at the surface of the membrane with relatively small transmembrane pressure modifications. This can be done with little modification of the fluid shear at the membrane surface. The technique has the ability to decouple mechanotransduction effects from mass transfer in flow-induced studies. The methodology takes advantage of modest alterations of the transmembrane pressure normal to membranes that can make tremendous variations in concentration gradients at the membrane surface (and thus mass transfer) but offers virtually little change in the associated fluid shear stress experienced by the cells. The methodology is flexible and robust, can be used with mass transfer-limited and reaction-limited processes, and can address a number of controllable scenarios.

Keywords – Mechanotransduction, mass transfer, vascular signaling

10.2 INTRODUCTION

It has long been accepted that mechanotransduction, and not mass transfer, is the fundamental mechanism for hemodynamic forces modulated endothelial signaling pathways and their downstream gene products. The underpinning criteria used to determine the dominance of mechanotransduction largely draws on the relationship between signaling behavior and shear rate and shear stress, relative to changes in viscosity. However, in our work, we computationally and experimentally evaluate mass transfer-limited in-vitro parallel flow chamber systems with respect to this accepted criteria. These results show similar viscosity-dependency relative to shear rate and shear stress, previously thought to be sufficient conditions for mechanotransduction. Thus, mass transfer considerations should be carefully examined when studying triggering methods in signaling cascades.

A wide use of parallel flow chambers have been employed to study the effect of flow stimulations physiologically. Parallel flow chambers have been utilized by enumerous researchers from a little less than half a century both *in-vivo* and *in-vitro* [1-15]. A cell monolayer is attached to one of the internal plate surfaces and the cells are subjected to fluid flow by creating a pressure gradient tangential to the surface. For finite fluid dimensions, the fluid velocity remains parabolic between the plates but vanishes at the boundaries of the rectangular channel suggesting an inlet velocity that has to be considered (Shown in Chapter 8) [16-19]. Practically, more than 85% of the surface is exposed to a homogenous wall shear stress for $b=h > 20$.

However, responses of endothelial cells to shear profiles have been found to be rather complex, owing to cell contact guiding, vascular remodelling, pathological diseased conditions. Previous studies have utilized a modification of the parallel flow chamber to obtain the importance of cellular cues. Both the base rotation and the initial shape of the cilia grown on cells were accounted to experimentally capture a more accurate estimate of flexural rigidity [19]. In yet another study, the effects of fluid shear forces on cellular responses to profiled surfaces in-vitro were investigated [20]. The complexities associated with *in-vivo* vascular geometry and architectural properties, have necessitated the need for novel modeling strategies to determine local shear stress magnitudes and gradients.

Here, we propose a novel, *in-vitro* experimental methodology using membrane separations technology. The proposed technique can decouple mechanotransduction effects from mass transfer in flow induced studies. The methodology takes advantage of modest alterations of the transmembrane pressure normal to cells seeded on membranes that can make tremendous variations in concentration gradients at the membrane surface (and thus mass transfer) but offers virtually little change in the associated fluid shear stress experienced by the cells. The methodology is flexible and robust, in can be used with mass transfer-limited and reaction-limited processes and can address a number of controllable scenarios.

As evident from our previous results [21], the use of viscosity variation relative to shear rate and shear stress are not enough to eliminate mass transfer in determining the

signaling mechanism in endothelium processes. Thus, it remains plausible that biomolecular mass transfer may be significant in vascular signaling pathways. This work shows that a more cautious analysis that delineates endothelial mechanotransduction from mass transfer remains warranted. Carefully examining the effect of mass transfer will prove to play a quintessential role in elucidating endothelial flow-dependent signaling.

10.3 MATERIALS AND METHODS

10.3.1 Computational modeling

To examine this theory, a 2D computer simulation was performed to investigate the effects of modified transmembrane pressure on shear rate, shear stress and concentration profile for a species entering the membrane module at the feed location. Here Comsol Multiphysics® (Version 3.5, Burlington, MA, USA) is again used. The flow chamber was designed with a channel half-height of 0.015 cm and a length of 0.5 cm. The membrane was modelled as porous media using the Brinkman equation with a porosity of 0.84 and permeability of 15 x 10^{-9} cm^2. The initial feed concentration on the single species was 6 moles/cm^3 on the retentate side of the membrane and a mass flux of -7x10^3 moles-cm^2-s^{-1} was imposed on the filtrate side of the membrane. The inlet pressure P_1, was set at 20 dynes-cm^{-2} and the outlet P_2, was set at 10 dynes-cm^{-2}. The transmembrane pressure was varied by adjusting P_3 between the values of -2 and 4 dynes-cm^{-2}.

10.3.2 Design of transmembrane device

Essentially, it is well known that, in tangential membrane processes, the flux through the membrane pores can be several orders-of-magnitude lower than the flux across the membrane surface (reference). Thus the overall contribution of the permeate flows contribution to the tangential shear rate or shear stress is negligible. Given that the Schmidt number ($Sc = \nu/D$) is on the order of 20,000 for aqueous systems and the boundary layer heights for mass transfer, δ_C, and momentum, δ_H, are related as

$\delta_H/\delta_C \sim Sc^{1/3}$, the hydrodynamic boundary layer is on the order of 25 times greater than that for mass transfer. Thus, it is postulated that gradients in mass transfer can be altered in a narrow region near the membrane surface without substantial change in the momentum gradients.

The aspect ratio of the designed membrane device is 60:1 (1.5/0.025). An aspect ratio of less than 80 is necessary to ensure laminar flow across the system. Figure 10.1 shows the designed device with a provision of employing membrane of interest. The effective area of the membrane that is incorporated in the diafiltration module is 1.5 x 6.62 cm^2.

10.3.3 Membrane preparation

Experiments will employ asymmetric nitrocellulose membranes (0.22 μm, Whatman) with an effective area of 8 x 2.5 cm^2. The membrane will not allow the passage of ions/molecules smaller than 10 kDa. The membranes are treated with PBS-Triton 100X to remove the hydrophobic layer on one side of the membrane. Membranes will then be thoroughly rinsed with deionized water to remove wetting agent, after which they are ready to be used.

10.3.4 Solution preparation

Two different solutions were utilized in the feed streams consisting of red and blue dyes with absorbance 380 nm and 560 nm respectively.

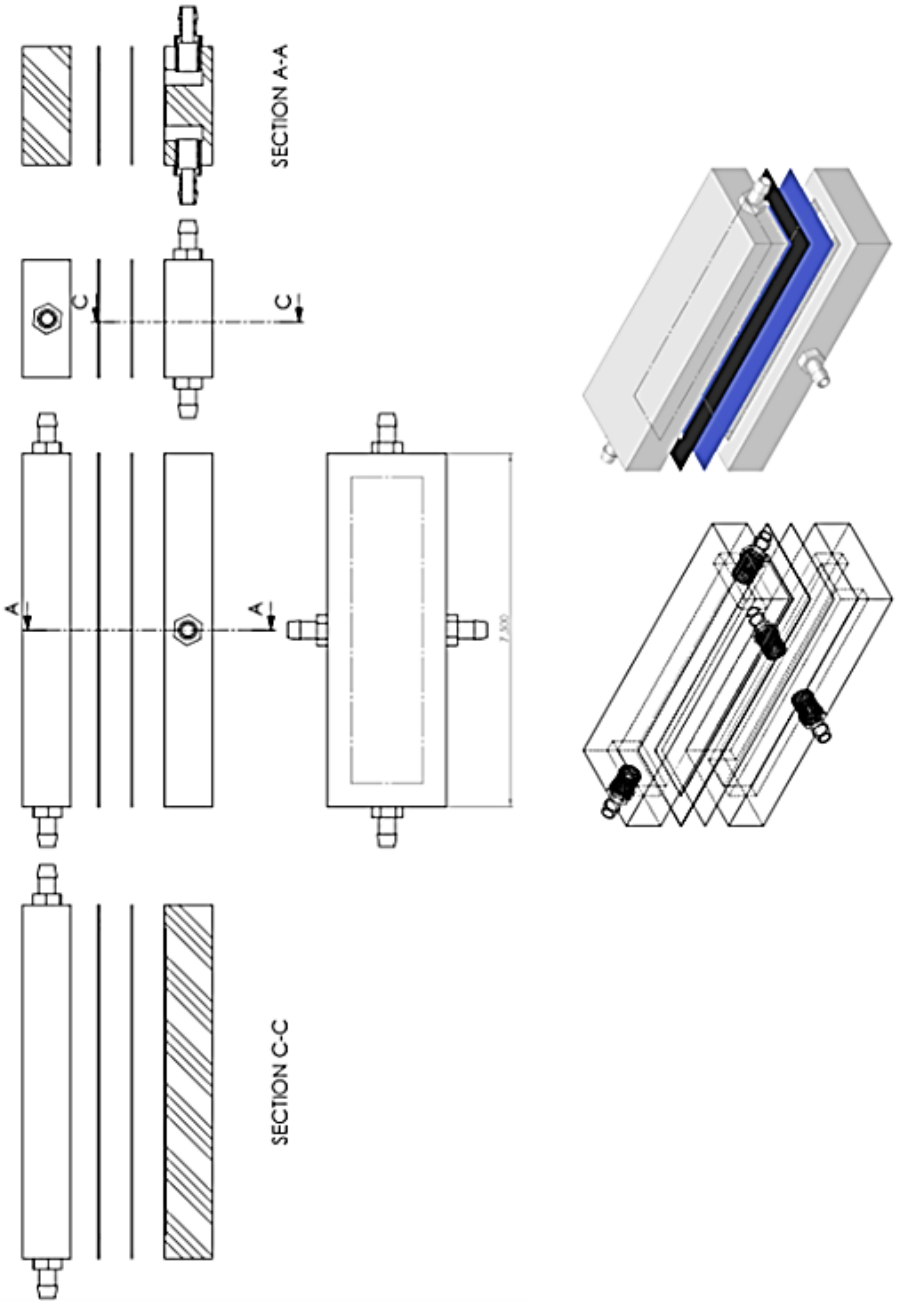

Figure 10.1| Illustration of effects of modest transmembrane pressure (TP) on the shear field and mass transfer above the nitrocellulose membrane in a laminar flow chamber. As shown, modest changes in TP can result in dramatic alterations in the concentration gradient at the cell surface with little effect on the momentum shear field. Feed solutions available both at the top and bottom of the membrane can provide variation in the experimental protocol.

10.3.5 Setting up flow circuit

For each experiment, the flow circuit will be sterilized in an autoclave and assembled in a flow hood. A parallel-plate flow channel will be used to impose laminar flow on the membrane. Care will be taken to avoid entrapment of air bubbles in the flow channel. The experiments will be performed using measured quantities of dye solutions, delivered through a rectangular tangential-flow diafiltration module as shown in Figure 2 with the nitrocellulose membrane.

The proposed experimental design exploits the use of transmembrane pressure, $T_P = \frac{P_1+P_2}{2} - P_3$, where $P_1 - P_2$ represents the tangential pressure drop across the membrane surface, and P_3 is the pressure below the membrane surface. P_3 will be varied over an operating range using a head pressure such that the shear stress and shear rate remain constant but the Ca^{2+} concentration flux, $J = L_P(T_P)$, across the membrane varies (where L_p is the hydraulic permeability).

Media in feed reservoirs (P1 and P3, as shown in Figure 10.2) will be pressurized by nitrogen gas and forced through the membrane test module. A peristaltic pump (Masterflex Inc.) will be used to control back-pressure and flow, and to recycle the solutions back to P1 and P3. Dye analytes will be collected at the retentate exit operating at P_2.

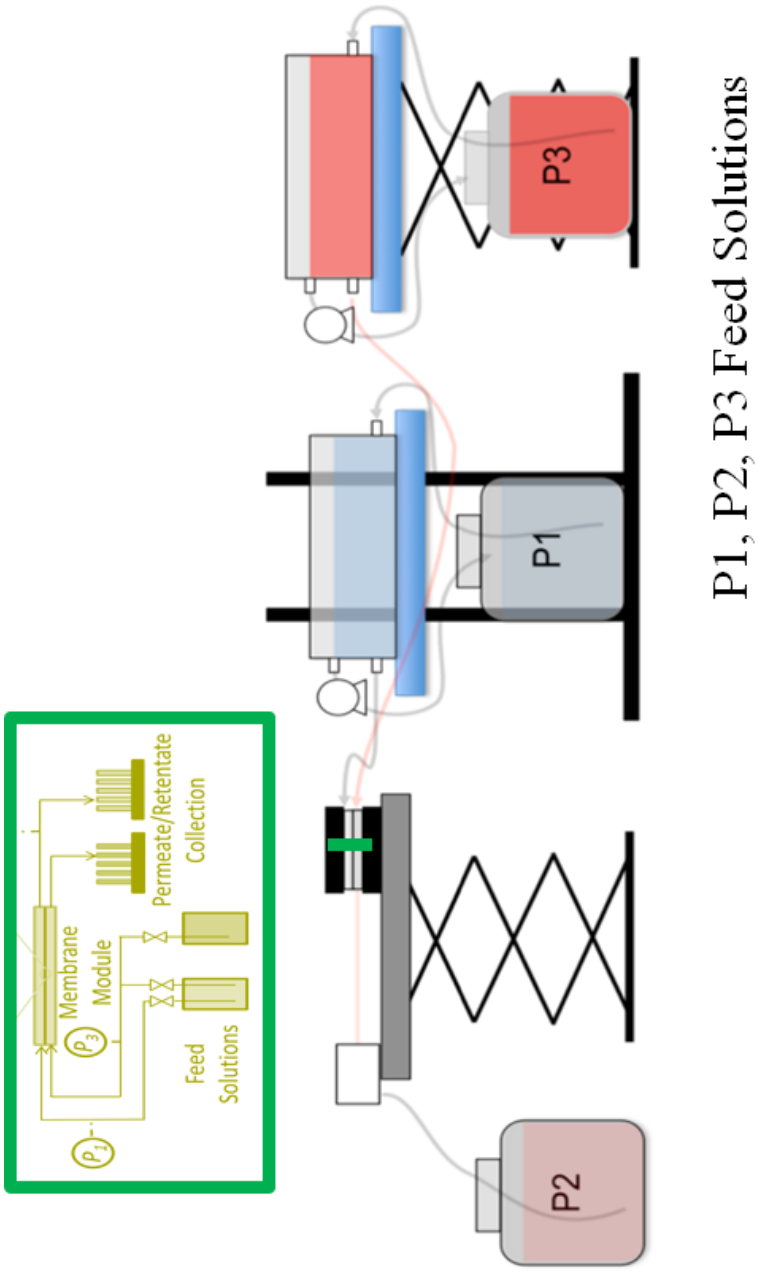

Figure 10.2| Illustration of effects of modest transmembrane pressure (T_p) on the shear field and mass transfer above cells seeded on a membrane in a laminar flow chamber. As shown, modest changes in T_p can result in dramatic alterations in the concentration gradient at the cell surface with little effect on the momentum shear field. Feed solutions available both at the top and bottom of the membrane can provide variation in the experimental protocol.

10.3.6 Measuring hydraulic conductivity using transmembrane pressure device

The constant-head method was employed to measure the hydraulic conductivity of the membrane when DI water was used across the membrane. Our procedure allows water to flow through the membrane under a steady head condition while the volume of water flowing through the nitrocellulose membrane is measured over a specific time period. By measuring the quantity of water, *m* (g), the cross section area of the membrane being used (cm^2), and the time for which the water was being collected (t), and the head pressure ($g\text{-}cm^{-2}$), the hydraulic conductivity can be calculated as mass flux, $J = \frac{m}{At}$. Using Darcy's Law, we can express hydraulic conductivity as $L_P = \frac{J}{\Delta P}$.

10.3.7 Measuring analytes

The experiments shown in Figure 10.2 were performed with a water solution through P_1 and dye water solution through P_3. Analytes were collected at P_2 and a Vis spectrophotometer (Cary50, Varian Inc.) was used to quantify the dye collected.

10.4 RESULTS AND DISCUSSION

10.4.1 Computational modeling

10.4.1.1 Capturing shear stress profiles and concentration gradients

Figure 10.3 shows the results of this work. As can be seen, while the shear stress and shear rate remain constant at the membrane surface, the concentration gradient was altered by a factor of 5. Thus, this example illustrates how this approach can be used to decouple mass transfer effects from mechanical forces in the same system. We will use this methodology with *in-vitro* studies with cells seeded on membrane surfaces to investigate the signaling processes outlined here. Figure 10.3 illustrates the relationship between the concentration and momentum gradients for the proposed research. Here, transmembrane pressure can be modified to result in relatively low flow across the membrane in either direction.

Figure 10.3 simulates the experimental setup shown in Figure 10.2. A 2D rectangular chamber of dimensions 0.04 cm x 0.5 cm was simulated. The length of the simulated flow chamber was much greater than the entry length (0.43 mm) calculated for a constant *Re* (Reynolds number) of 23. The cell culture medium was assumed to be homogeneous, incompressible and a Newtonian fluid having a density of 1.2 g/cm^3.

The Navier-Stokes equation was used for fluid flow. In a parallel flow chamber, the mass transfer of ions can be attributed to the velocity (v) and viscosity (μ=0.0098 g/cm-s) of the media and the diffusion coefficient of Ca^{2+} (D=3.2 x 10^{-5} cm^2/s). The fluid phase is governed by the continuity equation (1) and the incompressible Navier-Stokes equation (2). The chemical species flowing through the system follows the equation of conservation of mass flowing through an incompressible medium and Fick's Law of Diffusion (3).

10.4.1.2 Comparing mass transfer in bulk flow versus that of transmembrane pressure

For this study, we study the effect of species mass that is available at the simulated endothelial cell bed for two cases by varying: (1) species mass flowing through the bulk flow (using no transmembrane pressure and (2) species mass flwoing across the transmembrane test module (using constant bulk flow). The results demonstrate that a minimal change in transmembrane pressure allows for a wide range of species mass to reach the surface of the test bed. The species concentration gradient reaching the test bed was approximately 0.13 mol/cm^4 when the bulk flow was reduced by 75% and the transmembrane pressure was reduced by approximately as low as 2%. Hence, these results demonstrate the importance of using transmembrane flow to delineate the impact of mass transfer from mechanical forces.

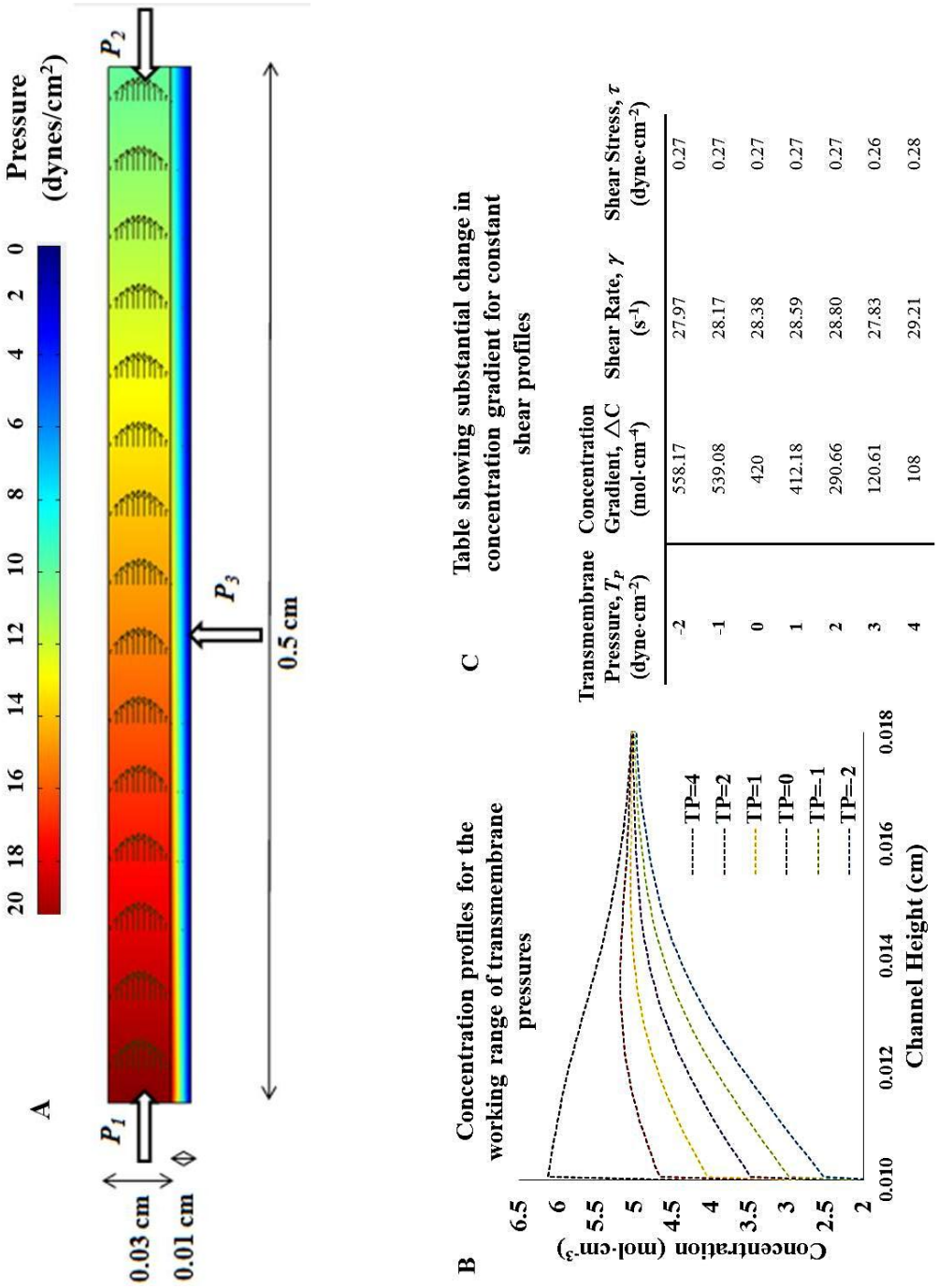

Figure 10.3| Summary of 2D computational investigation of methodology to decouple mass transfer and momentum flux. Figure 3A is an illustration of the velocity profile and pressure map for the case where P_3 is set to zero. As can be seen, variation of transmembrane pressure (TP) does not affect shear rate or shear stress (Figure 3C) but has a dramatic effect on concentration gradient (Figures 3B and 3C).

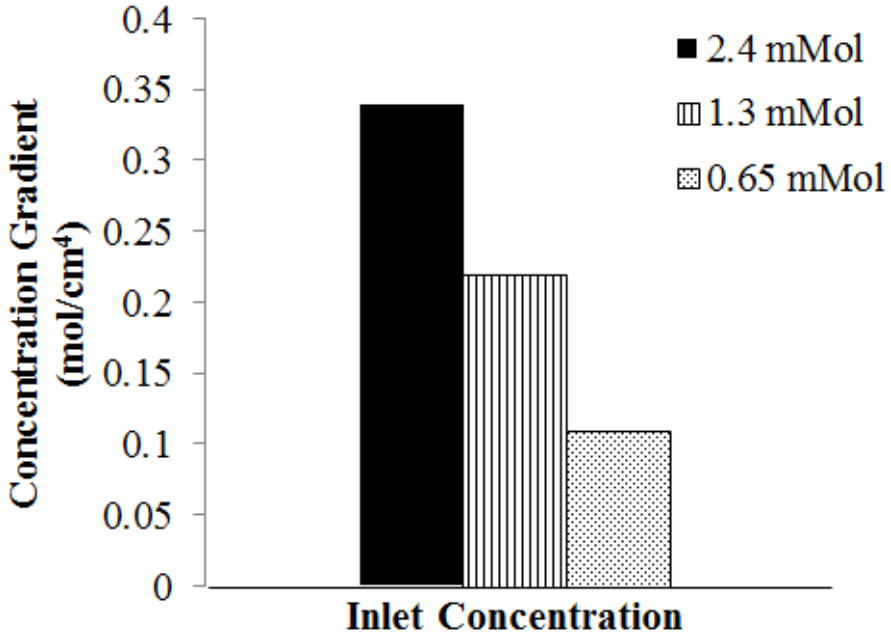

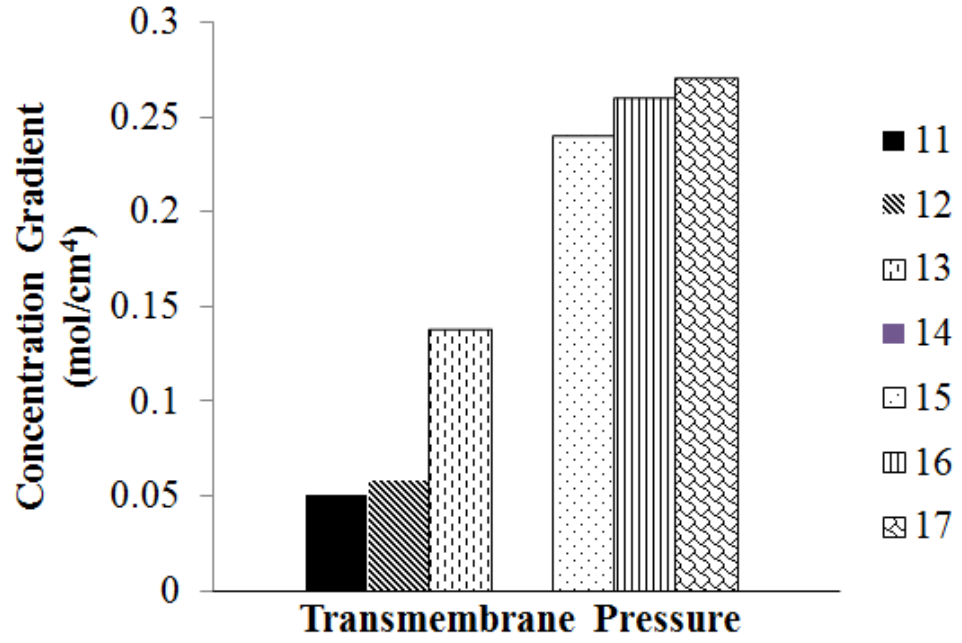

Figure 10.4| Comparing the concentration gradient on the membrane in mol/cm^4 for varying (A) inlet concentration of ions in the inlet, (B) transmembrane pressure across the membrane.

10.4.2 Experiments

10.4.2.1 Characterizing the behavior of the system

Red dye was initially pumped out of P1. P3 was then introduced with a blue dye. As the transmembrane pressure increased, we observe the concentration of both the P1 and P3 inlets drifting in P2 (outlet) with a decrease in red dye. The blue dye from P3 overpowers the P1 and we observe the concentration of P3 increasing in the final measured analytes. These results demonstrate that the device we designed using our membrane technology provides us consistent results (with an extremely low standard deviation, less than 10^{-3}).

It is noteworthy to remind ourselves at this time that the shear stress is almost constant (19 H_2O-cm). With a change in transmembrane pressure, we observe As shown in Figure 10.6, the dye transferred across the membrane was varied for varying T_P with a constant shear stress (τ=7.9±0.02 dyne/cm^2).

10.4.2.2 Measuring hydraulic conductivity for varying soaking conditions

Hydraulic conductivity of nitrocellulose membranes was measured for the following conditions (A) untreated, (B) DI water, (C) PBS-Triton 100X, and (4) DMEM.

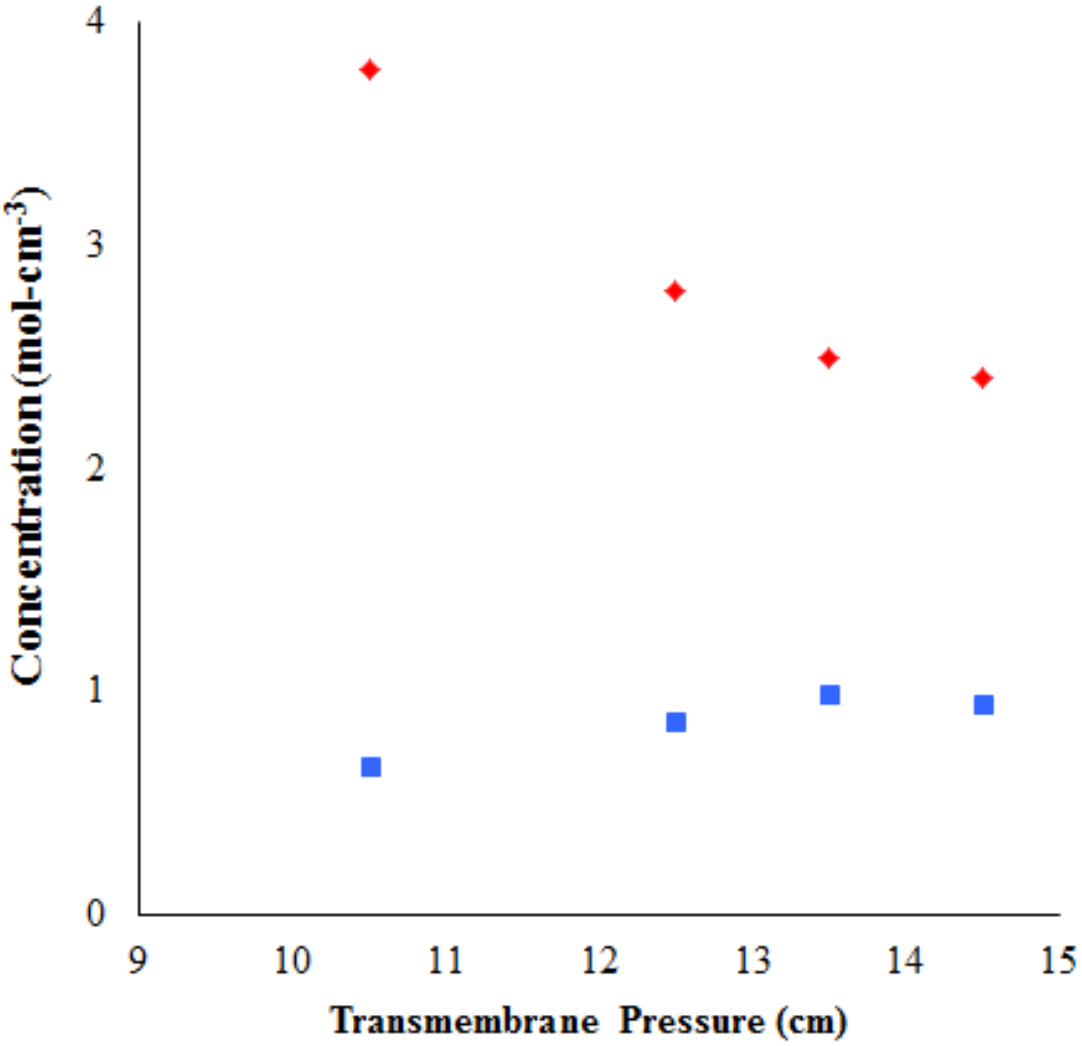

Figure 10.5| The figure shows huge variations in dye - water studies for changes in T_P. n=5

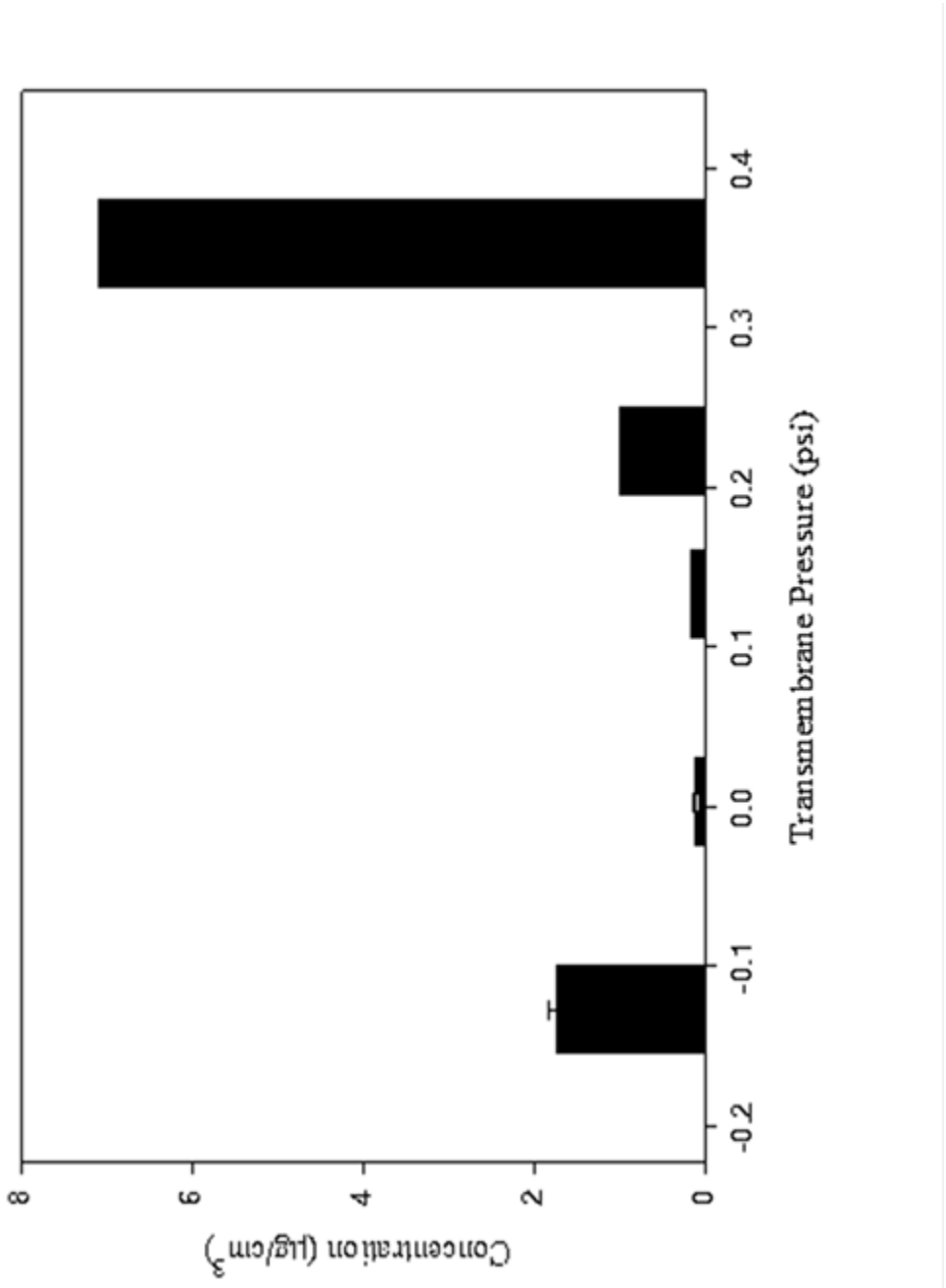

Figure 10.6 | The figure shows significant variations in dye - water studies for changes in T_P.

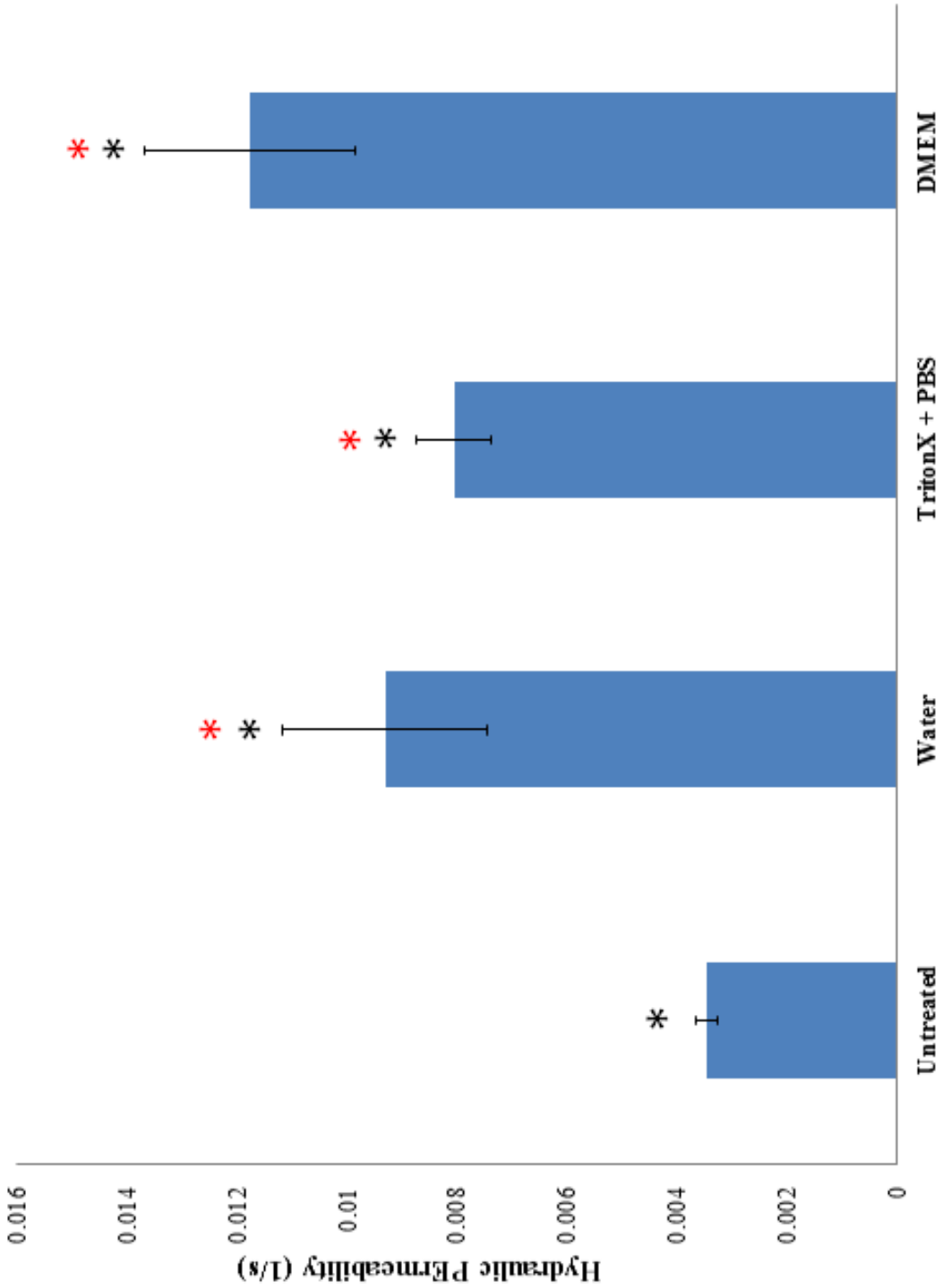

Figure 10.7| The figure shows hydraulic conductivity for different soaking conditions. * denotes statistical significance when $p<0.05$ and * denotes no statistical significance when $p<0.1$.

10.5 CONCLUSION

Both species mass transfer and mechanotransduction have been suggested as the underlying mechanisms for activating endothelial signaling pathways. However, in recent years, the dominance of mechanotransduction at the endothelium has been qualitatively demonstrated through *in-vitro* experiments attempting to emulate the vasculature. In this work, we design a novel in-situ streaming potential device to delineate mass transfer from mechanotransduction which can be implemented for various systems. The results obtained through our computer model and experimental model authenticate the appropriate utilization of this methodology to study the vascular system. Here, we propose a novel; *in-vitro* experimental methodology using membrane separations technology. The proposed technique can decouple mechanotransduction effects from mass transfer in flow-induced studies. The methodology takes advantage of modest alterations of the transmembrane pressure normal to cells seeded on membranes that can make tremendous variations in concentration gradients at the membrane surface (and thus mass transfer) but offers virtually little change in the associated fluid shear stress experienced by the cells. The methodology is flexible and robust, in can be used with mass transfer-limited and reaction-limited processes and can address a number of controllable scenarios.

10.6 REFERENCES

1 Frangos, J.A., Eskin, S.G., McIntire, L.V., Ives, C.L., 1985. Flow effects on Prostacyclin production by cultured human endothelial cells. Science 227, 1477–1479.

2 Jacobs, C.R., Yellowley, C.E., Davis, B.R., Zhou, Z., Donahue, H.J., 1998. Differential effect of steady versus oscillating flow on bone cells. Journal of Biomechanics 31, 969–976.

3 Orszag, S.A., Patera, A.T., 1983. Secondary instability of wall-bounded shear flows. Journal of Fluid Mechanics 128, 347–385.

4 Ando J, Yamamoto K. 2009. Vascular mechanobiology: Endothelial cell responses to fluid shear stress. Circ J **73**:1983–1992

5 Ballermann BJ, Dardik A, Eng E, Liu A. 1998. Shear stress and the endothelium. Kidney Int 54:S100–S108

6 Dai G, Kaazempur-Mofrad MR, Natarajan S, Zhang Y, Vaughn S, Blackman BR, Kamm RD, García-Cardeña G, Gimbrone MA. 2004. Distinct endothelial phenotypes evoked by arterial waveforms derived from atherosclerosis-susceptible, -resistant regions of human vasculature. Proc Natl Acad Sci USA 101:14871–14876.

7 Davies PF, Remuzzi A, Gordon EJ, Dewey CF, Jr., Gimbrone MA, Jr. 1986. Turbulent fluid shear stress induces vascular endothelial cell turnover in vitro. Proc Natl Acad Sci USA 83:2114–2117.

8 Frangos JA, McIntire LV, Eskin SG. 1988. Shear stress induced stimulation of mammalian cell metabolism. Biotechnol Bioeng 32:1053–1060.

9 LaMack JA, Friedman MH. 2007. Individual and combined effects of shear stress magnitude and spatial gradient on endothelial cell gene expression. Am J Physiol Heart Circ Physiol 293:H2853–H2859.

10 Lawrence BJ, Devarapalli M, Madihally SV. 2009. Flow dynamics in bioreactors containing tissue engineering scaffolds. Biotechnol Bioeng 102:935–947.

11 Nagel T, Resnick N, Dewey CF, Jr., Gimbrone MA, Jr. 1999. Vascular endothelial cells respond to spatial gradients in fluid shear stress by enhanced activation of transcription factors. Arterioscler Thromb Vasc Biol 19:1825–1834.

12 Sucosky P, Osorio DF, Brown JB, Neitzel GP. 2004. Fluid mechanics of a spinner-flask bioreactor. Biotechnol Bioeng 85:34–46.

13 Yazdani SK, Tillman BW, Berry JL, Soker S, Geary RL. 2010. The fate of an endothelium layer after preconditioning. J Vasc Surg 51:174–183.

14 Bao X, Lu C, Frangos JA. 1999. Temporal gradient in shear but not steady shear stress induces PDGF-A and MCP-1 expression in endothelial cells: Role of NO, NF kappa B, and egr-1. Arterioscler Thromb Vasc Biol 19:996–1003.

15 Barbee KA. 2002. Role of subcellular shear-stress distributions in endothelial cell mechanotransduction. Ann Biomed Eng 30:472–482.

16 Brown, T.D., 2000. Techniques for mechanical stimulation of cells in vitro: a review. Journal of Biomechanics 33, 3–14.

17 Belansky, R., Wanser, K., 1993. Laser doppler velocimetry using a bulk optic Michelson interferometer: a student laboratory experiment. American Journal of Physics 61, 1014–1019.

18 Booij, W., de Jongh, A., de Mul, F., 1995. Flow profile study using miniature laser-doppler velocimetry. American Journal of Physics 63, 1028–1033.

19 Matthew E. Downs, An M. Nguyen, Florian A. Herzog, David A. Hoey & Christopher R. Jacobs (2012): An experimental and computational analysis of primary cilia deflection under fluid flow, Computer Methods in Biomechanics and Biomedical Engineering.

20 Brown A, Meenan BJ. 2007. Investigating the effects of fluid shear forces on cellular responses to profiled surfaces in-vitro: A computational and experimental investigation. Conf Proc IEEE Eng Med Biol Soc 2007:5387–5390.

SECTION 4:

CHARACTERIZING ENDOTHELIAL SIGNALING PATHWAYS IN EXTRACELLULAR MILEU DURING ATHEROSCLEROSIS

PRELUDE

Proteins such as AMPK, SIRT1 and KLF2 have been shown to be key players in maintaining vascular homeostasis. However, the mechanism(s) by which blood flow elicits protein signaling in the endothelial cells remain(s) unclear. Although mechanotransduction of hemodynamic forces has been continuously shown to be the reason behind signaling, we have evidence that now suggests biochemical mass transfer cannot be ruled out. Further, initiation and progression of vascular diseases such as atherosclerosis is biomarked by varied expression of extracellular proteins and altered composition of extracellular matrix (ECM) leading to a dysfunctional endothelium. Delineating the mechanism (biomechanical, biochemical or both) through which ECM-integrin interactions vary the intracellular and extracellular composition of the vessel during atherosclerosis also remains vague. Hence, elucidating these signaling mechanisms can facilitate the development of therapeutic responses.

Our objective is to decouple and determine the effects of mass transfer and mechanotransduction contributions to the flow-induced downstream targets for AMPK, KLF2, and SIRT1 signaling pathways. Here we will investigate AMPK phosphorylation, and SIRT1 and KLF2 activation as a response to varied flow dynamic parameters. Our goal is to understand the mechanism(s) by which vascular blood flow alters the functioning of such signaling pathways. We hypothesize that flow dynamics display an intricate interaction of both shear flow and mass transfer. Both these components will be used as our input parameters and we will focus on nitric oxide (NO) and thrombomodulin (TM) as the downstream targeted outputs. NO plays an important role in cardiac diseases

such as atherosclerosis whereas TM is crucial for the functioning of the coagulation system.

This study proposes varied mass transfer during different stages of atherosclerosis leading to altered signalling pathways. We will investigate the behavior of signaling pathways corresponding to the altered composition and organization of the extracellular milieu (collagen (Col), fibronectin (FN), vitronectin (VN)), as a response to varied flow-dependent scenarios.

CHAPTER 11

AMPK-SIRT1-eNOS ACTIVATION IN EXTRACELLULAR MATRICES DURING ATHEROSCLEROSIS

ABSTRACT

Atheroma is initiated and progressed in the unhealthy and artheroprone region of the blood vessel. During the process, the collagenous subendothelium (in the command of signaling pathways) is converted to a fibrillar subendothelium. This process involves the deposition of fibronectin and vitronectin which alters the release of NO and the compliance of the vessel wall. Appropriate ECM composition establishes the functioning of the endothelial signaling pathways in the vascular intima [2]. In this work, we use immunocytochemical methods that employ the distinct variations in extracellular matrix to study the characteristic behavior of endothelial cells in atheroprotective and atherogenic stages. We hypothesize that owing to different ECM configuration, AMP modified protein kinase (AMPK) phosphorylation will vary with flow. For each experiment, the sterilized flow circuit is maintained at 37°C, ventilated with 95% humidified air - 5% CO_2, and connected to the peristaltic pump. A parallel-plate flow channel is used to impose laminar flow at 12 dyne/cm^2 for stipulated time intervals on a confluent monolayer of endothelial cells (ECs). The contribution of extracellular matrix for atheroprone, atherogenic, and atherosclerotic stages of the vasculature and their effects on AMPK signaling pathway is explored through these *in-vitro* experiments. Exploring the stress-related AMPK signaling pathway provides striking insights into the onset and progression of atherosclerosis. We identify a possible feedback response between NO production and ECM.

11.2 INTRODUCTION

The vascular endothelium of the tunica intima vibrantly and sensitively counters to the fluid dynamics of the blood and hormonal stimuli such as vasoactive factors. It responds by releasing a large number of vasoactive biomolecules that regulate vasomotor function, modulates inflammation, and influences vascular homeostasis. The well-established vasodilators produced by the endothelium are nitric oxide (NO), prostacyclin, and different endothelium-derived hyperpolarizing factors; and vasoconstrictors are endothelin-1, angiotensin II, reactive oxygen species and many more [1-16]. Scientists extensively study endothelial cells under flow parameters to identify atherogenic gene products that may be used as therapeutic agents. Appropriate endothelial functioning is hence a synergistic effect of many biomolecules (such as JNK, FAK, Src, AMPK, Tyrosine Kinases, and PGCα) [17-20]. In this proposal, we will be investigating the mechanistic behaviour of three such important endothelial flow modulating pathways (AMPK-KLF2-SIRT1) on regulating downstream activation of eNOS and TM. We briefly account on these representative pathways and we subsequently propose the integrated signaling pathway that we will be working on.

11.2.1 AMPK

AMP modified protein kinase (AMPK) is a master switch regulator and induces a cascade of intracellular events in response to the ever changing energy demand of the cell [21-23]. Subsequently, AMPK controls downstream signaling pathways to regulate vascular haemostasis and to prevent the aggregation of monocytes and

lipocytes on the interior walls of blood vessels [24]. Shear stress (physiologically ranging between 5 and 20 dynes/cm^2) affects cell arrangement and proliferation of endothelial cells. The laminar velocity profile characterizes a quiescent endothelium stage, during which the vascular monolayer of endothelial cells are confluent and the subendothelial actin networks of ECM are reconfigured to stress fibres in the direction parallel to the blood flow [25]. The aligned cells are stiffer causing an increase in ATP utilization i.e., an increase in [AMP]/[ATP] and instigating AMPK [26]. In response to turbulent flow, the endothelium increases the division rate of the cells, decreasing the [AMP]/[ATP], resulting in a transient or no AMPK (depending on the nature of turbulence) activation [26].

11.2.2 KLF2

Krüppel-like factor2 (KLF2) has been identified as a key molecular button that is up-regulated by atheroprotective flow [27-35] but down-regulated by athero-prone flow and proinflammatory stimuli [36-39] hence modifying important aspects of vascular functions and diseases. Many studies suggest that KLF2 is involved with regulations of endothelial thrombotic function and vascular tone [39]. KLF2 has been identified as a novel transcriptional regulator of endothelial thrombotic function by inducing thrombomodulin (TM) and suppressing several pro-coagulants such as tissue factor (TF) and plasminogen activator inhibitor-1 (PAI-1) [40]. KLF2 has been identified as an inducer for eNOS expression and activity [36]. Further, KLF2 acts as a central transcriptional switch point between the quiescent and activated states of the adult

endothelial cell. KLF2 usually binds to GC-rich or CACCC sequences in the promoter region of target genes to regulate their transcriptional activity [40].

11.2.3 SIRT1

SIRT1 is an NAD-dependent deacetylase that acts as a master metabolic sensor of NAD and modulates cellular metabolism and life span [41]. SIRT1 delays the onset of age related atherosclerosis [42-44]. SIRT1 manifests a prominent role in vascular biology and may regulate aspects of age-dependent atherosclerosis [45]. Part of these effects may come through regulation of lipid and cholesterol metabolism and is implicated in modulating ischemia. Recently, SIRT1 has been shown to deacetylate and regulate eNOS activity, a key regulator of vascular tone [46]. SIRT1 has been implicated in the control of energy metabolism through deacetylation of FOXO and PGC-1α [47,48].

11.2.4 Accounting for AMPK-KLF2-SIRT1 cross-talk

SIRT1 has been shown to be an upstream regulator for the AMPK-LKB1 regulating hepatocyte lipid metabolism suggesting an avenue of pharmacological intervention in slowing down age-related atherosclerosis [49,50-53]. Additional data by the Co-PI Shyy's Lab showed that laminar flow causes a marked increase in SIRT1 level, and AMPK and SIRT1 synergistically increase the eNOS-derived NO bioavailability in ECs responding to laminar flow [54]. An in-depth review of SIRT1 and AMPK regulation has been discussed with clinical response and a possibility of their

dysregulation which predisposes to atherosclerotic cardiovascular diseases suggesting a favorable drug therapy [55]. AMPK acts as the prime initial sensor that translates this information into SIRT1-dependent deacetylation of the transcriptional regulators PGC-1a and FOXO1, culminating in the transcriptional modulation of mitochondrial and lipid utilization genes [55]. A counter-balancing model involving the cross-talks between SIRT1 and AMPK, another stress and energy sensor, is suggested for controlling the senescence program in mammalian cells [55]. accounted that AMPK triggers KLF2 when endothelial cells are exposed to shear stress. [55].

11.2.5 Integrins-ECM Interaction

Integrins are integral membrane receptors that mediate attachment between the cell and extracellular environment (adjacent cells or the surrounding ECM) [56]. They play an important role in paracrine cell signaling and define cellular shape, mobility, and regulate the cell cycle. Integrins act as a liaison between the cells and the extracellular matrix to evoke an endothelial response. They transduce information from the ECM to the cell as well as disclose the status of the cell to the ECM, detecting and communicating the response to its dynamic ambiance. During vascular shear stress, integrins converse external blood flow patterns into internal cell signaling pathways [57]. Of the large number of signaling pathways, the response of the shear induced c-Jun N-terminal kinase (JNK) pathway to altered ECM compositions has recently been explored [58]. When cells are influenced by transient blood flow, an integrin–ECM mediated cell signaling cascade is triggered, ultimately leading to the

phosphorylation of receptor tyrosine kinases (RTKs) mitogen activated protein kinase kinase 4 (MAPKK4), the phosphorylation of JNK in the nucleus, triggering downstream cellular responses, and activating genes that transcribe VCAM, ICAM, and Interleukin [59].

11.2.6 Mass transfer in the endothelium - emphasis to Ca^{2+}

Ionic mass transfer i.e., transfer of ions such as Ca^{2+}, Cl^{-}, Na^{+}, Zn^{2+}, Mg^{2+}, ATP play a central role in the control of growth, contractility, and function of the vasculature [60-62]. Ca^{2+} signaling is one of the premier signaling mechanism by which endothelial cells respond to external stimuli and maintain haemostasis [63-64].

Release of Ca^{2+} from the extracellular medium into the cytosol requires its continuous refilling which is dependent on the convective transport of the Ca^{2+} from the blood to the endothelial bed. AMPK has been shown to be phosphorylated by LKB-1 or Ca^{2+}/calmodulin kinase-kinase β (CAMKKβ) [65-68]. Our preliminary results (shown in Figure 4) also demonstrate the importance of Ca^{2+} in ACC phosphorylation *via* AMPK. Increase in extracellular Ca^{2+} alters vascular tone and results in an increased blood pressure [69]. Ca^{2+} has also been to show an important role in eNOS phosphorylation and translocation. Owing to the ease of measuring the change in Ca^{2+} concentration, we will be emphasizing on the effect of Ca^{2+} on the proposed integrated signaling network.

11.2.7 Proposed integrated signaling pathway network

After exploring the interaction between these three model proteins (AMPK, KLF2, and SIRT1) and their downregulated endothelial targets (eNOS, TM), we syudy the signaling cascade depicted in Figure 11.1. The interaction between AMPK-ECM-integrin pairs, AMPK-TM, and any possible interaction between eNOS and integrins will be mapped out.

11.2.8 Biomarkers and stages of atherosclerosis

These lesions modify the subendothelial ECM configuration and allow for the retention of cholesterol-rich lipoproteins which sets the stage for plaque (atheroma) formation. Variations in the morphology of intimal fibronectin in atherosclerosis is manifested by interrupted fibronectin [70]. Dysfunctional endothelium is less compliant and less effective to dynamic changes in blood flow and marks the onset of atherosclerosis. As atherosclerosis progresses, the fibronectin of endothelium defragments and disintegrates to fibrinogen. The facilitated lipid deposits on vascular intima thickens and hardens the arterial walls in atherosclerosis [71]. The interplay of all the aforementioned factors convert the endothelium from a quiescent atheroprotective stage to a dysfunctional atherogenic stage. As atherosclerosis is initiated and progressed, the collagenous subendothelium (in the command of signaling pathways) is converted to a fibrillar subendothelium.

This process involves the deposition of fibronectin and fibrinogen which would alter the release of NO and the compliance of the vessel wall. Atheroma is initiated

and progressed in the unhealthy, artheroprone region of the blood vessel. We will use immunocytochemical methods that employ the distinct morphological qualities of blood vessels to study the characteristic behaviour of endothelial cells in atheroprotective and atherogenic stages (Table 1). We will computationally simulate the different vascular stages.

To elaborate, proteins such as AMPK, SIRT1 and KLF2 have been shown to be key players in maintaining vascular homeostasis. However, the mechanism(s) by which blood flow elicits protein signaling in the endothelial cells remain(s) unclear. Although mechanotransduction of hemodynamic forces has been continuously shown to be the reason behind signaling, we have evidence that now suggests biochemical mass transfer cannot be ruled out. Further, initiation and progression of vascular diseases such as atherosclerosis is biomarked by varied expression of extracellular proteins and altered composition of extracellular matrix (ECM) leading to a dysfunctional endothelium. Delineating the mechanism (biomechanical, biochemical or both) through which ECM-integrin interactions vary the intracellular and extracellular composition of the vessel during atherosclerosis also remains vague. Hence, elucidating these signaling mechanisms can facilitate the development of therapeutic responses.

These experiments have been guided with preliminary computational simulations to provide methodical insight into the working of signaling pathways. The corresponding results of these experiments will provide new mechanistic acumen in understanding the triggering of AMPK, KLF2, and SIRT1 signaling pathways and downstream targets. Further, the relationship between AMPK, SIRT1 and TM; and the phosphorylation of

AMPK, KLF2, and SIRT1 in response to ECM composition will be studied for the very first time. The data obtained will provide implications, not only in elucidating these signaling pathways, but also on the spectrum of signaling pathways that play a role in endothelial dysfunction.

Table 11.1 Summary of biomarkers that characterize atheroprotective, atherogenic, and atherosclerotic stages of blood vessels.

Stages of Blood Vessel	***Atheroprotective***	***Atherogenic/ Artheroprone***	***Atherosclerosis***
Characteristic Feature	Three layered Vessel [72]	Inflammation [73] Fatty streak	Extracellular Calcification [74]
Vascular SmoothMuscle Cells [105]	Spindle Shaped, Confluent	Migration, Proliferation	Abundance
ECM Configuration	Collagen [75]	Fibronectin [75]	Vitronectin [75]
Integrins	$\alpha_1\beta_1$, $_2\beta_1$ [76]	$\alpha_v\beta_3$, $\alpha_5\beta_1$ [77]	$\alpha_{IIb}\beta_3$ [78]
Shear stress at TI [79]	5-20 dynes/cm^2	---------- <5 dynes/cm^2 -------	
Velocity of blood [80]	Sustained Laminar	---------- Turbulent ---------	
Viscosity of blood [81]	6.72 cP	7.24 cP	7.79 cP
[NO] [82]	0.012 nM	?	?
[Ca^{2+}] [83]	2.2 mM	?	?

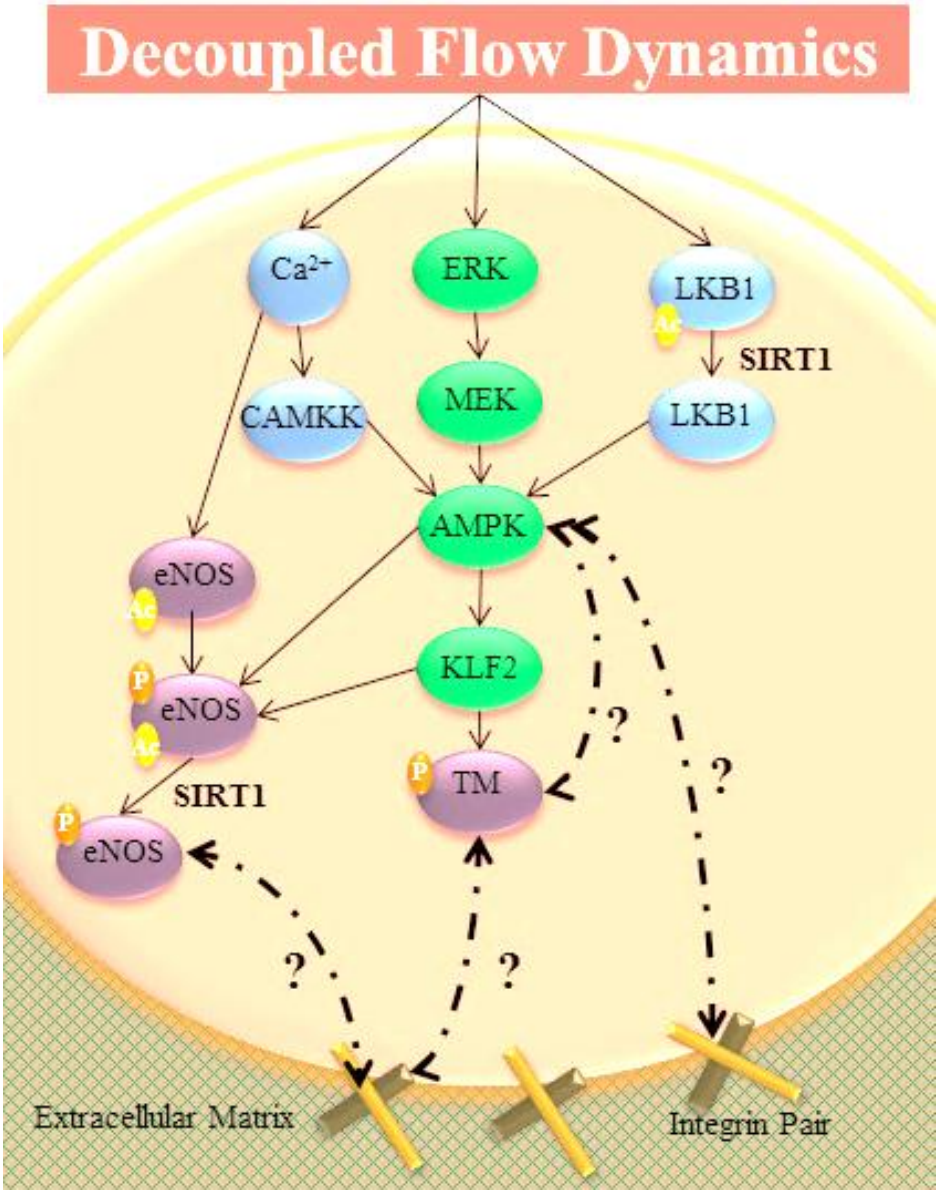

Figure 11.1: The integrated signaling cascade between key players: AMPK, KLF2, and SIRT1 with the downstream target (eNOS).

11.3 METHODS

These *in-vitro* experiments correlated the flow parameters, ECM configuration and AMPK activation.

11.3.1 Cell culture

A variant of endothelial cells (EA926s) were cultured in DMEM (Invitrogen, Carlsbad, California) supplemented with 10% fetal bovine serum, 100 g/mL penicillin, and 100 g/mL streptomycin. ECs were maintained in a humidified 95 % air -- 5 % CO_2 incubator at 37 °C. EA926s

11.3.2 Coating of slides with ECM proteins

To determine whether the activation of AMPK by shear stress depends on the subendothelial matrix, EA926s were placed on glass slides coated with either Collagen (Coll I - 6 μg/cm^2), Fibronectin (FN- 5 μg/cm^2), or Fibrinogen (FG- 5 μg/cm^2) for 2 hours. The ECM proteins were spread as confluent monolayer on the slides and air-dried overnight to allow complete adsorption. The slides were washed three times with PBS and EA926s were seeded on the slides in the absence of serum.[20] Cells will be subjected to laminar shear stress (12 dyne/cm^2) in a parallel plate flow chamber for six hours.

11.3.3 Fluid shear stress experimental setup

For each experiment, the flow circuit was sterilized in an autoclave and assembled in the hood. The flow system was maintained at 37 °C, ventilated with 95% humidified air - 5% CO_2, and connected to the roller pump. The circuit was primed with DMEM to ensure a standardized fluid column through the hose. A parallel-plate flow channel was used to impose laminar flow on confluent monolayer of EA926s as shown. A slide coated with a monolayer of EA926 will be positioned on the parallel flow chamber. In between the EA926 seeded slide and the parallel plate rectangular chamber, a gasket of 0.0254 cm thick was placed as shown in Figure 11.2(A). Care will be taken to avoid entrapment of air bubbles in the flow channel. Figure 11.2(B) shows the entire setup of the parallel flow chamber experiencing laminar flow. EA926s will be exposed to a laminar flow at 12 dyne/cm^2 for time intervals (0, 2, 5, 15 minutes).

11.3.4 Lysis

EA926 cells were carefully scraped out into different aliquots and lysed with a buffer containing 10 mmol/L Tris, pH 7.4, 100 mmol/L NaCl, 1 mmol/L EDTA, 1 mmol/L EGTA, 1 mmol/L NaF, 20 mmol/L $Na_4P_2O_7$, 2 mmol/L Na_3VO_4, 0.1% SDS, 0.5% sodium deoxycholate, 1% Triton-X 100, 10% glycerol, 10 g/mL leupeptin, 60 g/mL aprotinin, and 1 mmol/L phenylmethanesulfonyl fluoride.

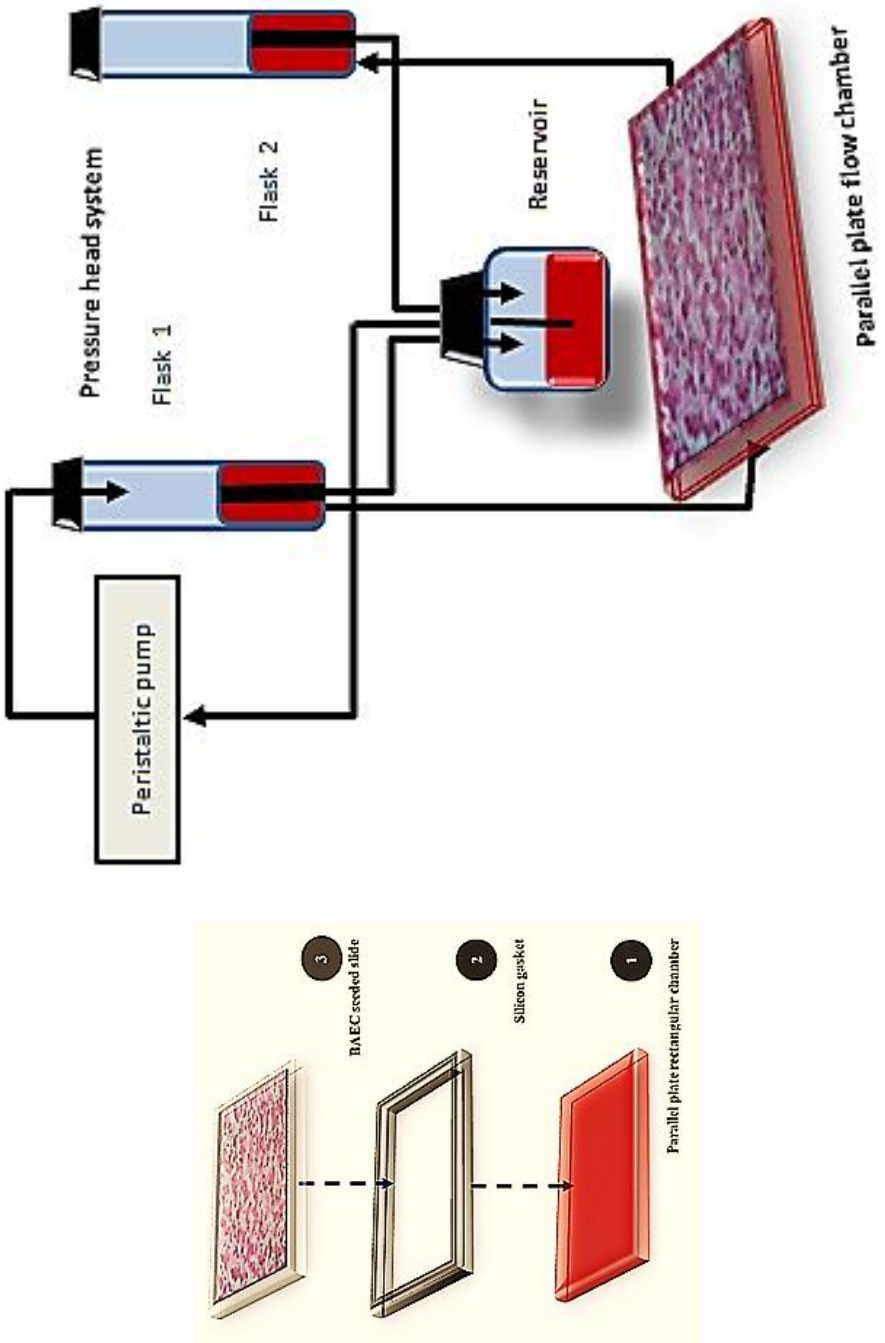

Figure 11.2| Experimental setup for flow experiments. **(A)** The assembly of the parallel flow chamber and **(B)** The parallel flow chamber experiencing shear.

11.3.5 Immunocytochemistry

Ti samples seeded with EA926 cells were washed with PBS three times for five minutes each. Cell samples were fixed and permeabilized with ice cold methanol in -20 ^{o}C for 20 minutes. Samples were again washed in PBS (1X) and incubated with blocking buffer (4 g BSA +80 mL PBS + 150 µL Triton X 100) for 1 hour followed by incubation with 5 µg/ml of rabbit polyclonal anti-peNOS (Ser1177), rabbit polyclonal anti-VCAM1, rabbit monoclonal p-AMPK, rabbit monoclonal anti-VWF, monoclonal VE Cadherin, and KLF2 primary antibodies (AbCAM, Cambridge, MA) in antibody dilution buffer (4 g BSA + 40 mL PBS + 120 µL Triton X 100) for 90 minutes in room temperature. Cells were rinsed 3 times with 10 minutes PBT and incubated with 5 µg/ml Alexa Fluor® 488 goat anti-rabbit secondary antibody or Texas Red 598® donkey anti-rabbit secondary antibody in antibody dilution buffer for another 60 minutes. Cells were washed three times with PBT for 5 minutes each.

11.3.6 Confocal imaging

EA926 cells seeded on the Ti surfaces were examined for all the indicated times and imaged using Leica M125 (Buffalo Groove, IL, USA) fully apochromatic corrected stereomicroscope with 12.5:1 zoom. Fluorescent images and transmitted images with 10X objective lens, binning of 4 x 4, gain of 8.0, and brightness of 1.2 were acquired. The seeded endothelial cells on the ECM seeded surfaces were examined for all the indicated times and imaged using Leica SP2 (Buffalo Groove, IL, USA). Spot Imaging

Software® (Sterling Heights, MI, USA) and ImageJ® 1.46 (NIH, Bethesda, USA) is used to acquire and process the images[100].

11.3.7 Atomic force microscopy

The fidelity and uniformity of the surface patterning was characterized using scanning electron microscopy (SEM) (SUPRA 55, Leo). Imaging was performed at 5 kV accelerating voltage without need for application of conductive coatings on either substrate. The surface roughness of the patterned substrates was characterized using atomic force microscopy (AFM)(DimensionTM 3100, NanoscopeIIIa, mfg). Commercially-available, silicon-nitride tips were used (tip radius of curvature < 10 nm, tip height = 14 - 16 μm, and cantilever spring constant = 1.2 - 6.4 $N \cdot m^{-1}$)(name, mfg). Imaging was performed in tapping mode with 1 Hz scan rate.

11.4 RESULTS AND DISCUSSIONS

11.4.1 Characterizing extracellular matrices

The AFM images were acquired for collagen, fibronectin, and vitronectin. We observed that collagen was not specifically shaped, however fibronectin and vitronectin was shaped as a network of extracellular matrices.As shown in Figure 11.3, individual molecules of collagen was observed. Monomers of collagen are nominally 280 nm long. Strands smaller than that were recognized as fragments. Through our AFMs, we observed higher collagen oligomers in the form of loops. The fibronectin strands, in contrast were linearly branched with a length of approximately 120 nm. Vitronectin molecules, on the other hand, were flattened, spread-out, and ellipsoidal in shape with its width and length of approximately 50 nm and 120 nm respectively.

Further, we characterized the charge properties of two extracellular matrices of interest: collagen and fibronectin. We observed that the charge of collagen and fibronectin was negative when compared with the charge of the membrane alone. Our studies also demonstrate a more negative zeta potential of fibronectin than collagen with a net charge difference of -3.6 mV.

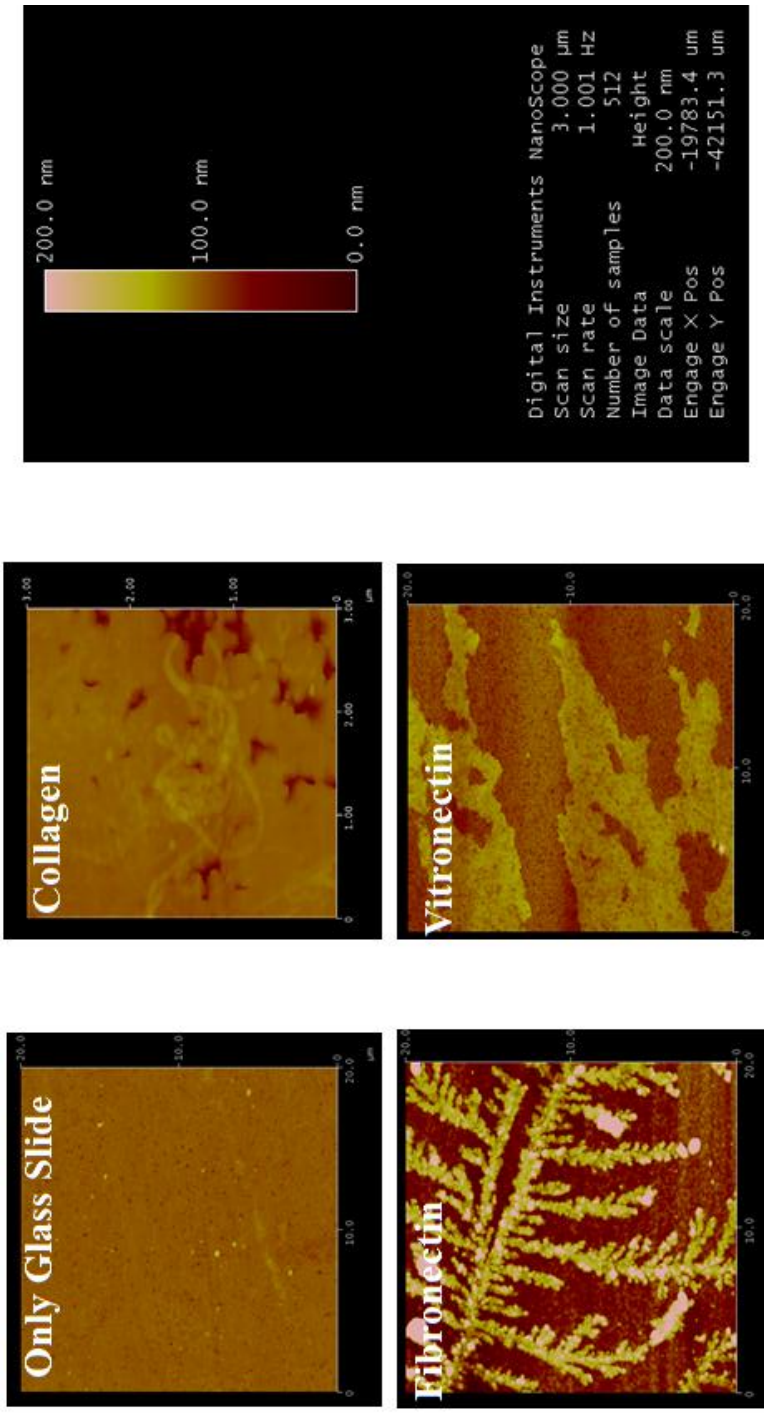

Figure 11.3| Characterizing extracellular matrices on glass slides using AFM technique. Images show glass slide only, collagen, fibronectin, and vitronectin.

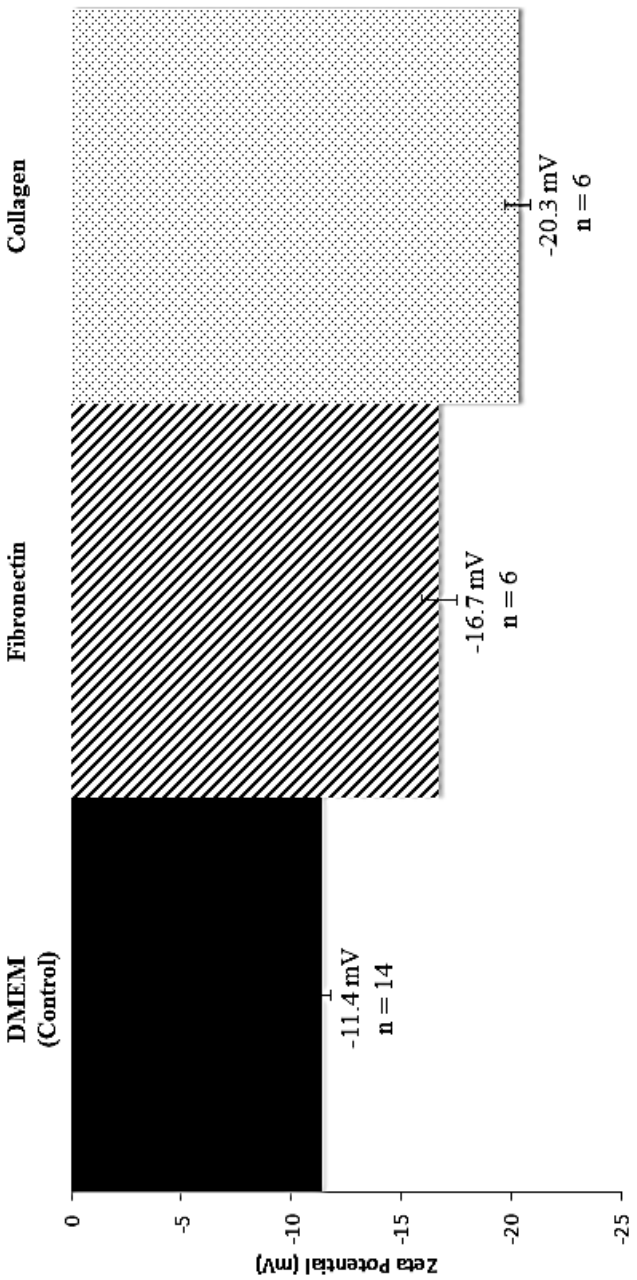

Figure 11.4| Characterizing the charge properties of the extracellular matrices for membrane soaked in medaia only and membranes coated with collagen and fibronectin.

11.4.2 Characterizing apoptosis and necrosis

Apoptosis is a carefully regulated process of cell death that occurs as a normal part of development. Inappropriately regulated apoptosis is implicated in disease states, such as Alzheimer's disease and cancer. Apoptosis is distinguished from necrosis, or accidental cell death, by characteristic morphological and biochemical changes, including compaction and fragmentation of the nuclear chromatin, shrinkage of the cytoplasm and loss of membrane asymmetry.

Furthermore, during apoptosis the cytoplasmic membrane becomes slightly permeant. Certain dyes, such as the green fluorescent YO-PRO®-1 dye can enter apoptotic cells, whereas other dyes, such as the red fluorescent dye, propidium iodide (PI), cannot. Thus, use of YO-PRO®-1 dye and PI together provide a sensitive indicator for apoptosis.

As shown in Figure 11.5, cells grown on collagen substrates were healthier than cells grown on both fibronectin and vitronectin substrates. We observed the cells on fibronectin surgaces and vitronectin surfaces were more prone to apoptosis and necrosis respectively aafter being stimulated to flow for ten hours. The endothelial cells formed clusters on vitronectin substrates and demonstrated the tendancy of cells to form aggregated clumps and the presence of higher adhesive forces intercellularly.

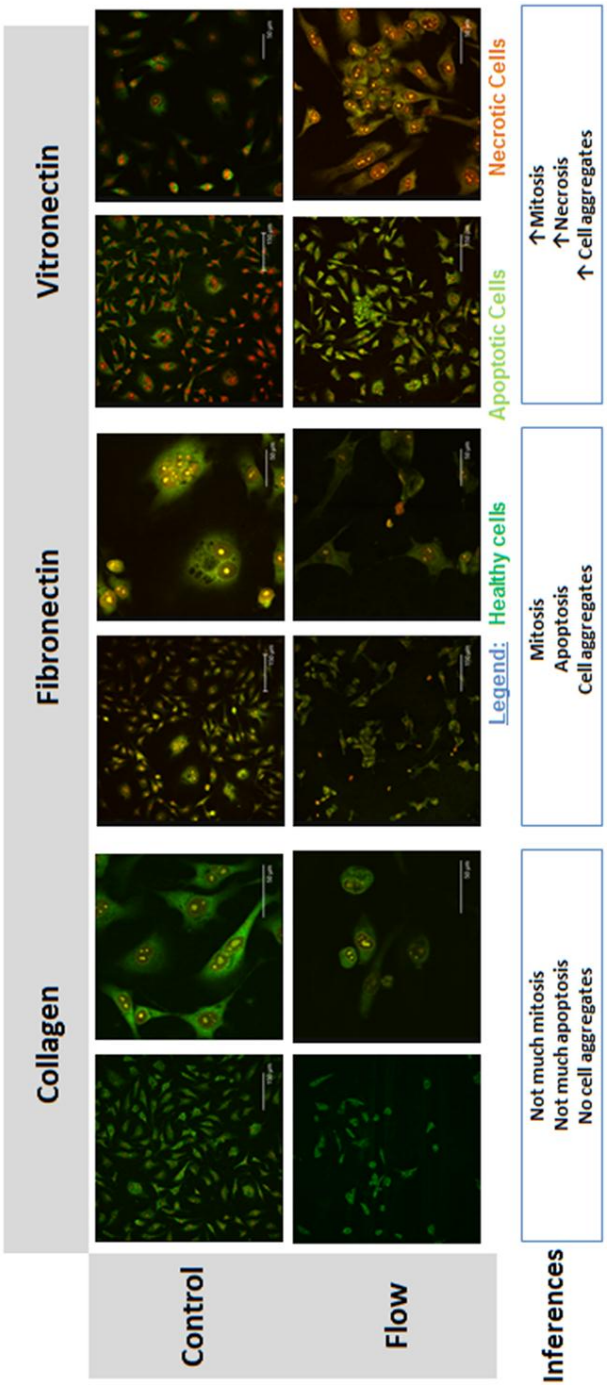

Figure 11.5| Confocal micrographs of endothelial cells seeded on collagen, fibronectin, and vitronectin coated slides. The cells were stained with YO-PRO1 and Propidium Iodide. Cells were imaged in static as well as flow conditions.

11.4.3 Studying signaling on the extracellular matrices

Our results demonstrate the effect on different extracellular matrices on the activation of p-eNOS, p-SIRT1, p-AMPK, and KLF2. We observe an increase in peNOS in static conditions on collagen and vitronectin (Figure 11.6). However, on fibronectin, we observed a decreased activation of eNOS (Ser 1177). Further, we observed an increased activation of p-AMPK (an upstream target of peNOS) on the collagen and vitronectin matrices. These results demonstrate differential activation of signaling molecules when cells are seeded on different extracellular matrix – seeded substrates.

We further exposed cells to shear stress of 12 dynes/cm^2 for a period of 15 hours and characterized the expression of p-eNOS (Ser 1177). We observed that p-eNOS (Figure 11.7) displays a higher activation on fibronectin and vitronectin compared to collagen. Our western blots demonstrate similar results.

When exposed to flow with shear stress of 12 dynes/cm^2 for a period of ten hours (Figure 11.8), we observed activation of KLF2 for the cells seeded on all the three extracellular matrices, minimal activation of p-SIRT1, and enhanced activation of p-AMPK for cells seeded on collagen- and vitronectin- coated substrates.

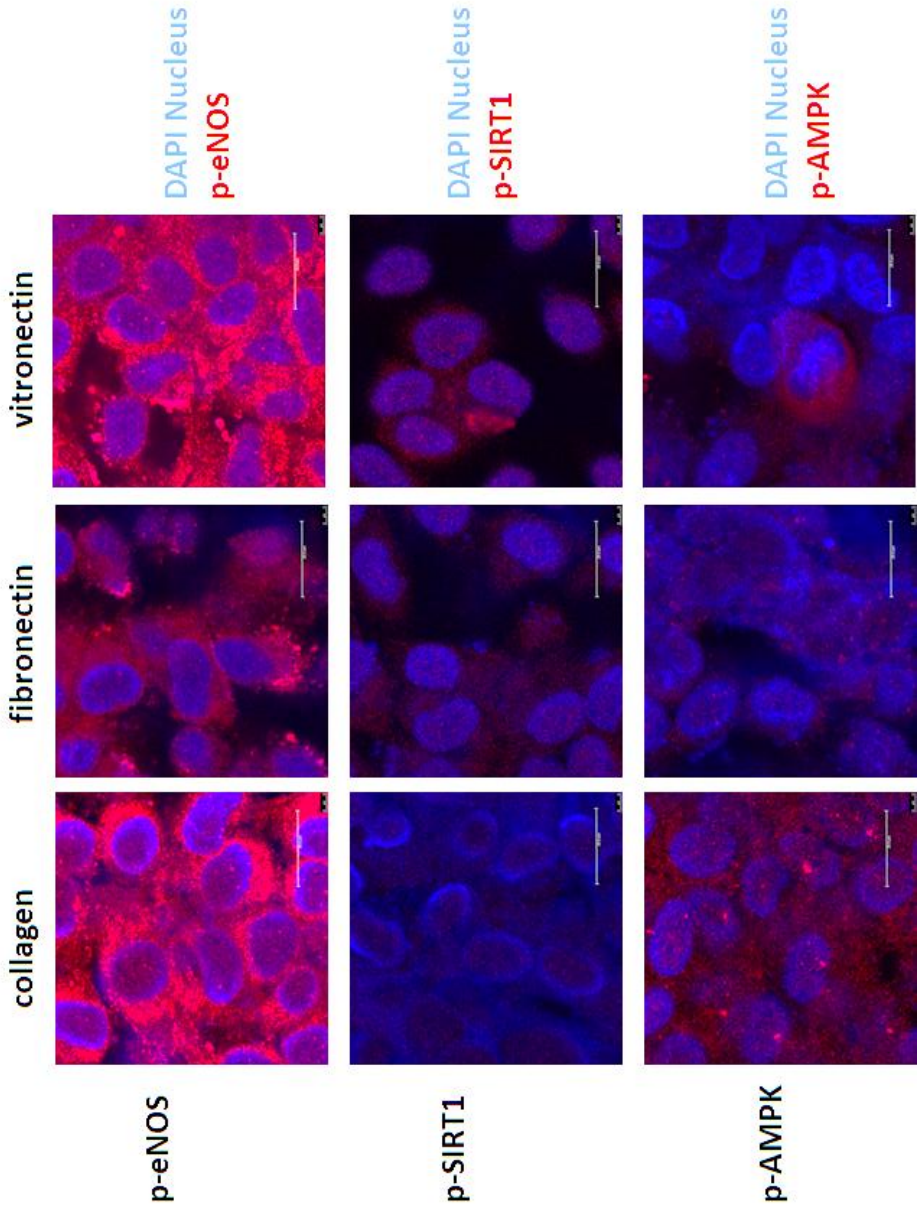

Figure 11.6| Immunocyto chemistry of endothelial cells in static conditions. The results demonstrate a higher p-eNOS and p-AMPK activation of cells seeded on collagen and vitronectin compared to fibronectin The cell nucleus was stained with DAPI and proteins were stained with Texas Red (λ=598 nm). Scale bar = 20 μm

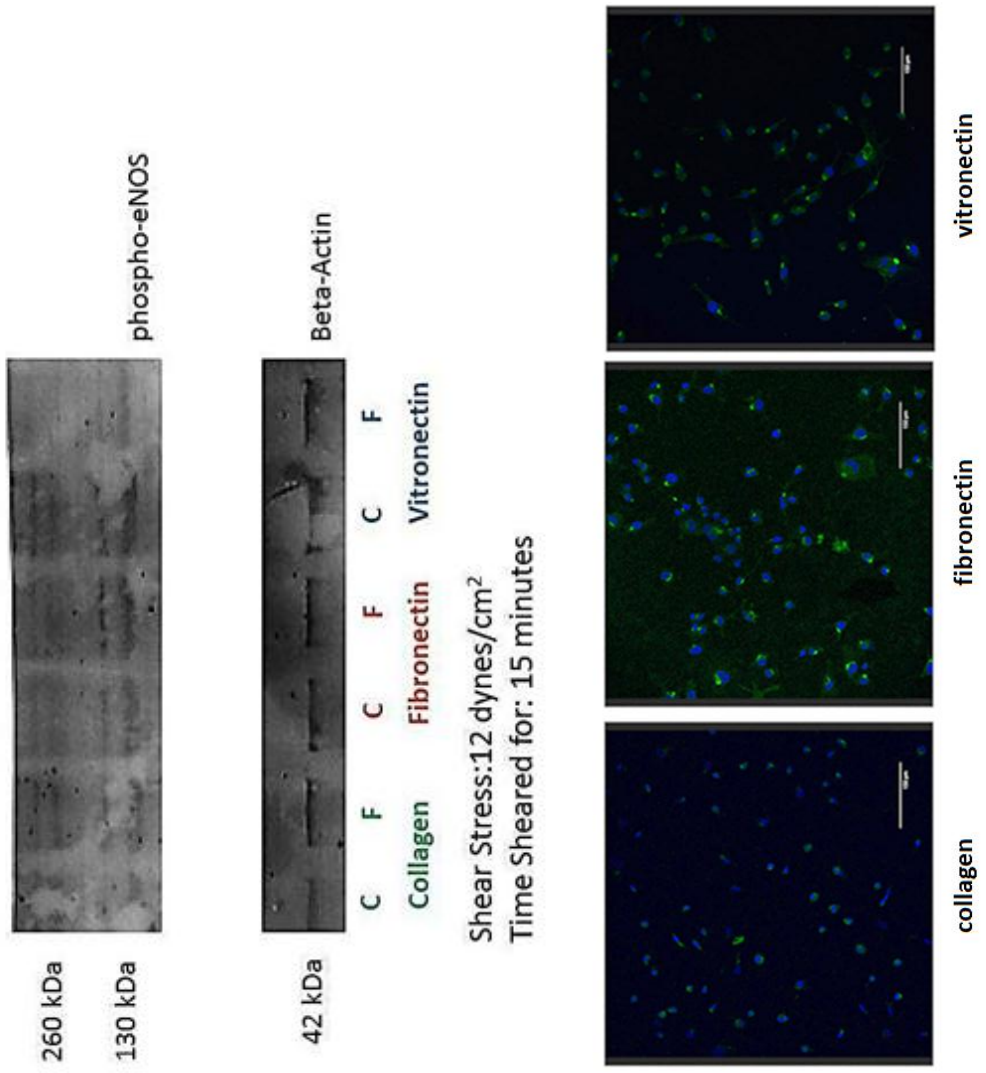

Figure 11.7| Images characterizing expression of eNOS in cells sheared at 12 dynes/cm^2 for 15 minutes. **(A)** Immunoblotting showing p-eNOS and Beta-Actin for collagen, fibronectin, and vitronectin. (B) Immunocyto chemistry demonstrates a higher activation of cells seeded on fibronectin compared to collagen and vitronectin. The cell nucleus was stained with DAPI and p-eNOS was stained with Alexa 488(λ=488 nm). Scale bar = 150 μm

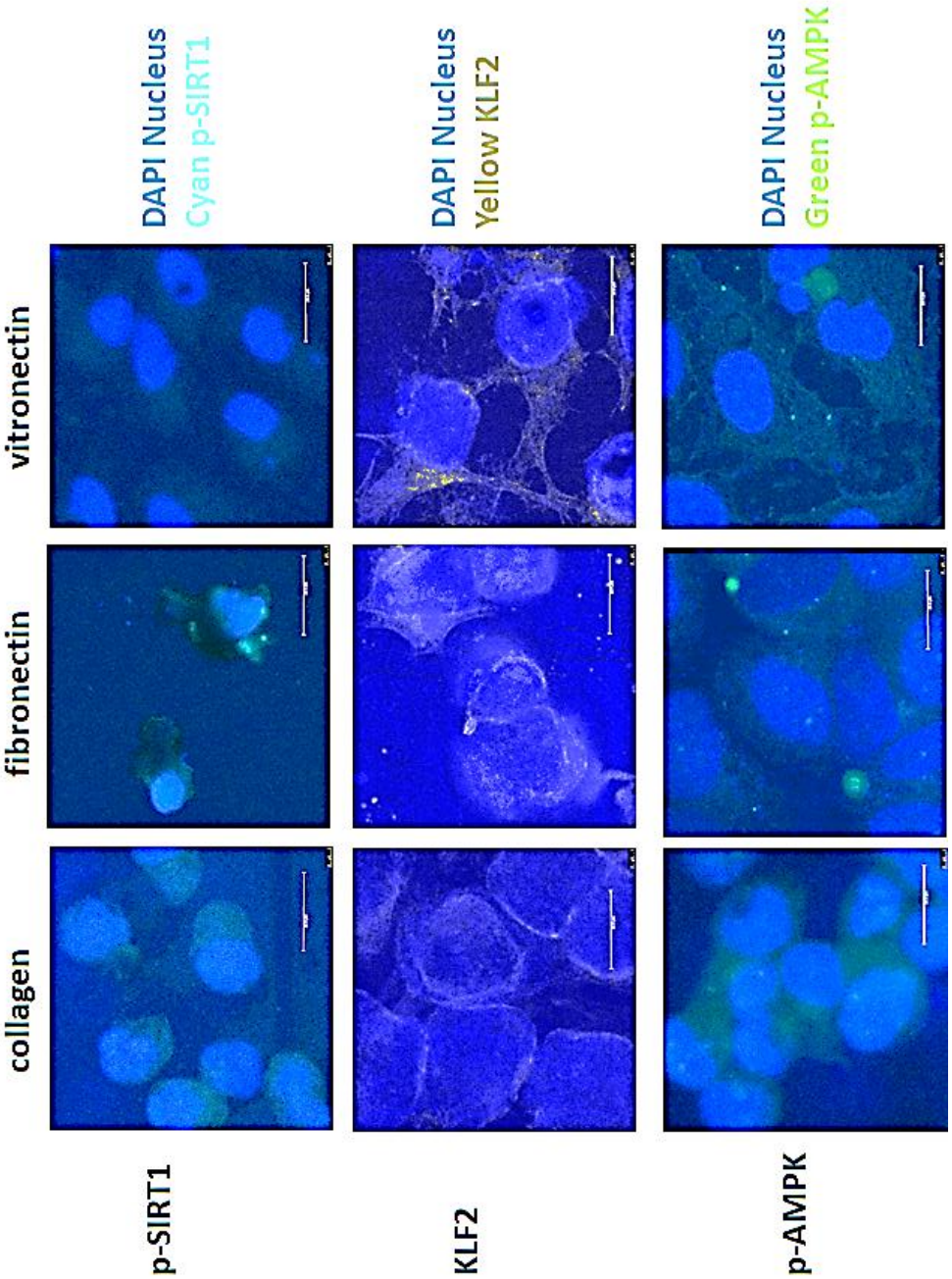

Figure 11.8| Immunocyto chemistry for flow of 12 dynes/cm^2 demonstrates a higher p-AMPK activation of cells seeded on collagen and vitronectin compared to fibronectin. The cell nucleus was stained with DAPI and proteins were stained with Texas Red (λ=598 nm). Scale bar = 20 μm

11.5 CONCLUSION

In response to varying flow parameters, the endothelial cells produce NO which is tightly controlled by shear stress and perhaps mass transfer induced Ca^{2+} influx, AMPK phosphorylation, and downstream eNOS phosphorylation. Along with shear stress and mass transfer, ECM configuration may have an adverse effect on the endothelial cell response. The interplay of all the aforementioned factors converts the endothelium from a quiescent atheroprotective stage to a dysfunctional atherogenic stage. Dysfunctional endothelium is less compliant and less effective to dynamic changes in blood flow and marks the onset of atherosclerosis. In this work, we observed a distinct correlation of ECM configuration to AMPK signaling pathway for flow parameters. Cells on collagen and vitronectin showed a marked increase in AMPK phosphorylation in response to flow, whereas cells on fibronectin showed a sustained response compared to static controls. We observed an enhanced activation of p-eNOS on static conditions when seeded on collagen- and vitronectin- coated substrates. These results demonstrate the importance of both mechanical and chemical cues in activating signaling pathways and pave way to a number of therapeutic strategies.

11.6 REFERENCES

1 Frangos JA, Eskin SG, McIntire LV, Ives CL. (1985) Flow effects on prostacyclin production by cultured human-endothelial cells. Science 227(4693):1477-9.

2 Diamond SL, Eskin SG, McIntire LV. (1989) Fluid-flow stimulates tissue plasminogen-activator secretion by cultured human-endothelial cells. Science. 243(4897):1483-5.

3 Diamond SL, Sharefkin JB, Dieffenbach C, Frasierscott K, McIntire LV, Eskin SG. (1990) Tissue plasminogen-activator messenger-rna levels increase in cultured human endothelial-cells exposed to laminar shear-stress. Journal of Cellular Physiology. 143(2):364-71.

4 Sharefkin JB, Diamond SL, Eskin SG, McIntire LV, Dieffenbach CW. (1991) Fluid-flow decreases preproendothelin messenger-rna levels and suppresses endothelin-1 peptide release in cultured human endothelial-cells. J Vasc Surg.14(1):1-9.

5 Ranjan V, Xiao ZS, Diamond SL.(1995) Constitutive nos expression in cultured endothelial-cells is elevated by fluid shear-stress. American Journal of Physiology-Heart and Circulatory Physiology. 269(2):H550-H5.

6 Nollert MU, Hall ER, Eskin SG, McIntire LV. (1989) The effect of shear-stress on the uptake and metabolism of arachidonic-acid by human-endothelial cells. Biochimica Et Biophysica Acta. 1005(1):72-8.

7 Nollert MU, Eskin SG, McIntire LV. (1990) Shear-stress increases inositol trisphosphate levels in human endothelial-cells. Biochem Biophys Res Commun. 170(1):281-7.

8 Nollert MU, Diamond SL, McIntire LV. (1991) Hydrodynamic shear-stress and mass-transport modulation of endothelial-cell metabolism. Biotechnol Bioeng. 38(6):588-602.

9 Patrick CW, McIntire LV. (1995) Shear-stress and cyclic strain modulation of gene-expression in vascular endothelial-cells. Blood Purification. 13(3-4):112-24.

10 Sampath R, Kukielka GL, Smith CW, Eskin SG, McIntire LV. (1995) Shear stress-mediated changes in the expression of leukocyte adhesion receptors on human umbilical vein endothelial-cells in-vitro. Annals of Biomedical Engineering. 23(3):247-56.

11 Uematsu M, Ohara Y, Navas JP, Nishida K, Murphy TJ, Alexander RW et al. (1995) Regulation of endothelial cell nitric oxide synthase mrna expression by shear stress. American Journal of Physiology-Cell Physiology. 269(6):C1371-C8.

12 Mitsumata M, Fishel RS, Nerem RM, Alexander RW, Berk BC. (1993) Fluid shear-stress stimulates platelet-derived growth-factor expression in endothelial-cells. Am J Physiol. 265(1):H3-H8.

13 Resnick N, Collins T, Atkinson W, Bonthron DT, Dewey CF, Gimbrone MA. (1993) Platelet-derived growth factor-b chain promoter contains a cis-acting fluid shear-stress-responsive element. PNAS USA 90(10):4591-5.

14 Nagel T, Resnick N, Atkinson WJ, Dewey CF, Gimbrone MA.(1994) Sheer stress selectively up-regulates intercellular-adhesion molecule-1 expression in cultured human vascular endothelial-cells. Journal of Clinical Investigation. 94(2):885-91.

15 Resnick N, Gimbrone MA. (1995) Hemodynamic forces are complex regulators of endothelial gene-expression. Faseb Journal. 9(10):874-82.

16 Malek AM, Gibbons GH, Dzau VJ, Izumo S. (1993) Fluid shear-stress differentially modulates expression of genes encoding basic fibroblast growth-factor and platelet-derived growth factor-b chain in vascular endothelium. Journal of Clinical Investigation. 92(4):2013-21.

17 Malek AM, Izumo S. (1994) Molecular aspects of signal-transduction of shear-stress in the endothelial-cell. Journal of Hypertension. 12(9):989-99.

18 Go Y-M, Park H, Maland MC, Darley-Usmar VM, Stoyanov B, Wetzker R, Jo H. (1998) Phosphatidylinositol 3-Kinase Gamma mediates shear stress-dependent activation of JNK in endothelial cells. American Journal of Physiology. 275:H1898-H1904.

19 Ricci R, Sumara G, Sumara I, Rozenberg I, Kurrer M, Akhmedov A, et al. (2004) Requirement of JNK2 for scavenger receptor A-Mediated foam cell formation in atherogenesis. Science. 306:1558-1561.

20 Carling D. (2004) The AMP-Activated Protein Kinase Cascade - a unifying system for energy control. Trends in Biochemical Sciences. 29:18-24.

21 Scott MW, Christopher C, Liya T, Dean W, Angela McN, Hong R, Charles C, Xiaomei Z, Patrick V, Mark McH, Yichen C et al. (2004) Experimental therapeutics, molecular targets, and chemical biology: BAY 43-9006 exhibits broad spectrum oral antitumor activity and targets the RAF/MEK/ERK pathway and Receptor Tyrosine Kinases involved in tumor progression and angiogenesis. Cancer Res. 64:7099-7109.

22 Hardie DG, Salt IP, Hawley SA, and Davies SP. (1999) AMP-Activated Protein Kinase: an ultrasensitive system for monitoring cellular energy charge. Biochemical Journal. 338:717-722.

23 Hardie DG, Carling D, and Sim ATR. (1989) The Amp-Activated Protein-Kinase - a multisubstrate regulator of lipid-metabolism. Trends in Biochemical Sciences. 14:20-23.

24 Sanders MJ, Grondin PO, Hegarty BD, Snowden MA, and Carling D. (2007) Investigating the mechanism for AMP activation of the AMP-Activated Protein Kinase cascade. Biochemical Journal. 403:139-148.

25 Arad M, Seidman CE, and Seidman JG. (2007) AMP-activated protein kinase in the heart - Role during health and disease. Circulation Research. 100:474-488.

26 Levesque MJ and Nerem RM. (1985) The elongation and orientation of cultured endothelial-cells in response to shear-stress. Journal of Biomechanical Engineering-Transactions of the ASME. 107:341-347.

27 Nagata D, Mogi M, and Walsh K.(2003) AMP-Activated Protein Kinase (AMPK) Signaling in endothelial cells is essential for angiogenesis in response to hypoxic stress. Journal of Biological Chemistry 278:31000-31006.

28 Dekker, R. J., R. A. Boon, et al. (2006) KLF2 provokes a gene expression pattern that establishes functional quiescent differentiation of the endothelium. Blood. 107(11): 4354 63.

29 Dekker, R. J., S. van Soest, et al. (2002) Prolonged fluid shear stress induces a distinct set of endothelial cell genes, most specifically lung Kruppel-like factor (KLF2). Blood. 100(5): 1689-98.

30 Dekker, R. J., J. V. van Thienen, et al. (2005) Endothelial KLF2 links local arterial shear stress levels to the expression of vascular tone-regulating genes. Am J Pathol. 167(2): 609-18.

31 Huddleson, J. P., N. Ahmad, et al. (2006) Up-regulation of the KLF2 transcription factor by fluid shear stress requires nucleolin. J Biol Chem. 281(22): 15121-8.

32 Huddleson, J. P., N. Ahmad, et al. (2005) Induction of KLF2 by fluid shear stress requires a novel promoter element activated by a phosphatidylinositol 3-kinasedependent chromatin-remodeling pathway. J Biol Chem. 280(24): 23371-9.

33 Huddleson, J. P., S. Srinivasan, et al. (2004) Fluid shear stress induces endothelial KLF2 gene expression through a defined promoter region. Biol Chem. 385(8): 723-9

34 Parmar, K. M., H. B. Larman, et al. (2006) Integration of flow-dependent endothelial phenotypes by Kruppel-like factor 2. J Clin Invest. 116(1): 49-58.

35 Parmar, K. M., V. Nambudiri, et al. (2005) Statins exert endothelial atheroprotective effects via the KLF2 transcription factor. J Biol Chem. 280(29): 26714-9.

36 Wang, N., H. Miao, et al. (2006) Shear stress regulation of Kruppel-like factor 2 expression is flow pattern-specific. Biochem Biophys Res Commun. 341(4): 1244-51.

37 Lin, Z., A. Hamik, et al. (2006) Kruppel-like factor 2 inhibits protease activated receptor-1 expression and thrombin-mediated endothelial activation. Arterioscler Thromb Vasc Biol. 26(5): 1185-9.

38 Lin, Z., A. Kumar, et al. (2005) Kruppel-like factor 2 (KLF2) regulates endothelial thrombotic function. Circ Res. 96(5): e48-57.

39 Sucharita SB, Samy M, Zhiyong L, Anne H, Atkins GB, Hiranmoy D, Pallab B, Ajay K and Mukesh KJ (2005) Kruppel-Like Factor 2 as a novel mediator of statin effects in endothelial cells. Circulation 112:720-726.

40 Atkins GA and Mukesh KJ. (2007) Role of Krüppel-Like transcription factors in endothelial biology. Circulation Research 100:1686-1695.

41 Ota H, Akishita M, Eto M, Iijima K, Kaneki M, and Ouchi Y. (2007) Sirt1 modulates premature senescence-like phenotype in human endothelial cells. Journal of Molecular and Cellular Cardiology. 43: 571–579

42 Minamino T, Miyauchi H, Yoshida T, Ishida Y, Yoshida H, Komuro I. (2002) Endothelial cell senescence in human atherosclerosis: role of telomere in endothelial dysfunction. Circulation 105:1541–4.

43 Mattagajasingh I, et al. (2007) SIRT1 promotes endothelium-dependent vascular relaxation by activating endothelial nitric oxide synthase. Proc Natl Acad Sci USA. 104: 14855–14860.

44 Orimo M, et al. (2009) Protective role of SIRT1 in diabetic vascular dysfunction. Arterioscler Thromb Vasc Biol. 29:889–894.

45 Toren F, Chu-Xia D & Raul M. (2009) Recent progress in the biology and physiology of sirtuins. Nature. 460: 587-591.

46 Chen Z, Peng IC, Cui X, Li YS, Chien S, Shyy JY (2010) Shear stress, SIRT1, and vascular homeostasis. Proc Natl Acad Sci U S A. 107(22):10268-73.

47 Yang Y, Hou H, Haller EM, Nicosia SV, Bai W (2005) Suppression of FOXO1 activity by FHL2 through SIRT1-mediated deacetylation. EMBO. J 24:1021–1032.

48 Lagouge M, et al. (2006) Resveratrol improves mitochondrial function and protects against metabolic disease by activating SIRT1 and PGC-1α. Cell. 127:1109–1122.49

Michael P. (2010) An energy-sensor network takes center stage during endothelial aging. Circulation Research. 106:1316-1318.

50 Cohen HM, et al. (2004) Calorie restriction promotes mammalian cell survival by inducing the SIRT1 deacetylase. Science. 305, 390.

51 David BS and Reuben JS. (2009) The LKB1–AMPK pathway: metabolism and growth control in tumour suppression. Nature Reviews: Cancer. 9:563-575.

52 Fisslthaler B and Fleming I. (2009) Activation and signaling by the AMP-Activated Protein Kinase in endothelial cells. Circulation Research 105:114-127.

53 Fan Lan and Yasuo Ido, Neil B. Ruderman, X. Julia Xu, Lauren Nelson, José M. Cacicedo, Asish KS (2010) AMPK and SIRT1: a long-standing partnership? Am J Physiol Endocrinol Metab. 298:E751-E760.

54 Carles C, Lake QJ, Atul SD, Chikage M, Agnes C, Marie L, Juleen RZ, and Johan A. (2010) Interdependence of AMPK and SIRT1 for metabolic adaptation to fasting and exercise in skeletal muscle. Cell Metabolism. 11:213–219.

55 Wang Y, Liang Y, and Vanhoutte PM. (2011) SIRT1 and AMPK in regulating mammalian senescence: A critical review and a working model. FEBS Letters.585: 986 994.

56 Hahn C, Orr AW, Sanders JM, Jhaveri KA, and Schwartz MA (2009) The Subendothelial extracellular matrix modulates JNK activation by flow. Circulation Research. 104:995-U180.

57 Iiyama K, Hajra L, Iiyama M, Li HM, DiChiara M, Medoff, Myron IC (1999) Patterns of Vascular Cell Adhesion Molecule-1 and Intercellular Adhesion Molecule-1 Expression

in rabbit and mouse atherosclerotic lesions and at sites predisposed to lesion formation. Circulation Research. 85:199-207.

58 Hynes RO.(1992) Integrins - Versatility, modulation, and signaling in cell adhesion. Cell. 69:11-25.

59 Jalali S, del Pozo MA, Chen KD, Miao H, Li YS, Schwartz MA, Shyy JYJ, and Chein S (2001) Integrin-mediated mechanotransduction requires its dynamic interaction with specific extracellular matrix (ECM) ligands. PNAS. 98:1042-1046.

60 Adams DJ, Barakeh J, Laskey R, Vanbreemen C. (1989) Ion Channels and regulation of intracellular calcium in vascular endothelial-cells. FASEB Journal 3:2389-2400.

61 Anant BP.(2010) Decoding cytosolic Ca2+ oscillations. Cell Review. 7:78-87

62 Dean AW, Sandra MW, Jason W, Maryann H, Jonathan EW and Stephen MB. (2006) Endothelial response to stress from exogenous Zn2+ resembles that of NO-mediated nitrosative stress, and is protected by MT-1 overexpression. Am J Physiol Cell Physiol. 291: C555–C568.

63 Ando J, Ohtsuka A, Korenaga R, Kawamura T, and Kamiya A. (1993) Wall shear-stress rather than shear rate regulates cytoplasmic Ca2+ responses to flow in vascular endothelial-cells. Biochemical and Biophysical Research Communications 190:716-723.

64 Nollert MU, Diamond SL, and McIntire LV.(1991) Hydrodynamic shear-stress and mass-transport modulation of endothelial-cell metabolism. Biotechnology and Bioengineering 38:588-602.

65 Wu Y, Song P, Xu J, Zhang M, Zou MH (2007) Activation of protein Phosphatase2A by palmitate inhibits AMP-activated Protein Kinase. J Biol Chem 282:9777-9788.

66 Winder WW, Thomson DM (2007) Cellular energy sensing and signaling by AMP-activated protein kinase. Cell Biochem Biophys 47:332-347.

67 Witters LA, Kemp BE, Means AR (2006) Chutes and Ladders: the search for protein kinases that act on AMPK. Trends in Biochemical Sciences 31:13-16.

68 Kakolyris S, Karakitsos P, Tzardi M, and Agapitos E (1995) Immunohistochemical detection of fibronectin in early and advanced atherosclerosis. In Vivo (Attiki) 9:35-40.

69 Nakashima Y, Fujii H, Sumiyoshi S, Wight TN, and Sueishi K. (2007) Early human atherosclerosis - accumulation of lipid and proteoglycans in intimal thickenings followed by macrophage infiltration. Arteriosclerosis Thrombosis and Vascular Biology. 27:1159-1165.

70 Ross R.(1999) Mechanisms of Disease - Atherosclerosis - An inflammatory disease. New England Journal of Medicine 340:115-126.

71 Stary HC, Chandler AB, Dinsmore RE, Fuster V, Glagov S, Insull W, et al. (1995) A definition of advanced types of atherosclerotic lesions and a histological classification of atherosclerosis. Circulation 92:1355-1374.

72 Raines EW, Koyama H, and Carragher NO. (2000) The extracellular matrix dynamically regulates smooth muscle cell responsiveness To PDGF. Atherosclerosis V: The Fifth Saratoga Conference 902:39-52.

73 Stenman S, Vonsmitten K, and Vaheri A. (1980) Fibronectin and atherosclerosis. Acta Medica Scandinavica 165-170.

74 Levenson J, Giral P, Razavian M, Gariepy J, and Simon A. (1995) Fibrinogen and silent atherosclerosis in subjects with cardiovascular risk-factors. Arteriosclerosis Thrombosis and Vascular Biology 15:1263-1268.

75 Heino J. (2000) The Collagen receptor integrins have distinct ligand recognition and signaling functions. Matrix Biology 19:319-323.

76 Schwarzbauer JE and Sechler JL. (1999) Fibronectin Fibrillogenesis: a Paradigm for extracellular matrix assembly. Current Opinion in Cell Biology 11:622-627.

77 Vinogradova O, Velyvis A, Velyviene A, Hu B, Haas TA, Plow EF, et al. (2002) A Structural mechanism of integrin Alpha(Iib)Beta(3) "Inside-Out" activation as regulated by its cytoplasmic face. Cell 110:587-597.

78 Bakker SJL and Gans ROB. (2000) About the role of shear stress in atherogenesis. Cardiovascular Research 45:270-272.

79 Gibson CM, Diaz L, Kandarpa K, Sacks FM, Pasternak RC, Sandor T, et al. (1993) Relation of vessel wall shear-stress to atherosclerosis progression in human coronary-arteries. Arteriosclerosis and Thrombosis 13:310-315.

80 Feldman CL, Ilegbusi OJ, Hu ZJ, Nesto R, Waxman S, and Stone PH. (2002) Determination of in-vivo velocity and endothelial shear stress patterns with phasic flow in human coronary arteries: A methodology to predict progression of coronary atherosclerosis. American Heart Journal 143:931-939.

81 Lowe GDO, Drummond MM, Lorimer AR, Hutton I, Forbes CD, Prentice CRM, et al. (1980) Relation between extent of coronary-artery disease and blood-viscosity. British Medical Journal 280:673-674.

82 Liu XP, Yan QT, Baskerville KL, and Zweier JL. (2007) Estimation of nitric oxide concentration in blood for different rates of generation - evidence that intravascular nitric oxide levels are too low to exert physiological effects. Journal of Biological Chemistry 282:8831-8836.

83 Wang YP, Shin WS, Kawaguchi H, Inukai M, Kato M, Sakamoto A, et al. (1996) Contribution of sustained Ca2+ elevation for nitric oxide production in endothelial cells and subsequent modulation of Ca2+ transient in vascular smooth muscle cells in coculture. Journal of Biological Chemistry 271:5647-5655.

CHAPTER 12
CONCLUSION

In this work, the impact of charge distribution, biomaterial geometrical cues, flow parameters and mass transfer have been studied both mathematically, computationally, and experimentally.

We designed a novel in-situ device which can capture the electrostatic potential of a confluent cell layer for the first time. Our results show that the microvilli developed on the mucosal cells positively contribute to the overall measured zeta potential. These results are important and can be successfully utilized for pharmaceutical applications.

The bio-interaction of endothelial cells with micro-patterned and nano-patterned titanium has been studied. Endothelial cells proliferate and align themselves to a healthy morphology in 0.5 μm Ti substrates. The dense extracellular matrix synthesized by the cells on the nano-featured 0.5 μm grooves provides extensive migratory cues to the cells. Further, signaling on the Ti substrates demonstrated higher endothelial functionality on the 0.5 μm grooved ti substrates. The cell spreading and the extracellular matrix synthesized by the cells determine the overall cell fate. In conclusion, endothelial cell fate is dependent on the modification of the extracellular matrix and the substrate or the micro-environment on which they are cultured and eventually differentiate into a mature EC phenotype. A better understanding of the role of occurring matrix in the various steps of angiogenesis would conceivably contribute to the intelligent design of tissue-engineered constructs where angiogenesis is critical for tissue repair and restoration.

It has long been accepted that mechanotransduction, and not mass transfer, is the fundamental mechanism for hemodynamic forces modulated endothelial signaling pathways and their downstream gene products. The underpinning criteria used to

determine the dominance of mechanotransduction largely draws on the relationship between signaling behavior and shear rate and shear stress, relative to changes in viscosity. However, in our work, we computationally and experimentally evaluate mass transfer-limited *in-vitro* parallel flow chamber systems with respect to this accepted criteria. These results show similar viscosity-dependency relative to shear rate and shear stress, previously thought to be sufficient conditions for mechanotransduction. Thus, mass transfer considerations should be carefully examined when studying triggering methods in signaling cascades.

Through our computational simulations, we demonstrate the impact of fluid dynamics and mass transfer of chemical species in signaling pathways regulating gene transcription and DNA synthesis. Our computational results show the importance of species mass transfer in triggering signal transduction pathways. We further designed another novel *in-situ* transmembrane device that provides significant variations in concentration gradient while constant shear profiles for modest variations in transmembrane pressure. These results can be applied to the vascular system to differentiate mass transfer from mechanotransduction.

To further understand the vascularization, an attempt to understand the extracellular matrices in healthy and pathological atherosclerotic conditions. The atomic force micrographs reveal the structure of the extracellular matrices. The streaming potential of the extracellular matrices adsorbed membranes is more negative when compared to membranes themselves. The hydraulic conductivity of the extracellular matrices also demonstrates a decrease. Further, after 12 hours of flow, cell seeded on

vitronectin observed both necrosis and mitosis to a larger extent. Cells also formed clumps on the vitronectin surface. Immunocytochemistry demonstrates a higher activation of p-AMPK on collagen and vitronectin implying the possible enhanced presence of ocal adhesion points on these substrates. These results in summary validate the importance of biotransport factors such as charge properties, geometrical transegrity, mass transfer, mechanical stimuli in triggering the underlying signaling pathways.

Appendix A

Abbreviations

AFM Atomic force microscopy

BSA Bovine serum albumin

DTT Dithiothreitol

EDTA Ethylenediaminetetraacetic acid

eNOS Endothelial nitric oxide synthase

FITC Fluorescein isothiocyanate

GAM Goat anti-mouse

GAR Goat anti-rabbit

HCl Hydrochloric acid

HRP Horseradish peroxidase

HSA Human serum albumin

IU International unit

KLF2 Kruppel Factor 1

mAb Monoclonal antibody

MW Molecular weight

o/n Over night

AMP Adenosine mono phosphate

ADP Adenosine di phosphate

ATP Adenosine tri phosphate

AMPK AMP activated protein kinase

PBS Phosphate-buffered saline

PFA Paraformaldehyde

RT Room temperature

SDS Sodium dodecyl sulfate

SDS-PAGE SDS-Polyacrylamide gel electrophoresis

SEM Standard error of mean

Si Silicon

SIRT1 Sirtulin 1

TBS Tris-buffered saline

TBST Tris-buffered saline with Tween

Ti Titanium

Tween-20 Polyoxyethylene sorbitan monolaurate

VWF Von Willebrand factor

Appendix B

Protocols

B1. Solutions and buffers

B1.1 Phosphate buffered solution - PBS (without Ca2+) – 10X

(a) NaCl 80 g

(b) KCl 2 g

(c) KH2POO4 2.4 g

(d) Na2HPO4 14.4 g

(e) Mix all the componenets using a maganatic stirrer in 800 mL of DI water.

(f) Once stirred up, add DI water to the solution to make it 1000 mL

(g) Check for pH. Ensure a pH od 7.4

(h) To make a 1 X PBS solution, add 100 mL of 10X to 900 mL of DI water.

(i) Autoclave.

B1.2 TBST – 10 X

(a) NaCl 80g

(b) Tris base (pH 7.4) – 24.23 g

(c) To make 1 X TBST, add 100 mL DI water and 1 mL Tween.

(d) When adding Tweeen, take a pipett tip and cut it's end when using it. Twin is highly viscous.

B2 Western blot recipes

B2.1 Resolution gel:	50ml	20ml	10ml
dH_2O	24.2ml	9.48ml	4.78ml
1.5M Tris-HCL(pH8.8)	12.5ml	5.0ml	2.5ml
10% SDS	500ul	200ul	100ul
40% Acrylamide/Bis	12.5ml	5.1ml	2.5ml
TEMED	50ul	20ul	10ul
10% APS(Fresh)	250ul	200ul	100ul

B2.2 Sacking gel:	20ml	10ml	5ml
dH_2O	12.66ml	6.28ml	3.1ml
0.5M Tris-HCL(pH6.8)	5ml	2.5ml	1.25ml
10% SDS	200ul	100ul	50ul
40% Acrylamide/Bis	1.95ml	1000ul	600ul
TEMED	40ul	20ul	10ul
10% APS	150ul	100ul	50ul

B2.3 Transfer buffer:	1500ml
Tris Base(no HCL)	4.54g
Glycine	21.7g
dH_2O	500ml and mix
Methanol	300ml mix with 200ml dH2O
Bring to 1500ml with dH_2O	

B2.4 Plain buffer:	100ml	50ml	25ml
1M Tris-HCL(pH7.5)	2ml	1ml	500ul(.5ml)
5M NaCl	2.75ml	1.37ml	680ul(.68ml)
Tween-20(100%)	100ul	50ul	25ul
Bring up with dH_2O to	100ml	50ml	25ml

B2.5 2X Dilution/Sample buffer 4ml

0.5M Tris-HCL(pH6.8)	1ml
Glycerol (100%)	0.8ml
10% SDS(Laryl Sulfate)	1.6ml
2-ME (□-mercaptoethanol)	0.4ml
0.05% Bromophenol Blue(dye)	0.2ml

B2.6 Stripping buffer

(a) 100 mM 2-mercaptoethanol

(b) 2% SDS

(c) 62.5 mM Tris-Cl pH 6.7 pr TBS pH 6.8

B2.7 0.5M Tris-HCL: 400ml

(a) 6.05g Tris base in 40ml dH_2O

(b) Adjust pH 6.8 with 1 N HCL

(c) Add dH_2O to 400ml total volume

B2.8 1.5M Tris-HCL: 500ml

(a) 91g Tris base in 300ml dH2O

(b) Adjust pH 8.8 with 1N HCL

(c) Add dH2O to 500ml total volume

B2.9 Coomassie blue G-250 staining solution

(a) Acetic acid 20ml

(b) dH_2O 180ml

(c) Coomassie blue G-250 0.05g

(d) Mix 1 hr. store RT

B2.10 Destaining buffer

(a) 50 parts acetic acid

(b) 165 parts methanol

(c) 785 parts dH_2O

B2.11 Running buffer (10X)

(a) Tris base (pH 7.4) 30.3 g

(b) Glycine 144 g

(c) SDS 10 g

(d) DI water 1000 mL

B2.12 Transfer Buffer (10X)

(a) Tris base (pH 7.4) 30.3 g

(b) Glycine 144 g

(c) SDS 10 g

(d) DI water 1000 mL

(e) For PVDF membranes, add 800 mL of 1X Transfer buffer and 200 mL of methanol.

(f) For Nitrocellulose membrane, use 1 X transfer buffer.

B2.13 Primary antibody

(a) 1 X TBST

(b) 5% BSA of TBST

(c) 100 X Sodium Azide

(d) Desired concentration of primary antibody

B2.14 Secondary antibody

(a) 1 X TBST

(b) Desired concentration of secondary antibody

B2.15 5% Milk

(a) Use non-fat dry milk

(b) Use 1 X TBST

(c) 5% milk powder

(d) Shake on the rocker overnight until milk completely dissolves in 4 ^{o}C

B3. Cell culture protocol

B3.1 Passaging cells

(a) Wear lab coat, gloves, and spray gloves with ethanol.

(b) Remove DMEM and Trypsin from 4 °C and place in water bath.

(c) Retrieve all necessity materials for cell culturing (i.e. pipet, pipet tips, flasks, PBS…etc) and spray with ethanol before placing in hood.

(d) Remove cell culture flasks from incubator. Tighten cap before transferring to hood.

(e) Remove all caps from culture flasks and place them in an area where they will not be in the way

(f) Use the pump with a pipet tip attached to the rod to remove the DMEM. Hold the flask at an angle while doing so.

(g) Add 5ml PBS to wash off any remaining DMEM

(h) Remove PBS

(i) Add approximately 2 ml of trypsin. Make sure the bottom the flask is covered.

(j) Remove trypsin immediately after adding it.

(k) Allow flasks to sit for a few minutes (Take this time to label new flasks)

(l) Check cells under microscope and see if they are detached and grouping.

(m) Take new flasks and add 10ml of DMEM.

(n) Add DMEM (enough to equally divide up into new flasks) to the flasks with cells.

(o) Suck up and down the DMEM with the cells.

(p) Add cells to new flasks.

(q) Check cells under microscope.

(r) Place flasks in incubator. Unscrew cap slightly after placing them in incubator

B.3.2 Making DMEM media

(a) Take 1000ml of DMEM

(b) Check front and see what has been added

(c) Add 10ml of Penicillin (or enough to make 1% concentration)

(d) Add 10ml of L-Glutamine (or enough to make 1% concentration)

(e) Add 10ml of Sodium Pyruvate (or enough to make 1% concentration)

(f) Add 100ml of FBS (or enough to make 10% concentration)

(g) Swirl the media to homogenize the solution.

(h) Filter the media using a 0.22 μm filter (milipore)

(i) Mark what has been added and date the media and write your name.

B.3.2 Making MEM media

Quantity: 2 Liters

(a) M199 powder 2 packages (1 package for 1 liter)

(b) HEPS 9.5 g (final content 20 mM)

(c) Heparin sodium 0.216 g (108 mg/L)

(d) NaHCO3 4.4 g (2.2 g/L)

Growth factors

(a) Prepare 1X PBS containing 0.1 % BSA

(b) Filter PBS with 0.22 um filter

(c) Diccolve B-endothelial cell growth factor 25 um [E1388 Sigma] by 8 mL filtered PBS.

(d) Ensure the stock solution to be of concentration 3.1 ug/ml.

(e) Store at -20 ^{o}C.

Prepare 100X Thymidine

(a) Add 25 mg of thymidine

(b) 10 mL of DI water

(c) Mix to dissolve and then sterilize using filter (0.22 um filter)

(d) Aliqout and store in -20 ^{o}C

Prepare complete M199 media (15% FBS)

(a) M199 media 850 mL

(b) FBS 150 mL

(c) Glutamine 10 mL

(d) Sodium Pyruvate 10 mL

(e) Penicillin/Streptomycin 10 mL

(f) Growth factor 1 mL

(g) Thymidine 1 mL

B4 Western blots and quantification

Western blot protocol

Cast Gel

(a) Assemble minigel apparatus (Ensure no leakage)

(b) Make resolution gel (recipe) and mix

(c) Add 7.5ml of resolution gel to plates; To ensure that the gel is bubble free, add ethanol

(d) Make stacking gel (recipe) → diwater—acrylamide/bis

(e) Resolution gel should be hard now, pour off water, blot with filter paper

(f) Finish stacking gel (temed, aps),shake gently. Add stacking gel until at top, not overflowing. ***Hurry and insert comb** **no air bubbles*****

(g) Wait for approx. 30min for gel to harden.

While waiting for stacking gel to harden:

Prepare samples

(a) Fill up ice in an ice bucket, turn heat block on

(b) Take samples out of the freezer into water bath to thaw if needed.

(c) Then place the samples in the ice bucket.

(d) Label eppendorf tubes

(e) Add Xμl of <u>sample</u> to tubes (λ= ug/ul)

Run gel

(a) Remove the combs

(b) Place both the gels in the electrophoresis setup

(c) Add running buffer (pour on side to prevent bubbles).

(d) Ensure gels are at eye level

(e) To load samples, press 1st stop, place tip in bottom of tube, lift sample slowly, no bubbles!!

(f) Load samples to the wells

(g) Assemble box.

(h) Run for 30 minutes at 80 V and approx.. 1.5 hours at 130 V.

(i) Keep checking the gel to prevent any errors.

Transfer electrophoresis

(a) Cut PVDF membranes (size of the gel)

(b) Soak the cut membrane in a plastic dish with methanol.

(c) Soak foam pads in transfer buffer to minimize the presence of any bubbles.

(d) Assemble the sandwich in the box. Take extra care to remove any bubbles.

(e) Sandwich: 2 foam pads→sheet of filter paper place on gel →1st gel (no bubbles)→membrane(no bubbles)→filter paper→2foam pads.

(f) Place in box apperatus--clamp--fill with transfer buffer--no leaking—pour into side

→ Run ~2hr at ~21v

Block membranes

(a) Add 20ml milk buffer and rocker 20min.

(b) Pour the milk out

Incubate membranes in primary antibody

(a) Add 10ml milk buffer with primary antibody in plates and rock 1hr. (Could stop here and put in 4^{o} over night.)

(b) ***save antibody***

(c) Add 10ml TBST and rock for 10 min. / pour out / repeat 3-4 times for 30 mins.

Incubate membranes in secondary antibody

(a) Add 10 ml of secondary antibody.

(b) Rock 30 min / pour out milk / repeat 3-4 times for 30 minutes.

Develop film

(a) Take saran wrap and cut a piece for each membrane

(b) In plastic sq boxes add detection reagent 3 ml. #1, and 3 ml. #2 ***mix***

(c) Blot membrane on sides

(d) Place membrane in detection reagent and shake for 1 min.

(e) Blot membrane lightly on sides, place on saran wrap(in cassette) and fold over

(f) Tape them down on the cassette / close

(g) In darkroom (red light) → place film on membrane and close box → for one minute

(h) Place film in autodev. Machine → check film.

B5 Flow experiments

(a) Coat extracellular matrices of interest on autoclaved glass slides.

(b) Let the slides be air-fried in the hood for atleast two hours.

(c) Seed 10 x 10^5 cells/cm^2 on the coated slides.

(d) Set the flow experimental setup and close the chamber with the gasket-sealed slide.

(e) Ensure that minimal or no air bubbles are trapped in the system.

(f) The two cylinders have to be separated with heights corresponding to the shear stress that has to be applied to the cell flow system.

(g) Perform western blots or immuno-cyto chemistry to visualize and quantify the protein concentration.

B6 Making samples for western blots

(a) Remove slides carefully and perform the subsequent steps on ice.

(b) Place cells in ice cold PBS

(c) Add lysis buffer on cells.

(d) Scrape of the cells into labeled and autoclaved epindorph tubes.

(e) Vortex the samples for a quick ten seconds.

(f) Place samples on ice.

(g) Once all samples are ready, centrifuge the samples for 15 minutes at 12K RPM

(h) Now pipette out the supernatant into corresponding autoclaved and sterile epindorf tubes.

(i) Ensure it to be done on ice.

B6.1 Bradford Assay to detect protein concentration

(a) Pipette out 4 ul of the supernatant and add it to 1 mL of commassie ble (Bradford assay).

(b) Repeat for all samples. Measure the concentration of the protein using a spectrophotometer (set λ=595 nm).

(c) Once the absorbance is obtained, multiply the absorbance with the calibration constant to obtain the concentration of the protein.

B6.2 Final steps

(a) Add loading sample into the epindorf tubes having the supernatant of the protein sample.

(b) Centrifuge for 1 minute.

(c) Boil the samples.

(d) Store in -20 ^{o}C or start running Western blots.

B7 Immunocytochemistry protocol

B7.1 Fixation

(a) Grow cells to 50-70% confluency. Fix cells onto plates or slides with **FRESH** 4% paraformaldehyde in PBS OR ice cold methanol for 5 minutes.

(b) Wash 3 times with PBS.

(c) To Prepare FRESH 4% paraformaldehyde: "Dissolve EM grade paraformaldehyde in PBS in small bottle with stir bar (2g into 50 mLs).

(d) Add a few drops of NaOH and heat in hood (keep bottle cap loose) at 60°C to dissolve.

(e) Cool to room temperature and adjust pH to 7.4. Make fresh prior to use.

B7.2 Permeablization

(a) Permeablize cells by exposure to 0.1% Triton X-100 in PBS for 5 minutes.

(b) Wash 1 time with 0.1% Triton-X 100 in PBS.

B7.3 Primary antibody

(a) Add primary antibody at proper dilutions (must test antibody first at several concentrations to know best dilution) in PBS + 30 mg/ml BSA + 0.1% Triton X-100.

(b) Incubate for 90 minutes.

(c) Wash 3 times consecutively with 0.1% Triton X-100 in PBS.

B7.4 Secondary antibody

(a) Add secondary antibody at proper dilutions in PBS + 30mg/ml BSA + 5% normal donkey or goat serum (depending on secondary antibody source) + 0.1% Triton X-100.

(b) Incubate for 60 minutes (room temperature) to overnight (4 degrees Celsius).

(c) Dilutions for molecular probes antibodies ~1:500.

(d) Wash 3 times with 0.2% Triton X-100 in PBS ~ 5 minutes.

5. Stain with 1 μg/ml DAPI in PBS for 1 minute.

6. Wash 3 times with 0.1% Triton X-100 in PBS.

7. Wash samples 3 times with PBS to remove triton-X 100

8. Image the cells.

B8 Monocyte binding experiments

Assay1:

(1) Starve EA926 cells for 24 hours prior to the planned experiments.

(2) Label the cells with Yo-Pro1 and PI for ten minutes.

(3) Harvest the EA926 cells by centrifuging at 800 rpm for ten minutes and suspend them in serum free media.

(4) Culture these suspended and labelled cells on Ti substrates.

(5) After four hours, EA926 cells can be treated with TNFα for four hours.

(6) Label the nuclei of the THP1s alone using Hoechest dye for 20 minutes.

(7) Harvest the THP1s by centrifuging at 800 rpm for ten minutes and suspend them at a concentration of 1×10^6 cells suspended in serum free media.

(8) Wash the monocyte pellet twice with serum free media and resuspend them in 10 ml serum free media.

(9) Place the THP1s in the incubator for one-two hours.

(10) Now, expose the EA926 cells to THP1s for two hours.

(11) Discard the cell culture media and wash the monocyte bound endothelial cells with 1XPBS three times.

Assay 2:

(1) Starve EA926 cells for 24 hours prior to the planned experiments.

(2) Harvest the EA926 cells by centrifuging at 800 rpm for ten minutes and suspend them in serum free media.

(3) Culture these suspended and cells on ECM coated slides.

(4) After four hours, EA926 cells can be treated with TNFα for four hours.

(5) Harvest the THP1s by centrifuging at 800 rpm for ten minutes and suspend them at a concentration of 1×10^6 cells suspended in serum free media.

(6) Wash the monocyte pellet twice with serum free media and resuspend them in 10 ml serum free media.

(7) Place the THP1s in the incubator for one-two hours.

(8) Now, expose/flow the EA926 cells with THP1s for two hours.

(9) Collect the cells and analyse with flow cytometry for Ly6c.

B9 Flow-cytometry experiments

Indirect Staining (With fluorochrome - unconjugated primary antibodies and fluorochrome – conjugated secondary antibodies)

(a) Label tubes.

(b) Add unconjugated primary antibodies to tubes. Use approximately 1 μg per tube.

(c) Add 100 μl of the prepared cell suspension (equal to 1 million cells) to each tube.

(d) Vortex and incubate for 15-30 min in a covered ice bucket.

(e) To wash off excess antibody following staining, add 1.5-2 ml of 1X PBS to each tube.

(f) Centrifuge in tabletop microfuge for 5 minutes at 2000 RPM (or 3000-4000 RPM for intracellular staining).

(g) Aspirate supernatant, being careful not to disturb pellet.

(h) Add 100 μl of 1X PBS to each tube.

(i) Add fluorochrome-conjugated secondary antibodies to tubes. Use 0.5-1 μg of antibody.

(j) Vortex and incubate for 15-30 minutes in a covered ice bucket.

(k) To wash off excess antibody following staining, add 1.5-2 ml of 1X PBS to each tube.

B10 Preparing SEM/TEM samples

The purpose of fixation is to solidify the protein sol to preserve the spatial relationships of the various organelles as they were at the instant of fixation.

(a) Fixation renders insoluble all the other chemical constituents of the cell such as nucleicacids, nucleoproteins, carbohydrates and lipids.

(b) Most common fixatives are aldehydes (formaldehyde and glutaraldehyde). They preserve structure but do not fix lipids.

(c) Osmium Tetroxide is used to fix lipids and provide electron contrast (fixative and stain).

(d) Potassium ferrocyanide enhances OsO4 staining making metal salt staining optional

At 4^{o}C on iice:

(a) Wash with PBS 1X for 5min

(b) Fix with 2% glutaraldehyde 1h

(c) Wash with PBS 1X for 5min

(d) Fix with 2% osmium tetroxide for 2 hours

(e) Wash with PBS 1X for 5min 3X

(f) Dehydrate the samples using series dilution for 100% ethanol.

(g) Start with 30%- 40%-50%-60%-70%-90%-100%

(6) Take the samples to the imaging center for further processing.

MakingOsmium:

To make 2% OsO4 (/2% K3; [Fe(CN)6])

4% aqueous OsO double strength buffer (0 2M) and K [Fe(CN)] 3X

4% aqueous OsO4 double strength buffer (0.2M), and K3

[Fe(CN)6].

B11 Using critical point dryer for SEM samples

Balzar's Critical Point Dryer Operating Instructions.

Drying and Cooling gas is CO_2.

Transferring liquid may be acetone, ethanol. Freon.

Approximately seven runs per tank of CO_2.

(a) Check the log book for number of runs -- log in.

Load

(b) Make sure all three valves are closed (gas inlet, gas outlet and gas metering).

(c) Unscrew the chamber lid. If there is pressure in the chamber (lid won't unscrew) open both the gas valves, then close again.

(d) Check to make sure that the magnetic stir bar and serrated disc are in place.

(e) Fill the chamber both enough of the transferring liquid (acetone, etc.) so that the specimens within the transfer baskets will be covered

(f) Rapidly transfer the sample lid down, hand tight only.

(g) Turn on the Main switch and open the valve on the CO_2 tank all the way.

Cool

(h) Set the chamber cooling temperature to +15 ^{o}C.

(i) Depress the TEMP button. The CPD will began automatically cooling the specimen chamber to the selected temperature. When 15 ^{o}C is reached exchange of the transferring liquid (acetone) with the drying gas (cm CO_2) can begin. The CPD will maintain a temperature of +15 ^{o}C, + or – 3^{o}C.

Exchange

(j) Slowly open the gas inlet valve. Observe via the sight glass the filling of the chamber.

(k)Note the Schlerin line patterns. These indicate the mixing of fluids and signals the beginning of exchange.

(l) When the chamber is nearly full close the Inlet valve. Depress STIRRER button. Let the fluids mix far 3-4 minutes. Do not use the magnetic stirrer when fragile specimens are to be dried.

(m) Switch off the stirrer.

(n) Open the gas out valve one or more turns. Slowly open the metering valve and drain the liquid from the chamber observing the float level through the sight glass.

(o) When the fluid level is lust above the specimen basket (or the specimens inside the basket); close the metering and gas nut valves.

(p) Repeat steps (j)-(o) until all traces if acetone is gone and until a fine spray of dry CO_2 is emitted during the surge.

Heat

(q) Fill the chamber almost to the top slight glass. To prevent damage to the burst membranes do not fill the chamber completely.

(r) Make sure all valves on the CPD are closed. Shut off the magnetic stirrer. Close the CO_2 valve all the way.

(s) Set the temperature to 42 ^{o}C. The CPD will automatically began warming the chamber. The pressure within the chamber wall also began to rise. Monitor the pressure carefully. If the pressure approaches 1500 psi, reduce the pressure both the gas nut and

metering valves to 1160-1230 psi. At 1600-2000 psi, the burst membrane will rupture and your samples will be ruined.

(t) As the critical temperature and critical pressure are approached. the CO_2 will go from a liquid to a gaseous state. If there has been an inadequate exchange CO_2 for the acetone in your sample, the pressure will not exceed 1000 psi, in which case the critical point is never reached. Samples may be salvageable, so proceed with pressure reduction.

(u) To ensure complete drying has taken place, wait until the critical temperature and pressure are exceeded:

Critical values of CO_2 are 31.0 ^{o}C and 1072 psi; so go to 40 ^{o}C and 1160-1230 psi.

(v) Begin pressure reduction by opening the gas out valve one or two turns and slowly open the metering valve. The metering valve allows you to regulate the rate of pressure reduction which should take 15-20 minutes. If the gas within the chamber begins to recondense, you are reducing the pressure too quickly.

(w) At 0 psi, fully open the gas put and metering valves. Unscrew the chamber lid and remove you samples. Samples will be very hygroscopic.

(x) Replace the lid but don't screw on the lid. Close all valves, release the temperature button, and Shut off the main valves.

Appendix C
Importance of Mass Transfer at the Vascular Endothelium

Abstract

In the endothelium, various signaling pathways regulate vascular homeostasis. The regulation of these signaling pathways has been credited to mechanical transducers on the endothelium. However, the mechanisms behind the working of these signaling pathways are not clearly known. We hypothesize that species mass transfer from the blood flow into the endothelium might explain the mechanism underlying the operation of signaling pathways. In this work, the importance of mass transfer will be studied by mimicking the effect of flow parameters occurring in an emulated vascular bed. The results of this work will help further elucidate the importance of mass transfer in signaling pathways associated with the feedback mechanism of vascular hemostasis.

Introduction

The endothelium is a monolayer of cells that lines the interior surface of blood vessels and hence experiences the dynamics of blood flow. Vascular homeostasis, as a consequence of ever changing blood flow dynamics, is regulated and maintained by various endothelial signaling pathways. Signaling between the blood flow and vasculature affects the accumulation of potentially atherogenic molecules (e.g., NO, VCAM1), transport of cellular nutrients (e.g., O_2, glucose), and removes metabolic wastes (e.g., CO_2, urea) from the arterial walls. For instance, activation of various endothelial signaling pathways (e.g., AMPK). regulates NO synthesis through ion transport (e.g., Ca^{2+}) from the vascular surface into the endothelium.[1] However, the working of these signaling pathways remains ambiguous.

The dominance of mechanical transducers and species mass transfer at the endothelium has been debated for half-a-century.[2-4] Mechanical transducers have been presumed to convert mechanical forces to chemical signaling pathways where as mass transfer has been defined as the transport of chemical species into the underlying system.

Nevertheless, previous studies have shown the dominance of mechanical transducers on endothelial signaling pathways.[5-7] In one such study, Korenaga *et al*.(1997) [5] correlate the down regulation of VCAM-1 mRNA levels to shear stress and shear rate. They hypothesize that the VCAM-1 dependency on shear stress is correlated to the effects from mechanical transducers and its dependency on shear rate is correlated to the effects from mass transfer. From their in-vitro experimental results (Shown in

Figure 1), they demonstrate shear stress dependency and shear rate independency suggesting the dominance of mechanotransducers at the endothelium.

We hypothesize that species mass transfer from the blood flow into the endothelium might explain the mechanism underlying the triggering of signaling pathways. In our studies, we revisit the experiments performed by Korenaga et al. (1997). to elucidate the importance of mass transfer by emulating a mechanotransducer-free vascular bed.

Materials and Methods:

We experimentally studied the effects of flow parameters and fluid properties on an engineered mass transfer system Mass transfer experiments were performed using an aqueous mixture containing measured quantities of Yellow #5 and #6 dyes, delivered through a rectangular tangential-flow diafiltration module. Water and dye solution are introduced into the module by two inlets and co-currently delivered on the other side of the module while invoking zero transmembrane pressure. The diafiltration module consisted of an upper and lower chamber and was divided by a hydrophilic membrane (Durapore 125 μm, Millipore Inc.,) as shown in Figure 2.

A separate set of mass transfer experiments introduced an aqueous solution of 40% glycerol and 40% glycerol-dye solution into the engineered mass-transfer system. The experimental protocol for glycerol experiments were the same as that of water and dye experiments.

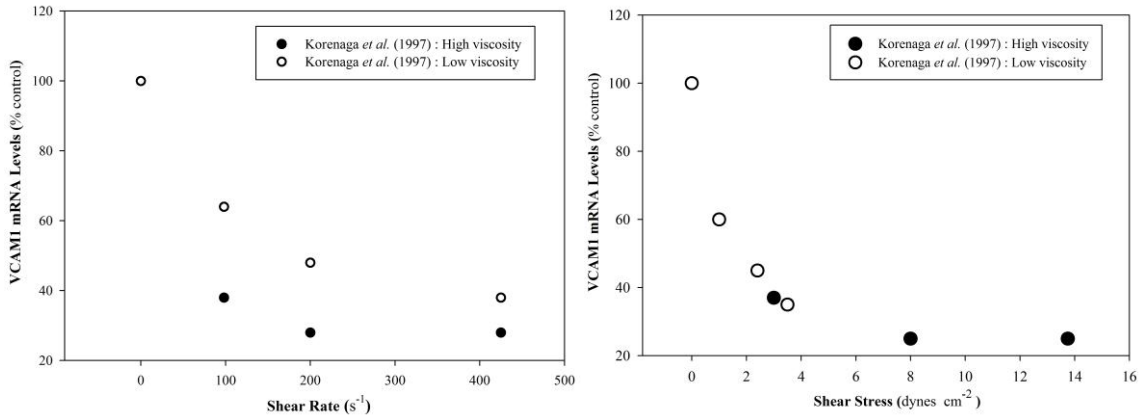

(A) **(B)**

Figure 1: Experimental Results by Korenaga *et al* (1997). The figure shows (A) the shear rate independency and (B) shear stress dependency of VCAM-1 mRNA transcription levels for a cellular system exposed to a medium having different flow rates and viscosities. The authors correlate the characteristic graphs to the dominance of mechanotransducers at the endothelium.

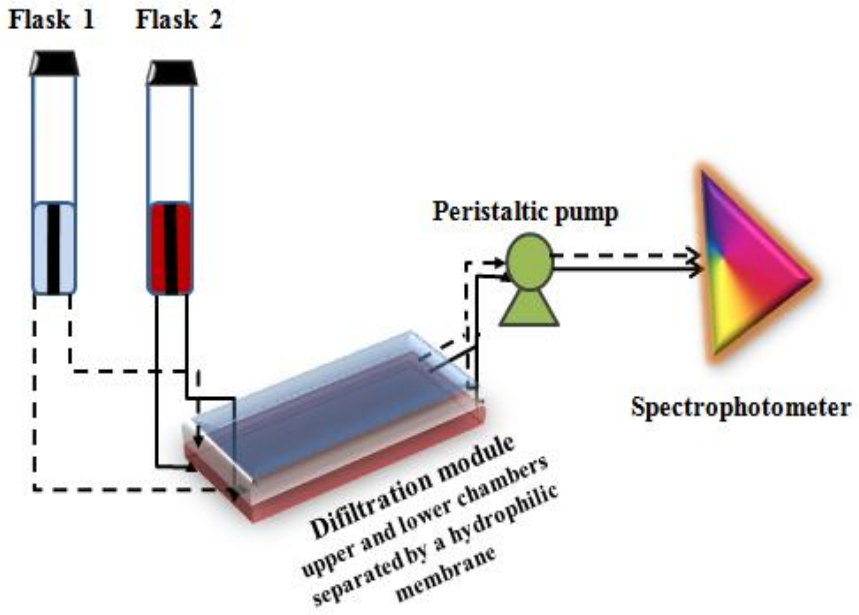

Figure 2: Experimental setup of the mass-transfer system. The difiltration module separates the upper and lower chambers of the system by a hydrophilic membrane.

The membrane was pre-soaked for 10 minutes and the system was primed and pressurized by the corresponding non-dye solution before and after each trial. The dye concentration of the inlet streams for the experiments was 0.25 g/l. Special care was taken while handling the glycerol samples by carefully stirring them to obtain spatially uniform concentrations of dye.

Samples were taken at different intervals for a time period of 10 minutes. A VIS (500 nm) spectrophotometer was used to quantify concentration of dye. SigmaPlot (Version 10.0.1.25) was used to analyze the data from the spectrophotometer. The resultant mass transport of dye was correlated to varied shear stresses and shear rates. Three trials of each experiment were performed.

Shear stress (τ) is defined as the tangential force of the fluid at the engineered-mass transfer system. It is the product of shear rate ($\dot{\gamma}$) and viscosity of the fluid.

$$\tau = \mu \dot{\gamma} = \mu \frac{\partial \mathrm{v}}{\partial \mathrm{x}} \tag{1}$$

The shear rate was captured by changing the viscosity of the fluid (water with a viscosity of 0.0098 g/cm/s and 40 % glycerol solution with a viscosity of 0.0378 g/cm/s).

Considering the dynamics of the emulated mechanotransducer-free vascular bed, the fluid phase is governed by the continuity equation (2) to ensure the mass conservation and the incompressible Navier-Stokes equation (3) to describe the momentum conservation.

$$v.\nabla v = 0 \quad (2)$$

$$\rho \frac{\partial v}{\partial t} + \rho v \cdot \nabla v = \nabla \cdot \left[\mu\left(\nabla v + (\nabla v)^T\right)\right] \quad (3)$$

where ρ is density of the water (or) glycerol solution.

The dye flowing through the system follows the equation of conservation of mass flowing through an incompressible medium and Fick's Law of Diffusion (4).

$$\frac{\partial C_o}{\partial t} + \nabla.\left(-D_{ij}\nabla C_o\right) = v.\nabla C_o \quad (4)$$

where, C_o is concentration and D_{ij} is the diffusion coefficient of the dye. C_o was 0.25 g/l and D_{ij} was 3.75×10^{-6} cm^2/s and 9.72×10^{-7} cm^2/s for water and glycerol solutions respectively.

Results and Discussion

(1) Calibration curve

The results of the experiments performed on this paper were based on the calibration curves obtained for the high viscosity and low viscosity solutions (Figure 3).

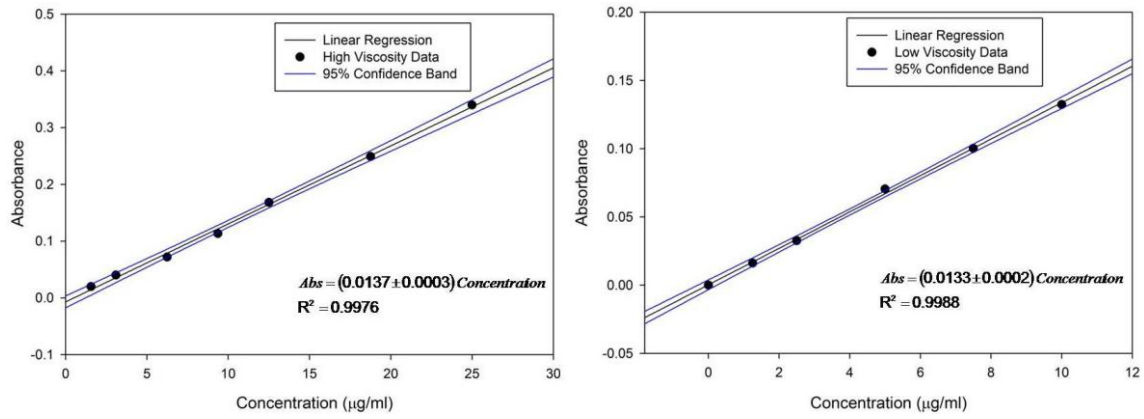

(A) (B)

Figure 3: Calibration curves for the (A) high viscosity solution and (B) low viscosity

(2) Concentration profiles: Mass transfer experiments for water and dye solutions were run at four flow rates: 8, 16, 32, and 64 ml/min and for glycerol-dye solutions were run at three flow rates: 7.42, 14.82, and 24.05 ml/min respectively. There were three trials run for every flow rate. All the trials reached a steady state concentration profile (the average concentration values are shown in Table 1) approximately after 5 time constants. Table 1 and Figure 4 show that as the flow rate increased, the concentration of dye increased for both high viscosity and low viscosity media.

Table 1: The Table shows the flow rates, calculated time constants, and steady state concentration values for low viscosity (water) and high viscosity (glycerol solution) respectively.

	Flow Rates(ml/min)	Calculated Time Constants(s)	Steady State Concentration Values(μg/cm^3)
Water	8±0.1	11.8	2.11±0.763
	16±0.13	6.0	2.69±0.205
	32±0.08	3.0	3.20±0.447
	64±0.2	1.5	4.41±0.385
40% Glycerol Solution	7.42±0.11	12.8	2.57±0.0942
	14.84±0.21	6.4	3.39±0.175
	24.05±0.31	3.95	3.95±0.105

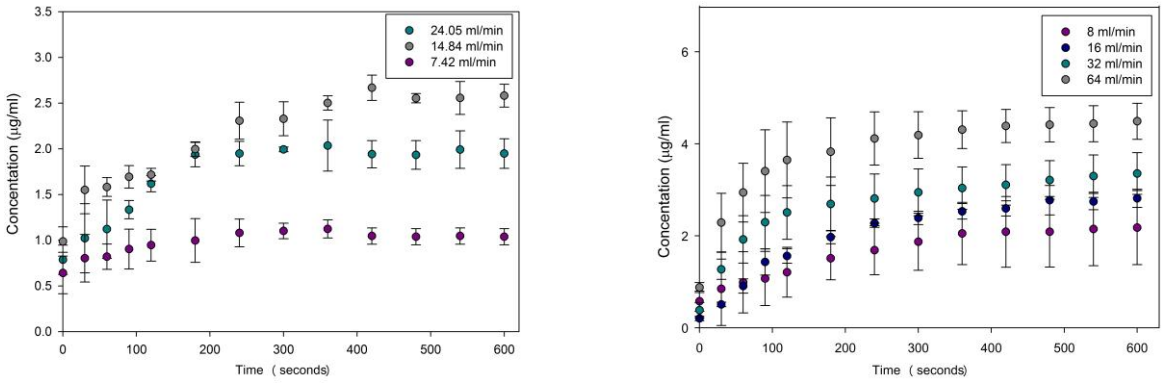

(A) **(B)**

Figure 4: Concentration profiles of Yellow #5 and #6 over time. The figure shows concentration profile reaching a steady value for (A) high viscosity solution and (B) low viscosity solution.

(3) Validating mass transfer system

The data from the above experiments were used to validate the mass transfer dependency of the engineered system. For a rectangular parallel flow chamber with laminar flow, The Sherwood Number(Sh),

$$\mathrm{Sh} = \mathrm{Re}^{n}\,\mathrm{Sc}^{m} \tag{5}$$

where, $\mathrm{Sh} \propto \mathrm{C}$ and $\mathrm{Re} \propto \mathrm{v}$, and *n* and *m* are Sherwood Coefficients. It has been shown that for a laminar flow, mass transfer corresponds to the one third order of the cross-flow shear rate at the membrane surface (or n=3).[10]

The log of all the concentration values versus the log of the velocities for the flow rates were plotted as shown in Figure 5. The Sherwood Coefficient, *n*, for our system was experimentally shown to be 0.3439±0.0132 and 0.366±0.0094 with an R^2 value of 0.97 and 0.9916 for low viscosity and high viscosity media respectively. This validates our engineered mass transfer system

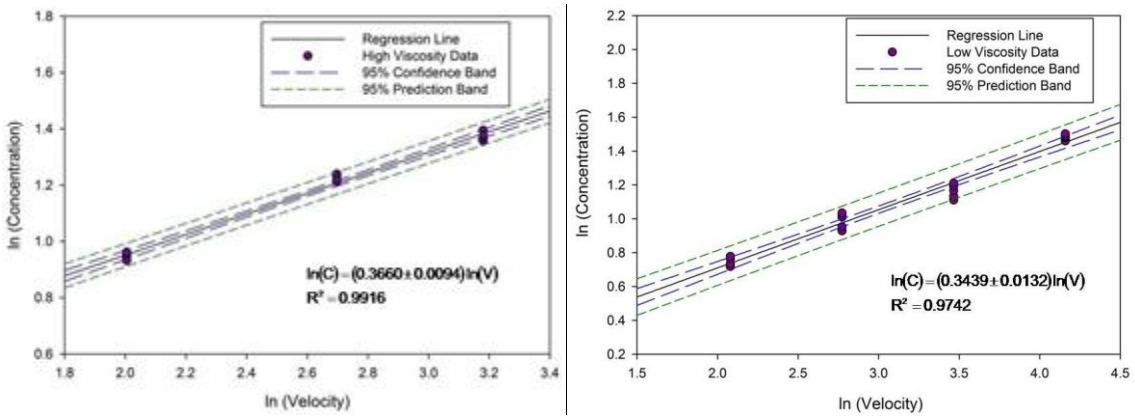

(A) (B)

Figure 5: Validating the in-house built mass transfer system. The figure shows the 95% confidence band and 95% prediction band for the system with (A) high viscosity solution and (B) low viscosity solution. (n=3) The high regression values demonstrates the success of the engineered mass-transfer system.

(4) Dye concentration for varied shear stress and shear rates

Figure 6 shows the shear rate versus normalized mass flux for two viscosities. These results follow the same results obtained by Korenaga *et al*. (1997) through their *in-vitro* experiments. We observe that for lower shear rate and higher shear rate, the consumed mass flux is independent of viscosities. For intermediate shear rates, consumed mass flux for the medium with higher viscosity is lower than that for lower viscosity. This can be accounted for by the thicker concentration boundary layer corresponding to higher viscosity of the medium.

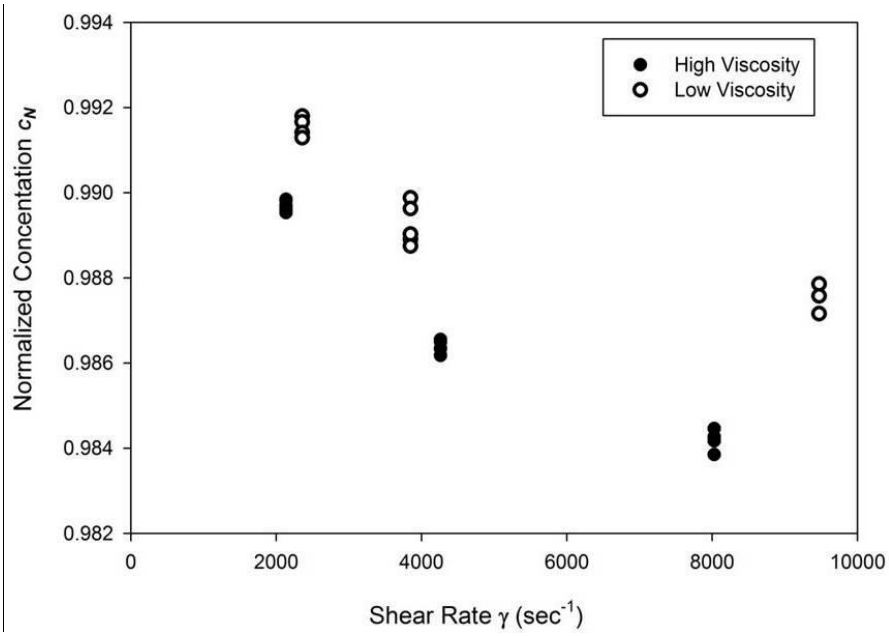

Figure 6: Results from the mechanotransducer-free emulated mass transfer system showing normalized consumed mass flux versus shear rate. As seen in the figure, mass transfer effect can account for the shear rate independency obtained from the in-vitro experiments of *Korenaga et al.* (1997) (shown in Figure 1A).[1]

Conclusion

The graphs of Figure 6 and Figure 7 validate our hypothesis that mass transfer at the endothelium surface plays a significant role in signaling pathways. The characteristic shear stress dependency and shear rate independency graphs that prove the importance of mechanical transducers in the vascular system[5], have been replicated in our mechanotransducer-free and mass transfer-only system. We conclude our paper by emphasizing the necessity of considering mass transfer variations while studying mechanisms of signaling pathways. Our future work will incorporate the use of a similar system to study the effect of pulsatile, oscillatory, and disturbed flows on species mass transfer.

References

1 Hardie DG, Salt IP, Hawley SA, and Davies SP. AMP-Activated Protein Kinase: an Ultrasensitive System for Monitoring Cellular Energy Charge. Biochemical Journal 1999;338:717-722.

2 Caro CG, Fitzgera JM, and Schroter RC. Atheroma and Arterial Wall Shear - Observation, Correlation and Proposal of a Shear Dependent Mass Transfer Mechanism for Altherogenesis. Proceedings of the Royal Society of London Series B-Biological Sciences 1971;177:109.

3 Ando, J. Cytoplasmic calcium response to fluid shear stress in cultured vascular endothelial cells. In vitro cellular & developmental biology, 1988, 24(9), 871

4 Ross R. Mechanisms of Disease - Atherosclerosis - An Inflammatory Disease. New England Journal of Medicine 1999;340:115-126.

5 Korenaga, R, and et al. "Negative Transcriptional Regulation of the VCAM-1 Gene by Fluid Shear Stress in Murine Endothelial Cells." *Am J Physiol Cell Physiol* 273 (1997): 1506-515.

6 Chien S. Effects of Disturbed Flow on Endothelium Cells.*Annals of Biomedical Engineering* 2008;36:554-562.

7 Chiu JJ, Wang DL, Chien S, Skalak R, and Usami S. Effects of disturbed flow on endothelial cells. Journal of Biomechanical Engineering-Transactions of the Asme 1998;120:2-8.

8 Fournier, Ronald L. *Basic Transport Phenomena in Biomedical Engineering*. Philadelphia, Pa.: Taylor & Francis, 1999.

9 Truskey, GA., Fan Y, and David FK. *Transport Phenomena in Biological Systems*. Upper Saddle River, N.J.: Pearson/Prentice Hall, 2004.

10 Wang, Y and Rodgers, VGJ.(2006) 'Ultrafiltration and Nanofiltration membranes', *Encyclopedia of Surface and Colloid Science*, 1: 1, 6394-6415

Appendix D
Computationally Evaluating Effects of Osteoconductive Bulking Agents on Stress Distribution in Reconstructed Mandible

Abstract

Previous studies of monkey mandibles were used to evaluate different forms of an osteoconductive bulking agent (compression-resistant matrix (CRM)) in a critical-sized mandibular defect.[1] Our research focuses on a finite element model which examines the mechanical efficiency of the CRM complex. We computationally modeled these matrix complexes using Comsol Multiphysics® to capture the von Mises stress as well as the deformation along the maxillary jaw. Subdomain conditions such as the density, Young's Modulus, and the Poisson's ratio were physiologically set. A separate subdomain within the jaw was modeled to represent the regenerative CRM complex defined with its physical properties. Two cases of mastication were considered: the closing stroke and the power stroke. Our aim is to ensure that the regenerated bone in the jaw can withstand the relevant mastication forces.

Keywords: Mandibular defects, Finite element model, Jaw clenching

Introduction

Functional and cosmetic defects to the mandible occur as the result of many different factors. These common factors include pathologic problems such as orofacial clefts, tumor excision, and post radiation necrosis [2]. Rare factors that cause damage to the mandible include injuries such as motor vehicle accidents, firearms, interpersonal assaults, burns, scalds, and electrical flashes.[2] Depending on the severity of the defect, it may be challenging to adequately repair the damaged mandible. A damaged mandible imposes a handicap on the individual such that there is a limited range of motion when attempting lateral and protrusive movements.[2-4] Other problems include difficulty with the contralateral muscles of mastication and malocclusion, which is when the teeth do not align correctly.[2- 4] Current research and work is being conducted to find ways to properly repair defected mandibles.

Previous research has found multiple approaches in addressing solutions for mandibular defects. Often mandibular reconstruction requires bone graft harvesting which results in donor site morbidity.[5] The use of tissue-engineered bone would correct this problem.[5] The works of Abukawa *et al.* (2004) have found a novel way in designing a scaffold and creating a new fabrication protocol to produce autologous tissue-engineered constructs to reconstruct segmental mandibular defects.[6] Another method found by Fennis *et al.* (2001) was to reconstruct the mandible by using specially designed osteosynthesis plates and screws.[7] Within these plates, autogenous bone graft was placed, along with platelet-rich plasma, which was used to speed up the healing

process.[7] David *et al.* (1988) found that the mandible can be reconstructed using vascularized iliac crest. [8] Iliac crest is the superior border of the wing of ilium in the pelvis.[8] In the study conducted by David *et al.* (1988) 35 patients underwent mandibular reconstruction with the vascularized iliac crest and 32 of the patients were reconstructed successfully with no donor site complications.[8]

Herford *et al.* (2012) used a novel recombinant human bone morphogenetic protein 2 (rhBMP-2) to reconstruct mandibular defects.[1] In doing the study, a compression–resistant matrix (CRM) was needed to ensure that there was sufficient space to avoid compression of the defected area while the new bone was forming. Thirteen Rhesus Macaque monkey mandibles were used to evaluate the rhBMP-2 and CRM against different forms of an osteoconductive bulking agent and an absorbable collagen. It was concluded that that the carrier system CRM combined with the rhBMP-2 resulted in higher bone density.[1]

For our study, we elaborated on the work conducted by Herford *et al.* (2012) by computationally examining the effectiveness of the rhBMP-2 and the CRM under two cases involved in mastication. Using finite element modeling, we were able to generate a mesh of a jaw with different subdomains that had different physical properties. From our computational model, we analyzed the von Mises stress and the deformation, in which we confirmed the effectiveness of the rhBMP-2 and the CRM in reconstruction of the mandible.

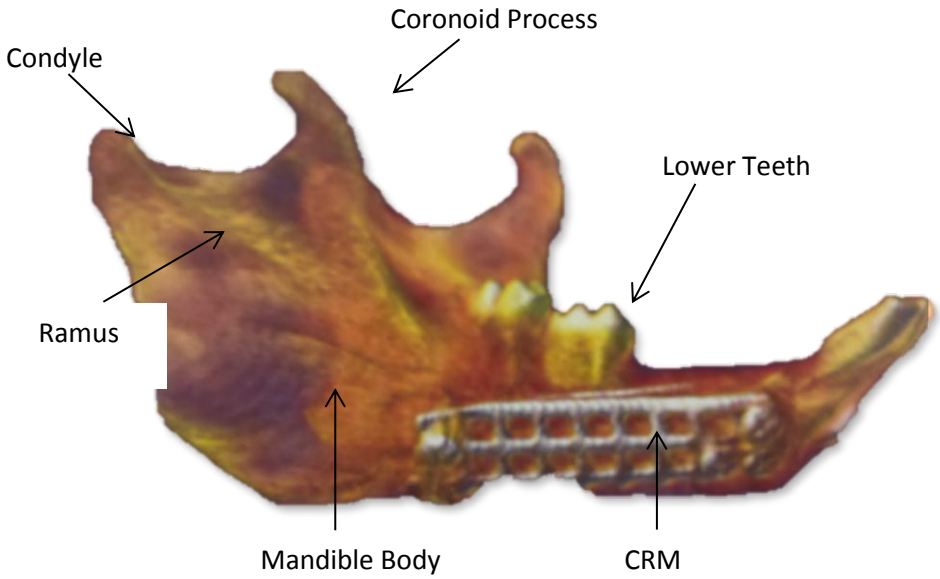

Figure 1: Amira® Figure illustrating a monkey jaw bone with CRM in a mandibular defect. Figure Courtesy of Herford *et al.* (2012)

Materials and Methods

Experimental methods

Thirteen Rhesus Macaque monkeys were used by Herford *et al.* (2012) to evaluate different forms of an osteoconductive bulking agent compared with an absorbable collagen sponge (ACS) alone placed into a critical-sized mandibular defect. The bulking agent they used was a mixture of hydroxyapatite (HA) and β-tricalcium phosphate (TCP) ceramic granules (Mastergraft Granules; Medtronic Sofamor Danek). Two different carriers were used for delivery of the rhBMP-2 solution. One was the ACS, and the other was a CRM composed of HA, β-TCP, and bovine collagen type I (Mastergraft Matrix). A total of 5 groups (26 defects) were evaluated by Herford *et al.*(2012): group A, rhBMP-2/ACS (1.5 mg/mL); group B, rhBMP-2/ACS with ceramic granules (15% HA /85% β-TCP) at 1.5 mg/mL; group C, rhBMP-2 (2.0 mg/mL) with a CRM; group D, rhBMP-2 (0.75 mg/mL) with a CRM; and group E, a CRM alone. [1] From the experimental work conducted by Herford *et al.*, they concluded that the group C, the rhBMP-2 (2.0mg/ml) with a CRM resulted in higher bone density.[1] This is where our focus is. We will be using the physical properties (Young's Modulus, Poisson's Ratio, and density) of group C in our computational model.

Computational model

For our study, we examined in Comsol Multiphysics (Module: Plane Stress; Version 3.5; Burlington, MA) the von Mises stress and the deformation with respect to the physical properties of the CRM and rhBMP-2 including Young's Modulus, Poisson's Ratio, and

density. The Young's Modulus captures the stiffness of an elastic material.[9] The Poisson's Ratio is the fraction of transverse strain to axial strain.[10] The von Mises stress is defined as the summation of all the stresses.

Model Properties

The mandible was separated into three different subdomains in Comsol Multiphysics® (Module: Plane Stress; Version 3.5; Burlington, MA), each with different physical properties such as Young's Modulus, Poisson's Ratio, and density. Subdomain A represents the original ramus and the mandible body. Subdomain B represents the regenerative matrix. Lastly, subdomain C represents the teeth. Physical properties respective to each subdomain can be found in Table 1.

Mesh Analysis

Initially we generated a 2D geometric replica of a mandible and ramus which contained 1830 mesh elements. This value was obtained by performing a tolerance test, which is used to determine the optimal value of the mesh elements. The results of the tolerance test were 0.339 seconds solving time and 0.99% tolerance.

Table 1: The table shows the values of the physical properties used in Comsol Mulitphysics® in each Subdomain. Subdomain A: ramus and mandible body; Subdomain B: regenerative matrix; Subdomain C: teeth

Subdomain	Density (Kg m^3)	Young's Modulus (GPa)	Poisson's Ratio
A	1400 [11]	1.5 [12]	0.33 [12]
B	4259 [13]	0.96 [14]	0.33 [12]
C	3140 [14]	89.7 [15]	0.33 [12]

Defining Cases: In our study we considered two cases involved in mastication.

Case 1: In Case 1, we simulated the closing stroke of mastication, which is defined by the initial closing of the jaw. In Case 1, only a loading force of 2 MPa[14] was applied in the Y direction at the tip of the tooth.

Case 2: In Case 2, we simulated the power stroke of mastication, which is defined by the clenching of the teeth. In Case 2, rotational forces were applied at the base of the mandible body. A force of 3.7 MPa[14] was applied in the X direction and a force of 6.5 MPa[14] was applied in the Y direction at the same time.

Case 1: Closing Stoke **Case 2: Power Stroke**

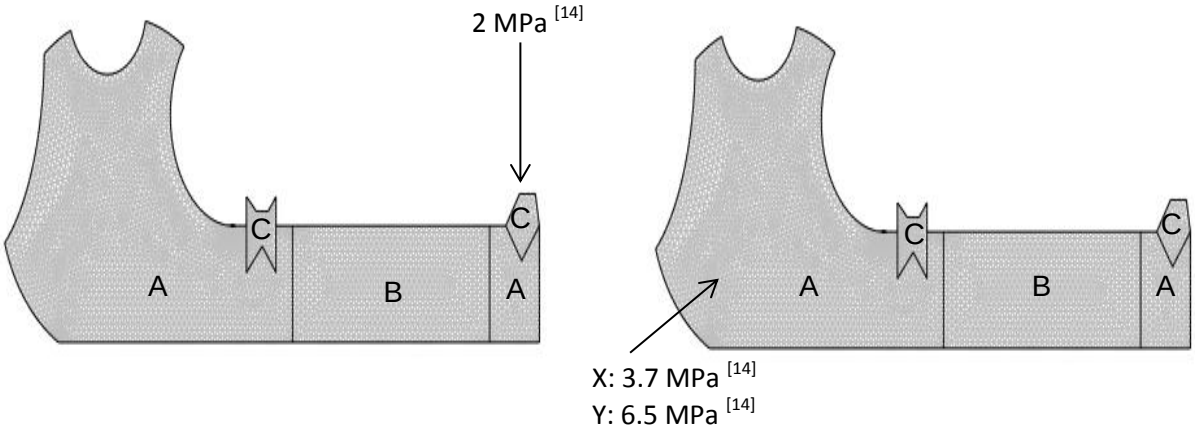

Figure 2: The Figure show the two cases of mastication. The figure on the left illustrates the closing stroke. The figure on the right illustrates the power stroke.

Results After simulating the two cases of mastication and post-processing, results were obtained illustrating the deformation and the von Mises stress for each case, respectively.

Case 1: In the closing stroke, maximum deformation was 3×10^{-6} cm. The deformation can be found around the tip of the tooth. The maximum von Mises stress was 5,865 Pa. The von Mises stress can be found mostly around the mandible body in subdomain A.

Case 2: In the power stroke, the maximum deformation was 0.22 cm. The deformation mostly found at the base of the mandible body in subdomain A. The deformation is distributed throughout subdomains B and C. The maximum von Mises stress was found to be 1.56×10^{7} Pa. The von Mises stress is predominately found in the ramus, the mandible body, the condyle, and the coronoid process.

An additional study was performed to examine the relationship between the Young's Modulus and the deformation independent of density and the Poisson's Ratio, with respect to the regenerative matrix, subdomain B. For this, the Young's Modulus was decreased from 0.96 GPa to 0.06 GPa in increments of 0.2 GPa. Deformation values were recorded for each case. Results (Table 3) obtained depict that with a decrease in the Young's Modulus there is an increase in the deformation.

Table 2: The table below shows the maximum von Mises Stress and the maximum deformation in the two cases.

Case	Max von Mises Stress (Pa)	Max Deformation (cm)
1	5,865	3×10^{-6}
2	1.56×10^{7}	0.22

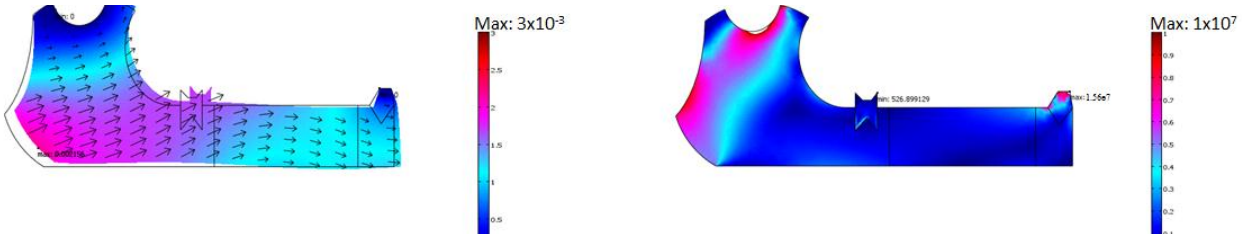

Figure 3: The figures above show the distribution of the von Mises Stress (Pa) and the deformation (cm) of each case.

Table 3: The Table below shows the relationship between Young's Modulus and deformation. As the Young's Modulus decrease, the deformation increases.

Young' Modulus (GPa)	Deformation (cm)
0.96	3.1
0.66	4.3
0.46	6
0.26	10
0.06	42

Discussion

Reviewing the two simulated cases, our results demonstrate that the deformation is minimal across the mandible body. Korioch *et al.* (1994) found the deformation in the mandible while the teeth were clenching (essentially Case 2, the power stroke) to be a maximum of 0.106 cm.[16] Even though our maximum deformation is higher (at 0.22 cm) than that found by Korioth *et al.* (1994), it is important to note that masticatory forces and the anatomy of the mandible vary within each individual.[17] This means that there can be a slight variation in deformation. This is of interest to us because it means that the regenerated section of the mandible is strong enough to withstand mastication without causing deformation to the jaw. It can also be seen that in both cases the deformation is never at a maximum in the subdomain representing the regenerative matrix.

The von Mises stress distribution also confirms that the regenerative matrix is strong enough to withstand mastication. Literature states that the cortical bone can hold anywhere from 92 to 188 MPa before breaking depending on the density.[18] The maximum von Mises stress calculated in our computational model is 15.6 MPa, which is well below the threshold of breakage. Almedia *et al.* (2011) found similar von Mises stress values when testing a mandible bone. They found their maximum von Mises stress value to be 27.9 MPa.[19] This is relatively close to our calculation of 15.6 MPa. We can therefore confirm that the regenerated segment of the jaw is capable of withstanding the two cases of mastication.

It was also found that with decreasing the Young's Modulus, there is an increase in the deformation. This holds true in that the Young's Modulus is a measurement of the stiffness of a material. This means that when the Young's Modulus is decreased, the stiffness of the CRM was decreased, which thus allows the mandible to deform more easily.

Conclusion

Herford *et al.* (2012) confirmed that the use of rhBMP-2 and the CRM is an effective means of regenerating bone.[1] The computational results we obtained, elaborated on the works of Herford *et al.* (2012) by confirming that the regenerated bone can withstand the forces relevant to cases of mastication. This furthers the possibility that in the future the use of rhBMP-2 and CRM will be a viable method of treating patients with mandibular defects. Future plans include utilizing a sample of the regenerative material to test for the actual physical properties (Young's Modulus, Poisson's Ratio, and density). These experimental values will be incorporated in a 3D computational finite element structure of the mandible.

References

1. Herford A, Buxton A, Henkin J, Caruso J, Rungcharassaeng K, Hong J, 2012 Recombinant Human Bone Morphogenetic Protein 2 Combined with an Osteoconductive Bulking Agent for Mandibular Continuity Defects in Nonhuman Primates, J Oral Maxillofac Surg, 70: 703-716

2. Rana M, Warraich R, Kokemuller H, Lemound J, Essig H, Tavassol F, Eckardt A, Gellrich N, 2011 Reconstruction of Mandibular Defects – Clinical Retrospective Research Over a 10-Year Period Journal of Head and Neck Oncology, 3:23

3. Foster RD, Anthony JP, Sharma A, Pogrel MA, 1999 Vascularized Bone Flaps versus Nonvascularized Bone Grafts for Mandibular Reconstruction: An Outcome Analysis of Primary Bone Union and Endosseous Implant Success Head and Neck, 21:66-71

4. Mehta RP, Deschler DG: 2004, Mandibular reconstruction in 2004:an analysis of different techniques. Curr Opin Otolaryngol Head NeSurg 12:288-93

5. Hadlock TA, Vacanti JP, Cheney ML: 1999Tissue engineering in facial plastic and reconstructive surgery. Fac Plast Surg 14:197

6. Abukawa H, Williams W, Kaban L, Troulis M, 2004 Reconstruction of Mandibular Defects with Autologous Tissue-Engineered Bone J Oral Maxillofac Surg, 62:601-606

7. Fennis J, Stoelinga P, Jansen J, 2001 Mandibular Reconstruction: A Clinical and Radiographic Animal Study on the use of Autogenous Scaffolds and Platelet-rich Plasma, J. Oral Maxillofac Surg, 31: 281-286

8. David DJ, Tan E, Katsaros J, Sheen R, 1988 Mandibular Reconstruction with Vascularized Iliac Crest: a 10-Year Experience Plastic and Reconstructive Surgery, 82(5):792-803

9. Rho J, Ashman R, Turner C, 1993 Young's Modulus of Trabecular and Cortical Bone Material: Ultrasonic and Microtensile Measurements, J. Biomechanics, Vol 26 111-119

10. Wortman J, Evans R, 1965Young's Modulus, Shear Modulus, and Poisson's Ratio in Silicon and Germanium, J. of Applied Physics 36: 153-156

11. S. Lovald, T. Khraishi, J Wagner, B Baack, J Kelly, J Wood 2006 Comparison of Plate-Screw SystemsUsed in Mandibular Fracture Reduction: Finite Element Analysis ASME Volume 128

12. F Zhang, J Chang, J Lu, K Lin, 2007 Fabrication and Mechanical Properties of Dense Porous β – Tricalcium Phosphate Bioceramics Key Engineering Materials. Vol 330-332

13. A Hartford, A Buxton, 2011 Recombinant Human Bone Morphogentic Protein 2 Combined with an Osteoconductive Bulking Agent for Mandibular Continuity Defects in Nonhuman Primates Journal of Oral Maxillafacial Surg.

14. M. Lupke, M. Gardemin, S. Kopke, H. Serfert, C. Stazsky 2010 Finite Element Analysis of the Equine Peridontal Ligament Under Masticatory Loading Vet Med. Austria 97 DOI: 10.4112-10-924

15. T. Huang, L. He, M. Darendeliler 2006 Correlation of Mineral Density and Elastic Modulus of Natural Enamel White Spot Lesions Using X-Ray Microtomography and nanoidentation.Acta Biomaterials Vol.6 Issue 12, 4553-4559

16. Korioth T, Hannam A, 1994 Deformation of the Human Mandible During Simulated Tooth Clenching J Dent Res: 73: 56-66

17. Hobkirk J, Havthoulas T, 1998 The Influence of Mandibular Deformation, Implant Numbers, and Loading Position on Detected Forces in Abutments Supporting Fixed Implant Superstructures J Prosthet Dent: 80: 169-174

18. S. Lovald, T. Khraishi, J. Wagner, B. Baack, 2007 Finite Element Analysis of Screw Plate Systems Fixation of Parasymphyseal Fractures of the Mandible Journal of Mechanics Vol 23:Issue 1 69-77

19. Almeida E, Rocha E, Assuncao W, Freitas A, Anchieta R 2011 Cortical Bone Stress Distribution in Mandibles with Different Configurations Restored with Prefabricated Bar-Prosthesis Protocol: A Three-Dimensional Finite-Element Analysis J of Prostdontics 20: 29-34